**THE MECHANICS OF SUBGLACIAL BASALTIC LAVA FLOW EMPLACEMENT:
INFERRING PALEO-ICE CONDITIONS**

by

Jefferson D. G. Hungerford

B. S. in Geology, University of Washington, 2002

Submitted to the Graduate Faculty of

The Kenneth P. Dietrich School of Arts and Sciences

in partial fulfillment

of the requirements for the degree of

Doctor of Philosophy

University of Pittsburgh

2013

UNIVERSITY OF PITTSBURGH

FACULTY OF THE KENNETH P. DIETRICH SCHOOL OF ARTS AND SCIENCES

This dissertation was presented

by

Jefferson D. G. Hungerford

It was defended on

November 8, 2013

and approved by

Dr. William Harbert, Professor, Department of Geology and Planetary Science

Dr. Thomas A. Anderson, Professor Emeritus, Department of Geology and Planetary Science

Dr. Daniel J. Bain, Assistant Professor, Department of Geology and Planetary Science

Dr. Tracy K. P. Gregg, Associate Professor, Department of Geology, University at Buffalo

Dissertation Advisor: Dr. Michael S. Ramsey, Professor, Department of Geology and

Planetary Science

**THE MECHANICS OF SUBGLACIAL BASALTIC LAVA FLOW EMPLACEMENT:
INFERRING PALEO-ICE CONDITIONS**

Jefferson D. G. Hungerford, PhD

University of Pittsburgh, 2013

Recent studies of terrestrial glaciovolcanic terrains have elucidated the utility of volcanic deposits as recorders of ice conditions at the time of eruption. Practically all of these investigations, however, have focused upon the associations of volcaniclastic and coherent lava lithofacies at or proximal to the source vent. Very few studies have documented the emplacement of effusion-dominated, basaltic glaciovolcanic eruptions and their distal deposits that more accurately reveal paleo-ice conditions. Both Mauna Kea volcano, Hawaii and the Tennena volcanic center (TVC), on Mount Edziza, British Columbia, Canada, preserve records of interaction between coherent lavas and an ice sheet inferred to be associated with the last glacial maximum (LGM). The identification, mapping and description of subglacial TVC lava flows reveal the spatial distribution and characteristics of primary volcanic lithofacies and associated glaciogenic lithofacies, and reveal the processes of the emplacement of the distal lava flows under thick ice. Exposure dating with cosmogenic nuclides proves the most effective technique to temporally constrain the emplacement of these subglacial lavas. This work shows; 1) classification schemes that utilize remotely sensed imagery are locally robust but are not readily viable as identifiers of subglacial lavas in other volcanic terrains, 2) the distribution of

primary hydrovolcanic clastic deposits at the TVC are confined to the cone, but coherent pillow lavas including distinctive vertically-oriented and distended pillows are widespread, 3) multiple lobes of massive sheet lavas record high initial magma discharge rates, 4) associated glaciogenic facies that underlie or onlap the TVC lavas indicate active subglacial meltwater drainage at the time of the eruption. Analyses of H_2O/CO_2 in pillow rim samples give broad constraints for emplacement pressures equivalent to 500-1400 m of overlying ice. No subaerial lava morphologies are found on the cone or in the proximal to distal lithofacies, and the sequence is interpreted as documenting an eruption of basaltic lava flows beneath either the LGM Cordilleran ice sheet or a Younger Dryas expansion of the still-extant Edziza ice cap. To further constrain the age of the eruption exposure dating with cosmogenic chlorine-36 is the most viable method as demonstrated on Mauna Loa explosive deposits.

ACKNOWLEDGEMENTS

TABLE OF CONTENTS

LIST OF TABLES

LIST OF FIGURES

1.0   INTRODUCTION

Volcanic rocks in high latitudes or high altitudes in tropical and subtropical terrains commonly exhibit evidence of lava-ice interaction. Eruptions taking place in the presence of ice may produce coherent and volcaniclastic deposits unique to glaciovolcanic environments. Volcanic eruptions under ice may produce deposits similar to those found in submarine environments or deposits resembling those found in typical subaerial volcanic terrains.

Assemblages of volcanic deposits in glaciovolcanic environments, however, tend to be quite unique to their environment. Many of the lithofacies assemblages have been described and interpreted as indicators of past glacial conditions. Investigations of glaciovolcanic deposits have focused mainly on deposits near their source vents, though a few have described vent distal deposits and their relationship to the environment in which they were placed. This dissertation is an attempt to identify distal glaciovolcanic deposits, describe their relationship with co-eruptive volcanic deposits and determine the parameters of their emplacement under a thick ice mass. Whereas other lava flows exhibiting ice-contact features have been identified, these flows were either erupted subaerially or were emplaced against thin ice. Distal basaltic lava flows found on Mount Edziza, British Columbia, Canada are identified and described and a model for their emplacement under thick ice is presented. Through subglacial lava flows like the massive sheet lava flows and pillow lava flows described here the thickness of the overlying ice mass may be inferred.

1

Ice thickness is a valid proxy for paleo climate conditions. However, the timing of subglacial eruptions must be established if they are to be of use as paleoclimate recorders, yet it is difficult to do so in eruptions perceived to occur after mid Wisconsin glacial stades. Given the paucity of organic carbon in glaciovolcanic terrains radiocarbon techniques are commonly not feasible in the dating of prehistoric glaciovolcanic eruptions occurring during or after the last glacial maximum. Though there are challenges, exposure dating techniques utilizing cosmogenic nuclides, chlorine-36 in this study, proves to be the best option to constrain the timing of eruptive events.

This dissertation comprises six parts including four manuscripts, each as a single chapter. Each manuscript is either in press or being prepared for submission to a peer review journal. The first manuscript, which comprises the second chapter, focuses upon the identification and differentiation of: 1) glaciated lava flows, 2) lava flows emplaced against or under ice and 3) non-glaciated lava flows based upon analyses of remotely sensed imagery. This chapter focuses on the development and implementation of a classification scheme to differentiate the lava flow types on unstudied volcanic terrains. The third chapter describes an entirely subaqueous glaciovolcanic basaltic eruption that took place within a thick ice mass on Mount Edziza, British Columbia, Canada. The fourth chapter focuses on the vent distal emplacement of coherent lava flows during the eruption described in chapter three. These lava flows were emplaced under a thick ice mass by exploiting the subglacial drainage system. The final chapter before the concluding remarks explores the use of cosmogenic chlorine-36 employing exposure-dating techniques applied to low-K, relatively young lava flows. This dating technique seems best if applied to relatively young lavas in vegetation free environments.

The deposits of glaciovolcanic terrains are increasingly being used as indicators of paleo-ice thicknesses and consequently as evidence of past climate conditions (e.g., Smellie, 2008; Smellie et al., 2008). The research results presented in this dissertation add to the capacity to constrain paleo-ice conditions at the time of eruptions and emplacement of distal lavas. This work may prove beneficial to those who wish to identify other terrestrial lava flows emplaced beneath ice.

2.0   IDENTIFICATION OF GLACIALLY WEATHERED LAVA FLOWS USING

ASTER

2.1   INTRODUCTION

The pervasive nature of Pleistocene glaciations is evident even in marine subtropical climes (e.g., Porter, 1986; 2005; Anslow et al., 2010). Within volcanic terrains, evidence of these glaciations lies within volcanic deposits (e.g., Allen, 1980; Smellie and Skilling, 1994; Schopka et al., 2006; Stevenson et al., 2006; Edwards et al., 2009; Tuffen et al., 2010; Edwards et al., 2011). More resistant to weathering than primary volcaniclastic deposits, lava flows can record both the temporal and spatial extent of glacial events. Both textural and chemical analysis of lava flows may reveal the presence of ice, and, in the case of glaciovolcanic activity, paleo-ice conditions. Glacially smoothed, gouged and striated lava flow surfaces typical of glacial weathering provide textural evidence of glaciations subsequent to flow emplacement. If subglacial conditions favor deposition of glacial sediments, these sediments may be preserved as sedimentary beds intercalated within lava flow sequences (Spooner et al., 1995). Lava flows emplaced in the presence of glacial ice commonly exhibit characteristic textures of subaqueous lavas and cooling surfaces from ice contact (e.g., Lescinsky and Fink, 2000; Edwards et al., 2002; McGarvie, 2009; Stevenson et al., 2009). Chemical analysis of ice contact lava flows can be used to constrain

cryostatic/hydrostatic pressures, and thus the ice thicknesses under which the lavas were emplaced (Dixon et al., 2002).

The use of remotely sensed data can potentially be an integral first step in the identification and differentiation of glaciated flows from subaerially emplaced lava flows. Further, an ability to differentiate ice contact lava flows from those that have been simply glaciated would be of great interest to researchers focused on using the products of volcano-ice interaction to discern information on paleo-ice conditions at the time of eruption.

This work analyzes remotely sensed data and investigates the capacity to differentiate the emissivity and reflectance spectral signatures of glacially modified lava flows from non-glaciated lava flows. Further, this work investigates the capacity to differentiate lava flows that were emplaced in the presence of ice from those that were emplaced subaerially and subsequently glaciated. The ability to identify and differentiate glaciated, non-glaciated and ice contact flows from one another would be an important tool in initial mapping efforts of volcanic terrains once subjected to Pleistocene glaciations, especially those in remote regions.

An Advanced Spaceborne Thermal Emission and Reflection Radiometer (ASTER) scene of Mauna Kea, Hawaii is used to classify the spectral characteristics of known glacially modified lava flows to those of non-glaciated flows and lava flows reported to have been emplaced against ice. The spectral characteristics of each are used to create end-member classes of glaciated, non-glaciated and ice contact lavas. These classes are used to create a classification scheme that could be used to identify glaciated and, possibly ice-contact lava flows, on other suspect volcanic terrains subjected to Pleistocene glaciation. In this study the classification scheme is applied to and ASTER scene of the volcanic terrain on the southern flanks of Mount Edziza, British Columbia, Canada.

Remotely sensed data from ASTER and other sensors have proven useful in identifying and mapping geologic features in both volcanic and non-volcanic terrains. These efforts to further increase initial mapping capacities within volcanic terrains are driven by the desire to identify and discriminate between lava flows possibly subjected to Pleistocene glacial events. A successful classification scheme differentiating glaciated and non-glaciated lava flows terrestrially could also be of use in identifying lava flows on Mars suspected to be emplaced in the presence of ice.

2.2 GEOLOGIC BACKGROUND

ASTER scenes of Mauna Kea and Mount Edziza were chosen for this study because there is evidence of Pleistocene glaciation on both volcanoes. Mauna Kea was chosen to test the classification scheme because glaciated, ice–contact and non-glaciated flows have been positively identified within the summit region. Mount Edziza was chosen as the test to apply the classification scheme to because investigators have identified evidence of lava–ice interaction but specific lava flows have not been well identified in the target study area.

2.2.1 Mauna Kea

There is ample evidence of late Pleistocene glaciations within the summit region of Mauna Kea (4205 m a.s.l.), whereas the summit region of Mauna Loa (4120 m a.s.l.) shows no evidence of glaciation. Mauna Loa, still in its tholeiitic shield building stage, erupts frequently enough to have covered 98% of its subaerial surface with lava flows less than 10 ka (Lockwood et al.,

1988; Lockwood, 1995; Trusdell, 1995). Mauna Kea, however entered the post shield phase 200 to 250 ka and last erupted approximately 4.5 ka (Wolfe et al., 1997). Much of Mauna Kea's surface comprises the alkalic hawaiite-mugearite lavas of the post shield Laupahoehoe Volcanic series (Stearns and Macdonald, 1942; Porter, 1979b). The lava flows and tephra cones of the Laupahoehoe volcanic series, initiating ~ 65 ka, make up the topography of the summit region (Figure 2.1).

2.2.1.1 Mauna Kea glaciations

Daly (1910) first reported evidence of Pleistocene glaciation on Mauna Kea (Porter, 1987). Investigators subsequently mapped the extent of glacial drift deposits, and described the timing of three Pleistocene glacial events (Wentworth, 1935; Gregory and Wentworth, 1937; Wentworth and Powers, 1941; Stearns, 1945; Porter et al., 1977; Porter, 1979b; Porter, 1986; Dorn et al., 1991; Porter, 2005). Recently, investigators have refined the timing and extent of the most recent glacial events on Mauna Kea, and used this information to reconstructed paleoclimate conditions (Blard et al., 2007; Pigati et al., 2008; Anslow et al., 2010).

Exposed in ravines on the Southern flank of the edifice, deposits of the oldest glacial event are intercalated with lavas of the Hamakua volcanic series, which precedes the Laupahoehoe series. The age of this glacial event, the Pohakuloa glaciation, is poorly constrained at ~150 ka (Dorn et al., 1991; Wolfe et al., 1997; Porter, 2005). The spatial extent of the Pohakuloa glaciation was roughly as great as the younger Waihu glacial event, which occurred 60 to 70 ka (Dorn et al., 1991; Porter, 2005). Moraines of the Waihu glaciation extend to an elevation of c.a. 3000 m on the southern flank, which is 1200 m below the summit of Mauna Kea (Porter, 2005).
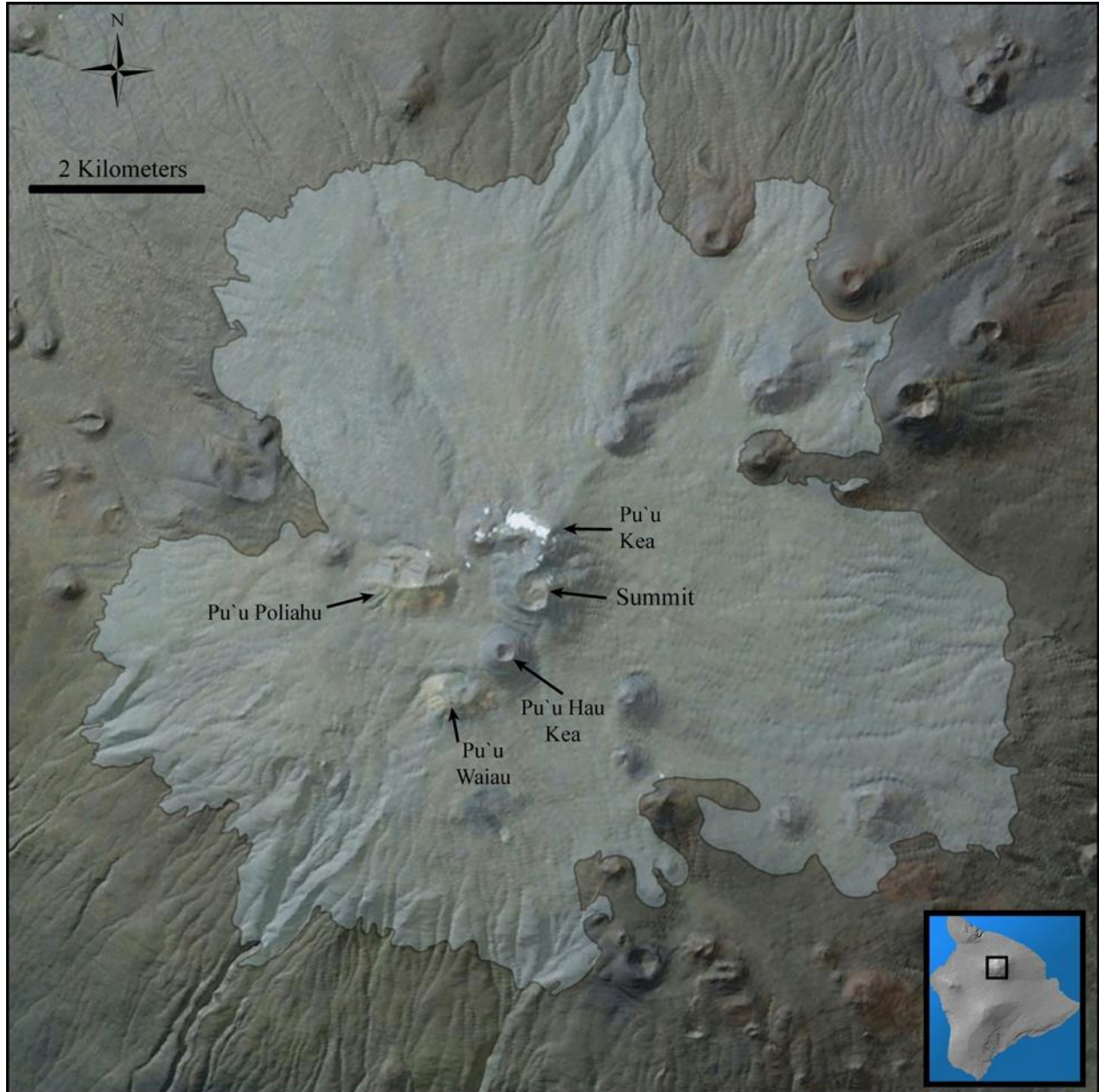
Figure 2.1. The extent of the youngest glaciation (Makanaka) within the summit area of Mauna Kea Volcano, Hawaii.

An ESRI basemap image overlies a DEM derived hillshade of the summit region of Mauna Kea. The location of the summit and prominent tephra cones are labeled. The area shaded in white represents the extent of the Makanaka Glaciation as mapped by Wolfe, et al., (1997). The location of the summit area noted in the boxed overlay of the Island of Hawaii. (Source: USGS. ESRI, DigitalGlobe, Icubed, USDA, AEX, Getmapping, Aerogrid, IGN, IGP, swisstopo and the GIS User Community)

The extent of the youngest glacial event, the Makanaka glacial event, is delineated by moraines that extend down to 3420 m elevation on the southeast flank (Figure 2.1). Two distinct glacial stades have been identified within the Makanaka glaciation. The maximum ice extent for these two advances occurred at 20.5 ka and 14.6 ka based on reported [3]He exposure ages (Anslow et al., 2010).

2.2.1.2 Mauna Kea glaciated flows

Tephra cones and surface flows within the extent of the Makanaka glacial ice are primarily lavas from the post shield stage Laupahoehoe Volcanics member, but older Hamakua Volcanics member basalt flows do crop out on the southern flank within the glaciated boundary (Porter, 1979a; Wolfe et al., 1997). All the surface lava flows within the extent of Makanaka glaciation predate the retreat of the younger Makanaka ice and are either covered with a veneer of poorly to unconsolidated glacial lag deposits or display evidence of mechanical weathering by glacial ice (Porter et al., 1977; Porter, 1979a; Porter, 1986; Wolfe et al., 1997). The lag deposits are poorly to unconsolidated, poorly sorted clasts comprising re-sedimented lava flow fragments and tephra deposits Figures 2.2a, 2.2b). Flows void of glacial drift deposits are commonly dense and fractured with glacially smoothed surfaces that commonly display glacial scour oriented parallel to sub-parallel to the dip of the aggregate topography (Figures 2.2c). The surface texture of these flows is the result of extensive glacial erosion that has removed the original flow surface breccia and rubble and exposed the dense centers to further glacial erosion (Figure 2.2d; Wolfe et al., 1997). Regolith of the glacially derived detritus commonly fills local topographic lows in the flow surfaces.
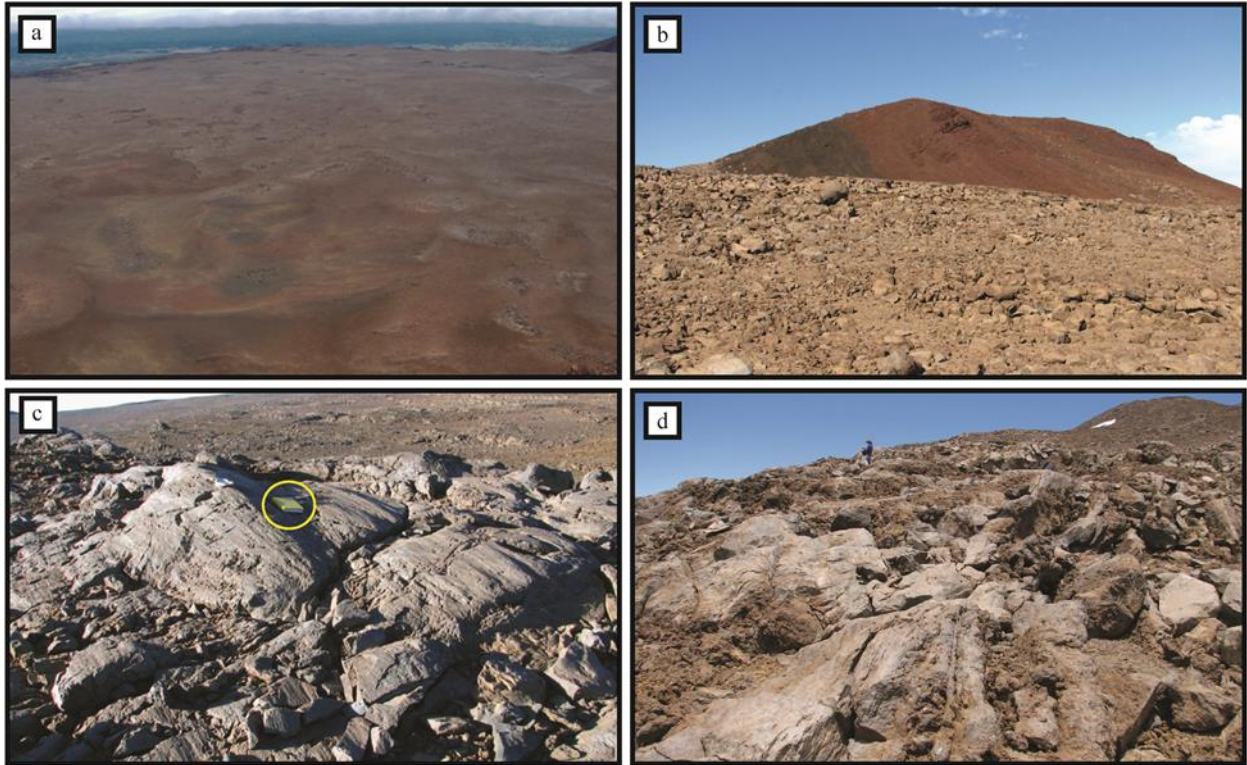
Figure 2.2. Images of glaciated lava flows on Mauna Kea.

(a) A view looking east from the summit looking east over glaciated lava flows. Tephra deposits lie atop the lava flows proximal to the base of the summit tephra cone from which the photograph was taken. Lavas distal to the summit cone are covered in glacial lag deposits and till. (b) A view looking east at glacial lag deposits and till lying atop a glaciated lava flow 1.5 km south of the summit. (c) A view looking north at glacial polish and scour on exhumed portions of interior lavas on the ice-contact lava flow north of Pu`u Poliahu. (d) A view looking southeast at a`a lava units on the surface of the Pu`u Kea lava flow. The surface clinker and vesicular zones have been removed by glacial erosion. The surfaces are well scoured and polished by subsequent glaciation.

2.2.1.3 Mauna Kea ice-contact flows

Among the glaciated lavas within the Makanaka glacial boundary are conspicuous lava flows with steep embayed margins and glassy surfaces that Porter (1987) described being emplaced subglacially. Porter (1987) described two subglacial lava flows, the Pu`u Poliahu flow and the Pu`u Waiau flow, that were emplaced southwest of the summit during the Waihu glaciation (Figure 2.3). Four flows were emplaced during the Makanaka glaciation (Figure 2.4; Porter, 1987). The Pu`u Hau Kea flow and the flow north of Pu`u Poliahu appear on Wolfe's (1997) geologic map of Mauna Kea. Wolfe (1997) also maps the western margin of the Pu`u Kea flow as a subglacial eruption but he does not discriminate the eastern extent of the flow from other glaciated flows as Porter (1987) illustrates (Figures 2.5, 2.6). The Pu`u Wekiu flow, while differentiated from glaciated flows by Porter (1987), does not appear on Wolfe's (1997) geologic map. The described lava flows are steep sided and tall, up to 30 m, stacks of individual lava flow units that display subaqueous emplacement lava textures (Figure 2.7a, 2.7b). Incipient to moderately well-formed, radially fractured pillow lava structures with well-developed glassy rinds are common along the flow margins (Figures 2.7c, 2.7d; Porter, 1987). Also along flow margins are zones of local palagonization and spiracles (Porter, 1987; Wolfe et al., 1997), though the glassy surfaces of spiracles have been interpreted as direct lava–ice contact textures (Figures 2.7e, 2.7f; e.g., Skilling, 2009).
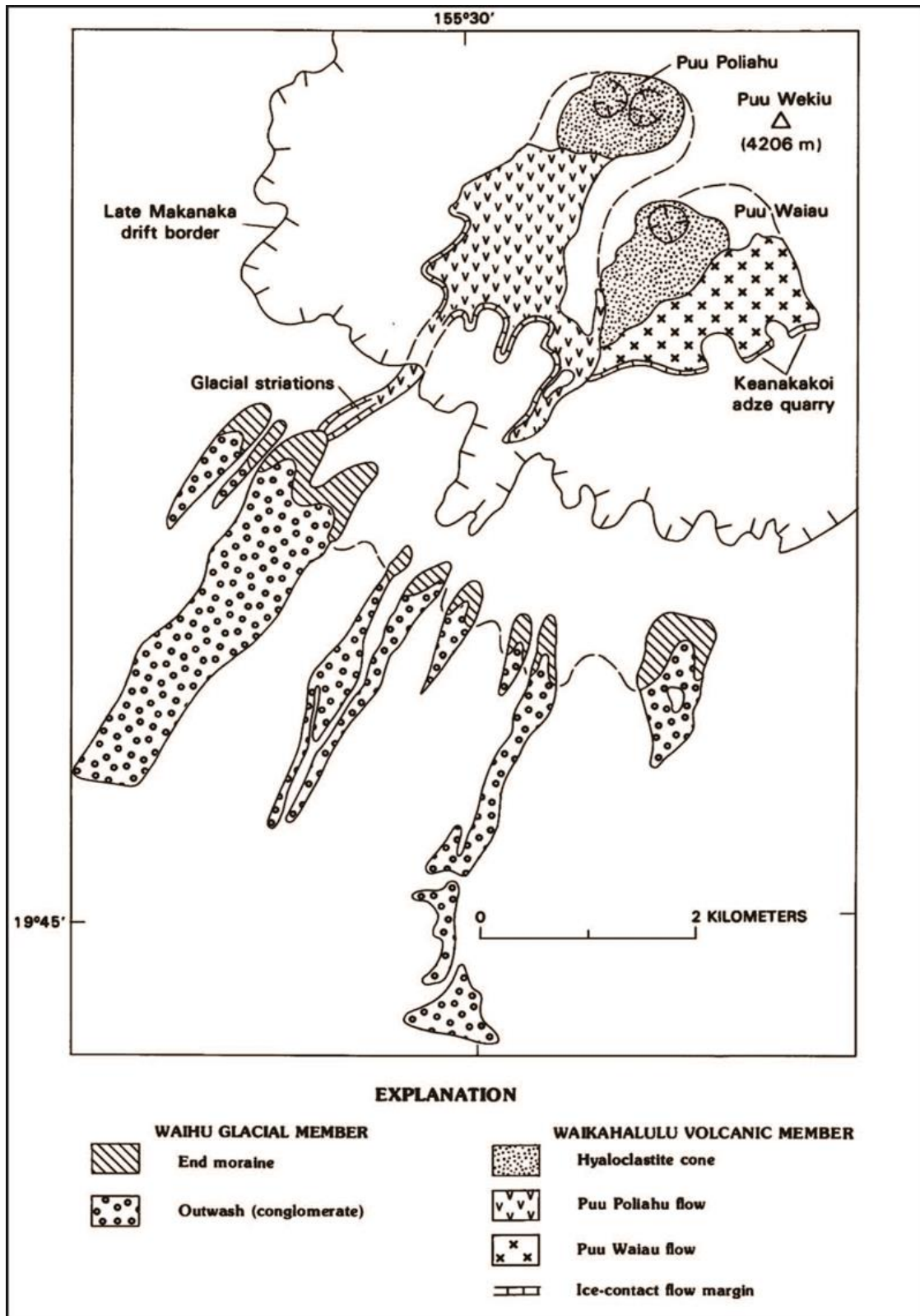
Figure 2.3 A cartoon from Porter (1987) of the subglacial or ice-contact lava flows emplaced during the Waiau glaciation.

12
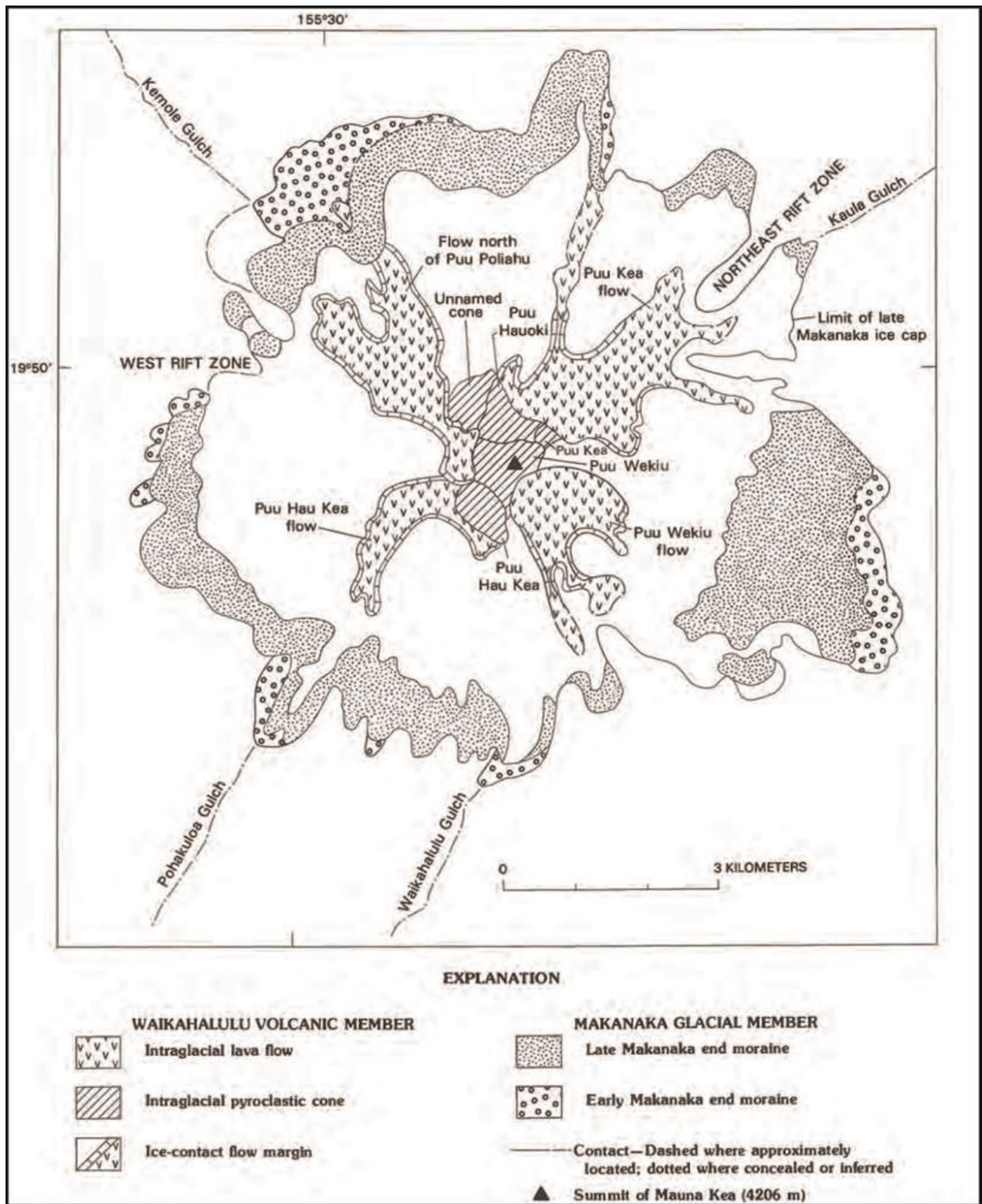
Figure 2.4 A cartoon from Porter (1987) of the subglacial or ice-contact lava flow emplaced during the stades of the Makanaka glaciation
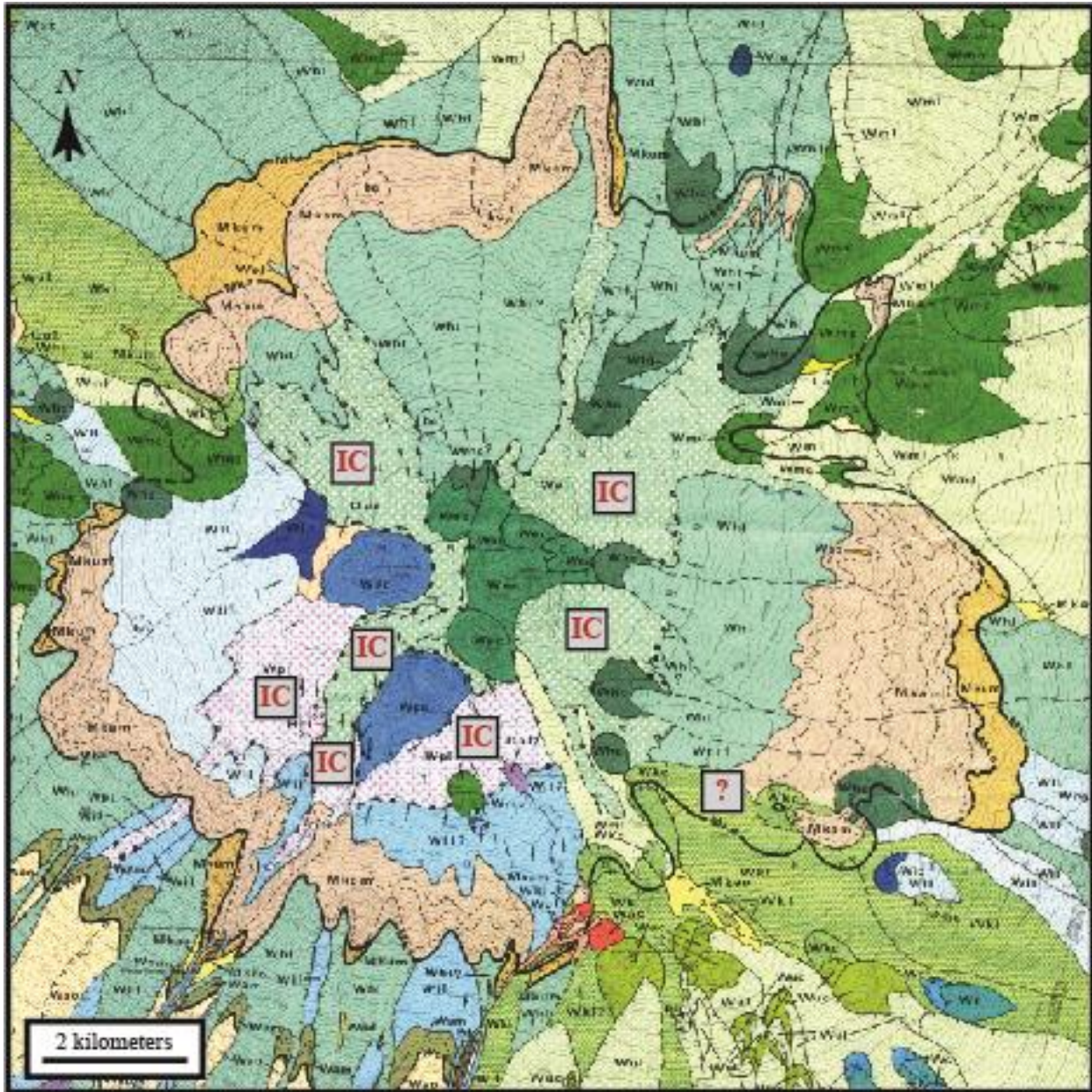
Figure 2.5 A geologic map of the summit region of Mauna Kea (Porter, 1979).

The purpose of this figure is to indicate the location of the ice-contact lava flows shown in figures 2.3 and 2.4, which are indicated with boxes containing the letters IC. The box containing a question mark (?) indicates the position of a lava flow that is clearly classified as an ice-contact lava flow but is not mapped as such by either Porter (1979a) or Wolfe et al. (1997).
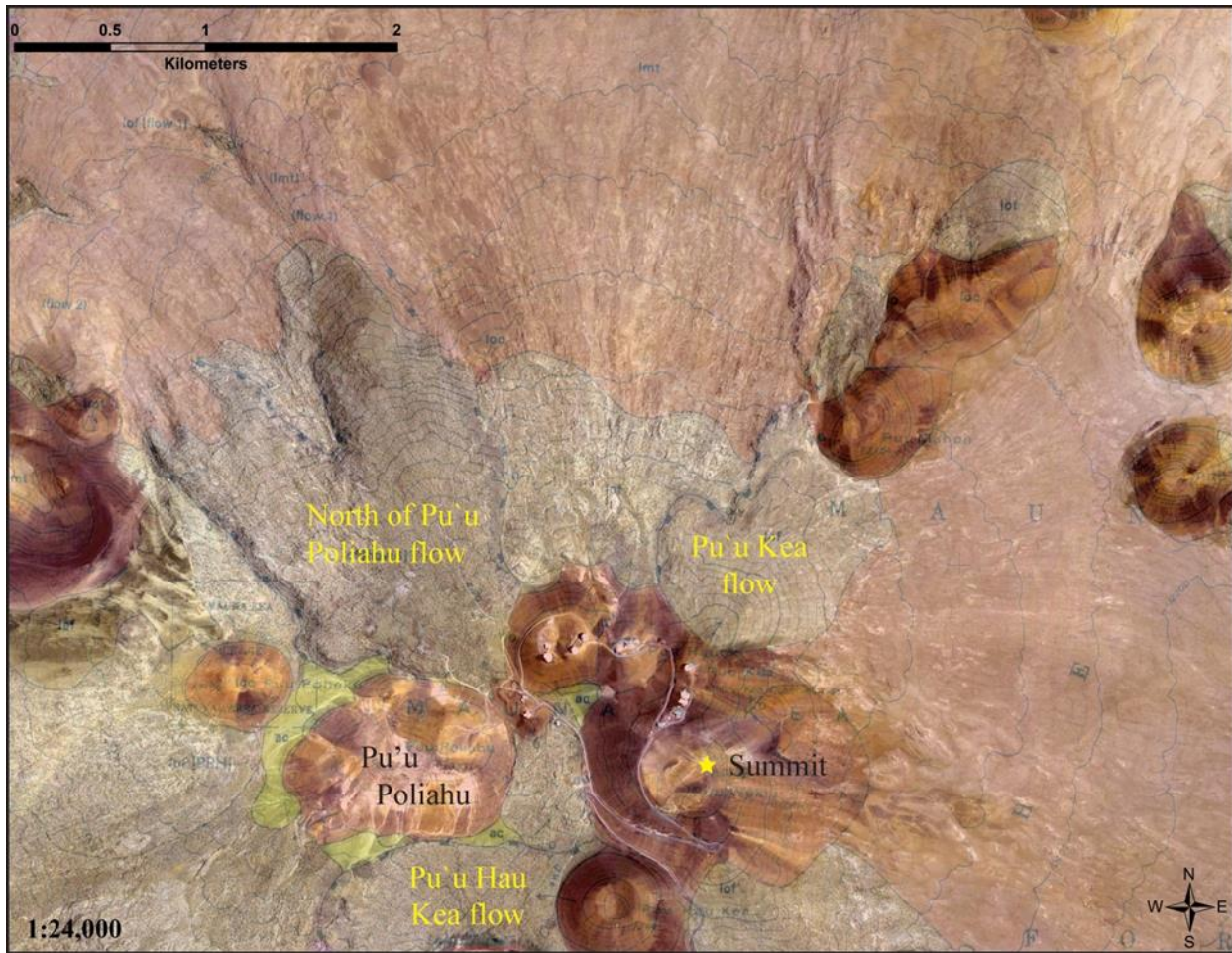
Figure 2.6. The Summit region of Mauna Kea.

A geologic map (Wolfe, et al., 1997) overlies an orthophoto or the summit area. Both images overlie a hillshade rendering with no vertical exageration. The three ice-contact lava flows mapped by Wolfe (1997) are labeled. Light orange and light gray areas are glaciated flows. Darker orange areas are tephra cones. Yellow shaded areas are colluvium. (Data source: USGS)
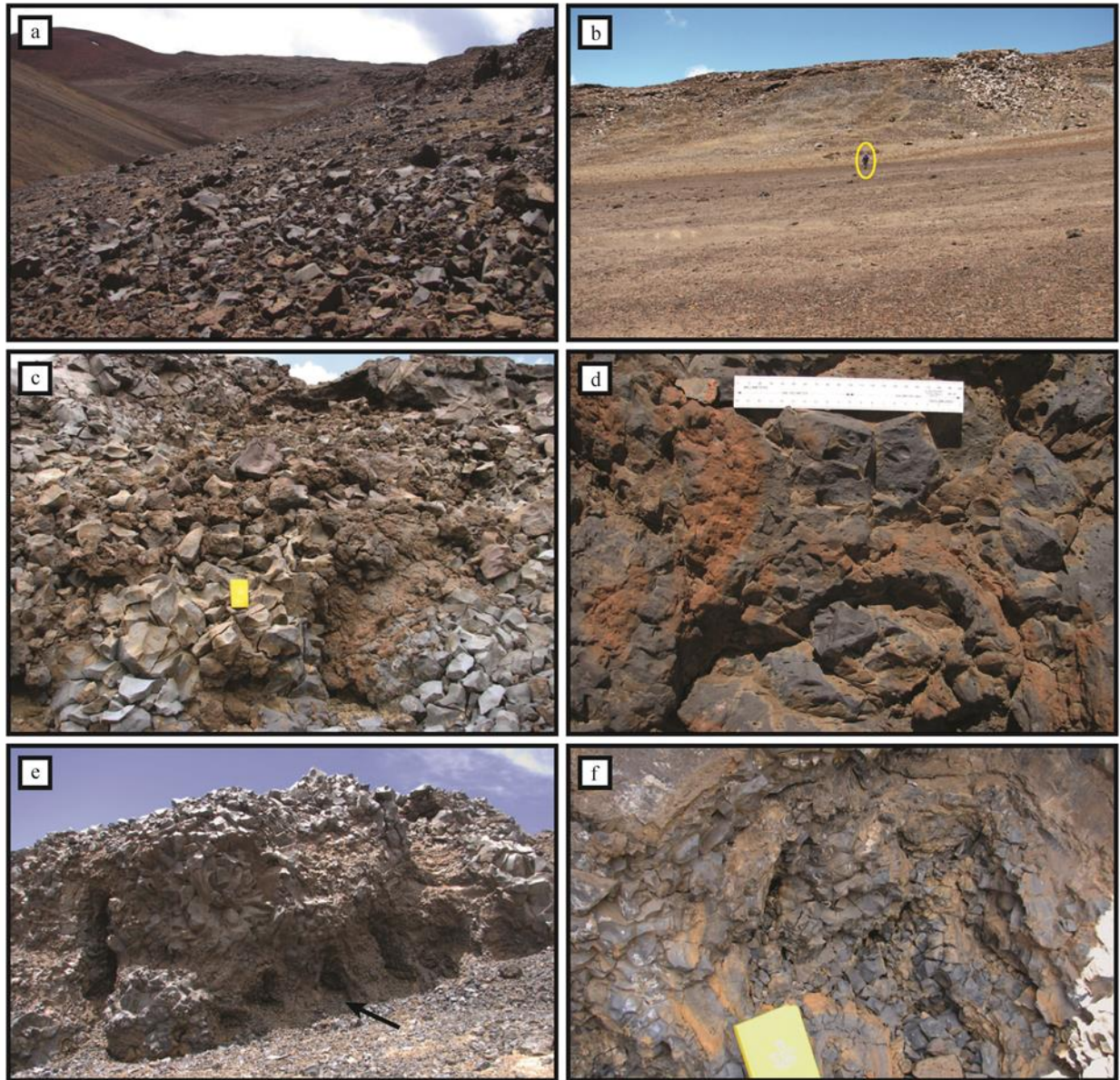
Figure 2.7. Images of ice-contact lava flows on Mauna Kea.

(a) A view looking west along the lateral margin of the ice-contact lava flow north of Pu'u Poliahu. Pu'u Poliahu is the brown, north-facing slope on the left center of the image. (b) A view looking north at the tall southern lateral margin of the Pu'u Kea flow. Notice the man for scale. (c) A view of incipient pillow lava structures and entablature in lavas of the Pu`u Kea flow. The yellow field book is 19 cm tall. (d) A view of pillow lava structures exhibiting concentric rings of insipient palagonization in the margins of the lava flow north of Pu`u Poliahu. (e) A view of spiracles or ice contact features an upper flow unit in the lava flow north of Pu`u Poliahu. The arrow indicates the location of Figure 6f. (f) A view of the interior of a spiracle or ice contact feature in Figure 6e. The glassy surfaces are intercalated with concentric band s of incipient palagonization. The top of the yellow book is 12 cm across.

Though Porter refers to these lava flows as subglacial, these flows are referred to here as ice-contact flows because there is no evidence these lavas were emplaced beneath ice masses or simply against ice or within ice-dammed bodies of meltwater. It seems reasonable, however, due to their high aspect ratios compared to other subaerially emplaced hawaiite lava flows of the Laupahoehoe Volcanic member, that these flows were emplaced in the presence of ice and, most likely, portions of abutted ice masses during their emplacement (e.g., Edwards et al., 2002).

2.2.2 Mount Edziza

Mount Edziza (2787 m a.s.l., $57^o42'58''N$, $130^o38'02''W$) is a long lived volcanic edifice in northern British Columbia Canada (Figure 2.8). The roughly 30 km long, 20 km wide edifice has been active since the late Miocene and last erupted within 2000 yr. B.P. (Souther, 1992). Souther (1992) mapped the edifice and characterized the evolution of the chemically bimodal volcanic activity into five cycles the begun with the eruption of alkalic basalts and culminated in peralkaline felsic lavas. The last eruptive cycle is known as the Big Raven Formation (BRF) and is marked by the eruptions of mostly alkaline basalts initiating within the waning stages of the last glacial maximum (Souther, 1992). Eruptions of the BRF primarily occurred on the northern and southern flanks of the Mount Edziza in local regions now known as the Desolation Lava field in the north and the Snowshoe Lava Field (SLF) on the southern flank. The ages of BRF volcanic activity are not well constrained but Souther (Figure 2.8; Souther, 1992) suggested the volcanic activity occurred during and after the last glacial maximum, and reported a Holocene radiocarbon age of 1340±130 BP for the youngest Desolation Lava field eruption.
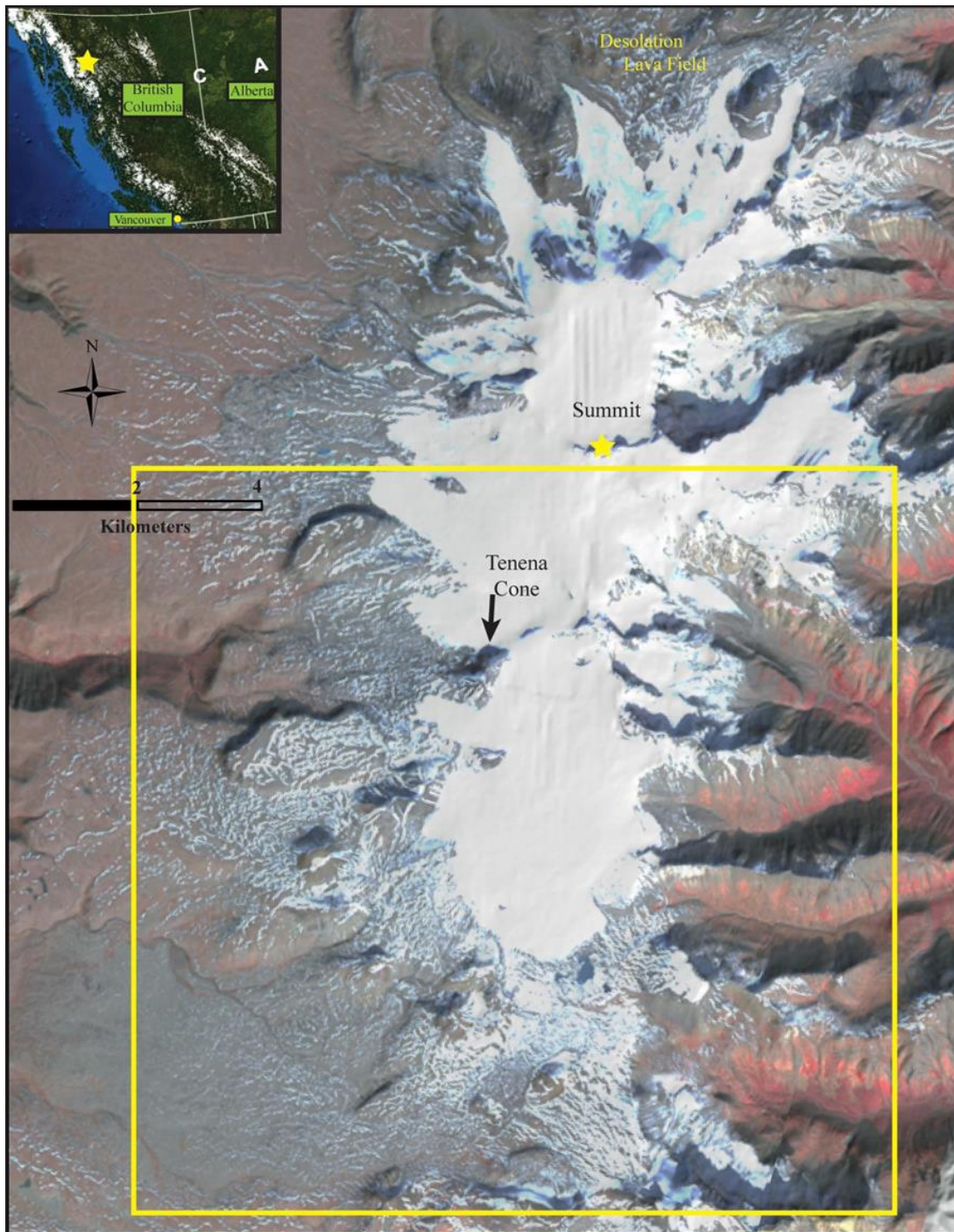
Figure 2.8. An RGB image of Mount Edziza

RGB image of Mount Edziza with bands 3, 2 and 1 of an ASTER scene collected on October 3, 2003 overlain on a DEM rendered hillshade of Mount Edziza. Tennena Cone, used as a location reference in Figure 2.8 is noted on the map. The yellow box indicates the extent of the ASTER scene used in the classification the Snowshoe Lava Field on the southern flank of Mount Edziza. The box in the upper left corner indicates the location of Mount Edziza in British Columbia, Canada.

There is evidence for lava–ice interaction in the SLF (Figure 2.9). Souther (1992) identified areas of lavas deemed to have been erupted in the presence of ice, erupted subaerially, and those that transitioned from subaqueously to subaerially erupted. The lavas of the SLF are of interest in this study. The intent is to differentiate individual glaciated SLF lava flows from non-glaciated flows, and further differentiate glaciated lavas from those emplaced in the presence of ice.
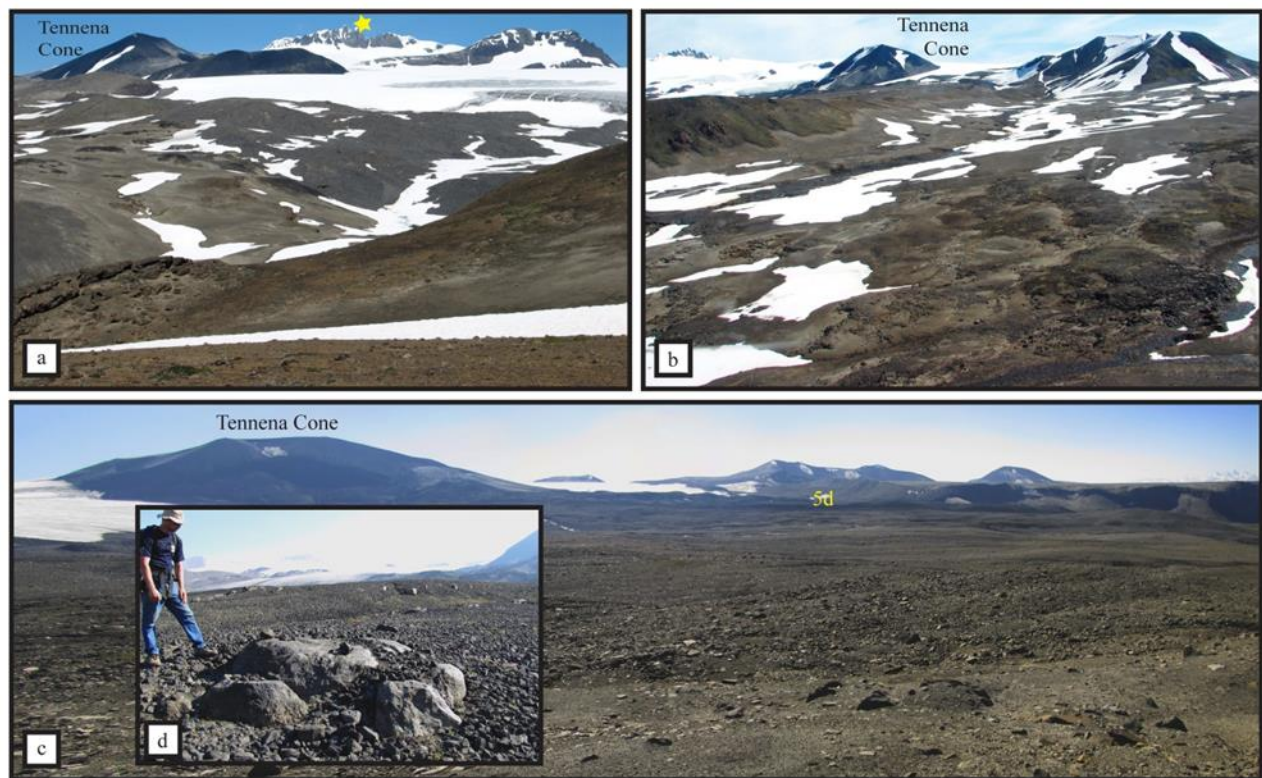
Figure 2.9. Images of Snowshoe Lava Field, Mount Edziza
Tennena Cone is indicated in each of the images as a spatial reference point. (a) View looking NNE at glaciated lavas of the Snowshoe Lava Field in the foreground. Tennena Cone, the glacier and the summit nunatak of Mount Edziza, which is indicated by the yellow star, are in the background. (b) A view looking northeast at Snowshoe Lava field flows further north on the southwest flank of Mount Edziza. Tennena Cone lies in the background. (c) A view looking SSE at the plateau west of Tennena Cone. The plateau is covered in a veneer of unconsolidated glacial lag deposits. The location of Figure 8d is indicated. (d) A view of an outcrop of a lava flow emerging from the veneer of boulder pavement. The lava flow outcrop has been glacially scoured and polished.

2.3   METHODS

The purpose of this study is to identify and differentiate non-glaciated lava flows from glaciated flows, and, if possible ice-contact lava flows, in remotely sensed data. Two ASTER scenes were selected; ASTER scene of Mauna Kea volcano (AST_L1A.003:2007429977) that contains known glaciated and ice-contact lava flows, and an ASTER scene of lava flows on Mount Edziza (AST_L1A.003:2025156522). Porter (1992) and (1979a) have mapped both glaciated flows and subglacial on Mauna Kea, but the extent of glacial interaction with individual lava flows in the study area on Mount Edziza is not well constrained.

The basic workflow of this study was to first to select ASTER scenes of the known glaciated volcanic edifice, in this case Mauna Kea, and select an ASTER scene of the SLF targeted area on the Mount Edziza volcanic edifice. The two scenes were preprocessed, corrected and then analyzed in the Environment for Visualizing Images (ENVI) software package. A classification scheme was developed from identified Mauna Kea lava flows and applied to the Mount Edziza ASTER scene that contains poorly constrained flows. The classification scheme was applied to the unknown flows and analyzed for its viability as an indicator of targeted flows.

2.3.1   Data preprocessing of the ASTER scenes

ASTER scenes were acquired on June 2, 2002 and October 3, 2004 for Mauna Kea and Mount Edziza, respectively. The ASTER level 2 visible and near-infrared (VNIR) and short wave infrared (SWIR) crosstalk corrected (07XT) data for both scenes were ordered and converted from DN to reflectance values by multiplying the pixel values by a band scale factor of 0.001. ASTER SWIR data for both scenes were resampled from 30 m to 15 m pixel resolution data

using ENVI software and with the 15 m VNIR to create on file for each scene. The thermal infrared ASTER (TIR) atmosphere corrected surface radiance data for both scenes were converted from DN values to radiance by multiplying TIR bands 10 through 14 by band specific band scale factor values. The ASTER TIR bands were further recalibrated to correct for drift in the TIR instrument over time (Tonooka et al., 2004). Corrected TIR radiance file were then separated into temperature (K) and emissivity using the ENVI emissivity normalization function (and an assumption of max emissivity of 0.985). These files were finally resampled to 15m data using the ENVI resize data function and the nearest neighbor option.

A master file for each scene comprising the reflectance, emissivity, and temperature values at 15-m/pixel resolution was created by combining the VSWIR and TIR files. A micron-scale roughness model was run on the TIR emissivity data using laboratory end-member spectrum data from volcanic glass and a blackbody (Ramsey and Fink, 1999). The micron-scale roughness model is a least squares deconvolution model based on a linear mixing relationship between a low emissivity, silicic glass blackbody end member and a high emissivity, rough surface end member (e.g., vesicular lava) at TIR wavelengths (Ramsey and Fink, 1999). The micron-scale roughness model data was also resampled to 15 m pixel resolution using the ENVI resize data function and the nearest neighbor option. The micron-scale roughness model data was then added to each master file to create a 16 band file that comprises VNIR, SWIR, TIR, temperature and vesicularity data at a 15 m/pixel resolution. Finally, the headers of the two files were edited to update the band names and wavelength values.

2.3.2   Mauna Kea scene analysis

The analysis of the 16 band preprocessed ASTER scene of Mauna Kea was limited to a 900 x 900 pixel section roughly centered on the summit region of the volcano. From this scene section classes were derived and used as the regions of interest in the classification scheme applied to the rest of the 900 x 900 pixel Mauna Kea summit scene.

2.3.3   Creation of classes

An unsupervised K-means classification was first performed on the Mauna Kea ASTER scene to check the viability of producing a supervised classification scheme for the Mauna Kea ASTER data (Ramsey and Fink, 1999). The K-means classification was set to six classes and run through ten iterations. The K-means classification produced a scene with visually recognizable classes resembling the target classes defined for this study (Figure 2.10a).

The Mauna Kea ASTER scene was then processed through the minimum noise fraction transform (MNF) function in ENVI to determine the variance in pixel values for each band over a background noise or data error threshold (Lloyd, 1982). Greater variance of the data between pixels is expressed as a large eigenvalue for each MNF transformed band. Eigenvalues at or below 1 indicate only noise is left in the transformed band (Boardman and Kruse, 1994). Values for the MNF transformed scene were highest for VNIR bands and approached 2.5 in the TIR, temperature and roughness bands (Table 2.1). All bands therefore have a variance in pixel values above the noise threshold.
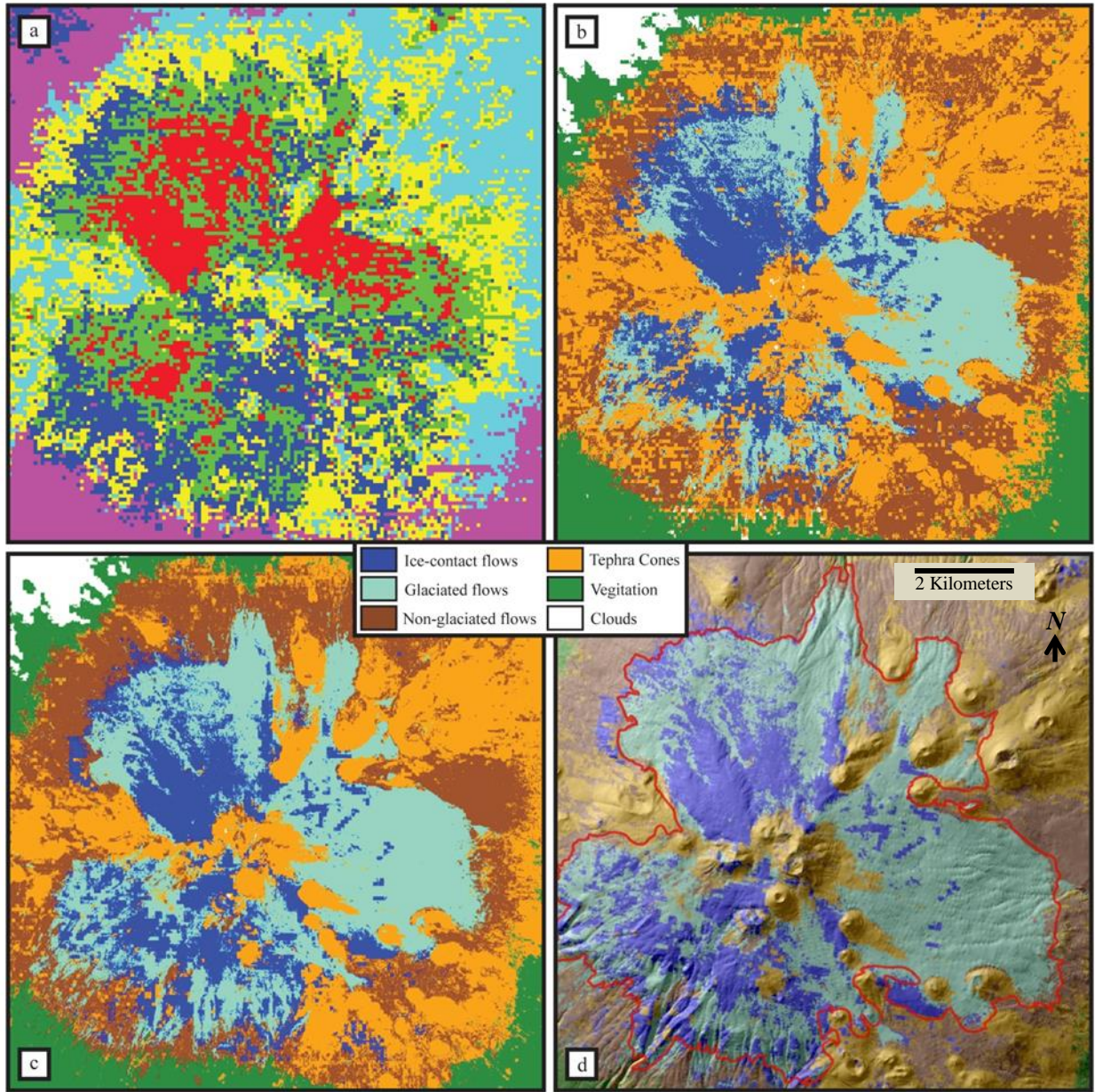
Figure 2.10. Classification images of the Mauna Kea Summit area.

(a) An image of a 6 class, unsupervised k-means classification of the Mauna Kea summit area. (b) An image of a 6 class, supervised Maximum Likelihood classification using all wavelength bands and the temperature (band 15) and micron scale roughness band (band 16). (c) An image of a 6 class, supervised Maximum Likelihood classification using wavelength bands 1-5, 11, 12, and the temperature (band 15) and micron scale roughness band (band 16). (d) An image of the classification shown in Figure 2.9c draped over a DEM derived hillshade of the Mauna Kea summit area. The red line indicates the extent of the Makanaka glaciation ice boundary. The legend overlying c and d identifies the classes in b, c and d only.

Table 2.1. Wavelength band Eigenvalues for the Mauna Kea ASTER scene

Band	Eigenvalue
1	365.16
2	121.75
3	91.44
4	44.20
5	34.85
6	21.17
7	17.47
8	13.51
9	11.85
10	8.29
11	5.27
12	3.37
13	2.96
14	2.83
15	2.79
16	2.75

Classes representing hawaiite-mugearite ice contact, glaciated and non-glaciated lava flows and tephra cones were created from deposits identified in geologic maps created by Wolfe et al. (1997) and Porter (1979a, 1987), USGS orthophotos, and field observations. The classes were then developed as regions of interest (ROI) within ENVI software. Classes for vegetation and clouds were derived directly from the ASTER scene of Mauna Kea in ENVI.

A polygon was drawn around the lava flow north of Pu'u Poliahu to represent the ROI of ice-contact lava flows (Figure 2.6). Glaciated lava flows were represented by polygons drawn on portions of lava flows within the extent of the Makanaka glaciation that were not identified as subglacial or ice-contact lava flows. Portions of Holocene lava flows outside the extent of the Makanaka glaciation were chosen as the non-glaciated lava flow ROI. Portions of readily

identifiable tephra cones, clouds and vegetated areas were used as ROIs for their respective ROI classes.

The mean VNIR, SWIR and TIR spectral data of the four ROIs representing ice-contact flows, glaciated flows, non-glaciated flows and tephra cones were plotted (Figure 2.11). Wavelength bands with the greatest variance between the mean ROI values, along with the temperature (band 15) and micron-scale roughness band (band 16), were chosen to discriminate between the ROI's. The nine wavelength bands selected were VNIR bands 1-4, SWIR band 5, TIR bands 11 and 12, band 15 and 16.
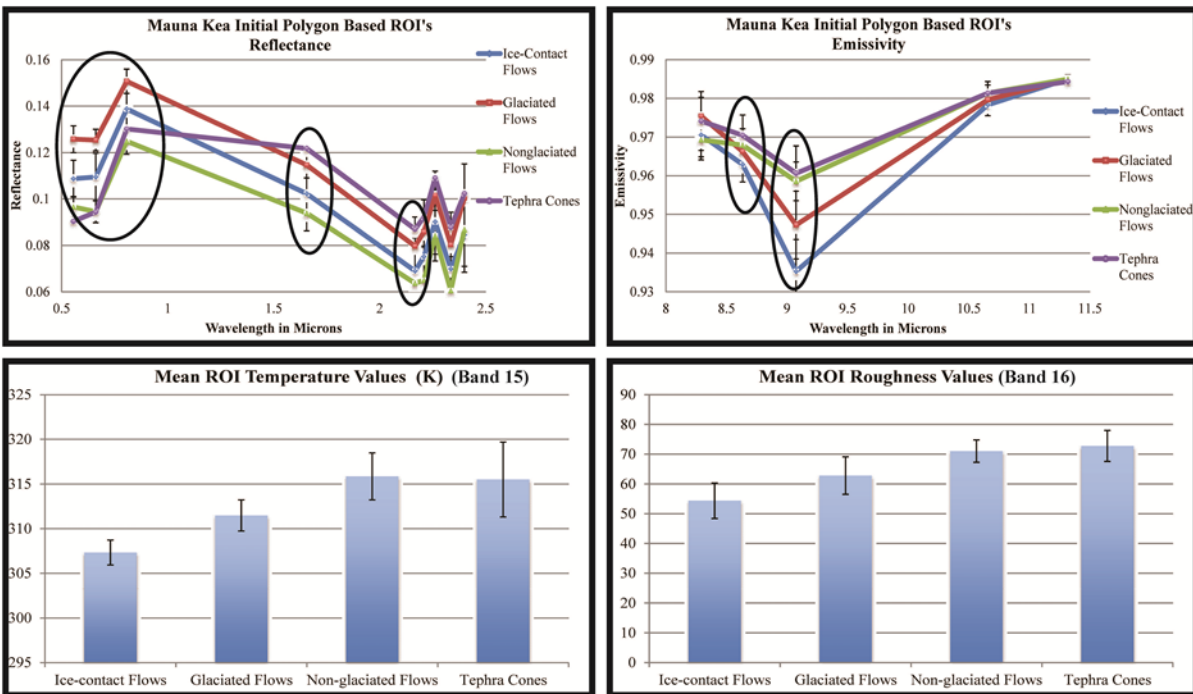
Figure 2.11. Graphs of the Mauna Kea polygon based ROI reflectance and emissivity values for the ASTER wavelengths

The bar graphs indicate values of the temperature (band 15) and micron scale roughness values (band 16) for the polygon based ROI's. The error bars represent the standard deviation of values for each band in each class.

The four lava, cloud and vegetation polygon based ROI's were loaded into the ENVI software n-D visualizer tool to create four classes with distinct spectral signatures by removing overlap in the spectral data for each of the classes. Each of the bands selected represented nine axes rendered in 2D space within the n-D visualizer. Clusters of the four lava ROI pixels overlapped in the n-D visualizer. Discrete boundaries were therefore drawn around the high ROI pixel density areas to spatially separate and discriminate between the ROI pixel clusters. These discrete pixel clusters replaced the polygonal, area based ROI's initially drawn. The new pixel based ROI's were now defined by mean spectral values for each of the nine bands rather than defined by the spatial extent based on mapping of the outcrops (Figure 2.12). The pixel based ROI's for the four lava end-members were plotted on the ASTER scene of Mauna Kea, and pixels lying outside of the spatial extent of the original, polygon based ROI's (>> 1% of pixels) were removed from the pixel based ROI's. These pixel-based ROI's were the six end-member classes used in the classification of Mauna Kea summit region lavas. The described method proved more effective than the other methods of creating pure end-member classes that were attempted. Other end-member class development methods either did not produce viable classification scheme outcomes or produced outcomes inferior to the described method.

2.3.4   ASTER classification of Mauna Kea

The end-member classes for the ice-contact, glaciated, non-glaciated lava flows and tephra cones were represented by the four pixel based ROI's. ROI's were also used to mask clouds and vegetated areas in the Mauna Kea scene. The spectral data from the six classes were entered into
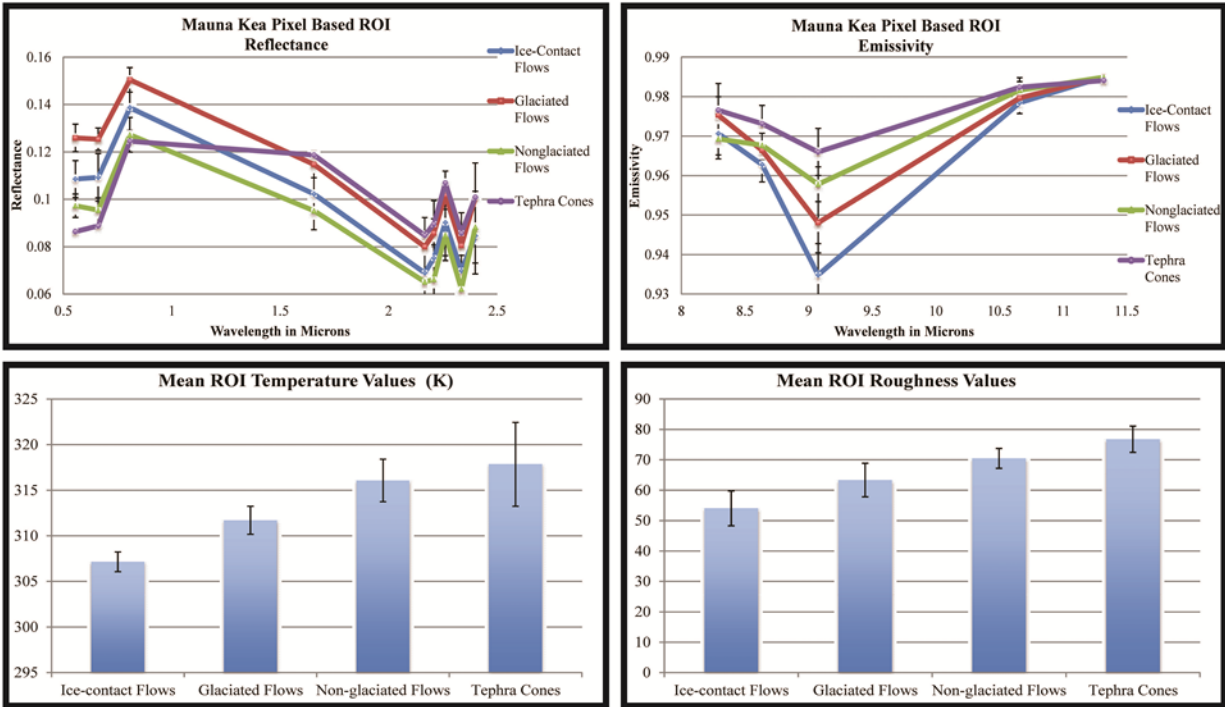
Figure 2.12. Graphs of the Mauna Kea based ROI reflectance and emissivity values for the ASTER wavelengths.

The bar graphs indicate values of the temperature (band 15) and micron scale roughness values (band 16) for the polygon based ROI's. The error bars represent the standard deviation of values for each band in each class.

several of the classification functions available in ENVI. The outcome of each classification function was then compared to the Mauna Kea ASTER scene and geologic maps, and the Maximum Likelihood classification scheme was deemed the most viable fit to the known data Wolfe et al. (1997).

2.3.5   ASTER scene classification of Mount Edziza

In the processed Mount Edziza ASTER scene an 800 x 800 pixel section containing the target Snowshoe Lava Field was chosen (Figure 2.13a). Two unsupervised K-means classifications with ten iterations, one with nine classes and one with eight, were performed on the 16 band

resampled ASTER dataset to determine the viability of subsequent supervised classifications (Figure 2.13b). ROI's for vegetated areas, ice, snow, clouds, and cloud shadows in the Mount Edziza ASTER scene were created to mask these areas from classification. The mean spectral data from the ice-contact lava flow, glaciated flow, non-glaciated flow and tephra cone ROI's developed in the Mauna Kea ASTER scene were used as class end-members in the Maximum Likelihood classification applied to the Mount Edziza scene. The classification was performed initially with the 9 bands used to classify the Mauna Kea ASTER scene then was performed again with all 16 available bands. The outcome was deemed inadequate because all lava flows were classified as tephra cones (Figure 2.13c). Multiple classification iterations were subsequently performed and the classification deemed the best fit was produced without the tephra cone class and with the 16 available bands. The classification scheme output was then assessed for its validity by comparing the class coverage to that of the geologic map (Richards and Jia, 1999) and field observations.

2.4   RESULTS

2.4.1   Classification of Mauna Kea flows

The best fit classification map was produced through Maximum Likelihood classification that used six classes and ASTER wavelength bands 1-5, 11, 12, the calculated temperature value (band 15) and the micron-scale roughness value (band 16). All pixels in the Mauna Kea classification image were assigned to one of the six classes by the Maximum Likelihood

28
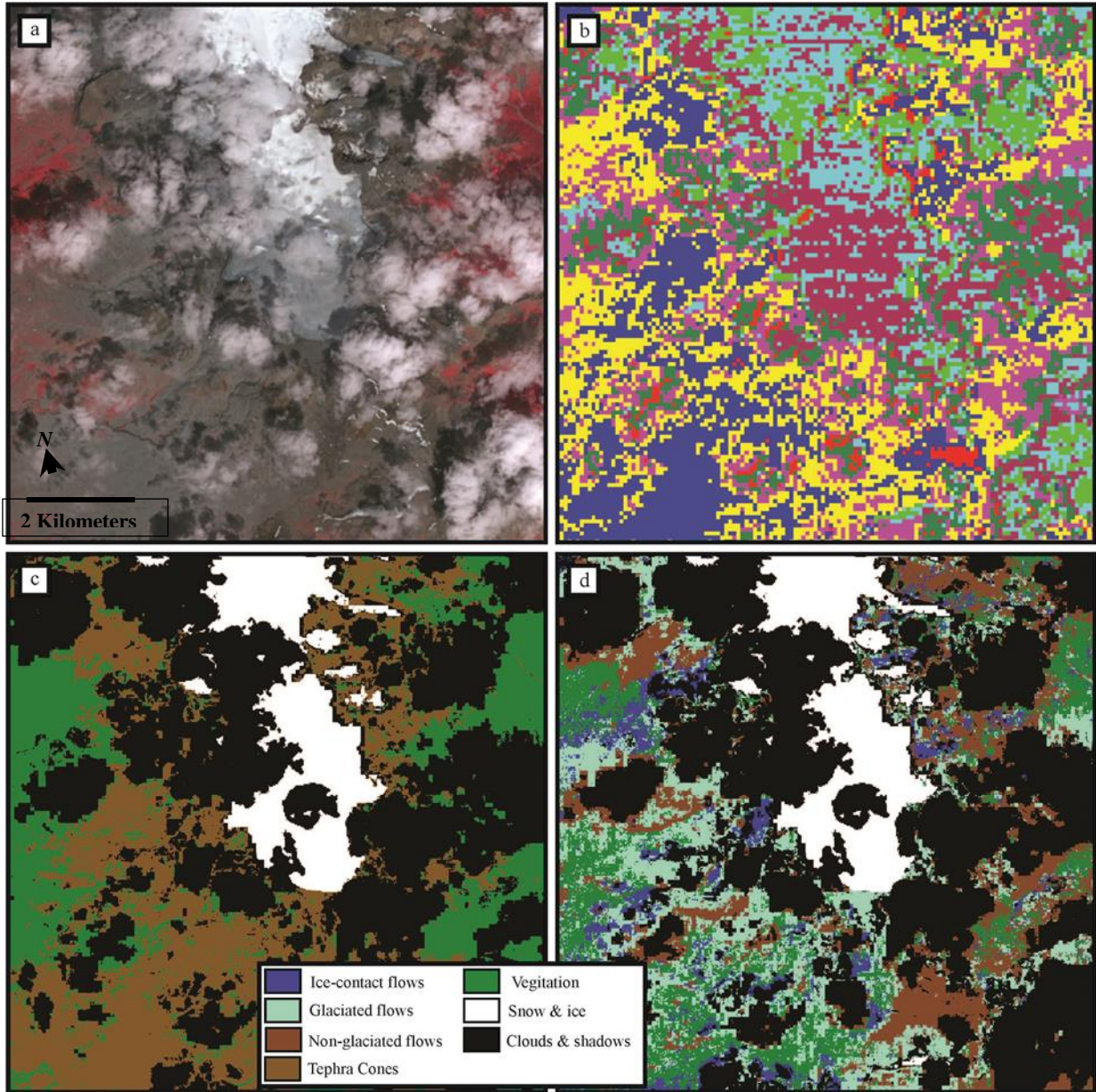
Figure 2.13 Images of the ASTER scene and classifications for the Snowshoe Lava Field on Mount Edziza.
(a) An RGB image of band 3, 2 and 1 of the ASTER VNIR data used in the classification of the SLF. (b) An image of an 8 class, unsupervised k-means classification of the Mount Edziza scene containing the SLF lavas. (c) An image of a 9 class, supervised Maximum Likelihood classification using all wavelength bands, the temperature (band 15) and micron scale roughness band (band 16). The tephra cones class was used and the classification resulted in classifying all lava flows a tephra cones. (d) An image of the best fit 8 class, Maximum Likelihood supervised classification using all wavelength bands and the temperature (band 15) and micron scale roughness band (band 16). In this classification the tephra cones class was omitted. The legend overlying c and d identifies the classes in c and d only.

classification scheme (Figure 2.10c). The class representing glaciated lava flows accounts for 21.7% of the scene area, the ice-contact lava flow class represents 12.4%, the non-glaciated flow class represents 24.4% of the area, and the tephra cones class represents 29.3% of the scene area. Vegetation and cloud classes are restricted to the periphery of the scene and represent 9.5% and 2.1% of the area.

Greater than 90% of the 38.8 km^2 area represented by the glaciated lavas class is restricted to the 140 km^2 area within the boundary of the Makanaka glaciation (Porter, 1979a; Porter, 2005). Pixels outside of the area, especially those on the southern flank, may represent either glacial drift from the older, more extensive Waihu glaciation or they may represent glaciofluvial outwash deposits from either of the last two glacial events. Inside the Makanaka glaciation boundary the glaciated flows class covers more area than the other classes. This result is consistent with the literature and geologic maps (Fig. 2.10d; Porter, 1987; Porter, 2005). Though this class represents a plurality of pixels within the glacial boundary, errors of commission and omission are present. Pixels within the area of the ice-contact Pu`u Hau Kea and Pu`u Kea flows are wrongly classified as glaciated flows. Conversely, the area of glaciated flows between the ice-contact Pu`u Kea flow and the flow north of Pu`u Poliahu is wrongly classified as ice-contact lavas. Pixels within glaciated flows on the south and southeast flanks are classified as tephra cones.

Lavas classified as ice-contact lava flows cover 22.2 km^2 within the scene area. Greater than 85% of theses classified pixels lie within the boundary of the Makanaka glaciation, and the pixels classified outside of the boundary tend to be adjacent to the boundary. The extent of lava flows classified as ice-contact is greater than the extent characterized by Wolfe (Porter, 1979a; Wolfe et al., 1997), and alludes to the extent characterized by Porter (1997). Both Wolfe and

Porter do agree on the existence of the three most distinct ice-contact flows. These three flows are classified in varying degrees of success. The flow north of Pu`u Poliahu is well classified as one would expect given that this flow was used to define mean class spectra values. The proximal to medial sections of the Pu`u Hau Kea flow were correctly classified yet the distal sections were classified as glacial flows. The extent of the Pu`u Hau Kea flow is not necessarily agreed upon in the literature, especially with regard to the eastern extent of the flow. Porter (1987) suggested the Pu`u Kea extends farther east than suggested on Wolfe's (1987) map. Both the unsupervised K-means classification, and an ENVI rendering of band ratios used to discriminate geologic structures indicate this Pu`u Kea flow does extend further east than Wolfe Wolfe et al. (1997) indicates, and resembles the characterization suggested by Porter (1997; Figure 2.5). This classification, however, only alludes to the rough outline of the Pu`u Kea flow, and classifies the majority of the surface area as a glaciated flow. This omission is a trade–off function between over and under-classifying ice-contact lavas. Other attempted classification schemes either over or under represent the extent of ice-contact flows.

Ice contact lava flows south of the summit, save the Pu`u Hau Kea flow, are older and thus their surfaces have been subjected to greater glacial modification. The classification of the flows is therefore not as well defined as the classification scheme indicates. There is a flow, however, between two tephra cones on the southeast flank, just inside the Makanaka glaciation boundary, that is clearly classified as an ice-contact lava flow (Figure 2.5, boxed question mark). This lava flow is not identified as an ice-contact lava flow in the literature but the distinctive classification warrants further study as to why this flow is clearly classified as an ice-contact flow. Other Ice-contact classified pixels proximal to the Makanaka glacial boundary represent

31

errors of commission. These misclassified lavas are commonly glacial drift deposits that may contain detritus from ice-contact lavas.

The majority of the 43.7 km^2 of area classified as non-glaciated lava flows lies outside of the Makanaka glaciation ice boundary. There are areas on the slopes of cones within the boundary that are classified as non-glaciated but should be classified as Tephra cones. Outside of the glacial boundary non-glaciated classified lava flows are found on comparatively evenly sloped topography of the edifice. Non-glaciated flows are also found intercalated with lavas classified as tephra cones proximal to cone structures and become the dominant class with increasing distance from the cone. This classification outcome is consistent with an expected distribution of airfall deposits on the surface of non-glaciated lava flows.

The majority of the 53.3 km^2 the class representing tephra cones covers lies outside of the Makanaka glaciation Boundary but a significant portion lies inside the boundary. All tephra cones within the scene are well represented by the class except for pixels of glaciated and ice-contact classes on Pu`u Poliahu and Pu`u Waiau. The tephra cone class also represents significant areas of flatter topography commonly found downslope of cones. These areas represent either airfall deposits on glaciated flows or glacial float or drift deposits comprised primarily of tephra from the adjacent tephra cone. Significant areas southwest of the summit are misclassified as tephra cones that should be classified as ice-contact or glaciated flows. The tephra cone class does not discriminate between cones emplaced subaqueously in an englacial environment, emplaced in transitional subaqueous to emergent settings, or those emplaced subaerially on Mauna Kea. Further, the class does not discriminate between primary and secondary deposition of tephra deposits. The tephra cone class is therefore, over represented as its mean spectral signature tends to overprint or cover glaciated flows and non-glaciated flows.

2.4.2   Classification of Mount Edziza Lavas

The best-fit Maximum Likelihood classification produced a less than optimal classification of the target area (Figure 2.13d). All ASTER data of the target area contains either significant cloud cover or snow cover. The image used is the best available ASTER scene of the target area. Clouds and cloud shadows compromise 45.5% of the scene. Snow cover beyond the glacier, however, is comparatively insignificant. Glacial ice and all snow account for 9.1% of the scene area. Vegetation, while over-represented in the classification scene, covers another 12.6% of the area. The remaining 33.2% of the scene is classified as either glaciated (15.9%), ice-contact (4.7%), or non-glaciated (12.6%) lava flows. Approximately 48 km^2 of the scene is classified as lava flows. Glaciated lavas represent the largest class and cover 22.9 km^2 of this area. Non-glaciated lavas cover 18.2 km^2 and ice-contact lava flows represent 6.9 km^2 of the classified lava flow area. Of these areas the classified lava flows in the Snowshoe Lava Field lie to the south and west of the glacier in the scene.

The areas classified as glaciated lava flows are appear in the glacially eroded cirques and valleys directly east and southeast of the glacier and in the valley west of Tennena Cone. Areas within two km, where not obscured by clouds and shadows are commonly classified as glaciated lava flows. Given the nearly 700 m of glacial retreat subsequent to the mapping of the area by Souther (1987), one would expect an area within ~ 2 km of the ice would be classified as glacial flows or possibly ice-contact flows. Areas near the glacier classified as vegetation therefore represent clear areas of omission of the glaciated lavas class. This holds true for non-glaciated classified lavas proximal to the glacier. These lavas should also be classified as glaciated lavas. Conversely, distal lavas classified as glaciated lavas are wrongly classified and should be classified as either non-glaciated flows or vegetation.

Lava flows classified as ice-contact are distributed haphazardly over the flatter terrain west and southwest of the glacier and on steep topography on the eastern valleys and the valley west of Tennena Cone. Most of the ice-contact classified lavas seem mis-classified as the areal extent of ice-contact lavas are over-represented in the classification scene. Any ice-contact classified lavas farther than 3000 m from the existing glacier are highly suspect and should be considered as errors of commission. Three areas of contiguous ice-contact classified pixels do seem worthy of further investigation. Pixels west of Tennena Cone, south of Tennena Cone adjacent to the glacier, and directly south of the glacier may correctly indicate ice contact lavas where compared to the geologic map of the area (Souther, 1992).

Non-glaciated classified lava flows are present on the steep ridge slopes above the eastern and southern valley walls within the scene. West of the glacier non-glaciated classified lavas are atop prominent bluffs that are covered in glacial detritus. In aggregate this class misrepresents the extent of non-glaciated lava flows in the scene. Lava flows west and southwest of the glacier that should have been classified as non-glaciated lava flows are misclassified as either vegetated or ice-contact lavas when compared to Souther's (1992) map. The non-glaciated lava flow class should be restricted to these flows in the southwest section of the scene.

In general, this classification of the Snowshoe Lava Field is suspect and does not provide information that can be assessed from the analysis of VNIR imagery other than the ice-contact classified areas near the western and southern margins of the glacier. The classification is also degraded by the cloud coverage in the ASTER scene.

34

2.5 DISCUSSION

2.5.1 Spectral identification of lavas

The purpose of this study was to assess whether lava lithologies could be identified and differentiated in remotely sensed data of volcanic terrains subjected to periods of glaciation. On Mauna Kea, the classification scheme was successful in differentiating glaciated lava flows (including ice-contact flows) from non-glaciated flows, and the scheme was moderately successful at differentiating glaciated flows from ice-contact flows. Yet, band eigenvalues suggest lava flows are best differentiated in VNIR wavelengths, and many of the glaciated and ice-contact lava flows on Mauna Kea could have been identified in VNIR imagery of the summit area if one knew to recognize them as such. For the purposes of visual identification, flows are best differentiated in VNIR and this is exemplified by the greatest variances in class band values within the VNIR wavelengths. Without the literature on Mauna Kea lavas, however, one would most likely only identify the few lava flows with distinct morphologies. Other glaciated or ice contact lava flows would likely remain unidentified, especially on large volcanic edifices like Mauna Kea, until they were mapped in the field with the assistance of a remotely sensed data based classification scheme that uses VNIR bands, select TIR bands and both TIR based temperature and micron-scale roughness models. Without the perspective of remotely sensed data, lava flows not well defined in previous work on Mauna Kea, for example, would remain misidentified.

The classifications scheme's capacity to discriminate between non-glaciated, glaciated and ice-contact lava flows within the Snowshoe Lava Field on Mount Edziza was not as successful compared to the result on Mauna Kea. The success of the classification scheme may

have been hampered by the significant cloud cover of the base ASTER scene, but the glacially deposited clastic detritus overlying lava flows masked the spectral profile of the underlying lava flows. Further refining of this classification scheme by incorporating digital elevation maps and lava flow chemical data may prove it a useful initial mapping tool that fully utilizes remotely sensed imagery. This classification capacity would prove an integral mapping tool to differentiate, identify and target volcanic outcrops of interest especially in inaccessible volcanic terrains in the Canadian and Alaskan Cordillera, the Andes, Kamchatka, Iceland and Antarctica, for example.

This study recognizes the capacity to differentiate ice-contact, glaciated and non-glaciated lavas from one another in remotely sensed data is as function of 1) flow surface texture, 2) flow topography and 3) lava chemistry. Lavas categorically variant in three parameters will exhibit significantly variant spectral profiles.

2.5.2 Surface Texture

Lava surface texture in volcanic terrains subjected to glaciation is determined by the environment at the time of emplacement, subsequent glaciation and subsequent eruptive activity. Lava flows emplaced subaerially before a glacial event can experience glacial erosion or burial by deposition of subglacial till or both. Airfall tephra deposits, aeolian deposition and weathering post glacier retreat may further modify the flow surface texture. For example, A majority of subaerially emplaced Laupahoehoe Volcanics hawaiite-mugearite lava flows on Mauna Kea are a`a flows (Wolfe et al., 1997). Glaciation following to flow emplacement of the a`a flows has mechanically eroded the surface clinker and left the dense flow interiors exposed to further glacial scour and polish (Figures 2.2c, 2.2d). The subglacial depositional environment commonly

becomes favorable to the deposition of subglacial diamict tills, which are exposed after glacial retreat. Finer grained material is commonly winnowed away and a remnant veneer of glacial lag deposits and boulder pavement are what remain on the lava flow surface (Figure 2.2b). Airfall tephra deposits either deposited on the ice surface during a period of glaciation or simple subaerial deposition post glaciation will further modify the flow surface texture (Figure 2.2a). The spectral profile of detritus covered glaciated lava flows will therefore be a function of the spatial extent, grain size and sorting of within the surficial deposits and also the chemistry and roughness of individual grains of till, boulder pavement and tephra. If grain size and chemical composition for the glaciated lava flow class approaches values of the tephra cone class the two end-member classes overlap, and result in misrepresentation of the classes. To avoid this problem the classification scheme excludes SWIR bands because their respective spectral values lie closely within error of each other. The exclusion of the SWIR bands has a detrimental effect on the differentiation of non-glaciated Mauna Kea lavas, predominately a`a lava flows with rough surface textures, from tephra cones as the two classes overlap in VNIR bands and are within error in roughness values. The incorporation of the micron-scale roughness model provides a capacity to differentiate variations in surface roughness (Ramsey and Fink, 1999). Given the thermal energy emitted from a surface of varying roughness represents a linear mixing of a glass end member and a rough end member, a value can therefore be assigned through a least squares deconvolution model incorporating TIR wavelength bands (Ramsey and Fink, 1999). The model roughness values for the Mauna Kea classes represent mean values for each pixel in the class. Commonly glacially polished, the ice-contact flows are the least rough and have low model values. Conversely, vesicular tephra cone deposits have the highest micron scale roughness values.

Glacially smoothed surfaces on Mauna Kea appear on both glaciated lavas and ice-contact lava flows but are common only on ice-contact lavas. On Mauna Kea, glacially smoothed, subaerially emplaced lava flow surfaces are dense flow interiors of a`a flows that are typically not steep sided, high aspect ratio lava flows like those emplaced against ice. Lava flows emplaced subaqueously in the presence of ice also display subsequent glacial scouring and polish features. Although the rheology of subglacial lava emplacement may not be well understood, there are distinct characteristics of ice contact and cooling fracture patterns that indicate these flows are emplaced in the presence of ice. Further, surficial brecciation along distinctive entablature jointing patterns particular to ice contact flows under the strain of glacial flow may differentiate these lavas from the brecciation patterns of subaerial lava flows subsequently eroded by glacial ice. The variation between glaciated lava flows and ice-contact lava flows on Mauna Kea, however, is the percent cover of glacial detritus. The relative paucity of glacial detritus on ice-contact lavas compared to glaciated lavas is the reflected in TIR and temperature bands.

2.5.3   Lava flow chemistry

Though published lava flow chemistry is commonly derived from the analysis of unaltered, non-weathered rock samples, the spectral signatures of lava flows is the function of the chemistry of the weathered flow surface and roughness (e.g., Ramsey and Fink, 1999; Byrnes et al., 2004). The spectral characteristics of a lava flow of similar to same chemistry may have a markedly different spectral signature given its age, weathering characteristics and surface roughness. The process of the lava flow weathering also matters. Lava flows of the same or similar chemistry that are glacially weathered will have a different spectral profile than a

38
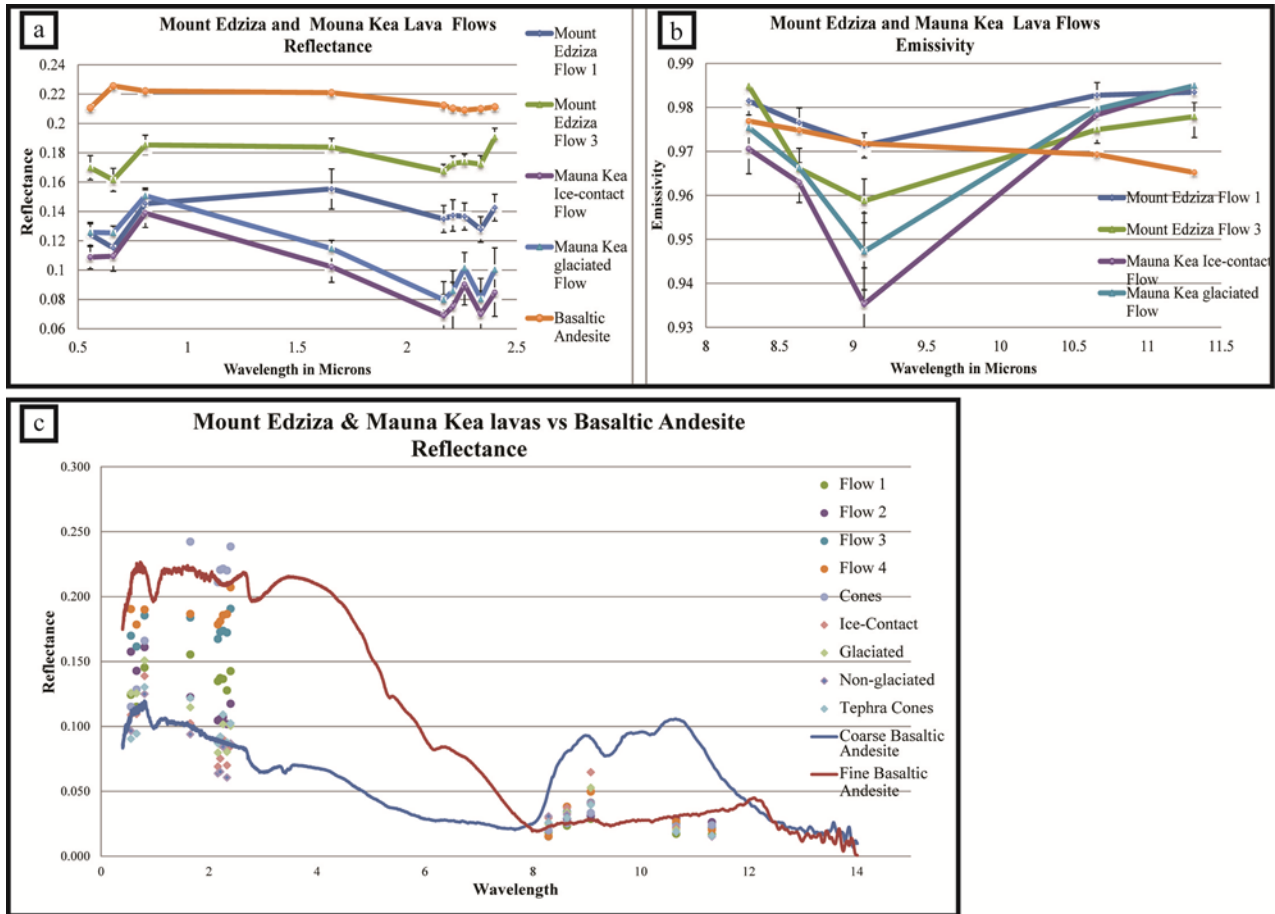
Figure 2.14. Spectral graphs of the Mauna Kea pixel based ROI, Mount Edziza SLF flows and generic basaltic andesite.

(a) Reflectance graphs of Mauna Kea, Mount Edziza SLF lavas and library values of basaltic andesite (orange curve) from John Hopkins University at ASTER wavelengths. (b) Emissivity graphs of Mauna Kea, Mount Edziza SLF lavas and library values of basaltic andesite (orange) from John Hopkins University at ASTER wavelengths. The error bars represent the standard deviation of values for each band in each curve in figures 2.13a and 2.13b. (c) Reflectance values of the Mauna Kea ROI's and the SLF flows are plotted as points against the reflectance values of both coarse and fine grained basaltic andesite from the spectral library provided by Johns Hopkins University.

39

similarly aged lava flow of the same chemistry. Consider the spectral characteristics of Mauna Kea and Mount Edziza lavas (Figure 2.14). The Big Raven lavas in the Snowshoe Lava Field are mildly alkalic to hawaiite in chemistry as are the hawaiite lavas of the Laupahoehoe Volcanics that comprise the majority of lavas at the summit area of Mauna Kea. If plotted against spectral library values of both coarse and fine grained basaltic andesite from the Johns Hopkins University spectral library, the spectral characteristics of both the Mauna Kea and Mount Edziza lavas vary significantly in the VNIR band wavelengths but variances moderate in the TIR wavelengths near the fine grained basaltic andesite spectral end-member (Figure 2.14b). So, it is the weathered surface of the exposed lava or glacial detritus, which has a greater effect on the VNIR spectral signature, that has a greater effect on the spectral signature of lava flows than does the variation in lava chemistry or roughness, which both affect the TIR spectral signature of the lavas.

A further subtle point in the spectral variance of like lava chemistries is demonstrated in the tholeiitic Mauna Loa summit lavas imaged in the same ASTER scene of Mauna Kea. These flows have not been subject to mechanical weathering by glacial ice, yet the chemical weathering and removal of the opalized surface rinds of the older ~12 ka a`a and pahoehoe lavas results in a markedly variant spectral signature in TIR wavelengths (Figure 2.15). The ~12 ka lavas do not vary greatly from the 1984 pahoehoe lava in the VNIR and SWIR wavelengths but the marked variation in the TIR spectral wavelengths, temperature values and micron-scale roughness values creates a difficulty in classifying like chemistry lavas of different ages but similar surface textures.
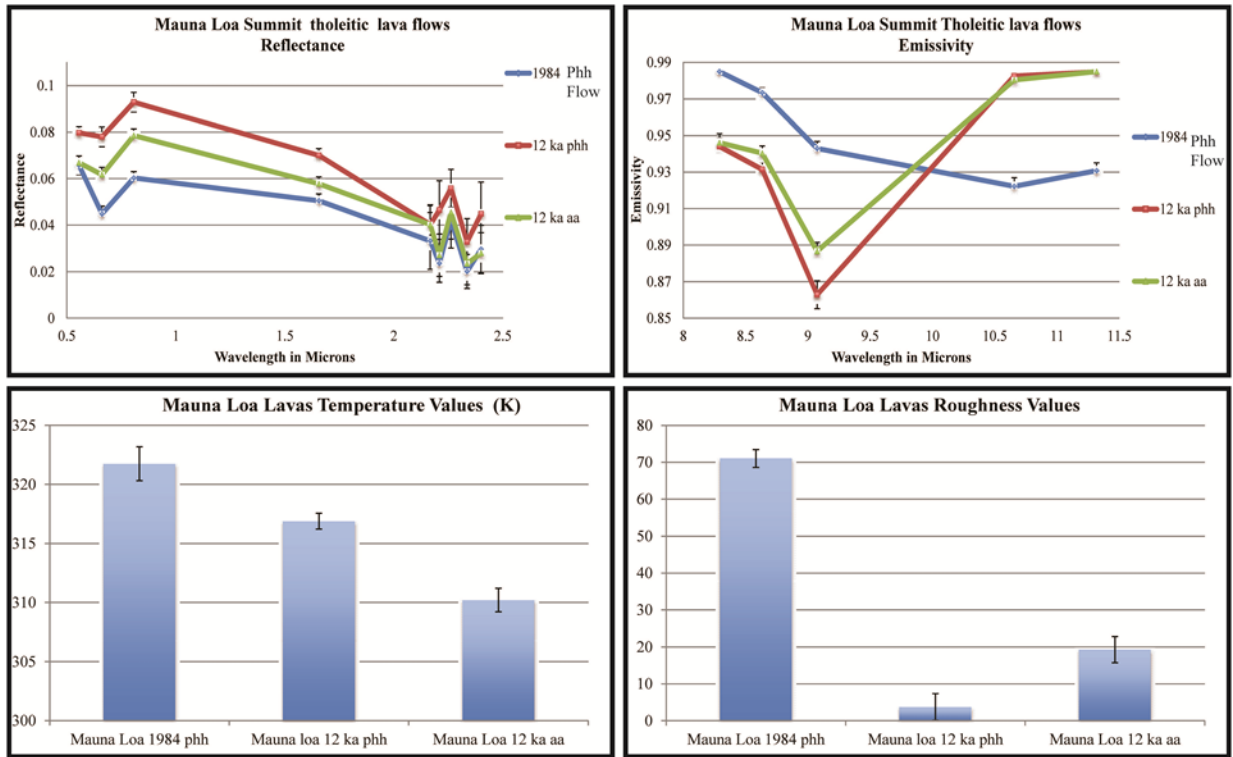
Figure 2.15. Graphs of the Mauna Loa summit area flows reflectance and emissivity values for ASTER wavelengths.
The bar graphs indicate values of the temperature (band 15) and micron scale roughness values (band 16) for the Mauna Loa lava flows. The error bars represent the standard deviation of values for each band in each class.

Although flow surface texture may be more significant to a classification scheme, assigning classes to lava flows should be performed on lavas of similar chemistry. If, for example, the classification applied to Mauna Kea were to be applied to the tholeiitic lavas of Mauna Loa the 12 ka, non-glaciated lavas would be classified as ice-contact lavas and the 1984 pahoehoe lavas would be classified as tephra cones. It is therefore imperative to take lava chemistry into account when creating spectral end-member classes.

41

2.5.4 Flow topography

A distinct characteristic of subglacially emplaced or ice-contact flows is their high aspect ratio compared to other lava flows. Though there are few examples of lava flows emplaced in the presence of ice, those that are display characteristically steep sides, ice contact cooling structures with glassy chilled rinds, and common pillow lava structures. Exposed interiors of ice-contact lava flows commonly display basal columnar jointing and entablature jointing in flow cores. These features indicative of ice-contact lava flow are not readily evident in remotely sensed data due to deficiencies in image resolution. The lack of image resolution may introduce simple bias into identifying steep sided, high aspect lava flows as ice-contact lava flows, because the great majority of thick, steep sided lava flows were not emplaced against ice (Wolfe et al., 1997). It is therefore important to have a cursory accounting of lava chemistry and an understanding of paleoclimate conditions at a target volcanic terrain before placing thick lava flows in a glaciovolcanic context.

The thick, steep sided lava flows on Mauna Kea have been identified as ice-contact lavas (Manley, 1992). Their comparative height variance with surrounding lava flow topography affected subglacial deposition under the alpine ice during the Makanaka glacial stades. Tallest sections of the three prominent ice–contact lava flows, the flow north of Pu`u Poliahu, the Pu`u Hau Kea and Pu'u Kea flows, lack significant cover of glacial lag deposits, whereas thinner sections of these flows are covered in a veneer of glacial lag deposits, though the deposits are not as thick, extensive or poorly sorted as those on glaciated flows. The comparative lack of glacial detritus on the ice-contact flows is reflected in the lower temperature and roughness values (Figure 2.11). Though the Mauna Kea lavas are relatively devoid of glacial lavas on Mauna Kea, ice-contact lavas elsewhere may not be. Glacial deposits on thick, steep sided ice-contact lavas

elsewhere, like those on Mauna Kea, may differ from the glacial deposits on surrounding lava flows, the composition of the glacial detritus may be locally derived and vary in clast size and sorting.

2.6   CONCLUSION

The capacity to identify and target area of interest in remotely sensed data is powerful initial step in an investigation of isolated volcanic terrains subject to glaciation. A classification scheme that successfully identifies lava flow types would be a great utility in identifying areas of future field study as more volcanic terrain emerges from ice cover. The classification scheme developed in this study was successful in differentiating glaciated lava flows from non-glaciated flows on the target volcanic terrain ion Mauna Kea volcano. The classification scheme also proved moderately successful in differentiating ice-contact lava flows from subaerial lava flows subjected to subsequent glaciation. The classification scheme also found lava flows that merit further study on Mauna Kea as they may have been misinterpreted or not studied thoroughly in the past. While the classification scheme was of use on Mauna Kea its utility was not directly transferrable to another volcanic terrain that exhibits evidence of recent glaciation. The classification scheme did not differentiate ice contact lavas, glaciated lavas and non-glaciated lavas in the Snowshoe Lava field on Mount Edziza with any degree of confidence. A successfully transferable classification scheme may benefit from the incorporation of digital elevation models to identify ice-contact lava flows, which tend to have higher aspect ratios compared to typical subaerial lava flows. Further, incorporating sample lava chemistry or lava chemistry derived from remotely sensed data into a classification model may further strengthen

the classification scheme. Though the application of a robust classification scheme can be an effective initial step in identifying outcrops, variances due to lava flow weathering or burial from subsequent glaciation will affect the spectral profile in remotely sensed data and thus the identification of target lava flows. Potential discrepancies in a classification scheme necessitate the physical mapping of target lava flows to complete the mapping process. Therefore, an investigation into a remote volcanic terrain should begin with a perusal of the existing literature of the target terrain to 1) identify lava chemistry, 2) identify the source of flow surface textures and 3) if possible, identify a known lava flow as glaciated or as ice contact in the remotely sensed scene.

3.0 EVOLUTION OF A SUBGLACIAL BASALTIC LAVA FLOW FIELD: TENNENA VOLCANIC CENTER, MOUNT EDZIZA VOLCANIC COMPLEX, BRITISH COLUMBIA, CANADA

3.1 INTRODUCTION

The emplacement mechanisms and resultant internal and surface structures of basaltic lava flows in subaerial, and to a lesser extent, submarine environments are well understood from field and analog modeling studies (e.g., Rowland and Walker, 1990; Walker, 1992; Gregg and Fink, 2000; Gregg and Smith, 2003; Bear and Cas, 2007). However, few studies on the emplacement of basaltic lava flows in glaciovolcanic environments have been published (Lescinsky and Fink, 2000; Loughlin, 2002; Smellie, 2008). Yet the ability to distinguish lava flows that have been emplaced under or against ice from those emplaced in an ice-free environment is critical, as the products of volcano-ice interaction are becoming a standard proxy for the presence and thickness of former ice (e.g., Mathews, 1947; Lescinsky and Fink, 2000; Edwards et al., 2002; Stevenson et al., 2006; Smellie, 2008; Tuffen et al., 2010; Edwards et al., 2011). Documenting the characteristics of basaltic lava flows emplaced beneath ice on Earth also has important implications for understanding the past climate history of Mars, where, for example, steep-sided and very thick lava flows on the flanks of Ascraeus Mons and Pavonis Mons have been interpreted as having been emplaced subglacially (Allen, 1979; Kadish et al., 2008).

45
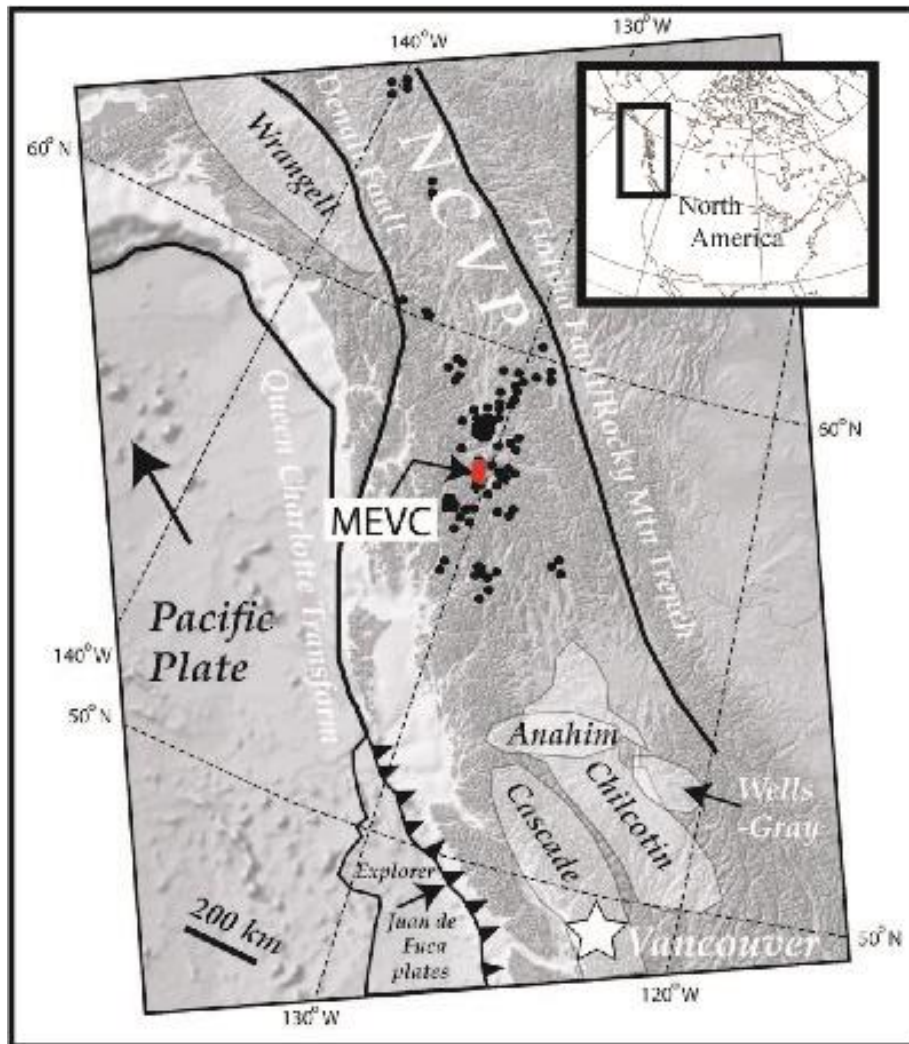
Figure 3.1. A map of British Columbia showing the location of the MEVC.

The Mount Edziza Volcanic Complex (MEVC) in the Canadian Cordillera lies within the North Canadian Volcanic Province (NCVP) approximately 375 km east of the Queen Charlotte Fault. The dots represent volcanic centers within the NCVP (hillshade derived from 30m DEM from the National Topographic Atlas, Geological Survey of Canada).

Here we present a new, detailed review of the Tennena volcanic center (TVC), which is located on the western flank of the Mount Edziza volcanic complex (MEVC) in northwestern British Columbia, Canada (Figures 3.1 and 3.2). The center is basaltic and formed during a glaciovolcanic eruption likely associated with the last glacial maximum (LGM). In this paper we: 1) describe and interpret coherent and volcaniclastic lithofacies of the TVC; 2) present new

46

geochemical data (major element and H_2O/CO_2 concentrations from glasses); 3) present a model for the evolution of Tennena Cone and the associated eruptive products; and 4) discuss the implications for local and regional ice thickness at the time of the eruption.

3.2 GEOLOGIC SETTING

The volcanic deposits of the Mount Edziza Volcanic Complex (MEVC) are part of the Neogene to Recent northern Cordilleran volcanic province (NCVP) in British Columbia, Canada, which comprises predominantly alkaline mafic volcanism related to minor trans-tension along the North American-Pacific plate boundaries (e.g., Edwards and Russell, 1999; Edwards and Russell, 2000; Abraham et al., 2005). The MEVC is the second largest volcanic complex in the NCVP, and is situated directly south of the Stikine River approximately 375 km east of the Queen Charlotte transform fault, which defines the North American − Pacific plate boundary (Figure 3.1).

Over the last 60 years investigators have extensively documented evidence of glaciovolcanism throughout the NCVP (Mathews, 1947; Allen et al., 1982; Moore et al., 1995; Edwards and Russell, 2000; Edwards et al., 2002; Harder and Russell, 2007; Edwards et al., 2011) including work at the MEVC (Souther, 1992; Spooner et al., 1995; Edwards et al., 2009). The geology of the MEVC was mapped in detail by Souther in the 1960s and 70s (Souther, 1992). He identified two distinct masses: the deeply eroded Spectrum Range to the south and the northern massif, referred to as Mount Edziza (2,787 m a.s.l.; Figure 3.2). Mount Edziza is approximately 40 km along its N10^{o}E trending long axis, 30 km wide, and is the most recently active area of the MEVC (Souther, 1992). The eastern slopes of Mount Edziza have been subject

47
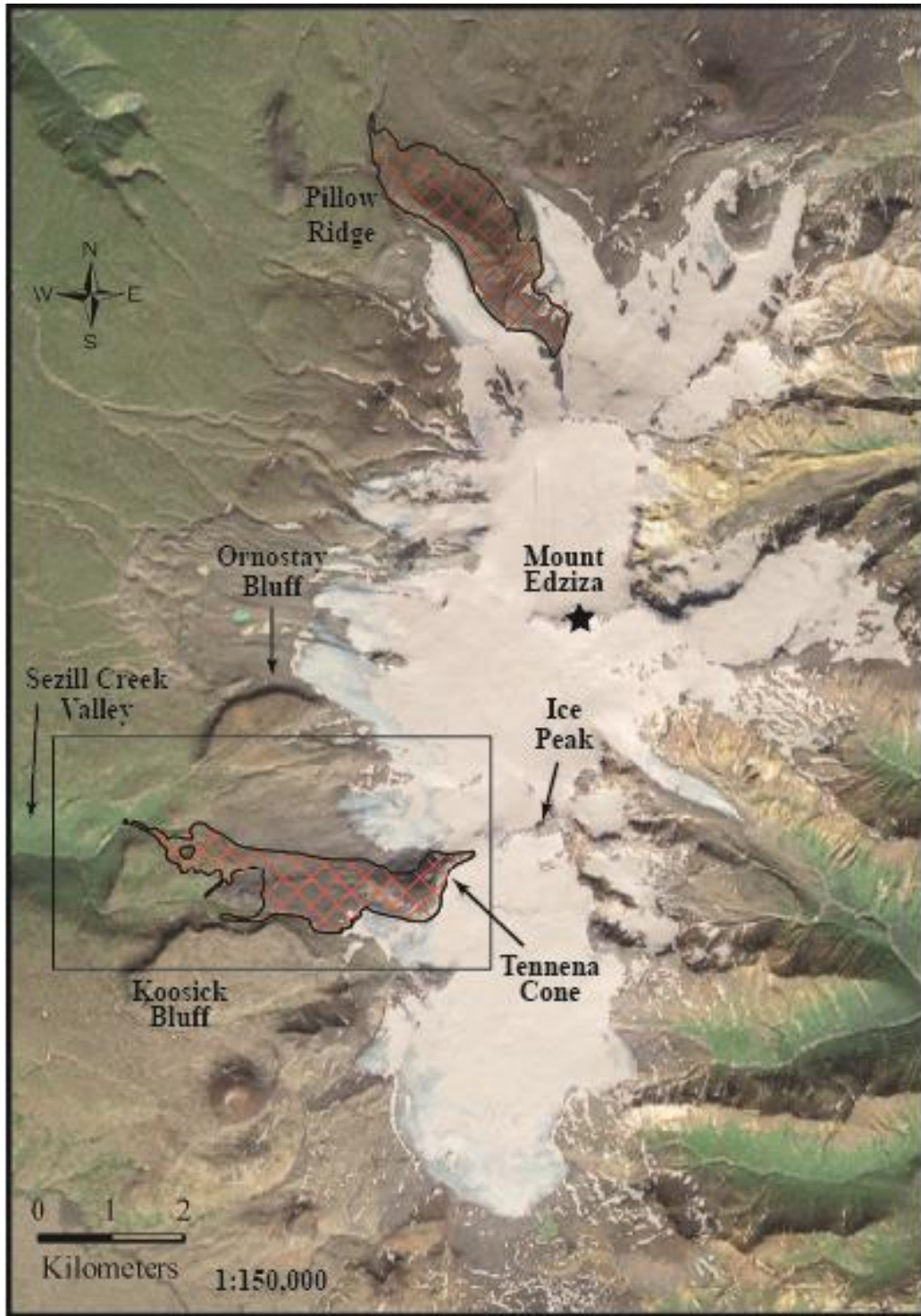
Figure 3.2. Image of Mount Edziza.

(b) Map of the MEVC showing the location of Tennena Cone and other important landforms of the MEVC. The crosshatched area indicates the extent of the exposed TVC and Pillow Ridge deposits. The box represents the area of Figure 3.3. The summit of Mount Edziza is represented by a star (Data sources: Geological Survey of Canada, ESRI, i-cubed, USDA, USGS, GeoEye, Getmapping, Aerogrid, IGN, IGP and the GIS).

to extensive glacial erosion. The other flanks are dominated by broad uplands or plateaus (Figure 3.2). Souther's work indicates the MEVC preserves an excellent record of late Pliocene and Pleistocene glaciovolcanism in northern BC because: 1) it has had a long eruptive history that dates back to at least 5.5 Ma (Souther et al., 1984; Souther, 1992), 2) its history has been dominated by effusion of erosion-resistant lava flows, and 3) glacial sediments are locally intercalated with the volcanic units (Spooner et al., 1995).

The onset of volcanism at the MEVC is somewhat ambiguous. K-Ar ages for the lowest exposed stratigraphic unit range from 11.4 ±1.5 Ma to 5.5 +/- 0.1 Ma (Souther et al., 1984; Souther, 1992). The most recent volcanic activity was initiated in the late Pleistocene during the LGM according toSouther (1992). This volcanic activity, including the eruption that produced the deposits described in this paper, is defined by Souther as the Big Raven Formation. Based on radiocarbon dating of plant material, this formation includes the youngest dated eruption within the MEVC at 1300 ± 130 yr B.P.(Souther, 1971; Souther et al., 1984; Souther, 1992).

On the southwestern flank of Mount Edziza, the TVC comprises a vitriclastic basaltic tuff cone, located at 57° 40' 57.705" N 130° 39' 43.138" W, and associated basaltic lava flows to the west (Figures 3.1 and 3.2). We have divided the volcanic center into four distinct spatial terrains based on the presence and distribution of the lithofacies described below (section 3). The four terrains are Tennena Cone, the proximal pillow lavas, the medial massive lavas and the distal pillow lavas.

Tennena Cone (2390 m a.s.l.) lies 3.5 km south-southeast from the summit nunatak (Figure 3.2), and is mantled on its north, east and south flanks by glacial ice. The cone is 200 m high, 1200 m long, and is up to 600 m wide (Figure 3.3). From the southwest base of TC, a 500 m wide area of hummocky terrain made up of mounds of pillow lavas extends southwest for

49
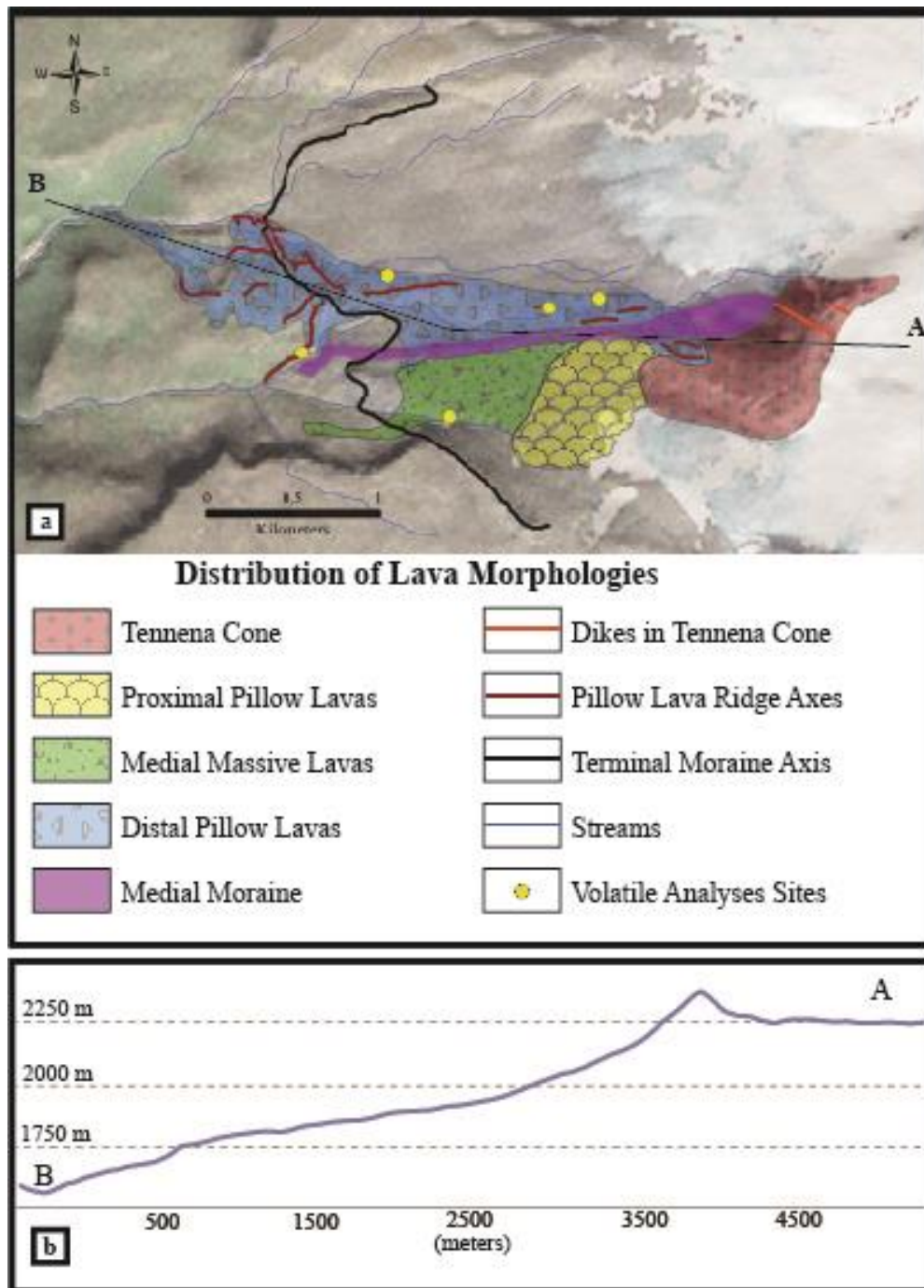
Figure 3.3. A lava morphology distribution map and a cross-sectional elevation profile of the TVC.
The box in Figure 3.2 indicates the location of the map and image. (a) Map of the lava terrains within the TVC. The extent of the different lava terrains is represented by the hued symbols displayed in the first column of the legend. The extents of the formations and deposits are based on the mapping work done by the J. Hungerford and J. G. Souther (1992) (Data sources: Geological Survey of Canada, ESRI, i-cubed, USDA, USGS, GeoEye, Getmapping, Aerogrid, IGN, IGP and the GIS). (b) The elevation profile of the line section AB in Figure 3.3a.

50
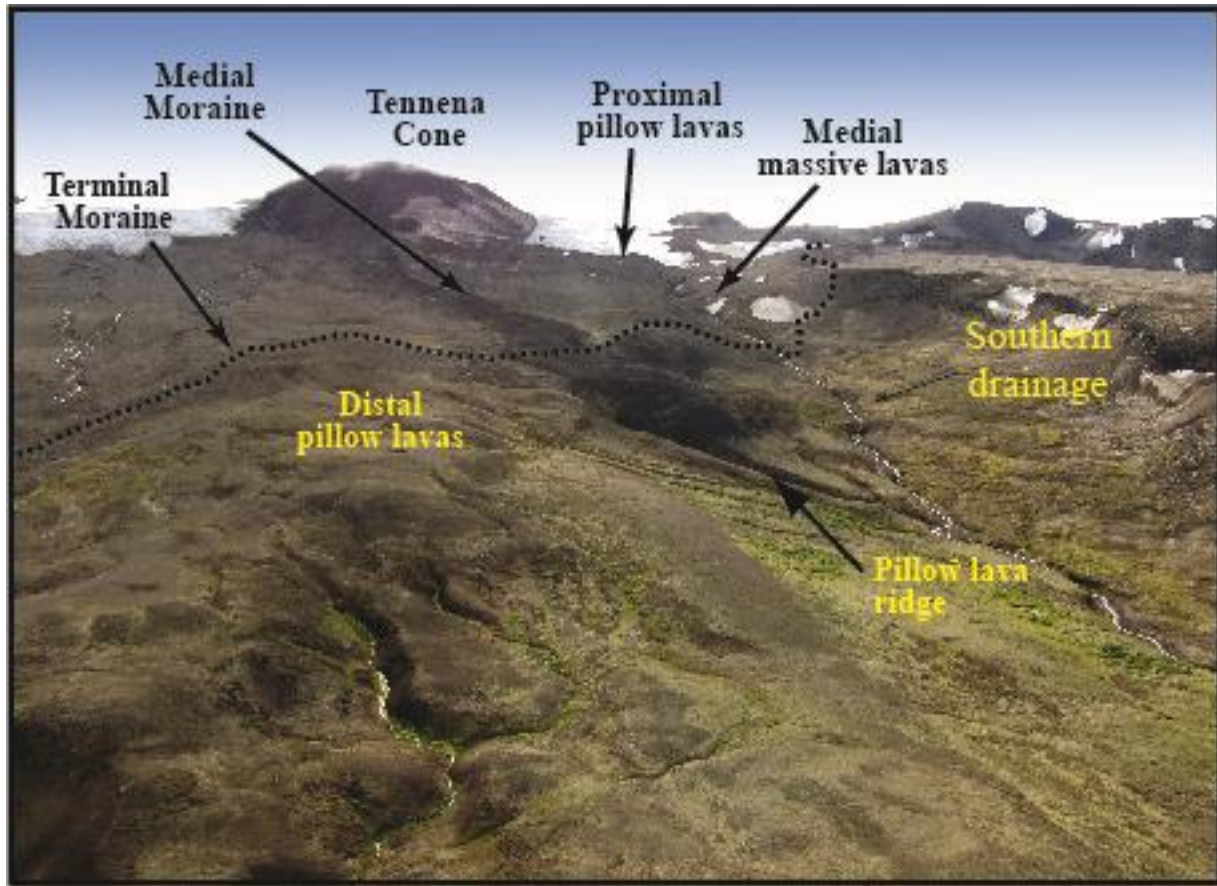
Figure 3.4. An aerial view looking east at the TVC.

Pillow lava morphologies of the distal pillow lava terrain make up the extent of the deposits in the foreground. Mounds of the proximal pillow lava terrain and the medial massive lava terrain lie above the terminal moraine near the western flank of Tennena Cone. The southern drainage flows west from the terminus of the glacial tongue at the southern foot of Tennena Cone on the right side of the image.

1600 m. Downslope of the hummocky terrain TVC lava flows form a 1.7 km wide plateau that extends 2 km to the west. A recently formed terminal moraine lies either on or very near the western edge of the plateau (Figure 3.3). TVC lava flows extend further downslope from this plateau to the northern fork of Sezill Creek at the head of Sezill Creek valley, 4.3 km west of TC (Figure 3.2 and 3.3). The topographic grade between the cone and the lava flow terminus does not exceed 6 percent except where vertical scarps, which range from 3 to 25 m in height and 15 to 200 m in lateral continuity, form steps in the underlying Ice Peak Formation lavas.

51

The hummocky terrain proximal to TC comprises mounds of pillow lavas and is referred to as the proximal pillow lava terrain. Within the plateau, just west of the proximal pillow lavas, is an area that we refer to as the medial massive lava terrain. Scarps of the low-aspect, massive (non-pillowed) basaltic lavas that define this terrain are located in the southern drainage just below the northern cliffs of Koosick Bluff. This terrain lies to the south of a prominent recent medial moraine and almost exclusively above the terminal moraine except for one lobe that extends west, under the cliffs of Koosick Bluff (Figures 3.2 and 3.3).

The lavas of the distal pillow lava terrain lie north of the medial moraine and west of Tennena Cone, and end at the head of Sezill Creek. West of the medial moraine, these lava flows cascade over the north and south ends of a 200 m wide step in the underlying Ice Peak Formation lavas. Below this step, the lavas comprise mainly pillows with orientations varying from horizontal to vertical.

3.3   LITHOFACIES DESCRIPTIONS AND INTERPRETATIONS

Based on our fieldwork, we define six primary volcanic lithofacies and three associated glaciogenic lithofacies (Table 3.1). The volcanic lithofacies include two primary volcaniclastic units - tuff breccia (TB) and lapilli tuff (LT) - and four coherent units - dikes (Ld), massive non-pillowed lava flows (Lm), pillow lavas (Lp_{1-2}) and vertical pillow lavas (Lv). Associated glaciogenic sedimentary lithofacies include diamicton (D), normally graded gravelly sands (gGs), and poorly consolidated bedded sandstone (Sh). We describe the primary volcaniclastic lithofacies with terminology fromWhite and Houghton (2006) and the reworked or resedimented lithofacies with terminology from Benn and Evans (1998) and Evans and Benn (2004).

Table 3.1. Lithofacies codes, descriptions, figures numbers and interpretations

Facies Code	Description	Figs.	Interpretation
Fragmental volcanic lithofacies			
TB	**Tuff breccia**: Black to dark gray, matrix to clast supported, very poorly sorted, massive to crudely bedded layers of angular basalt; clasts range from medium lapilli to ~80 cm, vesiculated crystalline lava blocks; matrix is coarse ash to fine lapilli sized, angular, poorly to well vesiculated; bed dips are either ~20° and uniform on strike or vary from ~20 to 40° and locally cross-cut underlying units in the western flank; well exposed in the glacially steepened areas of the western and eastern flanks of the cone.	3.5a, 3.5b, 3.9c, 3.9d, 3.9e	Subaqueous grain avalanche deposits of clasts derived from thermally quenched, mechanically spalled or phreatomagmatic clasts
LT	**Lapilli tuff**: Light brown to dark brown, crudely to poorly defined hummocky beds of coarse ash to lapilli sized clasts, which locally include large, angular coarse lapilli to ~40 cm blocks of crystalline basalt; finer grained beds are moderately to well sorted while thicker beds are poorly sorted; bedding dips range from 10° to 20°; well exposed on the glacially steepened southern and eastern slopes of the cone.	3.5c, 3.5d, 3.9d, 3.9e	Either Density currents fed by Surtseyan fragmentation or distal equivalent of TB facies deposited in local gravity driven mass flows
Coherent volcanic lithofacies			
Ld	**Dikes:** gray, coherent, crystalline, ~1m wide; subvertical with curviplanar margins; vary in orientations from roughly east-west perpendicular to cone to parallel to cone axis; dikes intrude LT and TB and Lp at the cone; contacts with the host tuff breccias and pillow lavas are commonly pillowed or fluidal; dike interior displays blocky to hackly fracture patterns producing blocks varying in size from 2 to 25cm.	3.9d	Late stage intrusions following cone formation
Lp$_{1-2}$	**Pillow lavas:** black to dark gray tubular bodies, 15cm to 2m in diameter, round to lobate in cross section; larger diameter pillows sometimes display sagging structures abundant in distal TC lavas; solid pillows have concentric zones of varying vesiculation from >5% to 20% with occasional pipe vesicles; rims to 1.5cm thick are dense and vitric; proximal lens within cone, medial mounds, and distal flows; interbedded hyaloclastite rare to absent; radial jointing common; locally hollow interiors with horizontally ribbed or shelved structures present	3.5c, 3.6a-4fi, 3.9d, 3.10c, 3.10d, 3.12c, 3.12d, 3.12f 3.12g, 3.12h	Subaqueous lava effusion at a local flux lower than that of proximal sheet lavas (Lm)
Lv	**Vertical lava structures:** black to dark gray, vertically to sub-vertically oriented tubular bodies, elliptical to pinched elliptical cross-sections, 40 – 150 cm long bodies that pinch and swell, up to 40 cm diameters; corrugated rinds, 20 – 35% vesicles, plagioclase porphyritic; rare in proximal and medial lavas, ubiquitous in distal lavas overlying flat to shallow substrate; occurs commonly in clusters	3.6g-3.6i, 3.12f, 3.12g,	Subaqueous emplacement of low local lava effusion rates over vertical or near vertical substrate

53

Facies Code	Description	Figs.	Interpretation
Lm	**Massive sheet lavas**: gray to dark red-orange and black when fresh; individual stacked lava units oblate in cross-section, 2 to 5 m thick and 15 m wide persistent jointing pattern of basal columns, medial blocky jointing and upper hackly jointing; relic pillow lava structures commonly make up the surfaces of the upper flow units; medial to cone	3.7a–3.7c, 3.11a-3.11e	Vent proximal to medial, high lava effusion rate subaqueous lava flows
Glaciogenetic lithofacies			
Dmm Dms	**Diamicton massive (Dmm) and stratified (Dms):** Dark gray to orange-brown or tan; matrix is sand to pebble sized angular to sub-rounded grains, clasts are either monomict TC basalts (Dmm$_1$) or oligomict 1cm to 1.2 m (Dmm$_2$) and are round to angular; Dmm beds up to 2m thick, stratified (Dms) beds 1.0cm to 3m thick in outcrop that is 9m thick; Dmm is poorly (Dmm$_1$) to well (Dmm$_2$) consolidated, massive and matrix supported; Dms beds are consolidated, poorly sorted, matrix supported, massive to normally graded, discontinuous beds, thinner beds are finer grained; Dmm underlies Lp or Lm and lower contacts are obscured by scree, Dms underlies Lp and overlies gGs; Dmm exposed in southern drainage below proximal pillow lavas and massive lavas, Dms exposed in southern drainage below distal pillow lavas.	3.8a-3.8d, 3.10d, 3.11b-3.11e, 3.12c, 3.12d	Dmm$_1$ - tillite of glacially modified fragments of older lavas deposited prior to the Tennena Cone eruption, Dmm$_2$ - flow front sands and breccia deposited in a concentrated flow, Dms - glacial detritus deposited as numerous debris flows, possibly emplaced during the TC eruption.
gGs	**Graded gravel-sand couplets:** Tan to brown; black grains of dense to poorly vesiculated medium sand to granule sized grains; beds sets from 2 to 7m with defined bed/laminae thicknesses varying from 0.5 to 10cm; beds subparallel, lensoid or cross-stratified, thin beds/laminae well sorted, thicker beds poorly sorted with angular oligomict clasts, infrequent subvertical fracture planes cut beds with minor slump/offset (<20cm), southernmost beds directly below TC lavas almost exclusively clasts derived from crystalline TC lavas; overlain by Dms to north and TC lavas south, overlie Ice Peak lavas where bottom contact exposed; found in southern drainage west of terminal moraine.	3.8e, 3.8f, 3.12d	fluvially emplaced within a subglacial meltwater drainage system, deposition coeval with the Tennena Cone eruption.
Sh	**Planar cross-bedded sands**: black and dark brown; sub-angular to round, moderate to high sphericity, vitric sand sized grains; thickly laminated to thinly bedded; poorly consolidated, well sorted, normally graded, and well-developed ripple and dune bedding; upper surface commonly conforms with vegetated soil horizon, overlies both Ice Peak and distal Tennena Cone lavas; highest stratigraphic unit west of the recessional moraine.	3.8g, 3.8h, 3.12e	Subglacial fluvial deposits of sands derived from TC lavas deposited in during the same glacial stage present at time of TC eruption.

3.3.1 Primary volcaniclastic lithofacies

Primary volcaniclastic lithofacies are only found within the flanks of Tennena Cone, and are characterized as tuff breccia and lapilli tuff.

3.3.1.1 Tuff breccia (TB)

      Tuff breccia (TB; Table 3.1) exists in near vertical scarps cut into the flanks of Tennena Cone. Whereas typically massive, some sections of TB display crudely bedded layers with dips of ~20-40°. Bed contacts, if visible, are wavy to lenticular and defined by gradational changes in clast size from coarse ash to coarse lapilli. Angular lithic blocks of basaltic lava, 20-80 cm across, commonly disturb these bedding contacts, but unequivocal bomb sag structures are not evident. Blocks that are not angular commonly display fluidal glassy rinds like those found on pillow lavas. TB is clast-supported with clasts typically in the medium lapilli range, and a matrix of coarse vitric ash to fine vitric lapilli (Figure 3.5a). The lapilli are poorly sorted, black to dark grey, poorly vesicular to moderately vesicular, angular crystalline to glassy basalt (Figure 3.5b). Some clasts are clearly porphyritic with plagioclase phenocrysts.

      Bed dip angles of 20° or greater, the poor sorting and crude bedding of the breccia clasts, indicate the TB lithofacies is either: 1) subaqueous grain avalanche deposits (White, 2000; Skilling, 2002), with the clasts derived from thermally quenched and/or mechanically spalled fragments from the margins of advancing vesiculated pillow lava flows, or 2) deposits generated during mildly explosive phreatomagmatic eruptions. The steep primary dips, coarse lithic components, and presence of dikes suggest the TB deposits are vent-proximal. The absence of
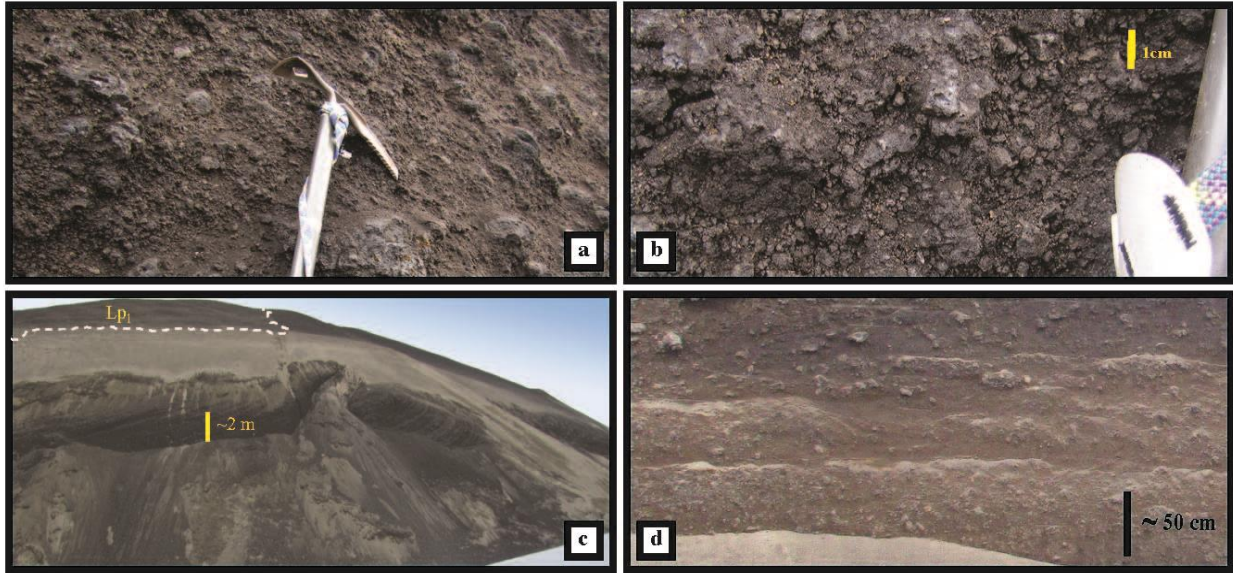
Figure 3.5. Field images of primary volcaniclastic lithofacies.
(a) Oblique view of the poorly sorted tuff breccia (TB) within the eastern slopes of Tennena Cone. The head of the ice ax is 26 cm across. (b) A closer view of the smaller, poorly vesiculated, angular clasts of basalt that make up the TB matrix on the eastern slope of Tennena cone. (c) View of lapilli tuff (LT) beds in the over-steepened southern slopes of Tennena Cone. The tan - overburden is Sheep Track pumice, the youngest trachytic deposit exposed on Mount Edziza. A thin carapace of pillow and fluidal coherent lavas overlies the southwestern LT beds. (d) A closer view of southwest dipping beds of lapilli tuff (LT) in the southeastern slope of Tennena Cone. The massive to normally graded beds have wavy to irregular contacts that pinch off and are disrupted by up to 40 cm monomict basalt clasts.

bomb sags is most consistent with subaqueous deposition, although the coarseness of the deposits may have precluded their development.

3.3.1.2 Lapilli tuffs (LT)

The lapilli tuff (LT, Table 3.1) lithofacies is exposed within the inaccessible scarps on the southern and eastern flanks of Tennena Cone (Figure 3.5c). Beds of LT are light brown to dark brown, medium bedded (10 to 30 cm), with dip angles of 10-20°, and are crudely defined by wavy to irregular erosive contacts between massive to normally graded beds of vitric, coarse ash

to lapilli-sized juvenile clasts (Figure 3.5d). The matrix tends to be finer grained and better sorted in thinner than in the thicker beds. Crystalline basaltic lava blocks with both fluidal glassy surfaces and angular fracture surfaces of up to ~40 cm in size, are locally prevalent. No sags are present beneath the blocks, but beds of overlying LT commonly drape the blocks.

Given the dominance of vitric lapilli, bed angles, erosive contacts, lack of bomb sags, and the presence of outsized lava blocks, we interpret this lithofacies as either 1) grain avalanche deposits that have been resedimented by subaqueous high-concentration density currents, or 2) deposits from density currents fed directly by subaqueous explosive eruptions. In either case, the LT deposits could represent more distal equivalents of the TB lithofacies, or may indicate a shift from effusion to explosive subaqueous eruptions. The spatial relationship, however, with TB described below (section 3.4) may preclude the resedimentation of TB as a source of the LT beds.

3.3.2   Coherent lithofacies

Coherent lithofacies are subdivided into dikes (Ld), pillow lavas (Lp), vertical pillow lavas (Lv) and massive (non-pillowed) lavas (Lm).

3.3.2.1 Dike (Ld)

Two dikes are exposed within Tennena Cone. A 1m wide vertical basaltic dike (Table 3.1, Ld) with a strike of N70°W is exposed on the east and west facing flanks of Tennena Cone, and along the summit ridge. A 5 m high remnant of another 1 m wide dike is exposed 50 m further north on the east flank of the cone. The dikes comprise coherent, gray, plagioclase-phyric rock that is fragmented in blocky to hackly fracture patterns with blocks varying in size from 2 to 25

cm. The dikes vary from nearly dense to ~30% vesicular in 1-5 cm thick, margin-parallel bands. The vertical margins of the dikes display pillowed or fluidal margins, which is consistent with intrusion into an unconsolidated, wet substrate (Skilling, 2002).

3.3.2.2 Pillow lavas (Lp$_{1-2}$)

Pillow lavas (Table 3.1, Lp$_{1-2}$) crop out on Tennena cone and are the volumetrically dominant lava facies in outcrops of the lava flows to the west of the cone. The pillow lava lithofacies is subdivided into normal pillow lavas (Lp$_1$) and mega-pillow lavas (Lp$_2$).

Normal pillow lavas (Lp$_1$): Pillow lavas with diameters less than 1 m are referred to as normal pillow lavas (Lp$_1$). Bodies of Lp$_1$ pillows are closely stacked with little or no fragmental material between the pillow tubes. Their cross-sections are spherical to elliptical, commonly radially jointed, and are 0.15 to 1 m in diameter (Figure 3.6a). Complete Lp$_1$ pillow tubes are not exposed but up to 3 m long sections are sometimes present in steep-sided outcrops (Wells et al., 1979, Figure 3.6b), where they display "pinch and swell' characteristics perpendicular to the direction of pillow propagation. The Lp$_1$ lavas have dense, vitric rinds up to 1.5 cm thick that diffusely grade into the pillow interior. Pillow cores have concentric zones displaying 20% to 40% vesicles and occasional < 3 cm long pipe vesicles. The pillow lavas are porphyritic with 5% to 20% plagioclase crystals that are up to 7 mm long. The Lp$_1$ lithofacies is present in each of the four TVC lava terrains, though its volume relative to that other lithofacies varies by domain.

The physical controls on the formation of subaqueous lava flows are well documented and include lava viscosity (e.g., Walker, 1992), substrate slope and local effusion rate (Griffiths and Fink, 1992b; Gregg and Fink, 1995; Klingelhöfer et al., 1999). As the Lp$_1$ lavas appear to be relatively homogeneous with respect to composition, vesicularity, distribution of phenocrysts, and depositional slope, we suggest that they were subaqueously emplaced at lower lava fluxes

than those that favor the formation of mega-pillow or massive flow morphologies found in the other TVC terrains.

3.3.2.3 Mega-pillow lavas (Lp$_2$)

Pillow lavas that are greater than 1 m in cross-sectional diameter are referred to here as mega-pillow lavas (Walker, 1992; Batiza and White, 2000; Goto and McPhie, 2004; Bear and Cas, 2007). Mega-pillow lavas can be elliptical in cross-section or commonly display pinched cross-sections where the bottom of the pillow has sagged to fill underlying voids. Mega-pillow lavas often display rosettes of colonnade-jointed fracture patterns (Figures 3.6c and 3.6d). Both cylindrical and pinched Lp$_2$ shapes can be up to 2.5 m in diameter. The lavas are porphyritic with plagioclase phenocrysts, contain 5 to 35 vol. % vesicles, and are black to gray when fresh and dark red-orange when weathered. Mega-pillow lavas are common in the distal pillow lava terrain but are also found less commonly in the medial massive lava terrain.

The large size and uniform radial colonnade fracture patterns of the mega-pillows suggest that they represent either (1) subaqueous lava tubes filled with lava or (2) are true pillows that inflated more than the normal pillows before budding (Gregg and Fink, 2000). If some or all Lp$_2$ are lava tubes, then the distal pillow lava lavas were likely fed from such master feeder tubes that developed during the course of the eruption (Figure 3.6d; Walker, 1992; Goto and McPhie, 2004; Bear and Cas, 2007).

Lp lavas with hollow interiors are commonly intercalated with pillows completely filled with lava in the distal pillow lava terrain. The hollow pillows locally contain multiple void spaces that are segregated by 2 to 4 cm thick, horizontal shelves of solidified lava 3.5 to 5 cm apart (Figure 3.6e). Within the void space, surfaces are smooth and glassy with drip structures on the cavity ceilings. Locally the shelves have either been eroded away or have collapsed upon one
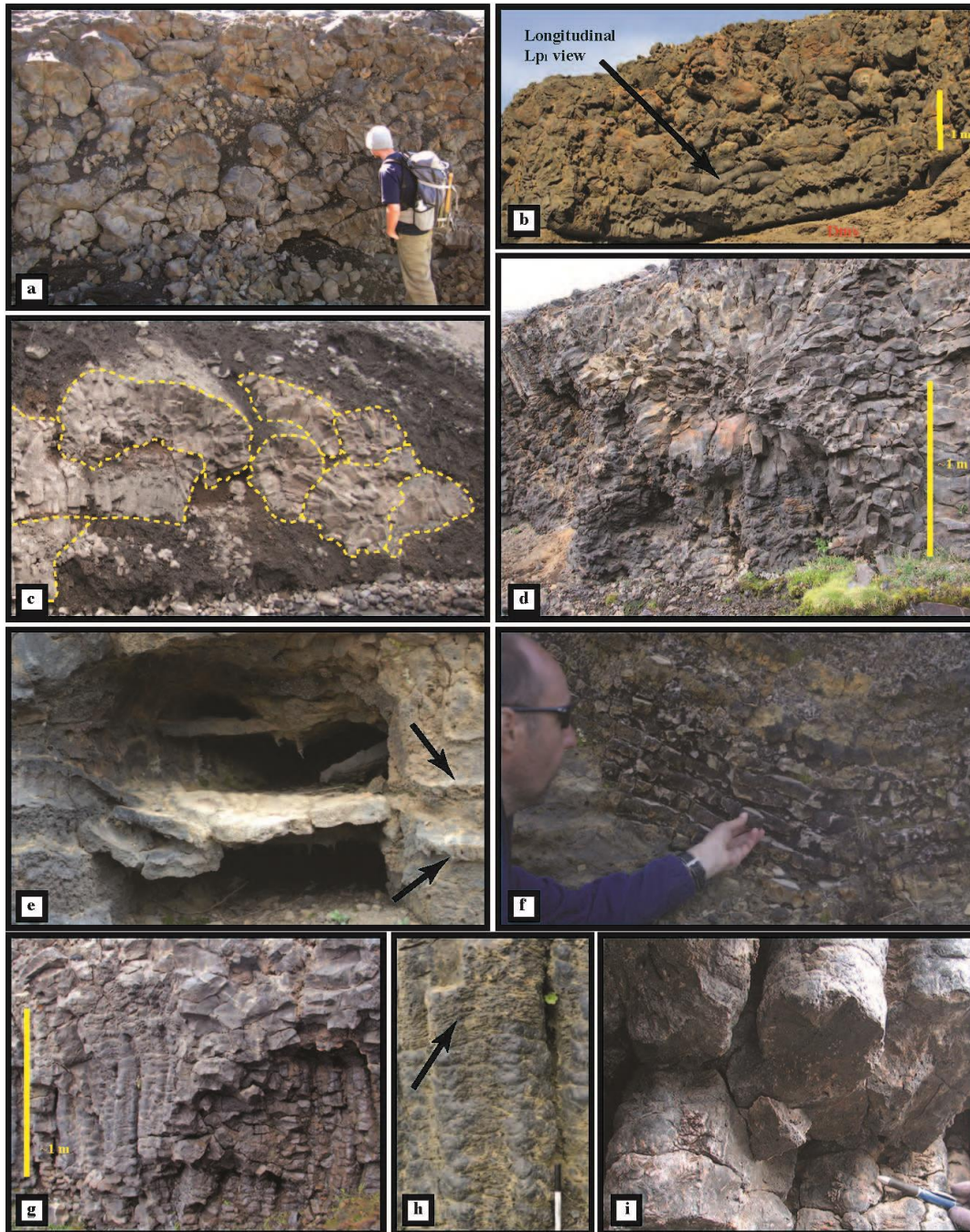
Figure 3.6. Field images of the pillow lava (Lp$_{1-2}$) and vertical pillow lava (Lv) lithofacies.

(a) View showing pillow lavas (Lp$_1$) exposed proximal to the western base of Tennena Cone. The stacked pillow lavas are round to oblate and less than 1m wide in cross section. (b) View showing Lp$_1$ exposed within a pillow lava ridge on the southwest periphery of the TVC. The longitudinal view shows basal pillows oriented parallel to the ridge axis and pillows more chaotic in their orientation up-section. (c) View showing mega-pillow lavas (Lp$_2$) exposed in the southern drainage above the terminal moraine. Individual lobes are outlined with dashed yellow lines. (d) Oblique view at a cross section of a mega-pillow lava 100 m upslope from the pillow lavas in Fig. 4b. The Lp$_2$

60

Figure 3.6 continued. Field images of the pillow lava (Lp$_{1-2}$) and vertical pillow lava (Lv) lithofacies.
unit displays a radial-jointing pattern. (e) View showing a hollow Lp$_1$ in the distal pillow lava terrain. The comparatively well preserved, 2 to 3 cm thick shelves of this hollow pillow represent a change in lava flux within the drainage structure. (f) View showing the collapsed shelves within a drainage structure across the stream cut from 5e. The higher number of shelves in this image is more common, especially in larger hollow pillows, than the few found in 5e. (g) View showing vertical pillow lavas (Lv) next to the mega pillow lava in 5d. These Lv lavas are 20 to 30 cm in diameter and, as is common in other locations, are tightly clustered together. (h) A close up view of an Lv structure in the distal TVC lavas. Smoother surfaces are the inner rind exposed when the rougher, horizontally corrugated outer surface has been eroded. The arrow points to an intact outer rind. (i) Oblique view of the cross section of an Lv structure. Vertical lava structures abut one another and commonly resemble pinched cylinders in cross section.

another (Figure 3.6f). The once horizontal, now collapsed shelves display a stacked, concave-up pattern, and ribs on the interior walls represent the remnant of the shelf (Figure 3.6e).

Although hollow pillow lava structures in normal and mega-pillow lavas have been recognized in submarine environments, no consensus on the mechanism of their formation has been reached (Moore, 1975; Ballard and Moore, 1977; Moore and Charlton, 1984; Yamagishi, 1985; Bear and Cas, 2007). However, the smooth, glassy interior rinds and vertical drip structures found on the underside of the horizontal shelves resemble the fluidal surfaces of gas cavities found in subaerial basaltic pahoehoe flows. The rinds resembling subaerial gas cavity surfaces could indicate that the void left by the exiting lava was occupied by a gas phase that was exsolving from the cooling lava. The presence of multiple shelves clearly indicates several episodes of lava drainage from each pillow.

3.3.2.4 Vertical pillow lavas (Lv):

Vertical pillow lava structures (Table 3.1, Lv) are vertically to sub-vertically oriented, distended pillow-like lava bodies 0.4 to 1.5 m in length, up to 0.4 m wide and 0.2 m thick (Figures 3.6g, 3.6h, and 3.6i). Lv commonly comprise tightly packed clusters of extended lava bodies (Figures

3.6g and 3.6i), which are broadly similar to normal pillows, except they typically resemble a more elliptical cylinder compressed along the long axis. In cross-section they frequently resemble a pinched ellipse or "peanut" shape. Like Lp_1 lavas, however, they pinch and swell at wavelengths of 7 to 15 cm along the extent of their length (Figure 3.6g and 3.6h). The intact surfaces of Lv are corrugated normal to the direction of the long axis of the structure (Moore, 1975; Yamagishi, 1985). The relief of the horizontal corrugations is < 1 cm and apexes of the ribs are spaced < 1 cm apart (Figure 3.6h). When the < 1.5 cm thick corrugated surface has been weathered away a slightly bulbous, smooth, glassy surface is commonly exposed (Figure 3.6h). The Lv lavas are porphyritic with tabular plagioclase crystals up to 1 cm in length, and contain 20 to 35 volume percent of ~1 mm spherical vesicles and less commonly 5 mm diameter pipe vesicles. Vertical pillow lava structures are ubiquitous in the distal pillow lava terrain and are rare, but present in the medial massive lava terrain (Figure 3.7c).

Vertical pillow structures are interpreted in the same manner as those previously referred to as prograding pillow tubes in that they create aggrading, vertical to near vertical sets of pillows that draped a near vertical substrate (Ballard and Moore, 1977; Basaltic Volcanism Study, 1981; Batiza and White, 2000). We interpret Lv as representing a series of vertical pillow lavas aggrading over very steep lava flow margins, which were likely generated by ice confinement, although clearly other mechanisms can generate very steep lava flow margins discussed below (section 3.6).

3.3.2.5 Massive Lavas (Lm)

The massive lavas (Table 3.1, Lm) are non-pillowed lobes of single lava flow units much larger than single Lp and Lv structures (Figure 3.7a, 3.7b). The Lm lithofacies occurs as either single lobes or vertically stacked lobes in the northern scarp of the southern drainage below Koosick

Figure 3.7. Field images of the massive lava (Lm) lithofacies.

(a) View of the basal columns and entablature jointing of the eastern-most massive lava flow unit exposed in the southern drainage. The basal columns overlie diamictite described below. (b) View looking north at stacked Lm flow units exposed in the southern drainage. Individual lobes are outlined with white dashed lines. A lava toe is indicated by the arrow. (c) View of a cross-section of a lobate flow unit. This flow unit has the common basal columnar jointing and interior entabulature jointing. Relic pillow lava structures make up the upper section of the flow unit.

Bluff (Figures 3.7a and 3.7b). The flow lobes are low aspect, oblate in cross-section, 2 to 15 m wide and up to 3 m thick. Where exposed the bottoms of the lower most lobes are fluidal or curviplanar. The lavas that are plagioclase-phyric and contain 10 to 35 vol % vesicles are dark gray on fresh surfaces and are gray to red-orange on weathered surfaces. The lobes commonly display poorly vesiculated basal colonnades. The roughly parallel colonnades are 10 to 20 cm in diameter and up to 80 cm high. Above the colonnade structures is an "entablature" zone of blocky jointing in the lava, with some areas of curved columns that average 10 cm in diameter (Figure 3.7c). Some Lm lobes contain only entablature jointing or display cylindrical rosettes of columns. Some of the lobes also display well defined vertical pillows (Lv facies) along their steep margins, though they are commonly more eroded than those in the distal pillow lava terrain (Figure 3.7c). The upper surface of some flow lobes displays hackly jointing or eroded pillows.

Observations of the lateral extent of the lavas, the internal cooling patterns and the glassy nature and locally pillowed upper surfaces are consistent with the lavas having been emplaced subaqueously as a series of narrow lobes (Griffiths and Fink, 1992b; Kennish and Lutz, 1998; Wilson and Head, 2002; Smellie, 2008). The lack of pillows in the bulk of the lavas, and the systematic fracture patterns, suggest that they were emplaced at higher volumetric fluxes than pillow lavas and were cooled by water ingress (Griffiths and Fink, 1992b; Gregg and Fink, 1995; Kennish and Lutz, 1998; Wilson and Head, 2002; Smellie, 2008).

3.3.3   Glaciogenic lithofacies

Glaciogenic lithofacies include massive (Dmm) and stratified (Dms) diamicton, graded gravelly sands (gGS), and bedded sandstones (Sh).

64

3.3.3.1 Diamicton (Dmm, Dms)

Diamicton lithofacies (Table 3.1) at the TVC are classified as either massive (Dmm$_{1-2}$, Figure 3.6a, b) or stratified (Dms, Figure 3.8c and 3.8d). The Dmm lithofacies is further defined as well consolidated (Dmm$_1$) or poorly consolidated (Dmm$_2$). Both are massive and matrix supported, and up to 3 m thick where it is well consolidated (Figure 3.8a), but less than 2 m thick where poorly consolidated (Figure 3.8b). Incipient fissile structures are apparent but rare in some sections of Dmm$_1$ and are evident in stratigraphically higher sections of Dmm$_2$. The matrix is dark orange in Dmm$_2$ to dark grey in Dmm$_1$ and comprises medium sand to small pebble, sub-angular to sub-rounded grains in clay-rich silt. In the well-consolidated Dmm$_1$ the clasts are oligomict, angular to sub-rounded, cobble to boulder-sized fragments of dense to poorly vesiculated basalt.

In the poorly consolidated Dmm$_2$ large clasts are more abundant downslope and is monomict with plagioclase porphyritic basaltic lava fragments, interpreted as having been derived from Lp$_{1-2}$ or Lm. Dmm$_2$ may be intercalated with Lm lavas, rest directly above them, or overlie well-consolidated Dmm$_1$.

Stratified diamicton, (Table 3.1, Dms) crops out in areas downslope of the terminal moraine. The unit is poorly sorted with parallel to irregularly beds, .01 to 3 m thick (Figure 3.8c). The beds are massive to normally graded and commonly defined by laminae of grey silt or sand. The thinnest beds are finer grained, gray and discontinuous. The matrix is gray to brown and comprises sand to very coarse sand sized angular to sub-rounded grains of Ice Peak Formation and older lavas. The clasts vary from pebble sized to boulders 1.2 m in length, are round to angular and are oligomict, comprising brown Ice Peak Formation lava clasts and greenish lava clasts. Striations are clearly displayed on the larger, sub-rounded to rounded lava clasts.
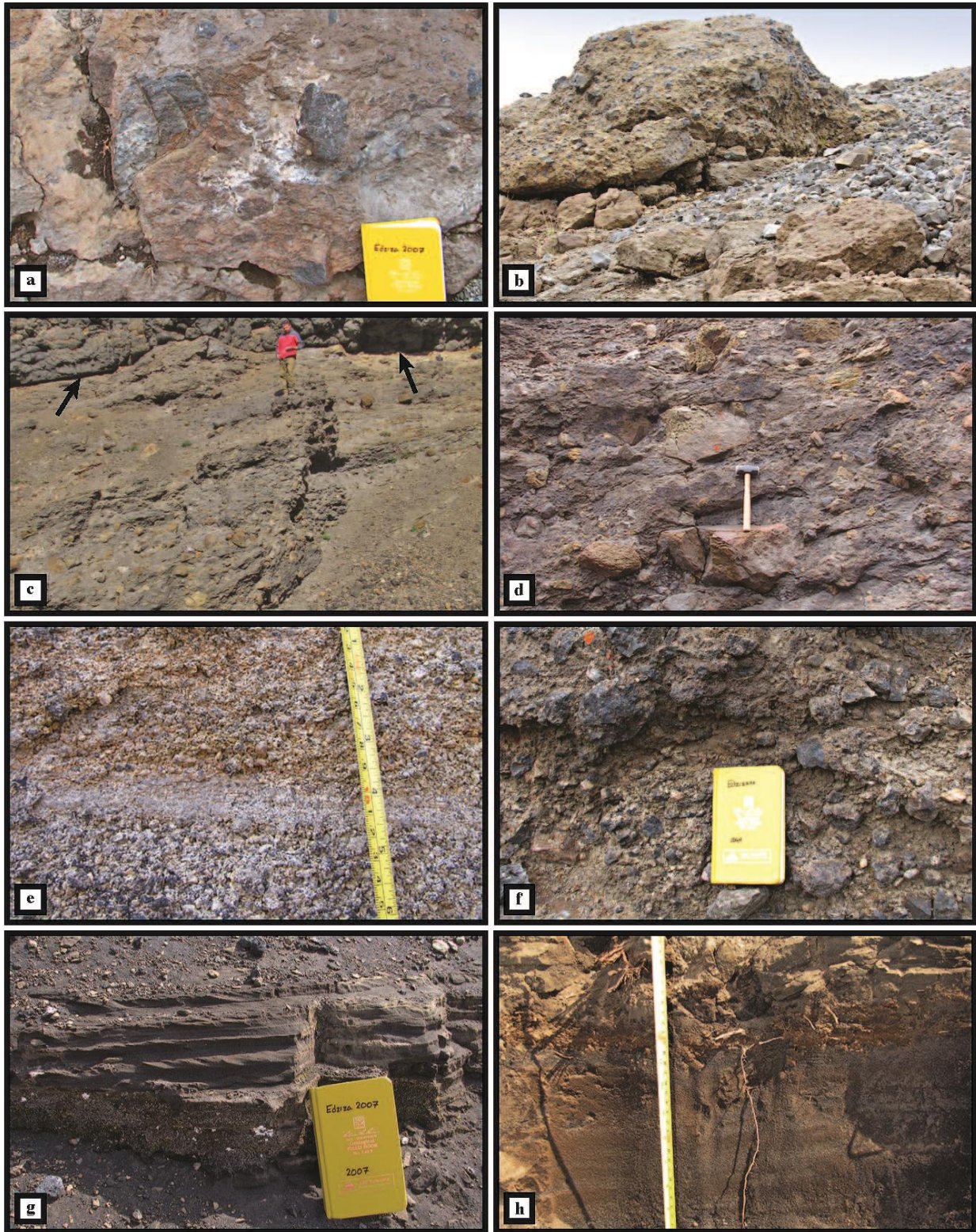
Figure 3.8. Field images of glaciogenic lithofacies associated with TVC lavas.

Figure 3.8 continued. (a) A close-up view of the massive diamicton (Dmm$_1$) that underlies the proximal pillow lava mounds and sheet lavas (Lm). This outcrop underlies Lm lavas in the north scarp of the southern drainage. (b) View showing Dmm$_2$ outcrop between lobes of coherent lava facies Lm. The angular clasts in the outcrop are fragments of TVC lavas. (c) View showing an outcrop of stratified diamictite (Dms) that underlies a pillow lava ridge below the terminal moraine. The contact between the overlying pillow lavas and Dms is indicated by the arrows. (d) A closer view of stratified diamicton (Dms). The diamicton beds are commonly defined by lamina of sand or silt. (e) A close-up view of sub-parallel to hummocky bedded sand and gravel couplets (gGs). The very thinly to medium bedded couplets are made up of consolidated, angular clasts of basaltic lava. (f) Within the beds of gGs are lenses of coarser grained scour and fill structures filled with poorly sorted gravel to cobble sized clasts. (g) View showing the vitric, stratified sands (Sh) and the associated underlying gravels. This cross-bedded outcrop onlaps a pillow lava ridge. (h) View showing the upper section of the ~2 m of stratified sands (Sh) that overlie distal lavas. The thin to very thin, hummocky beds are differentiated by the variation in mean grain size.

We interpret the well-consolidated Dmm$_1$ as a subglacially deposited lodgment tillite, on the basis of its massive, heterolithic, poorly sorted nature with striated clasts (Benn and Evans, 1998; Evans and Benn, 2004). Dark orange hues in the matrix of Dmm$_1$ near contacts with Lm flow units suggest thermal alteration by the overlying lava.

Given the dominant presence of TVC lava clasts in Dmm$_2$, we interpret this facies as representing coeval resedimentation of TB and LT lithofacies through meltwater transport with a very high concentration of clasts, perhaps as subaqueous debris flows.

The Dms deposits are interpreted as the products of subglacial meltwater drainage and deposition by hyperconcentrated meltwater flows occurring during the Tennena eruption or very shortly afterwards (Cas et al., 1989; Skilling, 1994; Benn and Evans, 1998; Schopka et al., 2006). The defined bedding, poor sorting and oligomict lithological make-up is interpreted to indicate re-sedimentation of a variety of clast sources with lower sediment concentrations than that which produced the Dmm facies.

3.3.3.2 Graded gravelly sand (gGs)

Consolidated graded gravelly sand (Table 3.1, gGs) crop out downslope from the terminal moraine (Figure 3.8e). These thickly laminated to medium bedded, tan to brown colored units are 2 to 7 m thick. The beds are defined by grain size variation and either display sub-parallel or

cross-stratification. Minor syn-sedimentary faulting is present. The thin beds and laminae are made of black, well-sorted sand sized, angular to sub-angular grains of dense to moderately vesiculated poorly crystalline to glassy lava (Figure 3.8e). Thicker beds are not as well sorted and include uncommon lenses of sub-rounded, red-brown or sub-angular, black lava cobbles (Figure 3.8f). Under the distal section of an overlying pillow lava ridge the uppermost gGs deposits are dark brown, poorly sorted beds with angular black pebble to large cobble-sized lava clasts.

We interpret the gGs deposits as glaciofluvial sediments emplaced in the subglacial drainage system during the Tennena eruption, or at least prior to the cementation of its clastic deposits, with the glassy clasts derived from the TB or LT lithofacies. The sorting and presence of traction current structures suggests that this facies represents the deposits of dilute streamflows.

3.3.3.3 Bedded Sandstones (Sh)

Poorly consolidated sandstone (Table 3.1, Sh) are found west of the terminal moraine where they overlie Ice Peak Formation and TVC lava flows (Figure 3.3, 3.8f, 3.8g). This facies is black and dark brown, thickly laminated to thinly bedded, and with horizontal to sub-parallel bedding. The clasts are sub- to well-rounded, well-sorted grains of basaltic glass. The sandstones display normal grading and areas of well-developed ripple and dune bedding are present.

Given good sorting, and parallel to rippled bedding we interpret the gGs as subglacial streamflow deposits, which are probably the distal equivalent of the gravelly sands facies (gGs), similarly derived from the TB and LT lithofacies at the TVC (Benn and Evans, 1998; Bennett et al., 2009).

3.4   LITHOFACIES ASSOCIATIONS AND ARCHITECTURE

We use the presence and spatial relationships of the lithofacies described above, to identify four distinct terrains within the TVC: 1) Tennena Cone, 2) proximal pillow lavas, 3) medial lavas, and 4) distal pillow lavas. Each of these four terrains records local changes in emplacement conditions during the course of the eruption.

3.4.1   Tennena Cone

Four volcanic lithofacies (TB, LT, Ld and Lp_1, Table 3.1) are exposed in near-vertical scarps of the western, eastern and southern flanks of the cone. Within the western scarp, TB is the only exposed lithofacies (Fig 3.9c). The stratigraphic relationships of the four lithofacies of the cone (TB, Lp_1, LT and Ld) are best exposed in the eastern scarp (Fig. 3.9d, 3.9f). Within the southern section of the eastern scarp, LT is the only lithofacies exposed. Apparent dip directions of LT beds vary from southwest in the southern section of the scarp to southeast in the middle and northern sections of the scarp. In the middle section of the eastern scarp, lithofacies TB is exposed above the scree apron and below beds of LT. Both Lp_1 lavas and lavas with incipient pillow or fluidal morphologies form a 150 m long wedge in the middle section of the eastern scarp. Well-formed Lp_1 lavas are found in the southern, downslope section of the wedge and fluidal lavas are volumetrically dominant in the northern section of the wedge (Fig. 3.9e). The contacts between the Lp_1 wedge, TB and LT display southeasterly apparent dips. A dike intrudes all three lithofacies in this middle section of the eastern scarp (Fig 3.9d).
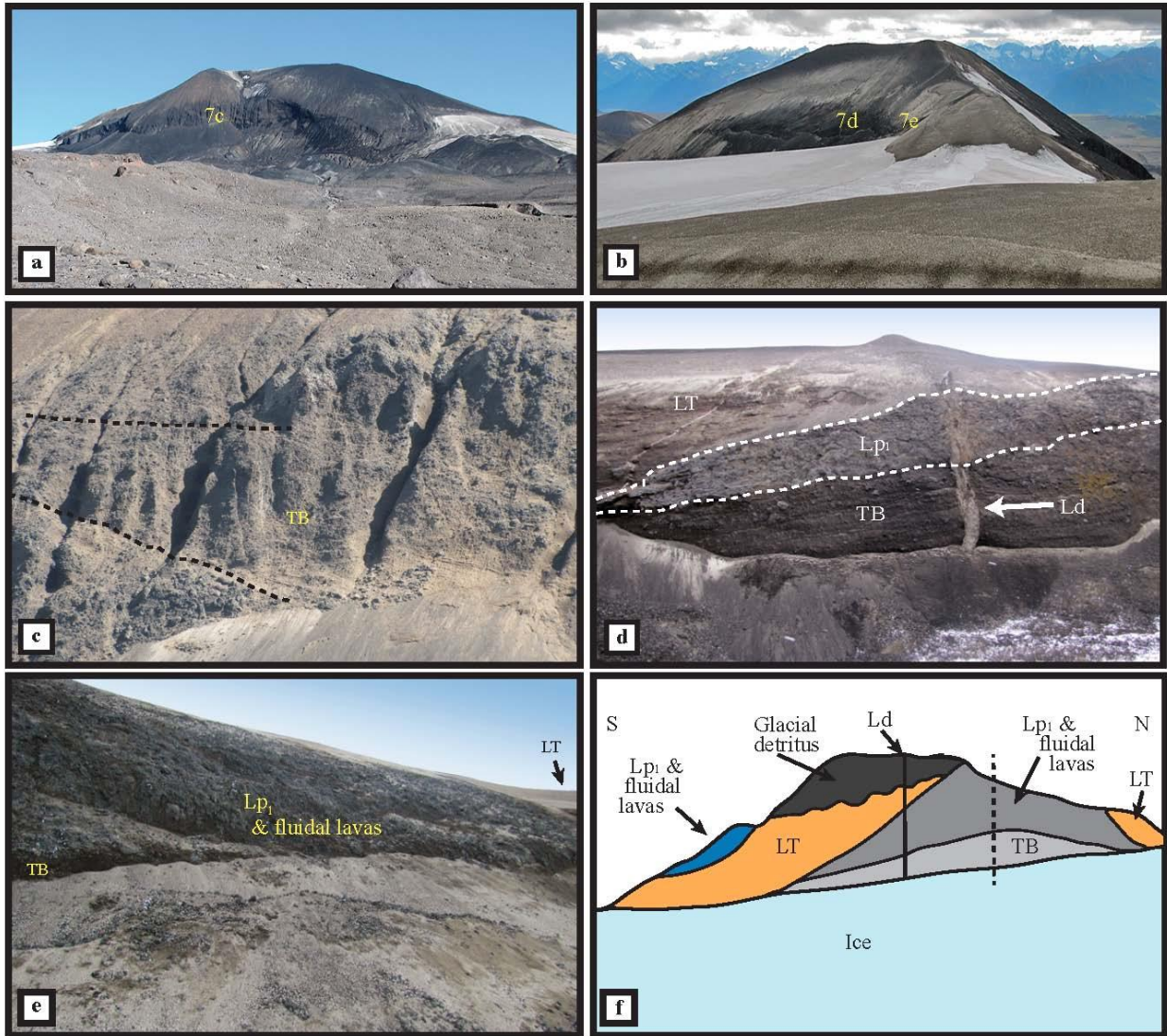
Figure 3.9.Morphology of Tennena Cone.

(a) View of the western flank and the glacially over-steepened western scarp under the 500 m long summit ridge of Tennena Cone. (b) View of the eastern side of Tennena Cone from Ice Peak. The locations of Figs. 10d and 10e are indicated. (c) A closer view of the scarp in the west flank of Tennena Cone. Crude bedding sequences that crosscut underlying beds of lapilli tuff (LT) are visible on the near vertical faces. (d) View of bedding in the eastern sub-vertical face of Tennena Cone steepened by glacial erosion. A wedge of pillow lavas and fluidal lavas, outlined by dashed lines, lies between beds of tuff breccia (TB) and lapilli tuff (LT) and thickens to the north. Both the pillow lavas and the overlying and underlying tuff beds are cut by the southern 1 m thick dike (Ld) shown in fig. 2a. (e) View of Lp_1 and fluidal lavas overlying TB in the northern section of the cone. Beds of LT make up the northern most section of the cone and are indicated in the right of the image. (f) A sketch of the lithofacies exposed on the east side of Tennena Cone. The dashed line indicates the change in the axial trend from north to northeast towards Ice Peak. Beds of LT overlie the coherent lavas comprising Lp_1 and fluidal morphologies.

70

Figure 3.9 continued. The coherent morphologies overlie TB. A carapace of Lp_1 and fluidal lavas overlie the LT beds on the southwest flank of the cone.

The interbedding of pillow lavas that parallel the bedding in the subaqueous volcaniclastic facies exposed in the flanks of the cone suggest the cone was emplaced entirely subaqueously. It is unclear whether variations in TB versus LT facies within the cone reflects proximity to a source of clast avalanching off a pillow lava front, variations in explosive efficiency, or a combination of both. Although dip variations within the lithofacies at the cone may indicate some vent migration during the eruption, we do not have enough data to pinpoint the exact location of the vents through time.

3.4.2 Proximal pillow lava terrain

The proximal pillow lava terrain comprises an ~0.45 km^2 area of hummocky topography at the southwestern base of Tennena Cone (Figure 3.10a). Souther (1992) indicated that a glacier covered this area in the mid 1960's and 1970's, but the glacier has since retreated at least 1.5 km to expose this terrain, which is made up of elongate mounds of Lp_1 that vary in height from 3 to 20 m and are up to 75 m in diameter at their base. The tallest mounds are closer to the cone in the northeastern part of the terrain (Figures 3.10a and 3.10b). The mounds in the southern extent are short, diffuse and covered by a veneer of unconsolidated glacial lag deposits but are evident in ~2 m deep incisions cut by streams fed by glacial runoff. The tops of the northern and central mounds comprise *in situ* brecciated pillows, or deposits comprising rotated <15 cm sub-angular fragments pillow lava.

71
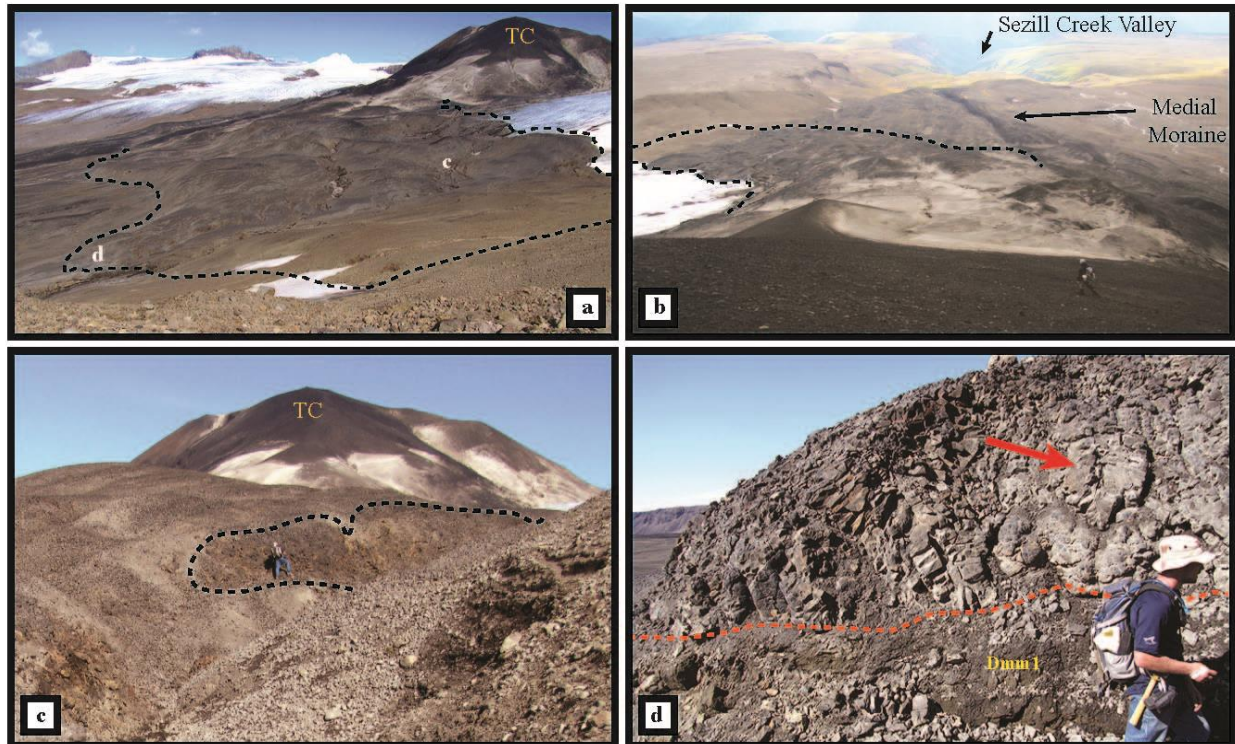
Figure 3.10. Field images of the pillow lava mounds proximal to Tennena Cone.

(a) View looking north-northeast at the distribution of the pillow lava mounds southwest of Tennena Cone (upper right of image). The letters within the image represent the locations of images c and d in Figure 3.10. A glacial veneer of predominantly pillow lava breccia covers the pillow lava mounds north of image location d, whereas the mounds south of letter d in the image are covered with a veneer of brown hued, oligomict boulder pavement. The light tan colored deposits on the lower southwest flanks of Tennena Cone are Sheep Track pumice. (b) View looking west-southwest downslope upon the pillow lava mounds from the summit ridge of Tennena Cone. The black dashed line indicates the extent of the pillow lava mounds. The mounds proximal to the cone are covered in a veneer of light tan Sheep Track Pumice. The location of the medial moraine is also noted in the center of the image. (c) View looking northeast within the pillow lava mounds with Tennena Cone (TC) in the background. The black dashed line surrounds an outcrop of Lp_1 that tend to be exposed on steeper slopes of the glacially modified mounds. A veneer of unconsolidated pillow lava debris covers shallow sloped surfaces. (d) View showing a cross-section of a pillow lava mound incised by the southern drainage. The dashed black line indicates the contact between the pillow lavas and the underlying well consolidated, matrix supported, massive diamictite (Dmm_1). The arrow indicates a near vertical pillow lava tube.

The principal trend of the mound axes is to the south-southwest, not to the west, which is the dip direction of the underlying topography (Figure 3.10a). A contact with underlying

diamicton (Dmm_1) is exposed where the southern drainage incised the pillow lava mounds (Figure 3.10d).

This terrain is interpreted as a group of subglacial, fissure-fed, pillow lava mounds, similar to those described at other basaltic submarine and glaciovolcanic centers (e.g., Skilling, 2009). It is not clear how much of their morphology has been controlled by direct contact with enclosing ice.

3.4.3   Medial massive lava terrain

The medial massive lava terrain is dominated by Lm (Figure 3.3, 3.11a) with an exposed area of ~0.4 km^2 across shallowly sloping (<2.5%) topography. Cross-sections of the Lm lavas in the southern drainage run roughly east-west with the eastern Lm units being the vent proximal lobes. The easternmost extent of the outcrop in the southern drainage is made of three or possibly four single flow units laterally abutting each other (Figure 3.7a, 3.11b). The lowest Lm lobes rest on diamicton (Dmm_1) substrate that dips roughly 10° to the west-southwest. The Lm flow units in the westernmost section of the southern drainage tend to be less than 1.5 m thick and display interbeds of oxidized, orange, TVC lava bearing Dmm_2 (Figure 3.11d, 3.11e). To the east of the single Lm lobes the poorly consolidated Dmm_2 unconformably overlies Dmm_1 and crops out as sporadic lenses intercalated with Lm lavas.

Normal pillow lavas (Lp_1) are more commonly associated with the western Lm flows than those up slope to the east. Well formed, 1.5 m stacks of Lp_1 lavas crop out on top of and at flow margins of the western-most Lm flows. Surfaces of upper Lm lobes are also commonly
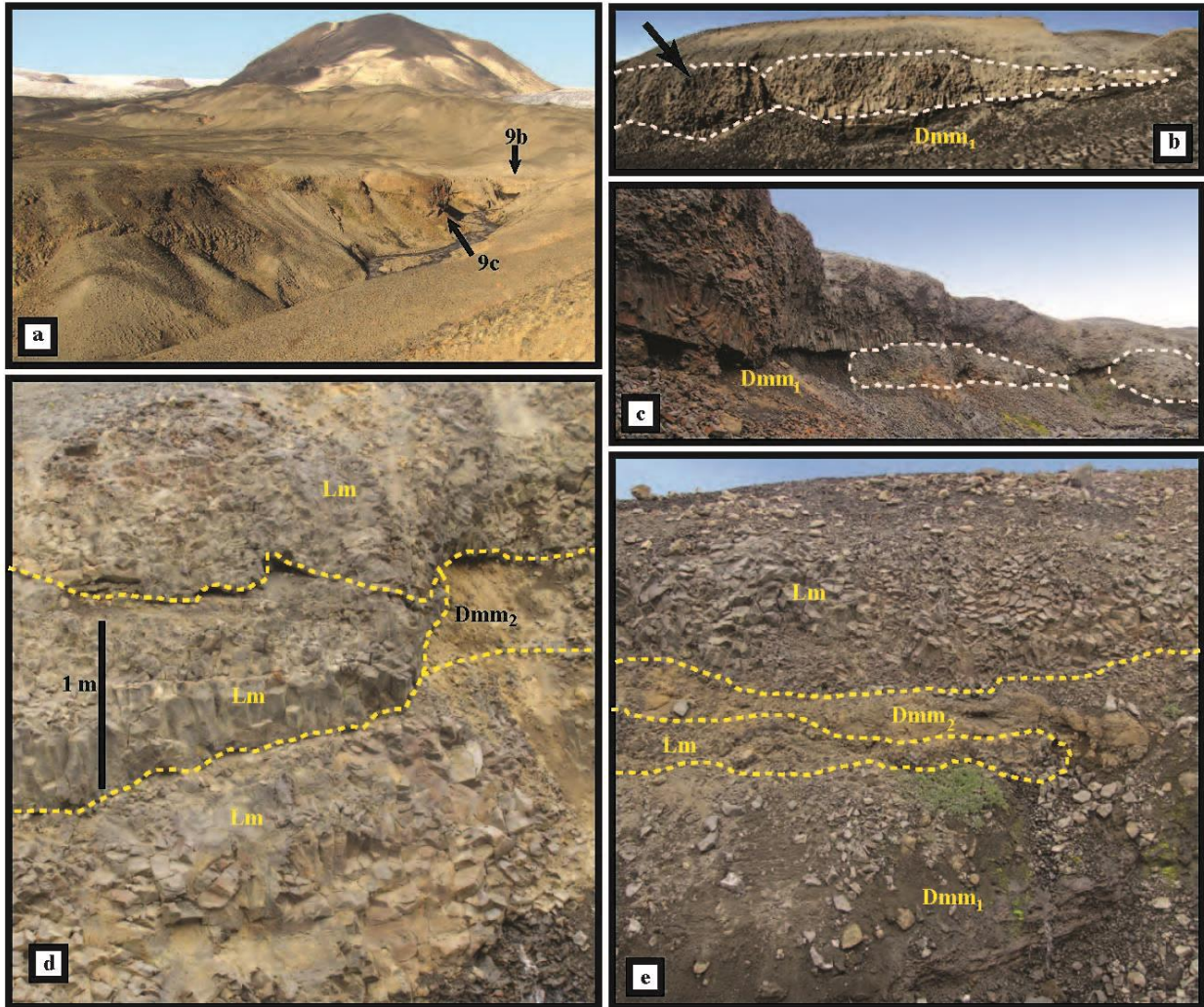
Figure 3.11. Field images of the massive lavas (Lm) just west of the proximal pillow lava mounds.

(a) View looking east-northeast at the Lm lavas exposed in the southern drainage. The pillow lava mounds and Tennena Cone lie in the distance. The location of Figure 9b is noted and 9c is indicated by the arrow. (b) View across the southern drainage of eastern most single Lm flow unit. The unit overlies diamicton and the arrow indicates an area of rosette colonnade jointing within the flow unit. (c) View looking northeast up the southern drainage at Lm flow units. The unit in the foreground has basal columnar jointing and entablature jointing in the flow interior. The white dashed line highlights flow units emplaced prior to the larger overlying flow. (d) A closer view of stacked Lm flow units and an intercalated lens of Dmm_2 in the southern section of the exposed Lm lavas in the southern drainage. Red dashed lines indicate the flow unit contacts. Basal jointing is either columnar or entablature and flow interiors display well-developed entablature. (e) View looking north at the distal, western lobate lava units outlined by dashed red lines. The flow units are intercalated with Dmm_2 and display entablature jointing. Here Dmm_2 directly overlies Dmm_1.

composed of relic pillow-like structures. Also within the western reaches of the Lm lavas a single, 25 m wide group of mega-pillow lavas (Lp_2) crop out below Lm lobes (Figure 3.6c). The tightly packed Lp_2 lava bodies dip to the south at ~20° and display incipient to well-developed radial jointing. Eroded vertical pillow lavas (Lv) locally drape steep sided sections of Lm lobes, especially to the west (Figure 3.7c).

The interbedding of glacial deposits and the massive lavas is consistent with subglacial emplacement of the lava flows. The steep margins of the lavas draped by vertical pillows (Lv facies) are interpreted as evidence of direct ice confinement. The massive lavas were emplaced at higher flux rates than the pillow lavas (e.g., Gregg and Fink, 1995).

3.4.4 Distal pillow lava terrain

West and north of both the medial massive lava terrain and the proximal pillow lava terrain, the distal pillow lavas extend 4.4 km from the western base of Tennena Cone to the terminus of the TVC deposits at the head of Sezill Creek Valley (Figure 3.3, 3.12a). The terrain comprises the coherent lithofacies Lp_1, Lp_2 and Lv. Lithofacies Lp_1 is the only coherent lava morphology evident above the terminal moraine in the distal pillow lava terrain (Figure 3.6a). The Lp_1 lavas in this area overlie shallowly westward dipping Ice Peak Formation lava flows and are covered by unconsolidated glacial lag deposits (Figure 3.12b). This lithofacies crops out as diffuse sinuous ridges of pillow lavas that are up to 10 m high and 20 m in diameter east of the terminal moraine. The Lp_1 lavas in the ridges are round to oblate in cross-section and tend to plunge downslope, and away from the curviplanar axes of the ridges. Hollow Lp_1 pillow tubes are extremely rare in these ridges. The ridges are traceable from the southwestern base of Tennena Cone westward beyond the terminal moraine.
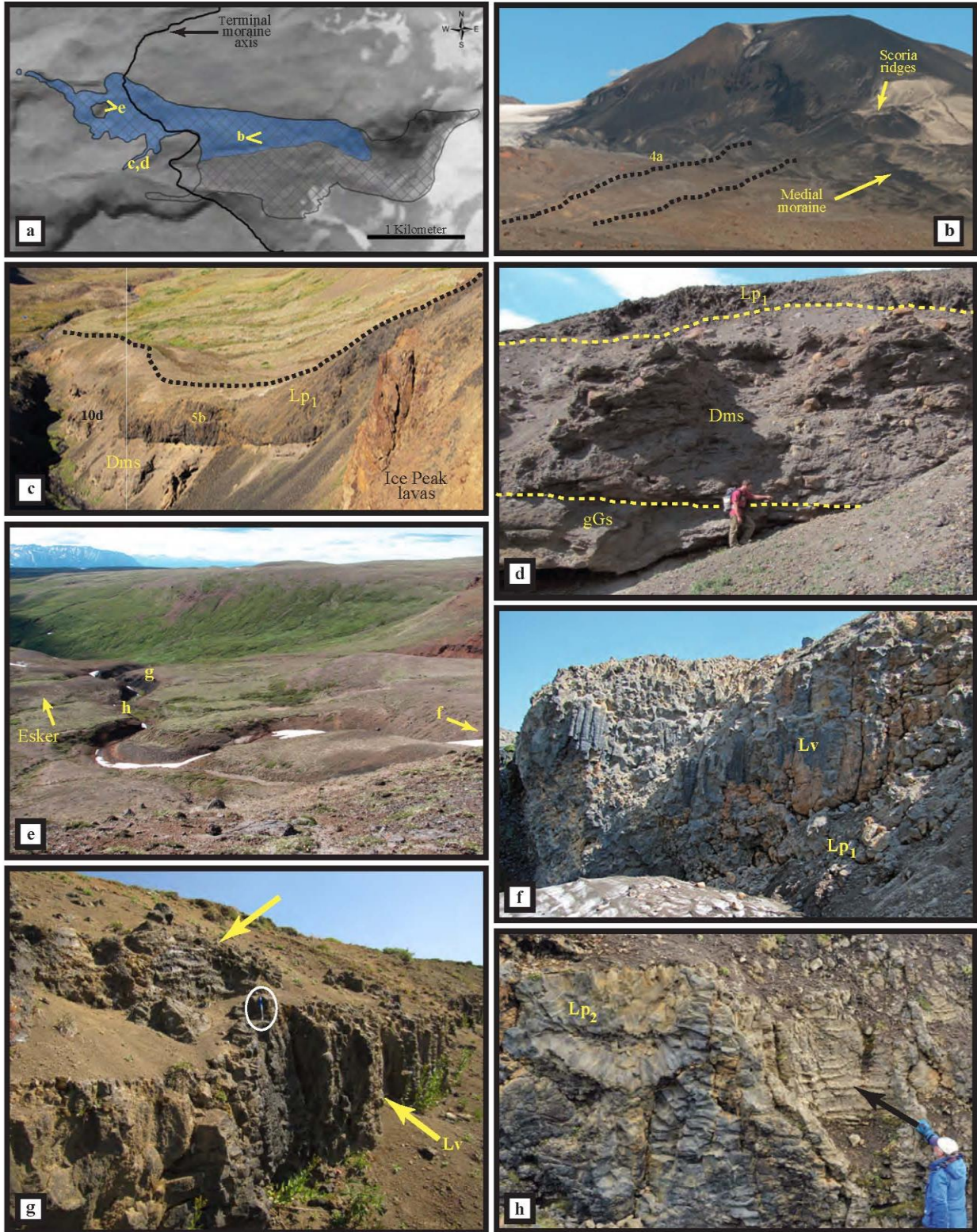
Figure 3.12. Field images of distal pillow lava morphologies.

Figure 3.12 continued. (a) A map showing the location of images b through e in Figure 10. The crosshatched area is the extent of TVC lavas. The shaded section of the crosshatched area is the extent of the distal pillow lava terrain. (b) View looking east-northeast at Tennena Cone. The black dashed line indicates the axes of two pillow lava ridges covered with unconsolidated pillow lava breccia and oligomict boulder pavement. The scoria ridges, indicated with an arrow, are interpreted as the source vent for the lavas in the distal pillow lava terrain. (c) Looking southwest at a pillow lava ridge below the terminal moraine. An arrow in Figure 3.4 shows the position of this ridge relative to other TVC lavas. The black dashed line represents the pillow lava ridge axis. The substrate under the pillow lava ridge is Ice Peak Formation lavas (IP) overlain by glacially derived sediments (gGs and Dms). Pillow lavas cascaded over a cliff in the IP lava substrate and advanced as a ridge Lp_1 lavas seen in Figure 3.6b. The location of Figures 3.7b and 3.12d are noted on the image. (d) View looking west-northwest, normal to the axis of the pillow ridge in Figure 3.12c, at the stratigraphic relationship between the underlying glaciofluvial sediments and the pillow lava ridge. Dashed lines indicate the contacts between the gGs, Dms and Lp_1 lavas. (e) View looking west-northwest over a 25 m cliff at the distal TVC. The TVC lavas are exposed in the stream cut that terminates at the head of Sezill Creek valley in the upper left of the image. The TVC lavas in the image are overlain with the glaciogenic lithofacies (Sh). An esker of bedded Sh, indicated by an arrow, also overlies the distal TVC lavas. The locations of f through h in Figure 3.12 are shown on the image. (f) View looking southeast at the incised TC lava ridge on the north side of the 25 m cliff in the Ice Peak lava substrate. Vertical pillow lavas (Lv) overlie an outcrop of basal Lp_1. (g) View of distal TVC lavas cropping out in the north wall of the drainage. The upper arrow points to relic shelves in a set of hollow pillow lava structures. The hollow pillows are perched above Lv lavas indicated by the bottom arrow. The pen, circled in the middle of the image, stands atop an Lv body that once abutted another Lv body that has subsequently weathered away. (h) View looking at an outcrop on the south side of the stream-cut in Figure 3.12e. To the left in the image are mega-pillow lava structures (Lp_2) and the right to a relic hollow pillow. Note the radial cooling pattern in the Lp_2 and the ribbed texture in the hollow Lp_2.

Within 100 m above the terminal moraine the underlying Ice Peak lava flows form a stepped topography with westward, shallowly dipping slopes between scarps that are up to 4 m high. Here the Lp_1 ridges are taller, less diffuse and bifurcate more than those further to the west. Below the terminal moraine the slope of the underlying topography varies more and scarps in the underlying Ice Peak lavas vary between 4 and 25 m in height. Here the coherent lava lithofacies of the distal pillow lava terrain directly overlie either Ice Peak Formation lavas or glaciogenic lithofacies (gGs and Dms). Two distinct flow morphologies are also present below the terminal moraine: 1) higher aspect ratio pillow lava ridges, and 2) lower aspect ratio, topography filling

flows. Higher aspect ratio pillow lava ridges are found on steeper slopes and are dominated by Lp_1 lavas (Figures 3.12c and 3.12d). Topography filling lava flows are found on shallower slopes and display a greater variance in pillow morphology where individual pillows vary in size from 0.15 to 2 m in diameter. Both Lp lithofacies and the Lv lithofacies are ubiquitous in the lower aspect ratio lavas.

West of the medial moraine terminus and 3.7 km west of the base of Tennena Cone, a well exposed, 300 m long pillow lava ridge is adjacent to a stream that flows southwest into the southern drainage (Figure 3.12c). The ridge of Lp_1 lavas is up to 3 m thick and thins to less than 1 m at its terminus 3 m from the southern drainage. The axis of this pillow ridge is curvilinear and its cross-section is broadly hemispherical. This ridge can be traced from the terminal moraine and followed over the vertical face of a cliff in an Ice Peak lava flow. A 10 m wide section of pillow lavas cascades over the cliff face and connects the pillow ridge to the more sheet-like lavas above the cliff. The Lp_1 lavas overlie a wedge of glaciogenic sediments below the cliff face (Figures 3.12c and 3.12d). The sediment wedge is thickest at the cliff and thins to less than 1 m in the southwest, near the terminus of the Lp_1 ridge. The wedge of glaciogenic sediments comprises up to 30 m of stratified diamicton (Dms, Figures 3.8c and 3.8d) and underlying graded gravels and sands (gGs, Figures 3.8e and 3.8f). The Dms beds dip to the southwest at an average angle of 20° and unconformably overlie well-consolidated gGs.

Further north other pillow lava ridges comprising Lp_1 tend to terminate when the underlying topography shallows (Figure 3.12d). The interior of these ridges is composed of Lp_1 lavas draped by Lv lavas (Figure 3.12f). The lavas are also overlain by a poorly to unconsolidated, clast supported pillow breccia with an oxidized matrix.

Below the 25 m cliff of Ice Peak lavas and between the two areas of pillow ridges TC lavas lie in a flat to shallowly westward dipping area (Figure 3.12e). Here they are overlain by poorly consolidated, planar to cross-bedded sands (Sh), and comprise two dominant lava lithofacies, mega-pillow lavas (Lp$_2$), and vertical pillow structures (Lv, Figures 3.12g and 3.12h). Many of the Lp$_2$ lavas are hollow and/or shelved (Figures 3.6e and 3.6f). The Lv lavas in this area are commonly found near or below intact or eroded hollow pillow lava structures (Figure 3.12g).

This terrain is interpreted as recording emplacement of pillow lavas within pre-existing sub-ice meltwater drainage tunnels, which locally cascaded over steep sub-ice topography. The sinuosity of at least one of the pillow lava ridges is similar to that seen in some esker deposits (Figure 3.12e). The common association of Lv along the steep margins of the pillow ridges is interpreted as evidence of ice confinement, and in combination with the associated glacial deposits supports our interpretation of sub-ice emplacement.

3.5   GEOCHEMICAL ANALYSES

In order to constrain eruption conditions, four samples of coherent units and six samples of glass from the rims of pillow lavas were analyzed for major element compositions (Table 3.2); the pillow glasses were also analyzed for H$_2$O/CO$_2$ concentrations (Table 3.3). Two samples were also analyzed for ^{40}Ar-^{39}Ar geochronology at New Mexico Institute of Mining and Technology. The results are analytically robust and yield near zero ages with errors of 33 ka (0.005 Ma +/- 0.033 Ma, 0.011 Ma +/- 0.033 Ma; W. MacIntosh, pers. comm., 2009). Though the resulting age

Table 3.2. Major element geochemistry for whole rock (WR)[a] and glasses (EMP)[b] from Tennena volcanic center samples.

Oxides	EJH06 07-04b WR	EJH06 09-42c WR	EJH06 13-03b WR	EJH06 15-02a WR n=3	EJH06 14-3A EMP n=3	EJH06 14-10A EMP n=3	EJH06 13-3A EMP n=2	EJH06 15-3A EMP n=2	EJH06 14-11A EMP n=2	EJH06 07-01B EMP n=3
SiO_2	47.41	47.87	47.98	47.50	49.99	49.50	49.95	49.72	49.90	49.27
TiO_2	2.33	2.12	2.01	2.36	3.12	3.07	3.06	3.21	2.89	2.93
Al_2O_3	15.44	15.73	16.76	15.38	14.95	14.08	14.35	13.99	14.39	14.78
Fe_2O_3	14.19	12.86	12.12	14.31	11.58	12.22	12.37	12.40	11.89	10.94
MnO	0.20	0.18	0.17	0.20	0.22	0.20	0.22	0.21	0.21	0.16
MgO	6.20	7.07	6.35	6.34	4.86	4.80	4.43	4.38	4.86	4.81
CaO	10.18	9.98	10.92	10.44	10.57	10.12	9.36	10.04	10.00	12.01
Na_2O	3.41	3.37	3.29	3.23	1.88	3.70	3.72	3.63	3.63	3.38
K_2O	0.84	1.05	0.80	0.75	1.53	1.21	1.31	1.15	1.12	0.67
P_2O_5	0.34	0.38	0.32	0.32						
SO3					0.42	0.38	0.42	0.43	0.40	0.21
Cl					0.04	0.04	0.04	0.04	0.03	0.02
H_2O[c]					0.86	0.68	0.78	0.79	0.68	0.81
Total	100.53	100.62	100.71	100.84	100	100	100	100	100	100
Ba	160	280	222	144	-	-	-	-	-	-
Ce	50	50	29	42	-	-	-	-	-	-
Co	51	41	44	40	-	-	-	-	-	-
Cr	262	466	368	269	-	-	-	-	-	-
Cu	54	98	86	91	-	-	-	-	-	-
Ni	75	103	77	74	-	-	-	-	-	-
Sc	20	20	15	23	-	-	-	-	-	-
V	243	193	203	249	-	-	-	-	-	-
Zn	98	80	75	93	-	-	-	-	-	-
Mg /	63.4	68.5	67.5	63.7	62.4	60.9	58.6	58.3	61.8	63.5
T liquidus	1150	1183	1147	1149	1122	1146	1133	1137	1146	1154
Liq Phase	Fo76	Fo80	Fo78	Fo76	Cpx	Cpx	Cpx	Cpx	Cpx	Cpx

(a) - analyses via XRF by McGill University Geochemical Laboratories;
(b) - analyses by Electron Microprobe Analysis at University of Wisconsin
(c) - analyzed by FTIR;
(d) - calculated using MELTS and assuming 1 weight percent H2O and fO2 set at -1 del QFM

Table 3.3. Analyses of H_2O, calculated liquidus temperatures, and estimated confining pressures, water depths, and ice thicknesses for samples of glass from pillow rims from Tennena volcanic center.

Sample Number	Sample Elevation m ASL	Wt. % H_2O[a]	T_{liq} (^{o}C)[b]	Wt.% CO_2	Method[c]	Pressure (MPa)	Ice Thick. (m)[d]	Min. Ice Elevation (m)[e]
EJH06_14_03A	1870	0.83	1122	25	N&L	12.5	1412	3282
				0	N&L	7.0	792	2662
EJH06_14_11A	1999	0.67	1146	25	N&L	9.7	1099	3098
				0	N&L	4.2	480	2479
EJH06_07_01B	1600	0.81	1154	25	N&L	11.6	1316	2916
				0	N&L	6.1	697	2297
EJH06_15_03A	1908	0.78	1137	25	N&L	11.3	1280	3188
				0	N&L	5.8	661	2561
EJH06_14_10A	1967	0.66	1146	25	N&L	9.7	1099	3066
				0	N&L	4.2	480	2447
EJH06_13_03A	1780	0.76	1133	25	N&L	11.1	1262	3042
				0	N&L	5.7	643	2423

(a) determined by FTIR at University of Wisconsin Milwaukee;
(b) calculated using MELTS (Ghiorso and Sack, 1995; Asimow and Ghiorso, 1998) from glass compositions and water contents (see Table 3.2);
(c) calculated using VOLATILECALC (Newman and Lowenstern, 2002) assuming default SiO_2 weight percent value of 49;
(d) calculated from $t = P/(\rho * g)$;
(e) simple addition of sample elevation and estimated ice thickness

estimates are analytically robust, the precision of the of the dating technique at young ages allows one only to presume TVC lavas were emplaced near LGM or possibly after.

3.5.1 Major element and volatile geochemistry

Glass Lp_1 rim fragments from various locations in the TVC (yellow dots, Figure 3.3) were picked under a binocular microscope, mounted in epoxy in an aluminum disk, and polished for electron microprobe analyses. Major elements along with S and Cl contents of the pillow glasses were measured using a Cameca SX-50 electron microprobe at the University of Chicago. Operating conditions were an acceleration voltage of 15 keV, a beam current of 25 nA, and a beam diameter of ~20 μm. Counting times for S and Cl were 90 and 60 seconds, respectively.

Barite and chloro-apatite were used as mineral standards for S and Cl, respectively. Three Smithsonian glass standards (VG-2, VG-A99, and an Indian Ocean glass) were also used to monitor accuracy and precision. An alpha scan for the S peak on the VG-2 standard necessitated a slight shift in the S peak from the mineral standard. VG-2 from the Juan de Fuca ridge was run nine times during the microprobe session with a mean S and Cl content of 0.147 ± 0.005 and 0.028 ± 0.005 wt% and is consistent with (Gurenko et al., 2005).

Based on major element classification, the material erupted at Tennena Cone is hawaiite to alkaline basalt in composition (Table 3.2, Figure 3.13). Mineral compositions of olivine, plagioclase and clinopyroxene reported by (Souther, 1992) are also consistent with alkaline basalt compositions.
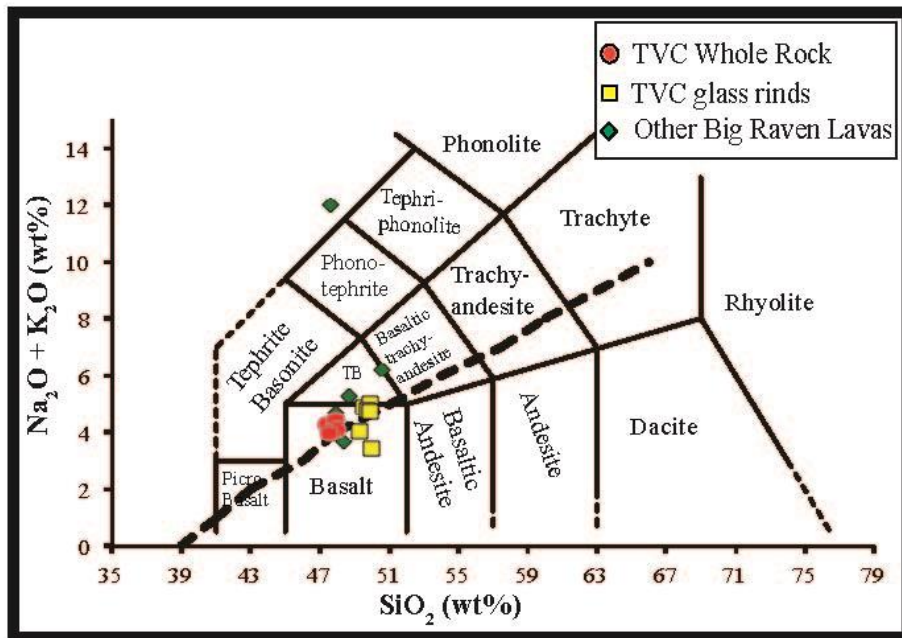
Figure 3.13. Summary of whole rock and glass geochemistry.
A total alkalis versus silica classification diagram (Le Bas et al., 1986) comparing data from analyses of samples from TVC lavas and other Big Raven formation lavas (Souther, 1992, this work). Whole rock analyses of the TVC lavas lie on or just above alkaline–subalkaline division of Irvine and Baragar (1971). The red circles represent whole rock analyses of TVC lavas, yellow squares represent electron microprobe analyses of TVC lava glass rinds, and the green diamonds represent analyses of other Big Raven Formation (of which the TVC lavas are a unit) samples collected by Souther (1992).

3.5.2 Volatile analysis and ice thickness interpretations

A selection of larger fresh glass chips was selected for FTIR analysis. These chips were made into doubly polished wafers approximately 100 μm thick. Dissolved total water contents were measured at the University of Wisconsin-Milwaukee using FTIR spectroscopy. Measurements were conducted on a Nicolet Nexus 470 FTIR with a Continuum Analytical-IR microscope attachment using KBr beam splitter and a liquid nitrogen-cooled MCT-A detector. A 100 μm diameter square aperture was used during the analysis. The size and shape of the aperture was modified owing to the vesicular and crystalline nature of the glass samples. Each spectrum consisted of 512 scans between 650 and 4000 cm^{-1}, taken at 4 cm^{-1} resolution. Glass wafer thickness was determined by a Mitutoyo digital micrometer, microscope focusing, and by FTIR interference fringes in reflectance mode.

Four glass samples were analyzed for CO_2 by step heated manometry, and were found to have measured concentrations of 25, 17, 31, and 24 ppm (Cameron et al., 2008). Saturation pressures were estimated by imputing the measured H_2O contents into the VolatileCalc program (Newman and Lowenstern, 2002). Assuming a basaltic composition of 49 weight percent SiO_2, eruption temperatures calculated using MELTS (Ghiorso and Sack, 1995; Asimow and Ghiorso, 1998), and 0 ppm carbon dioxide, eruption pressures range from 4.2 to 7.0 MPa (Table 3.3). Given the assumption that the pillow lava formed by eruption under water, rather than a mix of water and fragmental material, minimum and maximum ice thicknesses can be calculated for the likely range of CO_2 values.

If the eruption very rapidly melted through the overlying ice, most of the proximal pillow lavas would have been emplaced in an englacial lake; thus the confining pressure would be hydrostatic, not glaciostatic. The minimum ice thickness would be that necessary to confine a

lake whose depth is equal to the calculated confining pressure. If the eruption produced a water-filled cavity within the ice, the overlying pressure would be a combination of that exerted by the overlying ice and water.

Estimates are also strongly dependent on the CO_2 content of the glass. The absence of carbonate peaks during the FTIR analysis suggests that the glasses contain less than 30 parts per million, the accepted detection limit for FTIR. Assuming a water density of 1000 kg m^{-3} and 0 weight percent CO_2, the overlying pressure calculations for TVC lavas result in minimum ice thicknesses between 480 and 792 m (Table 3.3). Using an average CO_2 concentration of 25 parts per million based on manometry measurements, the maximum ice thickness values recorded by TVC lavas vary from 1099 to 1412 m (Figure 3.14).
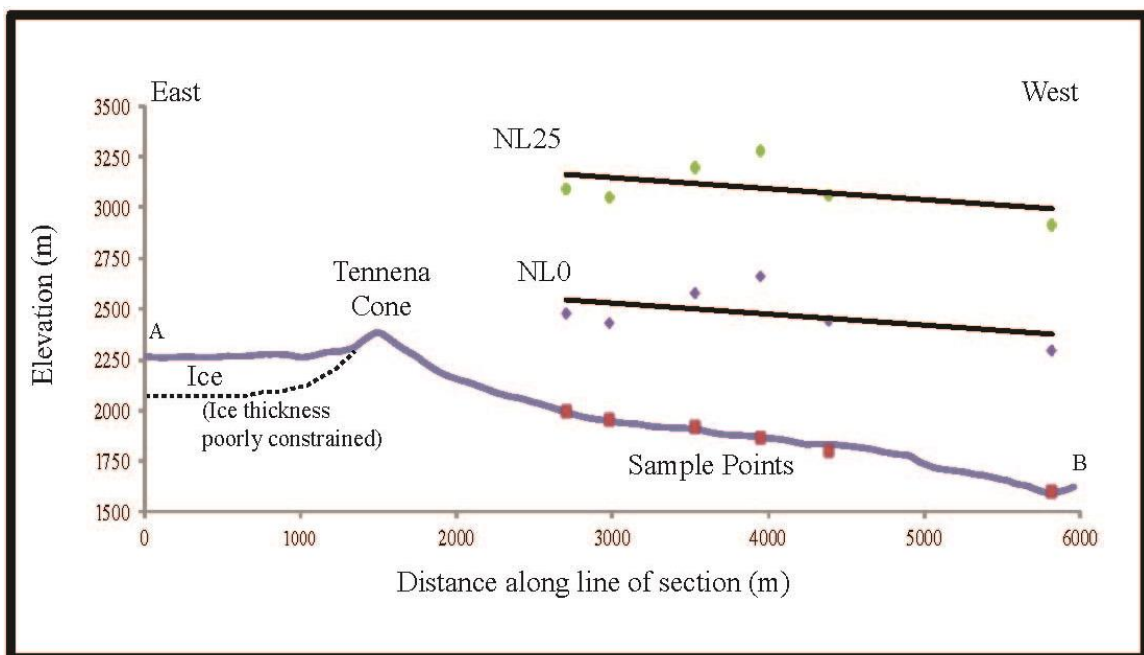
Figure 3.14. A topographic profile along line AB on Figure 3.3and the overlying ice thicknesses at the time of the TVC eruption

Calculated ice thicknesses (Table 3) are plotted above their sample location (red squares) along the cross section. The two straight lines represent the thickness of the ice as trendlines of both data point sets NL25 (green ovals) and NL0 (purple diamonds) calculated using VOLATILECALC (Newman and Lowenstern, 2002). Data point set NL25 represents ice thickness calculations between 1412 m and 1099 m thick assuming 25 weight percent CO_2, and NL0 represents ice thicknesses of 792 m and 480 m assumming 0 weight percent CO_2.

84

3.6   DISCUSSION

3.6.1   Eruption sequence

Based on the presence, distribution and associations of lithofacies at the TVC we interpret its formation as having taken place entirely subaqueously. Given the steep, glaciated terrain on which the eruption occurred, the only feasible origin for the water is melting of and confinement by glacial ice. We have modeled the eruption as comprising four stages, defined by changes in vent morphology, lava effusion rates, and changes in the sediment/water ratio in the meltwater drainage system.

3.6.1.1 Pre-eruptive conditions

The Tennena Cone and the lavas of the TVC were emplaced on eroded lava flows of the Ice Peak and Armadillo Formations. No other landforms to the south and west are higher than the cone, and no evidence supports the existence of any topography at the time of eruption that may have supported a perched body of water at the location of the cone. An ice mass therefore is the likeliest manner in which water was dammed, with estimates of ice thicknesses derived from H_2O/CO_2 analyses varying between ~500 and 1400 m. TVC lava flows follow the stepped topography into the head of the northern fork of Sezill Creek valley. The main valley is a prominent topographic feature now and is the focus of glacial meltwater and snowmelt drainage between Ornostay and Koosick bluffs. Although it is unclear whether Sezill Creek valley was an active drainage just prior to the Tennena eruption; its depth is consistent with formation over the course of multiple cycles of glacial erosion.

85

3.6.1.2 Stage 1 – Formation of Tennena Cone and the medial massive lava terrain

Formation of Tennena Cone initiated under ice with a minimum thickness of 500 m, given the present day elevation of the cone (Figure 3.15, Stage 1). The dips of basal TB are consistent with initial activity starting near the south scarp of the cirque/collapse feature west of the remnant Ice Peak edifice and north of the existing Tennena Cone summit. Although no basal pillow lava pile is evident in the flanks of Tennena Cone, the presence of possible pillow lava clasts in the basal TB unit is consistent with models for basaltic glaciovolcanic eruptions where volcanic activity initiates with the production of pillow lavas (Smellie, 2000).

In the case of the Tennena Cone eruption, the basal pillow pile assumed to be the initial product of many basaltic glaciovolcanic eruptions could be represented by the massive lavas (Lm) emplaced to the southwest of Tennena Cone. The Lm lavas of the medial massive lava terrain lie stratigraphically below the proximal pillow lava terrain, and are interpreted as the early stage high flux lava flows. Lobes of Lm lavas flowed west-southwest at emplacement rates greater than the melting rate of the ice mass, suggested by steep flow margins with local draping vertical pillows. Calculated emplacement rates of submarine sheet lavas (analogous to Lm lavas) and channeled sheet lavas proximal to the axial ridges along the East Pacific Rise have values of >100 m^3/s for vent proximal lavas and channeled sheet flows less than 300 m from the source vent (Kennish and Lutz, 1998). These values are most likely high for the emplacement rates of the Lm lavas, and are greater than the highest possible ice melting rates of 10^{-3} m/s (Edwards et al., 2012).
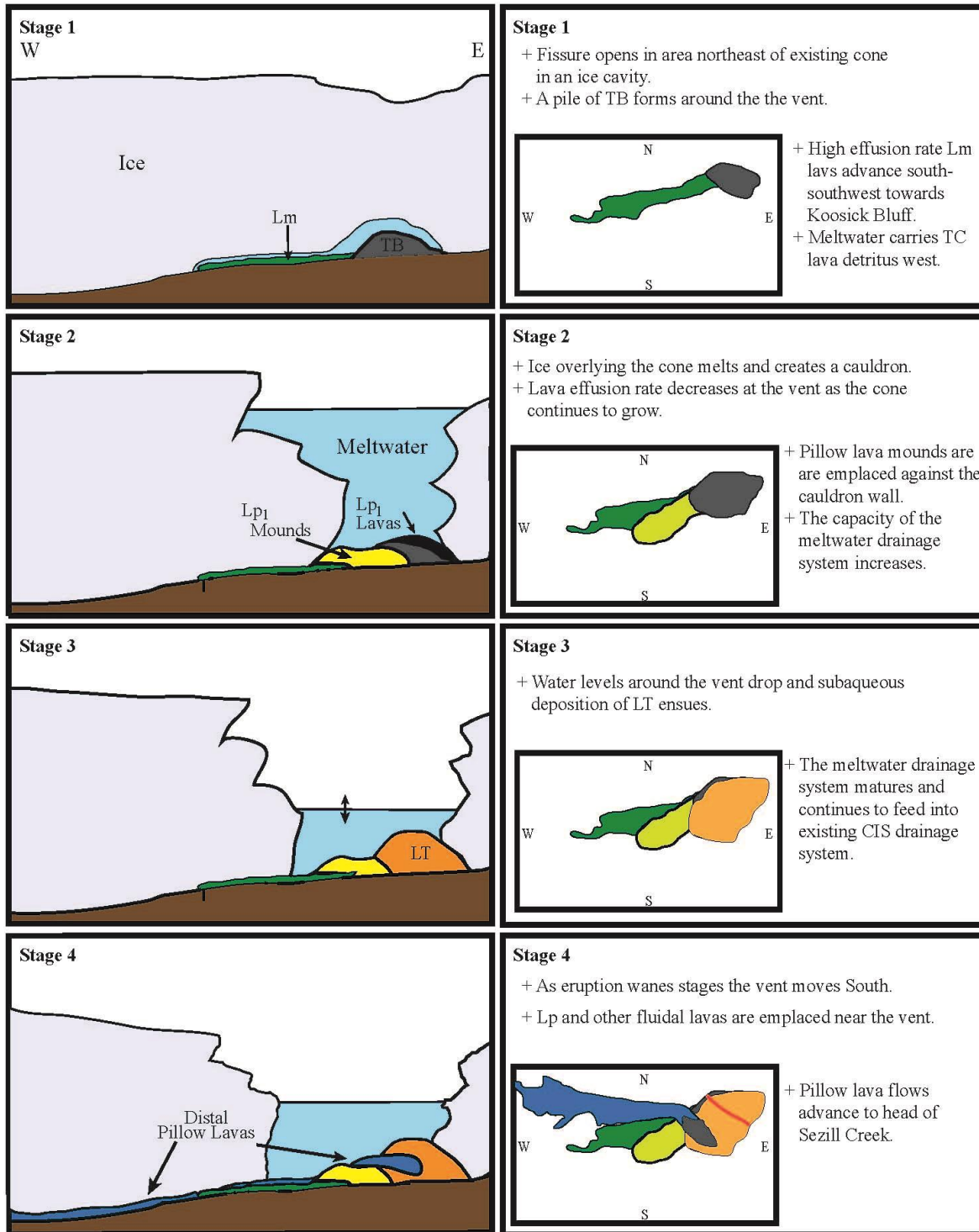
Figure 3.15. Cartoon of the evolution of the Tennena volcanic center eruption.
A schematic East – West cross-section of the four stages of the eruption appears in the left column. The right column includes a summary of each stage and a schematic plan view map of the relative spatial emplacement of the different lava morphologies over the stages of the eruption.

3.6.1.3 Stage 2 – Emplacement of the proximal pillow lava terrain

Within Tennena Cone, the near-vent piles of TB in the northern section are overlain by pillow lavas, which like the underlying unit, dip to the southeast and indicate the vent was still to the north-northeast of the present day cone (Figure 3.9e). If TB deposits were formed by collapse of advancing pillow lavas, the observed stratigraphic relationship may indicate that the advancing pillows simply overtook the pile of avalanche debris. However, if TB formed by phreatomagmatic activity, the transition to pillow lavas may indicate a more fundamental change in the eruption dynamics from explosive to effusive. Likewise, deposits of LT overlying Lp_1 at the cone could either represent a return to more energetic, explosive eruptions, or simply a shift in clast supply from more distally growing pillow lavas (Figure 3.15, Stage 2).

Much of the eastern extent of the proximal pillow lava terrain may still lie beneath the glacier mantling the cone to the south and east as the complete extent was under ice when the area was originally mapped (Souther, 1992). The axes of elongate pillow piles are oriented to the south-southwest. This orientation is nearly orthogonal to the gradient of the underlying local topography (Figure 3.10a). The western boundary of the proximal pillow lava terrain is presently steep; while that may be the result of post-eruption glacial erosion, it could demarcate the western wall of the ice cauldron forming around the vent at Tennena Cone. If the westward advance of the proximal pillow mounds was constrained by the walls of an expanding ice cauldron over the proximal Lm lavas, the ice mass overlying the Lm lavas may have failed as hydrostatic pressures diminished within the vault between the ice and Lm lava surface. Otherwise, the piles of Lp_1 would have progressed west, undeterred by ice, into the meltwater filled vault overlying the Lm lavas.

88

3.6.1.4 Stage 3 – Maturation of the meltwater drainage system

Up to this point in the evolution of the eruption the copious amounts of water produced by ice melting were probably largely confined to the eruption site by an inefficient subglacial drainage system. The hydrostatic pressure at the vent remained sufficient to favor effusive subaqueous activity at the end of stage 2 as the proximal pillow lavas advanced in piles of south-southwest (Figure 3.15, Stage 3). The deposition of poorly sorted Dmm_2 intercalated with and west of the distal Lm flow units during the first stage of the eruption is consistent with gradually increasing capacity of the meltwater drainage system. Westward meltwater flow, indicated by bedding attitudes of the associated glaciogenic lithofacies, follows the slope of the substrate into the pre-existing valley now occupied by Sezill Creek, a tributary of Mess Creek. The Mess Creek valley is thought to have been part of an active drainage system during Cordilleran glaciations (Ryder and Maynard, 1991). The meltwater produced during and soon after the eruption likely fed into the subglacial drainage system existing under the regional ice sheet (Ryder and Maynard, 1991).

West of the Lm lavas, beds of gGs record changes in water transport dynamics. Given the extent of the existing deposit, the area of the cavity was at least 200 m wide at the base of the step. Grain and bed-scale characteristics of gGs are consistent with sediment re-mobilization, entrainment, and deposition (Loughlin, 2002; Bennett et al., 2009) in a cavity, which was openly draining at velocities that varied through time.

The deposition of Dms in the cavity below the Ice Peak step as the eruption progressed is interpreted to indicate that the meltwater drainage system was, at least locally, increasing in the capacity to evacuate meltwater from the ice surrounding the Tennena volcanic center (Fig 3.12c, d).

3.6.1.5 Stage 4 –Emplacement of the distal pillow lava terrain

Based on the dikes that intrude the entire cone sequence, the last stage of the eruption initiated with the eruptive vent switching to the preserved portion of Tennena Cone. From this vent effusive eruptive activity, marked by near vent axial pillow lava piles, ensued (Figures 3.6a and 3.12b), and fed ridges of Lp_1 lavas emplaced within subglacial meltwater drainage tunnels (Figure 3.15, Stage 4). The pillow lava ridges, comprising only Lp_1 lavas east of the terminal moraine, advanced west over gently dipping plateau and bifurcated near the present day terminal moraine where the slope of the substrate steepens. Once the flows returned to a more shallowly sloping substrate the transitioned in part to larger lobes (Lp_2) and locally produced abundant Lv (Figures 3.12e, 3.12g and 3.12h).

On steeper substrate, the lavas of the distal pillow lava terrain are not laterally confined by topography, and no evidence suggests the ridges were confined by pre-existing topographic structures at the time of their emplacement. The propagation of pillow lavas in sinuous ridges may have been a result of formation around basal mega-pillow structures that acted as feeder tubes to the advancing flow front (Walker, 1992; Batiza and White, 2000). The sinuous pillow lava ridges may also have resulted from the emplacement of pillow lavas in subglacial drainage channels.

Direct observations of the 1996 Gjálp eruption, within the Vatnajökull ice cap in central Iceland, suggest the growth and maintenance of ice cauldrons capable of sustained meltwater confinement during subglacial basaltic eruptions in thick ice ($550 - 750$ m) are restricted to the close proximity of the volcanic vent (Gudmundsson et al., 2004). Although ice thickness at the Tennena vent is less certain, we assume the ice cauldron was also restricted to the vent area. If this assumption is valid, a significant volume of the coherent lava flows originating at Tennena

Cone was emplaced well beyond a perceived reasonable extent of the ice cauldron. Lavas of the distal pillow lava terrain, sourced at the southwest base of Tennena Cone, were emplaced over distances that reached over 4 km from the source vent, and, therefore, most likely advanced west beneath ice by exploiting Röthlisberger channels either produced or further excavated by elevated meltwater volumes created during the eruption (Schopka et al., 2006; Bennett et al., 2009). The sinuous shape of the pillow lava ridges reflects confinement to the geometry of the Röthlisberger channels.

3.6.2   Implications of Lv lithofacies for identifying lava-ice contact

One of the most unique deposits found at the Tennena volcanic center is the Lv lithofacies. It is most frequently associated with the flat or shallowly dipping substrate of the distal pillow lava terrain, although it is also found on the north side of a cliff where it overlies Lp_1 lavas (Figure 3.12f). We can envision at least three different scenarios by which this lithofacies can form: 1) by flowing over a steep Lp_1 flow front or margin, 2) as breakouts from larger Lp_2 or Lm bodies, or 3) from the collapse of perched Lp_1 or Lp_2 bodies. Field observations show that all three mechanisms of formation produced Lv lava morphologies within the TVC.

The first scenario is analogous to the formation of near vertical pillows in submarine environments. Local meter or decimeter scale roughness in the underlying topography retards the advancement of basal Lp_1 lavas. A new Lp_1 lava lobe advances over the head of the basal pillow and solidifies against the substrate. The process is repeated and the prograding flow front steepens until near vertical. Subsequent Lp_1 lavas overrun the underlying lobes and create sets of aggrading vertical pillows (Lv lithofacies) (Ballard and Moore, 1977; Batiza and White, 2000).

The second scenario involves breakouts from Lp_2 and Lm lavas. If the fluid pressure exerted by the magma in the lava body is greater than the tensile strength of the solid lava crust, the crust will experience brittle failure and allow lava to escape. If the Lp_2 or Lm body is not laterally confined, the fractures occur in the upper parts of the flow, and the flux of lava favors pillow formation, the lava emanating from the larger flow will drape over the steep side of the underlying flow until it contacts a horizontal or near horizontal surface. Once the Lv body stops advancing another Lv lobe could extrude from the breakout if the flux is sufficient. Lv lobes will continue to issue from the breakout and create aggrading curtains of Lv lavas as long as conditions (e.g., fluid pressure, flux) are favorable (e.g., Figure 3.6g). These Lv lobes represent the breakout from the Lp_2 structure in Figure 3.6d.

In the final scenario, Lv lavas may form from pillow lavas that are emplaced on top of above steeply sided lavas. This scenario was likely responsible for the majority of the ubiquitous Lv lavas found on the shallowly dipping slopes of the distal pillow lava terrain. If the pillow lavas perched above the vertical lavas experienced brittle failure, Lv lobes could have issued from the pillows, flowed over the underlying steep-sided lavas and terminated on contact with the substrate or other near horizontal surface (Figure 3.12g). Here, the steepness of the margins of the underlying lavas is assumed to form by lavas abutting confining ice. Subsequent Lv lobes may aggrade into a growing space between the lava mass and ice if the local lava flux is maintained (Figure 3.12g).

The Lv lithofacies has not been described in terrestrial deposits before. The only occurrences of somewhat similar morphology have been described by Bear and Cas (2007) from submarine deposits in New Zealand. They found small areas of pillows with similar surface textures, but not the same vertical morphologies. If our interpretations are correct, then the Lv

may represent a lithofacies that is unique to glaciovolcanic deposits. As such, it would represent a marker that could be used to definitively distinguish between effusive glaciovolcanic deposits and non-glaciovolcanic subaqueous pillow lava lithofacies. As the resolution of imaging of the surface of other planets such as Mars improves, identification of Lv could be an important tool for definitively distinguishing eruptions in ice-dominated environments.

3.6.3   Implications for late to post LGM Ice thickness

Souther (1992) suggested that the first eruptions of the Snowshoe lava field, of which Tennena Cone is part, initiated in the late Pleistocene during the Last Glacial Maximum (LGM). Although the Tennena eruption most likely occurred within the time of the last glacial maximum given the relatively fresh nature of these deposits, it is possible that the eruption could have occurred during the Younger Dryas stade or later. The Cordilleran Ice Sheet (CIS) during the last glacial maximum (LGM) reached thicknesses of 2,000 to 3,000 m asl (Ryder and Maynard, 1991; Stumpf et al., 2000). The thickness of the CIS over the Canadian Cordillera was largely controlled by the underlying topography (Fulton, 1991b; Stumpf et al., 2000). The 2787 m summit nunatak of Mount Edziza is a glacially eroded arête that was likely buried during the LGM, which occurred between 16 and 15 ka along the Coast Range mountains just west of Mount Edziza (Stumpf et al., 2000). If the Tennena eruption occurred at LGM, the surrounding ice would have been at least 2800 m a.s.l. given the height of the summit nunatak, and at least 700 m above the western base of Tennena Cone.

The present summit of Tennena Cone is at 2390 m. Glacial erosion has modified the top and sides of the cone, as is evident from the remaining moraine veneer. This erosion and deposition of morainal detritus suggests the overlying ice was significantly higher than the

present Tennena Cone. At 397 m below the present summit nunatak, the summit of Tennena Cone was likely emplaced in a surrounding ice cauldron within ice near or above the elevation of the present Mount Edziza summit.

The volatile calculations suggest that the combination of cryostatic and/or hydrostatic pressure extent during the emplacement of sheet and pillow lavas was equal to ~400 to ~1500 m of dense ice (Table 3.3; Figure 3.14). The analyses are from samples collected at elevations between 1800 and 1900 m a.s.l. Simple addition of sample elevation and the ice thickness calculations suggest that the ice surface was a minimum of 3100 m a.s.l. (Table 3.3; Figure 3.14). Since these values are consistent with CIS thicknesses at LGM, we suggest that TVC lavas were emplaced under Cordilleran ice rather than post-LGM alpine glaciers.

Pressure calculations based on volatile concentrations should be regarded cautiously for estimating paleo-ice thicknesses (Tuffen et al., 2010). Changes in magma degassing conditions melt hydration, petrological and chemical heterogeneity in rock samples, post-quenching sample movement and syn-emplacement pressure changes all pose significant challenges to obtaining relevant pressure calculations. However, at the Tennena volcanic center the physical evidence for ice thickness is broadly consistent with emplacement under thick ice likely associated with the Cordilleran ice sheet.

3.6.4   Implications for Glaciovolcanism

The Tennena volcanic center is unique in that it likely represents an almost complete record of a short-lived, effusion-dominated glaciovolcanic eruption. Several modern basaltic glaciovolcanic eruptions have been observed in the past twenty years (e.g., Gjalp 1996, Grimsvotn 1998, 2004, 2011). Yet these eruptions have all been dominantly explosive, and the proximal eruption

94

products either are relatively inaccessible or are covered within one to two years by snow and ice. Although some modern eruptions from ice-covered stratovolcanoes have produced lava flows (e.g., Mount Hudson, 1989, Villarica Volcano, 1991; Lescinsky and Fink, 2000), these have been in relatively thin ice of alpine glaciers on volcano flanks and have also been quickly covered with snow and ice. In older deposits, erosion removes many of the delicate features that have been preserved at TVC.

Evidence for ice confinement of effusive products generally relies on topographic position (e.g., Mount Rainier; Lescinsky and Fink, 2000) or of over-thickened lava flows that dammed against ice and inflated (e.g., Hoodoo Mountain; Edwards et al., 2002). The sinuous ridges of pillow lava emplaced on relatively flat topography at TVC are the best evidence found to date for ice confinement. Unlike putative ice-confined lava flows of higher viscosity, the presence of pillow lavas within the confined flow requires the presence of water, which at the elevation of the TVC virtually requires ice as the water source. Most descriptions of larger glaciovolcanic edifices do not include evidence of details such as sinuous pillow ridges that exploited R-channels. Commonly, larger edifices formed from many successive eruptions that likely modified or obliterated details of individual emplacement events (e.g., Pillow Ridge, Mount Edziza; Edwards et al., 2009).

3.7   CONCLUSION

The Tennena volcanic center preserves a unique record of an effusion dominated, eruption of a small basaltic lava flow field within thick (>500 m) ice. The lack of any subaerial lavas or their derived clasts suggests that the eruption occurred entirely in the presence of meltwater and ice.

The tephra pile with intercalated coherent lavas was constructed by a series of vents in an ice-confined cauldron of meltwater at varying hydrostatic pressures. Coherent lavas emanating from Tennena Cone vents were either emplaced against ice of the cauldron walls or exploited an expanding subglacial meltwater drainage system delivering water to an existing CIS drainage system. Among the most unique features of the center are the Lv lithofacies, which are vertical pillow lavas formed by effusion over vertical faces of aggrading pillow lavas or over-steepened margins of ice-confined lava flows. Descriptions of the coherent lavas within the Tennena volcanic center offer accessible analogues for sheet flow and pillow lava emplacement in submarine environments as well as lavas emplaced in similar environments on Mars.

4.0 THE EMPLACEMENT OF COHERENT BASALTIC LAVAS UNDER AN ICE MASS: ANALYSIS OF THE TENNENA CONE LAVAS, MOUNT EDZIZA VOLCANIC COMPLEX, BRITISH COLUMBIA

4.1 INTRODUCTION

Volcanic eruptions occurring within the confines of ice sheets and glaciers commonly produce individual coherent and volcaniclastic lava facies that are similar to those found in both subaerial and submarine environments, but the facies assemblages produced in glaciovolcanic environments tend to be distinctive (e.g., Mathews, 1947; Skilling, 1994; Smellie and Hole, 1997; Smellie, 2001; Loughlin, 2002; Edwards et al., 2011). Furthermore, facies that form from ice confinement or ice-contact are unique to these environments (e.g., Skilling, 2009; Edwards et al., 2012).

Published studies of glaciovolcanic deposits have largely focused on the primary deposition of vent-proximal volcaniclastic and coherent lavas to define eruption parameters and paleo-ice conditions; but a few studies have focused on coherent lava flows emplaced away from vent-proximal areas (Porter, 1987; Lescinsky and Sisson, 1998; Lescinsky and Fink, 2000; Loughlin, 2002; Mee et al., 2006; Spörli and Rowland, 2006; Smellie, 2008; Lodge and Lescinsky, 2009). Except for the work of Porter (1987), Loughlin (2002) and Smellie (2008), these studies have concentrated on the interaction between subaerial basaltic-andesitic, andesitic

or dacitic lava flows and thin ice (<250 m) of alpine glaciers on stratovolcanoes rather than thick ice (>250 m) commonly found in valley glaciers and ice sheets. These described subaerial, ice-contact lava flows characteristically have high aspect ratios (height-to-width) with near-vertical margins and display ice-contact surface textures and internal jointing unique to cooling in the presence of meltwater (Lescinsky and Fink, 2000; Spörli and Rowland, 2006; Lodge and Lescinsky, 2009).

Loughlin (2002) described the distal emplacement of transitional alkalic basalt flows on Eyjafjallajökull volcano, Iceland. He identified coherent lava flows intercalated with cogenetic volcaniclastic lithofacies emplaced within subglacial drainage systems, and lava flows emplaced kilometers away from the source vent, confined by valley topography and below ice masses (Loughlin, 2002). Although these lavas exhibit evidence of ice contact and subglacial emplacement, they were emplaced beneath <150 m of ice (Loughlin, 2002).

Conversely, Smellie (2008) described columnarly jointed, 1-to-100-m-thick basaltic lava flows as part of subglacial sheet-like sequences of monogenetic coherent and volcaniclastic lithofacies under thick (> 250 m) ice. These are called "Dalsheidi-type, sheet-like" sequences, and are exposed in the scarps of inverted topography, are laterally extensive, and the source vents of these lavas are not identified (Smellie, 2008). As described by Wilson and Head (2002), these Dalsheidi-type flows are interpreted to be emplaced as sills between the underlying substrate and overlying, thick ice mass (Smellie, 2008). This interpretation of their emplacement as sills is suspect, because sills intrude parallel to bedding planes where the upper layer is more rigid than the underlying surface (Kavanagh et al., 2006), and basal ice near the pressure melting-point temperature is commonly perceived as less rigid than coherent bedrock. Regardless, Smellie (2008) describes peperitic apophyses that intrude into overlying

volcaniclastic beds from the upper surface of the Dalsheidi-type flows. These peperitic intrusions indicate a less rigid deformable bed was deposited stratigraphically above the flows, before or concurrent to the emplacement of the lava flows. Thus, the emplacement mechanism of these basal lavas in Dalsheidi-type sheet like sequences remains unresolved.

Porter (1987) described hawaiite-mugearite flows as coherent lavas emplaced against ice masses during the last two glacial events on Mauna Kea volcano. The lava flows have a high aspect ratio (30 m: 300 m), are steep-sided ($\geq 60^{o}$), and display pillow lavas and surface structures indicative of ice-contact and cooling in meltwater (Porter, 1987). These lavas were emplaced englacially within thin ice (~170 m at its thickest point) located in the temperate alpine glacial ice cap that advanced to ~ 3650 m elevation at its greatest extent on the 4206-m-tall edifice (Porter, 2005; Anslow et al., 2010). Porter (1987) suggested that these lavas, although displaying ice-contact and subaqueous emplacement textures, were not necessarily subaqueous during their entire time of emplacement because glacial drainage may have effectively evacuated meltwater to elevations below the lava flows and ice-cap boundary during the eruption.

Given the paucity of research on basaltic lava flows emplaced under thick ice, the work described here on the mildly alkalic basalt lava flows emplaced distally under thick (> 500 m, locally) ice at the Tennena volcanic center (TVC) represents the first of its kind. From the source vent at Tennena Cone on Mount Edziza volcano, British Columbia, Canada, sequences of pillow lavas, mega-pillow lavas and massive sheet lavas represent distal lava emplacement under the thick cordilleran ice sheet (CIS) present through the last glacial maximum (LGM), or Younger Dryas glaciation. These lavas display features common in basaltic lavas emplaced in subaqueous or submarine environments as well as features unique to flows subjected to ice confinement. We see lavas currently unconfined by topography with subaqueous textures: namely, pillow lavas

and massive sheet lavas that display ice-contact features and internal jointing indicative of flows that cool in the presence of water (Lescinsky and Fink, 2000; Lodge and Lescinsky, 2009) and extend kilometers away from the source vent(s) at Tennena Cone. These TVC lava flows provide a first opportunity to describe the emplacement of kilometers-long basaltic lava flows under a thick ice mass.

The intent of this study is to: 1) further describe the sequences of massive sheet lavas and pillow lavas found distal to the source vent at Tennena Cone; 2) define the parameters of lava-flow rheology given viscosity calculations and reasonable lava flux rates; 3) explore the subglacial drainage conditions during the eruption; and 4) propose emplacement mechanisms of sheet lavas and pillow lavas under a thick mass of ice.

The identification, description and definition of the mechanism of emplacement of these subglacial lava flows allows other investigators to identify and interpret similar lavas and therefore interpret paleo-ice conditions at the time of their emplacement. Paleo-ice conditions have proven an integral variable in defining past climate conditions terrestrially and those on Mars (e.g., Smellie et al., 1993; Werner and Schmincke, 1999; Edwards et al., 2002; Loughlin, 2002; Smellie et al., 2006; Kadish et al., 2008; Smellie, 2008; Smellie et al., 2008; Keszthelyi et al., 2010; Pedersen et al., 2010; Edwards et al., 2011).

4.2   GEOLOGIC SETTING

4.2.1   Mount Edziza

Mount Edziza is a long-lived (Neogene to Recent) volcanic edifice, and the northern massif in the Mount Edziza Volcanic Complex (MEVC) in northern British Columbia, Canada (Figure 3.1). Souther (1992) mapped the MEVC and categorized the volcanic deposits into 13 formations that span the extent of eruptive activity. The last of these formations is the Big Raven Formation (BRF) of which the lavas of this study are part. Eruptions of the basalt-to-hawaiite BRF lavas initiated during the last glacial maximum, and the latest dated eruption has a radiocarbon age of 1340±130 yr. B.P. (Souther et al., 1984; Souther, 1992). The BRF contains two lava fields: the Desolation Lava Field on the north slope of Mount Edziza, and the Snowshoe Lava Field on the south and southwestern slopes of the edifice. According to Souther (1992), the lava flows and tephra cones of the early BRF eruptions represent subglacial to transitional lavas erupted in the presence of varying ice thicknesses, and the later eruptions are subaerial. The deposits of the TVC represent an early eruption of the BRF that occurred in the presence of ice.

4.2.2   The Cordilleran Ice Sheet in Northern British Columbia.

Mount Edziza is a long-lived volcanic edifice, and the records of several past glaciations are intercalated within its volcanic deposits (Souther, 1992; Spooner et al., 1995; Edwards et al., 2009). Evidence of late Pleistocene glaciation, and Holocene glacial stades, is present in the volcanic and associated sedimentary deposits of the early BRF lavas. Although not well

constrained by radiometric or absolute dating techniques, the inception of BRF activity is interpreted to have occurred within the last glacial maximum or late Fraser glaciation (Marine Isotope Stage 2) or Younger Dryas glacial stands. Souther (1992) describes the TVC eruption as the first of the Snowshoe Lava Field and thus the first eruption in the presence of ice.

The CIS reached its maximum extent during the late Fraser glaciation at 16.5 ka (Fulton, 1971; Clague and Mathewes, 1989; Menounos et al., 2009). The elevation of the CIS in the Mount Edziza area is not well constrained, but, based on the highest erratic and striation elevations, estimates of the minimum surface ice elevations prior to deglaciation in the central Onimeca Mountains roughly 300 km east are 2100 m, and 2300 m in the Cassiar Mountains 500 km to the northeast of Mount Edziza (Johnston, 1926; Roots, 1954; Gabrielse, 1963; Ryder and Maynard, 1991). Ice retreat continued to roughly 14 ka when a period of ice advance and retreat began, which included Younger Dryas advances. This period of advance and retreat continued until the inception of Holocene deglaciation at 11 ka (Ryder and Maynard, 1991; Menounos et al., 2009). Throughout the Holocene, there is ample evidence of multiple periods of glacier fluctuations after the decay of the Cordilleran ice sheet (Menounos et al., 2009).

The CIS had an extensive subglacial hydraulic system (e.g., Flowers and Clarke, 2002; Clarke, 2005; Burke et al., 2012; Livingstone et al., 2013). Evidence for local subglacial drainage at Mount Edziza lies on the glaciolacustrine and subglacial fluvial deposits of the Stikine River (at the northern base of Mount Edziza) and its tributary, Mess Creek, at the base of the western plateau on Mount Edziza (Spooner and Osborn, 2000). After the decay of the CIS in the Mount Edziza region, meltwater from fluctuating alpine glaciers on the slopes of Mount Edziza continued to flow into of the Stikine River through a system of tributaries emanating from the edifice. Mid- and late-Holocene glacier runoff from the SLF on the southern flank of Mount

Edziza occupied a system of coalescing streams that now form tributaries that flow west into Mess Creek and on to the Stikine River. Sezill Creek is the northernmost tributary within the SLF, and occupies the most prominent valley incised into the western plateau formed by Ice Peak Formation and older lava flows. The head of Sezill Creek Valley lies west of Tennena Cone and the most distal of the TVC lava flows were emplaced on the steep northeast slopes at the head of Sezill Creek.

4.2.3 Tennena volcanic center (TVC)

The TVC, on the southwest flank, is the oldest eruption center of the Big Raven Formation in the SLC. As described in chapter 3, the deposits of the TVC have been categorized by facies associations into 4 terrains that comprise Tennena Cone, pillow-lava mounds proximal to the cone, massive sheet lavas southwest of the cone, and pillow-lava sequences that extend from the cone to the distal extent of the TVC lavas (Fig 4.1). The cone is perched near the axis of the NNE-trending Mount Edziza edifice and southwest of Ice Peak, an ~ 1 Ma eruptive center and the described source of substrate lavas (Souther, 1992). The extent of TVC lava emanating from Tennena Cone to the east and south is obscured by present-day glacial ice. Exposed TVC lavas advanced west from the cone to the head of Sezill Creek between Koosik and Ornostay bluffs over stepped topography of shallowly dipping runouts and steep scarps cut into the Ice Peak lava flow substrate. Southern sections of the westward advancing TVC lavas were emplaced over consolidated diamict tills near the southern drainage.

All existing TVC clastic and coherent lava deposits are interpreted to have been emplaced subaqueously as described in chapter 3. There are no TVC lavas that display subaerial
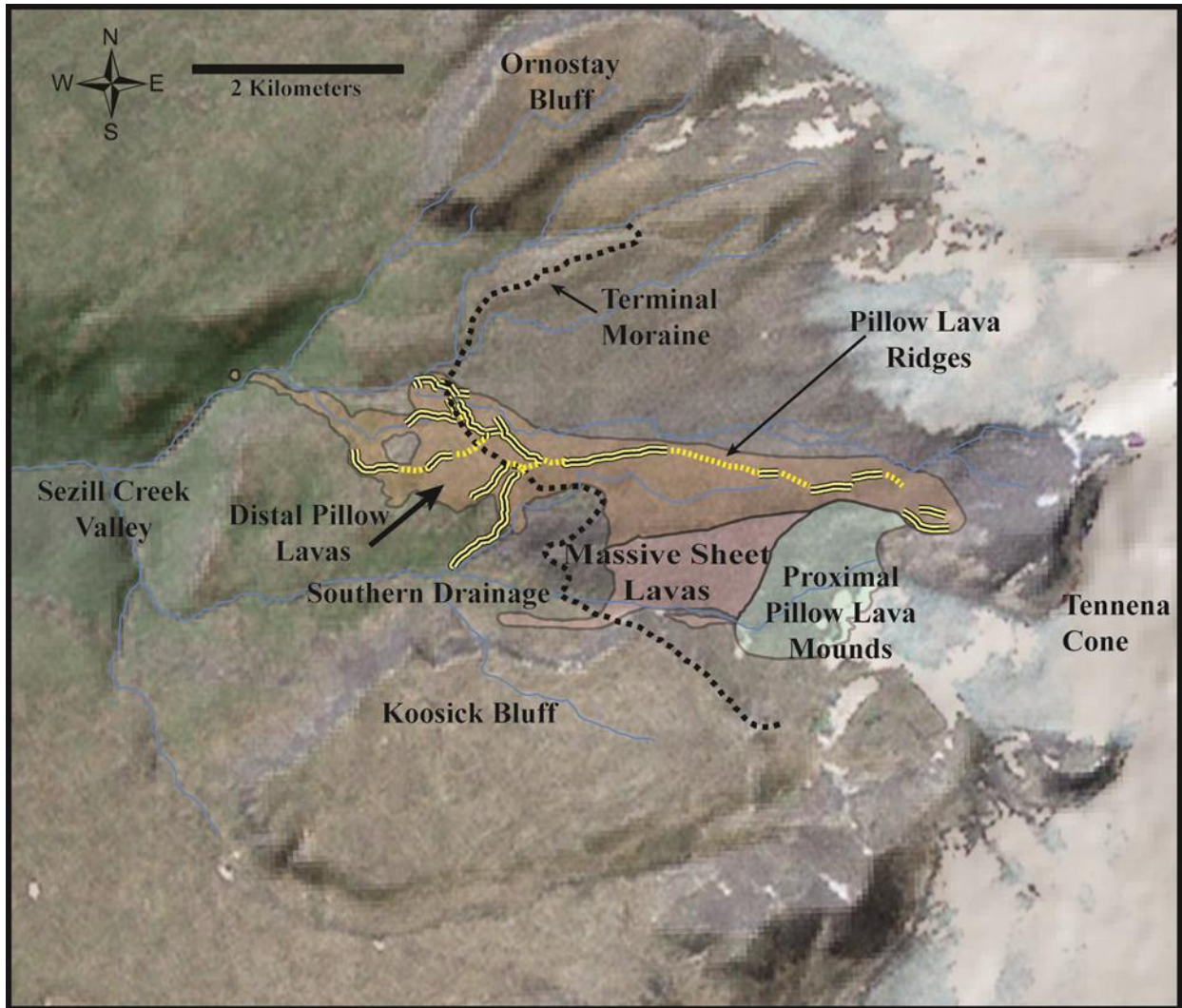
Figure 4.1. The Tennena volcanic center and local topographic features.

An ESRI image of the TVC and surrounding area overlain on a DEM-derived hillshade topographic relief with no vertical exageration. The terrains of the TVC lavas discussed in chapter 3 are labeled and demarcated by colored areas. The lava deposits that are the focus of this study are the massive sheet lavas and the pillow lava ridges found in the pillow ridge and pillow lava terrain. Traces of the pillow lava ridges are in bold and dashed lines. The axis of the terminal moraine from recent alpine glaciation is indicated by the black dotted line. (Source: Geological Survey of Canada, ESRI, DigitalGlobe, Icubed, USDA, AEX, Getmapping, Aerogrid, IGN, IGP, swisstopo and the GIS User Community)

lava textures except for surfaces of hollow pillow lavas that show glassy textures similar to those found in basaltic pahoehoe flows. There are no subaerial lavas atop Tennena Cone. The lack of subaerial lavas, or remnants of subaerial lavas in the glacial detritus derived from TVC lavas, suggests the TVC eruption was entirely subaqueous at the source vent and the distal lavas were also emplaced within the copious amounts of meltwater produced during the eruption. Volatile analysis calculations, discussed in chapter 3, indicate that the TVC lavas were emplaced under pressures equivalent to 500 to 1400 m of overlying ice. Measurements of volatile concentrations indicate the Tennena Cone, 200 m higher than the proximal TVC lavas to the west, was always subaqueous, and most likely formed in a meltwater-filled cauldron within the ice mass. The cauldron must have formed in an ice mass because there is no other topographic feature in the vicinity of the cone that could perch a body of water necessary to create the cone.

The prior to this study, the timing of the TVC eruption was confined by the stratigraphic relationship to other Big Raven Formation eruptive centers in the SLF, and the presence of pillow lavas and other subaqueous textures present in the TVC lavas, which combined suggested emplacement at a time of abundant ice (Souther, 1992). Samples of the lavas collected during this study were analyzed and robust Ar/Ar ages of 0.005 ± 0.033 Ma and 0.011 ± 0.033 Ma on two TVC samples suggest the near-zero ages ± 33 ka limit the eruption to within late Wisconsin or younger glacial events (see Chapter 3). Given the evidence for thick ice at the time of eruption and near-zero Ar/Ar ages that confine the eruption to within 40 ka, it is reasonable to interpret the TCV eruption occurring within Late Wisconsin/Fraser or Younger Dryas glacial stades (Souther et al., 1984; Souther, 1992).

Ample evidence for subglacial drainage systems active during volcanic eruptions in thick ice lies in the descriptions of sediment sequences in glaciovolcanic environments (e.g., Smellie,

2001; Gudmundsson et al., 2004; Schopka et al., 2006). Direct observation of the 1996 Gjálp eruption in Iceland provided further unambiguous evidence of coeval subglacial meltwater drainage under 600-to-700 m of ice (Gudmundsson et al., 1997; Gudmundsson, 2003; Gudmundsson et al., 2004). Recent work on glaciofluvial lithofacies assemblages attributed to the escape of elevated volumes of meltwater produced by lava–ice interaction further elucidates how copious volumes of meltwater exploit and modify existing subglacial drainage systems during an eruption (Bennett et al., 2006; Bennett et al., 2009). Glaciofluvial sediments associated with medial and distal TVC lavas (described in Chapter 3) also indicate a dynamic subglacial system was evacuating meltwater westward, into Sezill Creek. Exposed glaciofluvial sediment assemblages lying directly below distal TVC lavas are commonly oligomict in lower strata but the percentage of TVC-derived lava clasts increases up-section. Beds that form the lower contact with overlying TVC lavas are composed nearly exclusively of TVC lava clasts. Elsewhere, lenses of diamict glaciofluvial sediments comprising TVC lava-derived breccia and matrix are intercalated with TVC lava flows. These intercalated lenses are direct evidence of meltwater flow at the time of TVC lava emplacement.

4.3   THE MASSIVE SHEET FLOWS AND PILLOW LAVA RIDGES

This study focuses on the emplacement of two distinct lava morphologies found distal to Tennena Cone, which is interpreted to be the source of the lava flows. The two lava morphologies are the sheet lava flows, described in Chapter 3 as massive lavas (Lm) of the

medial massive lava terrain, and the pillow lavas of the pillow ridge and pillow lava terrain that advanced to the head of Sezill Creek, 4.3 km west of Tennena Cone (Fig 4.1). Other deposits of the TVC that form Tennena Cone and the mounds of pillow lavas found proximal to the cone are described in Chapter 3 and analogous deposits are described in the literature (e.g., Smellie and Skilling, 1994; Loughlin, 2002; Schopka et al., 2006; Edwards et al., 2009).

The term "sheet lava" is used here to refer to massive, coherent lava bodies that have a low aspect ratio (tens of meters wide and 1 to 3 m thick in cross section) and may be tens to hundreds of meters long (Dimroth et al., 1978; Ballard et al., 1979; Kennish and Lutz, 1998; Batiza and White, 2000). Individual sheet lava flow bodies of are referred to as sheet flow units here. The term "pillow lavas" refers to coherent lava flow forms with ≤ 1 m cross-sectional diameters that are circular to elliptical (Moore, 1975; Ballard and Moore, 1977; Yamagishi, 1985; Walker, 1992; Batiza and White, 2000). "Megapillow" lavas are analogous to pillow lavas but have a cross-sectional diameter > 1 m. Megapillows found in the TVC commonly have irregular cross-sectional shapes. The term "lobate" refers to lava forms that resemble flattened pillow lava fronts or pahoehoe lava toes that are not more than 2 m across (Ballard and Moore, 1977; Batiza and White, 2000). These defined morphologies are assumed to be emplaced subaqueously based on their similarities with submarine lava flow morphologies (Moore, 1975; Ballard and Moore, 1977; Walker, 1992).

4.3.1 The massive sheet lavas

The massive sheet flow units form a 1.7 x 2 km plateau just west of the pillow lava mounds at the southwest base of Tennena Cone. The plateau dips shallowly to the west and is

incised by the southern drainage, which flows west under the progressively steepening north-facing slopes of Koosick Bluff (Figure 4.1). These sheet lavas are well exposed in the northern, and infrequently on the southern, scarp of the southern drainage. Along the 1200 m of exposure in the southern drainage, both the interiors of individual sheet flow units and distal flow fronts are exposed. These sheet lavas, overlain by the pillow lava mounds proximal to the cone, represent high-volumetric-flux lavas sourced from vents within Tennena Cone and were emplaced during the initial phases of the eruption as described in Chapter 3. The sheet lavas advanced towards Koosick Bluff and terminated against the northern slopes of the bluff.

Although the flow fronts are well exposed in the southern drainage, the upper surfaces of the sheet lavas are commonly covered either in a veneer of glacial lag deposits or lodgment till southwest of the pillow lava mounds. Where exposed, the surfaces of the uppermost sheet lavas are lobate to the east, and to the west the exposed surfaces are hackly, jointed and brecciated or display relic pillow structures. The majority of the glacial lag deposits are brecciated fragments of TVC lavas either sourced from the pillow mounds to the east or from the brecciated pillow lavas and lobate lavas from sheet lava surfaces. The westernmost sheet flow units are exclusively covered in locally derived pillow lava breccia, relic pillow structures or < 5 m wide, 1 m thick outcrops of pillow lavas.

Under the easternmost or upslope sheet flow units, the substrate is diamict lodgment till described in Chapter 3. Further west down the southern drainage, the sheet lavas overlie poorly consolidated diamict glaciofluvial sediments with clasts and matrix derived from TVC lavas. The distal-most sheet flow units are intercalated with lenses of these sediments.

The sheet lavas form a 3-to-10-m-high scarp on the north side of the southern drainage. The easternmost (upslope) outcrops are formed by single sheet flow units <1 m thick to the east

that thicken to 2.5 m to the west along the exposure in the southern drainage (Figure 4.2a). As are the other lobes exposed in the southern drainage, the easternmost lobe appears to have been incised sub-perpendicular to the flow direction of the sheet. The exact flow vector is unknown because the lobe is covered in glacial detritus north of the southern drainage, masking typical flow-direction indicators. This 30-m-wide lobe abuts another lobe just west and downslope. Both of the easternmost lobes display 10-to-15-cm wide and 30-to-40-cm tall basal columnar jointing. Above the basal columns an entablature-jointed zone continues to the top of the exposed lobe where glacial detritus obscures the upper surface. In these two eastern lobes, there are two distinct 2-to-3-m wide areas of columnar jointing radiating from a center point. This rosette-style radial jointing pattern is also evident in thicker sheet flow units further west. A 3-m-wide, wedge-shaped body of pillow lavas lies atop the contact of these two easternmost sheet flow units.

Just west of the two easternmost sheet flow units, the sheet lavas are thinner (1-2 m), and are stacked 2 to 4 lobes high (Figure 4.2b). These lobes are 5 to 40 m wide and most commonly display basal columns and entablature jointing patterns similar to those found in the lobes to the east, although the jointing here may be more chaotic (Figure 4.2c). Further down the southern drainage, the stacked flows are laterally more extensive, 1 to 2 m thick, and display either basal columnar joining or entablature, or just entablature found most commonly in the upper lobes. Near half the distance of the sheet lava exposure in the southern drainage, the stacks of thin, laterally extensive sheet flow units overlie up to 3-m-thick, less laterally extensive basal flows that are exclusively entablature jointed with comparatively larger (up to 40 cm across) prismatic jointing faces (Figures. 4.2b, 4.2d).
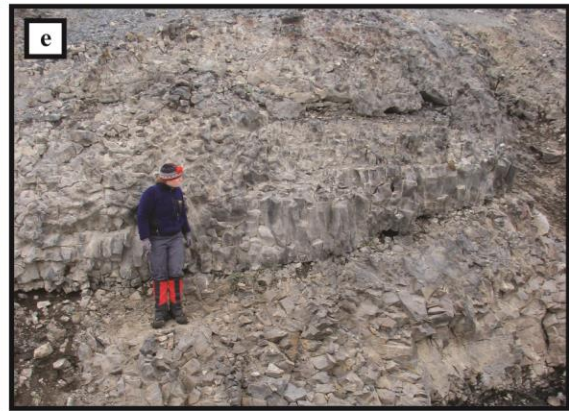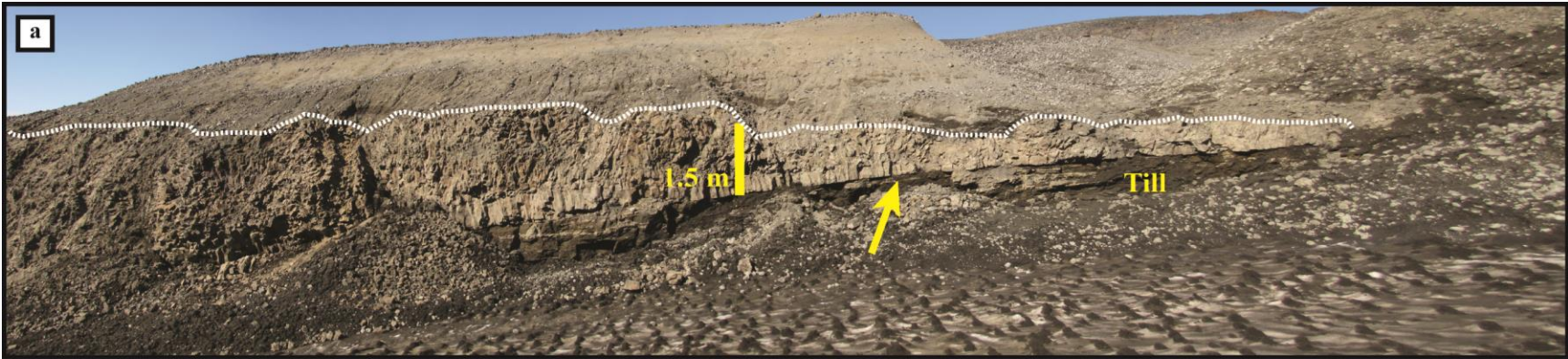
Figure 4.2. Images of the eastern sheet lava flows

(a) A view looking north at the easternmost sheet lava lobe (the top of which is marked in a white dotted line) overlying lodgment till. The arrow indicates the bottom contact of the sheet lava lobe. The yellow bar in the middle of the image is 1.5 m tall. (b) A view of the eastern most sheet flow units that are stacked on top of one another. The circled numbers indicate sheet flow units stacked in the sequence. The bottom lobe overlies till. The white dotted line is drawn around a basal thick, entablature-jointed sheet flow. (c) A view of the lower sheet lava lobe circled in white in Figure 4.2b. Notice the poorly developed basal columnar jointing below the entablature in the lower sheet. (d) A view looking north at stacked sheet flow units overlying a more equant in cross-section basal sheet flow with comparatively larger prismatic jointing faces. The white dotted line indicates the upper contact of the thick, entablature-jointed basal flow. The image location is noted in Figure 4.2d. (e) A view looking northwest at the stacked sheet flows near the western, most distal area of the sheet flow terrain.

From the midpoint west along the southern drainage, a similar pattern appears in the stacked sequences of sheet lavas. Intermittent entablature-jointed, basal sheet flow units of higher aspect ratio relative to the other sheet flow units lie upon the till substrate (Figure 4.3a). Horizontal distances between the thick entablature-jointed sheets can be up to 40 m. Either overlying the thick sheets or the substrate till are laterally extensive, 1-to-3-m thick sheet flow units that display basal columnar jointing and an upper, entablature-jointed zone. These laterally extensive sheets may be stacked 3 high. Atop the laterally extensive sheets are sheets of the same thickness but not more than 5 m wide and chaotically stratified. Larger upper sheets may display basal columnar jointing but commonly the upper sheets are exclusively entablature-jointed. This sequence is common in the middle 400 m of southern drainage exposure but there are two like sequences in the distal or western exposures (Figure 4.2e).

Approximately half the distance along the 1200-m-long outcrop, the sheet lava flows lie on substrate dipping roughly west with meter-scale local topographic variations. The attitude of the substrate west of the outcrop midpoint becomes progressively steeper and dip directions rotate to the south-southwest (Figure 4.3b). Approximately 750 m down the sheet lava exposure, the substrate is no longer lodgment till but is the diamict sediments derived from TVC lava

111
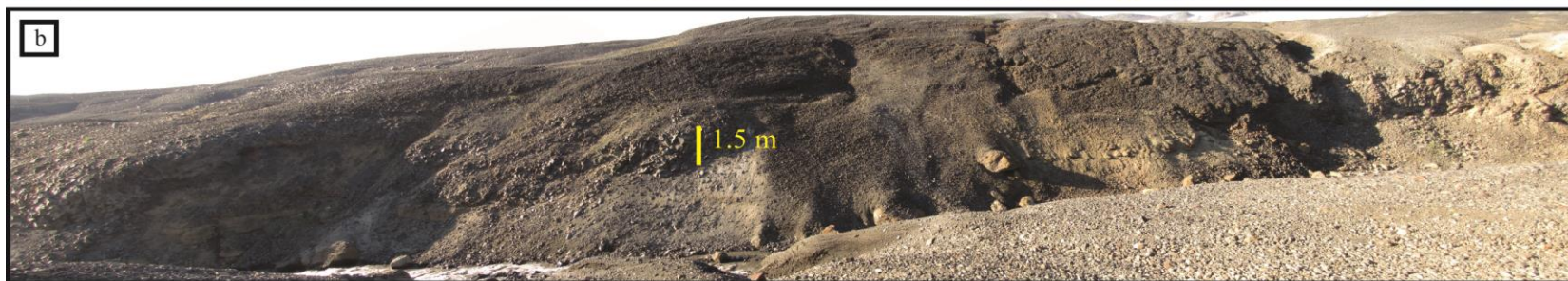
Figure 4.3. Images of the western sheet lava flows

(a) A view looking northwest at the middle sheet flows. The more equant, basal entablature-jointed lobe is overlain by a thin, extensive sheet lava lobe, which is overlain by upper chaotically shaped sheet flow units. (b) A view looking north-northwest at thin, laterally extensive sheet flows emplaced on steeper, southwesterly dipping substrate. (c) A view looking northwest at the western most, distal sheet lavas north of the southern drainage. The location of Figure 4.2e is noted.

breccia and finer detritus. The westernmost sheet lavas are intercalated with lenses of this concomitantly deposited diamict glaciofluvial sediment.

The western, distal sheet lavas overlying the coeval diamict sediments tend to be thinner and more laterally continuous than those to the east. The number of sheets in the stacked sequences diminishes westward until the sheets are no longer stacked and single sheets overly the steeply dipping diamict substrate (Figures 4.3b, 4.3c). Individual distal sheet lavas vary from common basal columnar jointed and entablature–jointed sheets to entablature-jointed with large prismatic faces to small-scale entablature. All the westernmost sheet flows are thinner than those further east except for one sheet flow that exhibits basal columnar jointing and an upper zone of entablature. All sheet lava flows are east or above the terminal moraine deposited by recent alpine glaciation except for a thin (~1 m) sheet flow that advanced west under the northwest cliffs of Koosick bluff approximately 3 km from the vent at Tennena Cone.

Based on thin-section and hand sample analysis of 20 samples taken from sheet lava units in the southern drainage, the sheet lavas are 3 to 5 vol.% plagioclase porphyritic with > 1 cm, tabular to lathe-shaped crystals. The sheet lavas have 15 − 25 vol.% vesicles with 1-to-3-mm diameter, round-to-oblate vesicles. The larger vesicles tend to be slightly oblate. The western sheet lavas approach 30 vol.% vesicles and the population of larger, 3-mm vesicles is comparatively greater and they tend to be oblate.

4.3.2 Pillow lavas of the distal terrain ridges

The lava morphologies of the pillow ridge and pillow lava terrain discussed in Chapter 3 are variations of pillow lava forms. The terrain comprises megapillow lavas, vertically oriented pillow lavas and hollow pillow and megapillow lavas or relic structures thereof. As discussed in Chapter 3, these lava morphologies are found distally and are interpreted to be the product of low and variant local lava fluxes on relatively flat terrain. Normal pillow lavas (pillows <1 m in cross-sectional diameter) however, make up the lavas in the medial and proximal areas of the pillow ridge and pillow lava terrain. This study focuses on the emplacement of these pillow lavas as pathways for lava transport to the distal lavas described in Chapter 3.

The pillow lavas of the pillow ridge and pillow lava terrain are sourced from a vent on the southwest flank of Tennena Cone, and they fan out ~600 m west from the source vent. A diffuse ridge of pillow lavas forms at the distal edge of this pillow lava fan and is traceable to the terminal moraine 2.3 km west of the source vent (Figure 4.4a). The ≤8-m-tall and ≤ 12-m-wide pillow lava ridge is covered with a veneer of glacial lag deposits and boulder pavement. Pillow lavas are exposed on lateral slopes and the trend of exposed pillows is between sub-parallel and 45° to the pillow ridge axis in the flow direction (Figure 4.4b). Pillow lavas above the terminal moraine are round to elliptical in cross-section, display radial fracture patterns and commonly lack well developed concentric bands of vesicles typically found in pillow lavas (e.g., Moore, 1975; Walker, 1992; Hoskuldsson et al., 2006). The pillow lava ridges have been subject to glacial modification at elevations above the terminal moraine. Within 75 m of the terminal moraine, the pillow lava ridge bifurcates into two main ridges that flow northwest and southwest. These two ridges supplied the lavas that occupy the distal area of the TVC.

The southwest ridge fed the lavas south-southwest of the point of bifurcation. The volume of lava transported through this ridge system is less than was transported through the northwest ridge based on the volume of TVC lava in the area of the ridge. The main branch of this southwest ridge system ridge system terminates 5 m from the southern drainage in a 3-to-4-m diameter, 600-m-long hemi-cylindrical ridge (Figure 4.4e). Pillow lavas are well exposed in a scarp cut roughly parallel to the ridge axis in the last 600 m of the ridge (Figure 4.4f). Exposed pillow lavas are oriented sub-parallel to the ridge axis low in the section and become chaotically oriented in the middle and upper sections of the pillow lava ridge.

After the first bifurcation of the ridge system, the northwest ridge continues for ~500 m and bifurcates into a westward-trending ridge and a northwest-trending ridge that terminates 200 m from the point of divergence. The westward ridge splits into two ridges, one trending northwest and another southwest. These two ridges continue west on either side of a 25-m-high scarp in the underlying Ice Peak Lava substrate and connect to the lavas found on the shallowly dipping substrate below the scarp. The unique lava morphologies are described in Chapter 3.

The length of individual basal or internal pillow lavas in the ridge system is not evident in TVC outcrops. The best exposure of individual pillow lava length is in the pillow lava ridge in figure 4.4e where the longest exposed longitudinal sections of basal pillow lavas are ~6 m long pillow ridge and pillow lava (Figure 3.4b). The origins or ends of these individual pillow lavas are not exposed in the outcrop so 6 m is a minimum length. Surficial pillow lavas on the pillow lava ridges, however, are commonly shorter than 3 m and their sinuous axial shape is reflective of the irregular topography formed by underlying pillow lavas.

The pillows, like all the TVC lavas, are plagioclase porphyritic (3 to 15 vol.%) with macro-phenocrysts 0.2 to 1.2 cm long that are equant to tabular. The range of apparent
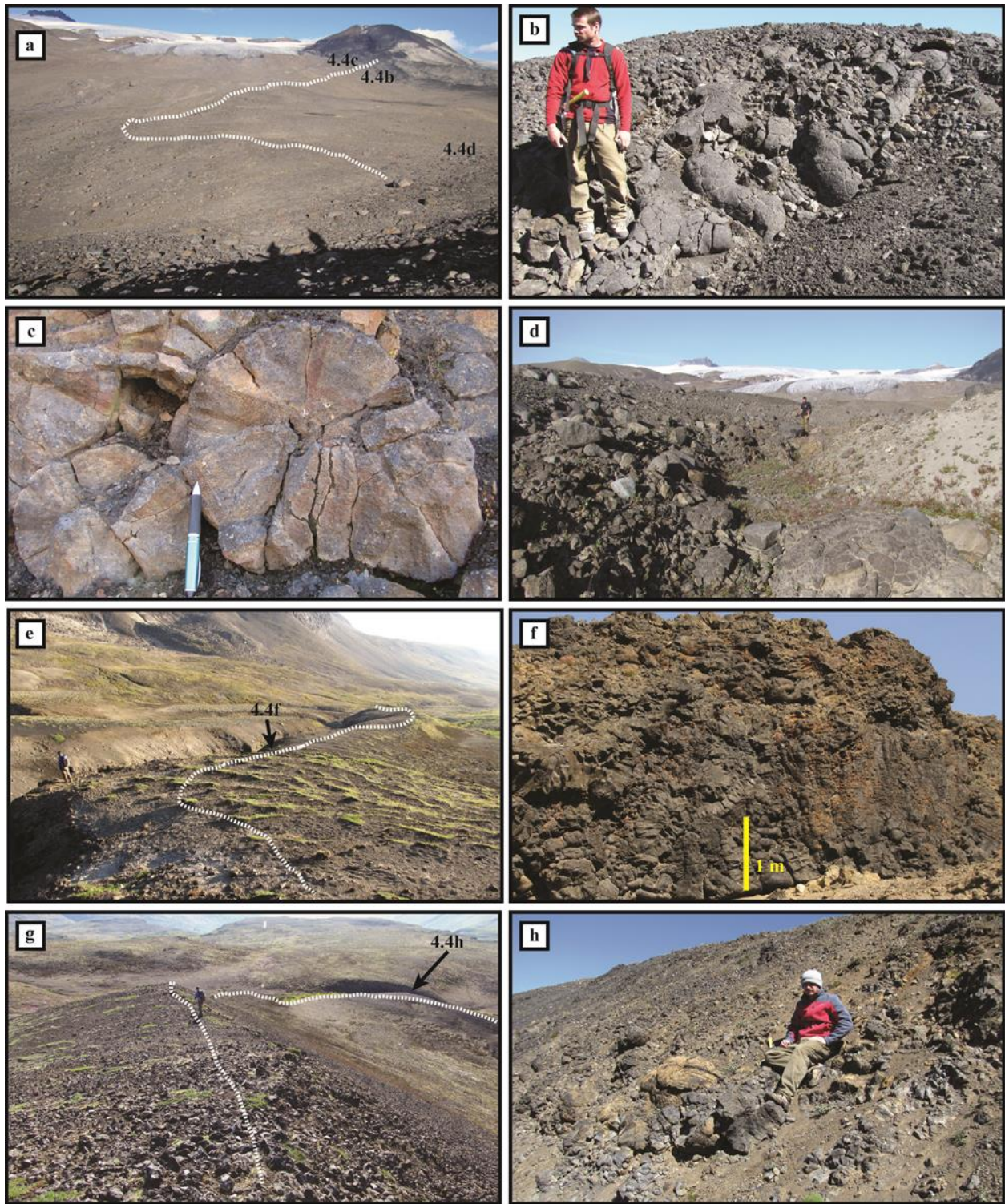
Figure 4.4. Images of the pillow lava ridges of the pillow ridge and pillow lava terrain.

(a) A view looking east at the main, diffuse pillow lava ridge from the source vent at the southwest base of Tennena Cone. The white dotted line indicates the pillow ridge axis. The locations of Figures 4.4b, 4.4c and 4.4d are noted.

Figure 4.4 continued. (b) A view of the surficial pillow lavas on an 8-m-tall section of the main pillow lava ridge proximal to the source vent. (c) A close-up view of pillow lavas found within 150 m of the source vent. The pen is 15 cm long. (d) A view looking northeast at the diffuse southern side of the main pillow lava ridge within 50 m of the first bifurcation. (e) A view looking southwest at the surface of a pillow lava ridge incised by a stream cut on the left of the ridge axis marked by the white dotted line. The pillow ridge terminates 5 m from the southern drainage. The location of Figure 4.4f is noted. (f) A view of the east side of the pillow lava ridge noted in Figure 4.4e. The orientations of pillow lavas higher in the section are more variable than the basal pillows. (g) A view looking west, down the axis of a distal pillow ridge south of the 25 m scarp in the underlying Ice Peak formation lavas. The ridge axis is noted with a white dotted line. The location of Figure 4.4h is noted with an arrow. (h) A view looking north along the western slope of the pillow lava ridge in Figure 4.4g. The pillows exposed on this ridge slope are corrugated unlike the smooth-textured pillows in ridges found above the terminal moraine, for example.

phenocryst shape may be a function of their lack of preferential orientation. Late-stage pillow lavas and other TVC lava morphologies tend to have higher phenocryst counts whereas early-stage TVC lavas approach 3 vol.% phenocrysts. These observations are based on thin-section and hand sample analysis of 40 samples taken from pillow lavas in the pillow lava ridges throughout the pillow ridge and pillow lava terrain.

Vesicles in pillow lavas in ridges above the terminal moraine are >2 mm and tend to be evenly distributed throughout the pillow lava body. Pillow lavas in distal ridges may display pipe vesicles and incipient concentric bands of increased vesicle volume. Any vesicle pattern in the distal pillows is overprinted by a uniform, well distributed >2 mm spherical vesicles found in the proximal pillow lavas.

Surface rinds on pillow lavas range between 0.75 and 2.5 cm thick. Rinds are commonly weathered away on exposed surfaces but are intact in the interstices of pillow ridges and piles. Except for the lavas in the pillow ridge and pillow lava ridge (Figure 4.4g, h), the pillow lavas are smooth-skinned. The exposed pillows in the distal ridge are well fractured but few intact surfaces display corrugated textures.

4.4 EMPLACEMENT VARIABLES

Coherent lava bodies emplaced in glaciovolcanic terrains exhibit textures found in submarine lavas as well as textures unique to emplacement against ice (e.g., Skilling, 1994; Smellie, 2000; Hoskuldsson et al., 2006). Pillow lavas are likely the most common morphology of coherent basaltic lavas found on Earth (Walker, 1992); the vast majority of these are emplaced subaqueously in marine environments, and they are ubiquitous in glaciovolcanic terrains(e.g., Smellie and Hole, 1997; Smellie, 2000). Although not as common in glaciovolcanic terrains, sheet lavas are also abundant in submarine environments (Fox et al., 1988; Kennish and Lutz, 1998). The two eruptive environments exhibit similar lava morphologies yet lavas emplaced in marine environments are emplaced at greater hydrostatic pressures (250 – 300 MPa at mid ocean ridges, for example) and coherent lava flows in glaciovolcanic terrains tend to be emplaced under pressures that represent <500 m of water (equivalent to ~50 MPa). Descriptions of lava morphologies from shallow submarine arc volcanism may provide examples of subaqueous flows that were emplaced under similar pressure environments (Yamagishi, 1991; Goto and McPhie, 2004; Bear and Cas, 2007; Sanchez et al., 2012). Although both deep and shallow submarine lava morphology is affected by substrate topography, neither are constrained by ice masses susceptible to dynamic exchange of heat, which may lead to ephemeral constraints on lava emplacement.

The TVC lavas were erupted and emplaced subaqueously, in meltwater constrained by an ice mass at least 500 m thick, according to geologic observations and lava volatile content calculations presented in chapter 3. As are other submarine lavas, the morphology of the TVC distal lavas is a function of variables intrinsic to lava rheology as well as the ambient conditions. Here, I examine the variables of lava viscosity, lava supply rates, cooling rates and topographic

slope to describe the emplacement of the TVC sheet lavas and pillow lava ridges, and how these morphologies can be emplaced beneath a thick ice mass.

Submarine/subaqueous emplacement of pillow lavas has rarely been observed and the emplacement of submarine sheet lavas has never been observed (Moore et al., 1973; Sansone, 1990; Resing et al., 2011). However, models of emplacement have been derived from investigations of subaqueous deposits and analog experiments (e.g., Moore, 1975; Griffiths and Fink, 1992a; Griffiths and Fink, 1992b; Walker, 1992; Gregg and Fink, 1995; Gregg and Fink, 1996; Gregg and Fornari, 1998; Gregg and Fink, 2000; Goto and McPhie, 2004; Bear and Cas, 2007). These investigations are imperative to our understanding of lava flow emplacement in glaciovolcanic environments.

4.4.1   Lava rheology

Subaqueous lava rheology and resultant flow morphology depends on lava viscosity, lava effusion rate, lava cooling rate and the topography of the underlying substrate (Griffiths and Fink, 1992b; Gregg and Fink, 1995; Gregg and Fink, 2000; Gregg and Smith, 2003). The differences in distal coherent TVC lava morphologies are a function of variations within these parameters and are examined here.

Table 4.1. Variables and constants used in equations

Parameter	Variable	Units	Value	Source
η	viscosity	Pa s		
η_{liq}	liquid viscosity (basalt)	Pa s		
$\eta_{liq+xtl}$	liquid & crystal viscosity	Pa s		
$\eta_{liq+xtl+vesc}$	liquid, crystal & vesicle viscosity	Pa s		
η_w	viscosity of water at 0° C	Pa s	1.742×10^3	Clarke, 2003
$\emptyset_c$	volume percentage of crystals in liquid	%		
$\emptyset_0$	max volume percentage of crystals in liquid	%	60%	Harris & Allen, 2008
$\emptyset_b$	volume percentage of vesicles in liquid	%		
$\bar{v}_{Bl}$	Bingham mean flow velocity of lava	$m^3 s^{-1}$		
w	width of lava flow	m		
h	height or thickness of lava flow	m		
g	acceleration due to gravity	m s^{-2}	9.81	
ρ_l	density of lava	kg m^{-3}		
ρ_i	density of ice	kg m^{-3}	913	Walder, 1986
ρ_w	density of water	kg m^{-3}	999	Hooke, 2005
θ	Substrate slope	degrees		
τ	shear stress	Pa		
τ_0	Bingham yield strength of fluid	Pa		
E_f	effusion rate	$m^3 s^{-1}$		
q_l	heat content	J		
V_l	lava volume	m^3		
V_w	meltwater volume	m^3		
V_i	ice volume	m^3		
L_l	latent heat of crystallization	J kg^{-1}	4.0×10^5	Gudmundsson, et al., 2004
L_i	heat of fusion of ice	J kg^{-1}	3.35×10^5	Clarke, 2003
C_l	heat capacity of lava	J kg^{-1}C^{-1}	1200	Gregg & Fornari, 1998
C_w	heat capacity of water	J kg^{-1} C^{-1}	4217	Clarke, 2003
T_l	temperature of lava	$^\circ$C		
T_w	temperature of meltwater	$^\circ$C		
T_i	temperature of ice	$^\circ$C	0	
S	R-channel cross sectional area	m^2		
Q	meltwater discharge rate	$m^3 s^{-1}$		
P_E	effective R channel pressure	Pa		
P_I	pressure of ice on R channel	Pa		
P_W	pressure of meltwater on R channel	Pa		

Table 4.1 continued. Variables and constants used in equations

Parameter	Variable	Units	Value	Source
U	channel radius deformation rate	m s^{-1}		
U_c	channel radius deformation rate from ice flow	m s^{-1}		
U_m	channel radius deformation rate from meltwater	m^2 s^{-1}		
U_s	channel cross-section area deformation rate	m^2 s^{-1}		
r	R channel radius	m		
n	Glen's flow law constant		3	Walder, 1986
A	Glen's flow law parameter for ice	Pa s$^{1/3}$	5.28x10^7	Clarke, 2003
v_i	specific volume of ice	m^3 kg^{-1}	1.1x10^{-3}	Walder, 1986
v_w	specific volume of water	m^3 kg^{-1}	1.0x10^{-3}	Walder, 1986
m	mass rate of melting per unit length of channel	Kg m^{-1} s^{-1}		
P_m	ice perimeter of R channel cross-section	m		
Kw	thermal conductivity of water	W m^{-1} C^{-1}	0.558	Clarke, 2003
Re	Reynolds number			
Pr	Prandtl number		3.5	Nye, 1976
R_H	Hydraulic radius	m		
$\acute{n}$	Manning's roughness coefficient	m$^{-1/3}$ s		

4.4.1.1 Lava viscosity

Lava viscosity is principally controlled by lava chemistry, crystal volume, and vesicle content and lava temperature. Initial models predicting liquid silicate melt viscosities were Arrhenian temperature dependence equations that accurately predicted Newtonian behavior of melts above liquidus temperatures (Bottinga and Weill, 1972; Shaw, 1972; Giordano et al., 2008; Harris and Allen, 2008). Experiments on silicate melt viscosities below melt liquidus temperatures, however, exposed the deficiency of temperature-dependent Arrhenian-based models to accurately describe sub-liquidus melt viscosities (e.g., Hess et al., 1996; Russell et al., 2002; Giordano and Dingwell, 2003). From these experiments, empirically derived models of silicate melt viscosity as a function of temperature and composition proved increasingly more accurate in predicting liquid viscosities of silicate melts. The viscosity model used here, and developed by Giordano et al. (2008), is a non-Arrhenian, multicomponent (3) chemical model based on

experimental viscosity measurements of silicate melts with known chemical compositions at different temperatures. The model predicts silicate melt viscosity as a function of temperature and composition with a particular dependence on H_2O and F concentrations in the melt at atmospheric pressures (Giordano et al., 2008). Although lavas erupted in subaqueous and submarine environments are subjected to pressures greater than atmospheric, the effective hydrostatic pressure on lava viscosity is treated as negligible. Pressure affects the degree of polymerization within a melt, and polymerization is strongly dependent on melt chemistry. Pressure effects on viscosity, however, occur at pressures greater than those found in shallow marine and glaciovolcanic environments. The viscosity of MOR basalt, for example, is virtually constant over a pressure range of 0 to 4 GPa, which is far greater than the > 15 MPa experienced in glaciovolcanic terrains (Bauchy et al., 2013).

Like other lavas from the BRF on Mount Edziza, the chemistry of TVC lavas resemble mildly alkalic basalts (Figure 3.11, Tables 3.2 & 4.1). The lava chemistry of samples collected in 2006 and 2010 were analyzed by XRF at two different laboratories, and the data vary within error between the two sample sets, although SiO_2 values for the 2006 samples are on average 0.85 wt% lower than the 2010 samples. Water contents for the TVC lavas were between 0.66 and 0.86 wt% and averaged 0.77 wt%. These values were produced from FTIR measurements of glassy rinds from TVC pillow lavas. The liquid viscosity of the TVC lava was calculated with the average values of the major oxides from the 2010 samples and the average H_2O wt%. The fluorine concentration for the TVC lavas was estimated to be 0.015 wt% F_2O, which is a value found in alkalic basalts with similar K_2O and P_2O_5 concentrations (Aoki et al., 1981).

At an average of 0.77 wt.% H_2O, the TVC lavas are relatively wet compared to some EPR MOR basalts and tholeiitic lavas from the 1984 Mauna Loa eruption (Rhodes, 1988;

Langmuir et al., 1992). Subsequently, the viscosity profile of the TVC lavas is less than EPR MOR basalts and 1984 Mauna Loa lavas across the calculated 700 to 1200° C temperature range (Figure 4.5a). Calculated from Giordano et al. (2008) at 1100° C, the liquid viscosities of TVC lavas are 65.5 Pa s, which is an order of magnitude lower than Mauna Loa or MORB lavas at 568 and 257 Pa s, respectively. Liquid viscosities of 2010 TVC lava samples are also an order of magnitude lower than BRF alkalic basalts. The variance between BRF and TVC values is a function of water content. Souther (1992) reported 0.1 wt.% H_2O, far below the water content measured in TVC glass samples. When recalculated with 0.77 wt.% H_2O, Souther's (1992) liquid viscosity values lie between values obtained for the 2006 and 2010 sample sets of TVC lavas.

Table 4.2. Major element geochemistry for whole-rock samples of TVC and BRF lavas

Oxide	EJH10 03-04a	EJH10 05-02a	EJH10 06-02a	EJH10 06-20a	EJH10 08-04a	EJH10 08-26a	EJH10 10-03a	EJH10 10-08a	EJH10 10-12a	BRF** Alkali basalt	
SiO_2	48.44	48.37	48.37	48.10	48.18	48.06	48.20	48.11	48.97	47.9	48.4
TiO_2	2.636	2.611	2.414	2.504	2.116	2.597	2.417	2.777	2.445	2.49	2.04
Al_2O_3	15.35	15.42	15.44	15.80	15.31	15.47	15.36	15.20	15.48	15.7	16.6
FeO*	12.63	12.43	12.66	12.16	11.42	12.63	12.90	13.06	11.94	11.8	10.71
MnO	0.187	0.186	0.192	0.182	0.179	0.188	0.190	0.191	0.188	0.19	0.16
MgO	5.44	5.34	6.14	5.47	7.35	5.40	6.25	5.18	5.87	6.48	7.54
CaO	10.14	10.18	10.29	10.30	10.42	10.10	10.47	10.04	9.39	9.58	10.9
Na_2O	3.58	3.60	3.39	3.44	3.26	3.50	3.29	3.64	3.84	3.5	3
K_2O	1.05	1.03	0.83	0.99	0.87	1.04	0.75	1.07	1.41	1.2	0.69
P_2O_5	0.424	0.415	0.335	0.394	0.350	0.414	0.321	0.445	0.508	0.46	0.26
Total	99.87	99.60	100.07	99.34	99.46	99.40	100.15	99.71	100.03	99.3	100.2

- Analysis via XRF by Washington State University Geo Analytical Lab, 2013.
*Total iron expressed as FeO.
** From Souther (1992)

Lava flows are rarely emplaced at temperatures above the lava liquidus, and their rheology is therefore best described as a multi-phase flow with two or more components. If we treat the liquid phase as a homogeneous silicate melt, the two most common components of a multi-phase silicate melt system below its liquidus temperature are crystals and vesicles from

volatile exsolution. The effect on the lava rheology of these two phases is best expressed as affecting bulk lava viscosity. The effect of crystal content on the lava viscosity is best estimated by the Einstein-Roscoe relationship (Einstein, 1906; Roscoe, 1952; Shaw, 1969; Ryerson et al., 1988; Harris and Allen, 2008):

$$\eta_{liq+xtl} = \eta_{liq} \left(1 - \frac{\emptyset_c}{\emptyset_0} \right)^{-5/2}$$

The resultant lava viscosity of the liquid and crystal content is dependent on $\emptyset_c$, the fraction of crystals in the melt, and $\emptyset_o$, the maximum concentration of crystals in the lava before the lava viscosity approaches infinite values (Harris and Allen, 2008). Values for $\emptyset_o$ range between 50% and 70% according to Pinkerton and Stevenson (1992), whereas Marsh (1981) proposed a value of 60% (Harris and Allen, 2008). A value of 60% was used here, along with liquid viscosities (η_{liq}) derived from the 2010 sample set of TVC lavas to calculate the TVC lava liquid + crystal viscosity (Figure 4.5b).

The crystal content of the TVC lavas varies from 3 to 15 vol.% based on point-counts of X thin sections, and it is the later-stage TVC lavas that tend to contain higher crystal volumes. The viscosity estimate of 3 vol.% crystals in the lava increases the viscosity to 74.4 Pa s from 65.5 Pa s for the liquid only; and the viscosity estimate at 15 vol.% crystals to 134 Pa s at 1100° C. Both values are still below viscosities for a dry MORB liquid.

Vesicularity has a dual effect on lava rheology because vesicles can directly affect the viscosity and cooling rate of the lava. The effect of vesicle volume and shape on the lava viscosity can also be described with the Einstein-Roscoe relationship (Roscoe, 1952; Harris and Allen, 2008). An increase of spherical vesicle volume will increase lava viscosity, but the presence of deformed or sheared vesicles will reduce the viscosity of a lava (Manga et al., 1998;

Manga and Loewenberg, 2001). The treatment of spherical or sheared vesicles on lava viscosity is reflected in the exponent function in the Einstein-Roscoe relationship (Pal, 2003).

The three phases - liquid, crystals and vesicles - of a silicate lava may be expressed in an equation developed by Phan-Thien and Pham (1997) to calculate the three-phase fluid viscosity (Phan-Thien and Pham, 2000; Harris and Allen, 2008). Phan-Thien and Pham (1997) developed three scenarios dependent on the relative size of vesicles and crystals: crystals larger than vesicles, crystals smaller than crystals and crystals of the same size as the vesicles. Because plagioclase phenocrysts in TVC lavas tend to be larger than the 1-2 mm vesicles, the equation representing the scenario where crystals are larger than vesicles is used to estimate the viscosity of the three phase TVC lava:

$$\eta_{liq+xtl+vesc} = \eta_{liq} \left[1 - \left(\phi_b \middle/ (1 - \phi_c) \right) \right]^{-1} (1 - \phi_c)^{-5/2}$$

In this equation, ϕ_b is the volume % of vesicles in the lava. The results of different scenarios that use two volume percent values of both crystals and vesicles are calculated with liquid viscosities (η_{liq}) derived from the 2010 TVC sample set and the resultant viscosities are slightly higher than the calculated liquid + crystal viscosities. At 1100° C, the lowest three-phase value (3 vol.% crystals and 5 vol.% vesicles) increases the viscosity value of the TVC lava by 0.08 Pa s, which represents no significant difference from lava viscosity calculated at 3 vol.% crystals (74.4 Pa s). When calculated with 30 vol.% vesicles and 15 vol.% crystals, the viscosity difference between the two-phase liquid-melt viscosity and the three-phase viscosity is 17.5 Pa s. Given the small variance between the two-phase and three-phase treatments of lava viscosity for TVC lavas, variances in TVC lava viscosity is largely dependent on H_2O concentration and crystal content at a constant temperature. Vesicle volumes of sheet lavas and pillows within
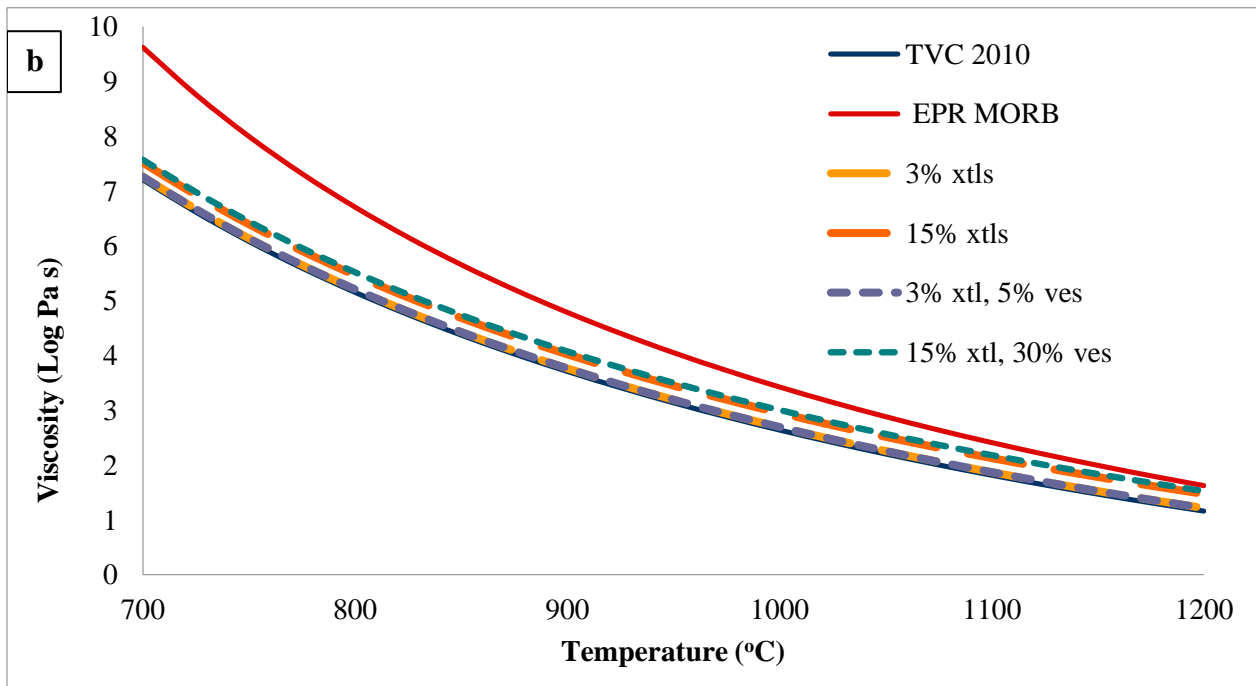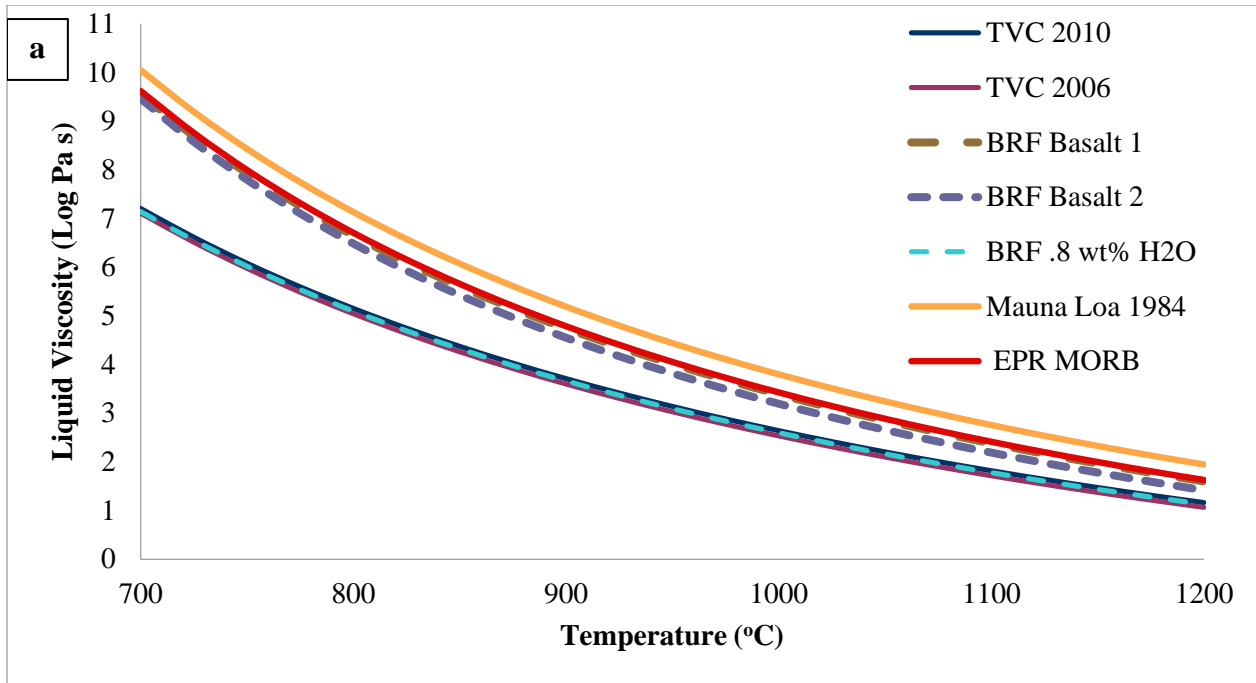
Figure 4.5. Lava viscosities of TVC and other comparative lavas.

(a) Liquid viscosities of TVC lava samples and Souther (1992) BRF lava samples calculated from Giordano et al. (2008). Mean chemical data for lavas from the 1984 Mauna Loa eruption and EPR mean chemical data are used as reference values (Rhodes, 1988; Langmuir et al., 1992). (b) Viscosities of liquid, liquid + crystals and liquid + crystals + spherical vesicles smaller than crystals of 2010 TVC lava samples. The curve for EPR MORB from (a) is used as reference.

pillow lava ridges may approach 30% but are commonly less than 20% and the vesicles tend to be spherical, uniform in size and evenly distributed throughout exposed lava interiors. These vesicles may represent post-emplacement volatile exsolution as the flow interior cools. If the extant vesicle population were present during emplacement of the lavas at viscosities at or below 1000 Pa s, one would expect vesicle ascent or migration and resultant accumulation zones of higher vesicle volume (Höskuldsson et al., 2006).

4.4.1.2 Lava effusion rates

Lava effusion rate also affects subaqueous lava flow morphology. Direct measurements of lava effusion rates in subaqueous environments are restricted to a few observations of pillow lava emplacement (Moore et al., 1973; Sansone, 1990; Resing et al., 2011). These observations of local effusion rates may not represent emplacement rates of the lava flow system or the effusion rate at the vent. In glaciovolcanic systems, the effusion rate at the source vent most likely produces both coherent and volcaniclastic material concurrently throughout the eruption regardless of hydrostatic/glaciostatic pressure, although the volume fraction of volcaniclastic material is inversely correlated with ambient pressure (Smellie, 2000; Tuffen, 2007). The effusion rate applied to the emplacement of subaqueous lava flows will therefore be some fraction of the effusion rate at the source vent or fissure. As an advancing lava flow system evolves, it tends to create distributary systems (Kilburn, 2000; Harris et al., 2007), which further diminishes the effusion rate to advancing lava flow units. The resultant changes of effusion rates in the entire lava flow will produce different lava flow morphologies. If, however, the effusion rates attributable to the distinct flow morphologies can be aggregated in a spatial and temporal context, an estimate of system-wide effusion rates may be inferred (Gregg and Smith, 2003).

Effusion rates at the local source of the lava flow unit are the rates that determine, along with viscosity, slope and cooling parameters, the morphology of a lava flow. Though rarely directly measured in subaqueous lavas, flow effusion rates have been determined by study of resultant flow morphologies and analogue experiments and numerical modeling of emplacement parameters of subaqueous lava flows (e.g., Griffiths and Fink, 1992b; Fornari et al., 1994; Gregg and Fink, 1995; Klingelhöfer et al., 1999).

In submarine environments it is generally accepted that, in the absence of steep ($>10°$) underlying slopes, "high" local effusion rates will result in sheet lava flows, and "low" lava effusion rates produce pillow to lobate lava morphologies (Ballard and Moore, 1977; Batiza and White, 2000; Gregg and Smith, 2003). This premise was confirmed and rate constraints to observed morphologies were assigned through analogue experiments with polyethylene glycol wax (Griffiths and Fink, 1992b; Gregg and Fink, 1995; Gregg and Fink, 2000). With an assumed lava viscosity of 10^2 P a s, extrusion rates (synonymous with local effusion rates in this text) of less than 1 m^3 s^{-1} result in the formation of pillow lavas and extrusion rates between 1 and 100 m^{3}s^{-1} result in the formation of lobate sheet flows (Griffiths and Fink, 1992b). These values constrain the formation of pillow lavas, which are emplaced in fractions of vent effusion rates approaching 10^4 m^{3}s^{-1} on the Juan de Fuca Ridge and East Pacific Rise (Gregg and Fink, 1995; Gregg et al., 1996; Fox et al., 2001; Gregg and Smith, 2003).

Vent effusion rates for the TVC eruption are not well constrained but were likely much less than 1000 m^{3}s^{-1} given the abundance of low effusion rate pillow lava morphologies relative to the volume of higher effusion rate sheet lava flows. Vent effusion rates fluctuated and dissipated in the later stages of the eruption, which were dominated by the distal emplacement of pillow lavas. Initial effusion rates at the vent were comparatively higher than late-stage rates and

resulted in the emplacement of the sheet lavas more than 2 km to the southwest of the source vent.

4.4.1.3 The substrate slope

Gregg and Fink (1995, 2000) performed analogue experiments with polyethylene glycol to describe the effects of the substrate slope on lava flow morphology. Holding cooling and extrusion rates constant, they concluded that an increase in underlying slope had the same effect as increasing the effusion rate. Extrusion rates favoring the formation of pillow lava at a 10° slope would form sheet lava morphologies at 30°, for example (Gregg and Fink, 1995; Gregg and Fink, 2000). Observations of submarine lava morphologies on the submarine Puna Ridge, Hawaii, refined these experimental findings (Gregg and Smith, 2003). On the Puna Ridge, sheet flows were restricted to slopes $\leq 15^o$ and lobate and pillow lava flows were found on slopes $\leq 25^o$, and on steeper slopes at lower effusion rates, pillow lavas were favored over sheet lava morphologies (Gregg and Smith, 2003).

The substrate underlying TVC sheet lava flows does not exceed 7° except where the western most and distal sheet lavas overlie coeval diamict glaciofluvial sediments based on field measurements and analysis of digital elevation models of the TVC. The pillow lava ridges also overlie substrate that slopes less than 15° west until they are downslope of the terminal moraine. The underlying slope of the substrate therefore seems to be less of a determinant of lava flow morphology than are local effusion rates, at least east of the terminal moraine. Substrate slope west of the terminal moraine seems to have a greater effect on flow morphology, however. Lava flow morphologies in the north and distal-most pillow ridge tend to be well formed at the base of the ridge but poorly formed or brecciated and chaotically oriented above the basal pillows on steeper slopes that vary between 15° and 45°.

4.4.1.4 Lava cooling and heat dissipation

Given the lack of subaerial deposits and other geological constraints, the emplacement of the sheet lavas and pillow lava ridges within the TVC is interpreted to have been entirely subaqueous. It is assumed the cooling of these lava morphologies also occurred subaqueously. All heat within the lava flows, therefore, is dissipated to the substrate, surrounding meltwater or ice. Heat from individual pillow lavas and sheet flow units often is dissipated to, or absorbed from, adjacent pillow lavas in the ridges or sheet flow units in stacked sequences.

The cooling of subaqueous lava flows is dominated initially by the convective heat loss of the lava body to the surrounding meltwater until the body surface reaches the glass transition temperature and a glassy rind forms. Glassy rinds on subaqueous lavas form quickly, within a second on MORB lavas (Griffiths and Fink, 1992b; Gregg et al., 1996), and act as an efficient insulating layer, which reduces the heat flux from the interior of the lava body to the surrounding meltwater (Gregg and Fornari, 1998). Once a glassy surface rind forms, conductive heat loss from the insulated flow interior through the surface rind largely controls cooling, and the rate of cooling is controlled by the ratio of surface area exposed to volume of the lava body: the greater the surface-area-to-volume-ratio, the greater the efficiency of heat transfer from the lava body to the surroundings (Griffiths and Fink, 1992b; Keszthelyi and Denlinger, 1996; Gregg and Fornari, 1998). Glassy surface rinds form quickly and are excellent insulators that prevent high-effusion-rate submarine lava flows from being cooling-limited if the surface rind remains intact. These lava flows can potentially be emplaced over greater distances than subaerial flows (Gregg and Fornari, 1998).

The sheet lavas that terminate at the northern slopes of Koosick Bluff are interpreted to have flowed from a vent now buried beneath the northern sections of the Tennena Cone. The

most distal sheet lava lobe flowed more than 3 km from the inferred vent location, but most flows terminated in the now extant southern drainage or against the north slope of Koosick Bluff ~ 2 km from the vent. Through a viscous flow equation of a Bingham fluid developed by Moore (1987), the mean velocity (v_f) of a 2 m thick (h) and 10 m wide (w) sheet flow unit over a 6° slope can be calculated with:

$$\bar{v}_{Bl} = \frac{h^2 g \rho_l \sin \theta}{3\eta} \left[1 - \frac{3\tau_0}{2\tau} + \frac{1}{2}\left(\frac{\tau_0}{\tau}\right)^3 \right]$$

where g is the acceleration due to gravity, ρ_l is the density of the lava, θ is the slope and

$$\tau_0 = \frac{g\rho_l h_0}{w}$$

and

$$\tau = g\rho_l h \sin \theta$$

The mean flow velocity of a TVC sheet flow unit is 14 m s^{-1} given a viscosity of 74.5 Pa s calculated at 1100° C with a lava density of 2400 kg m^{-3}, 5 vol.% crystals and 15 vol.% vesicles. The variable h_0 is the critical lava thickness required to induce flow and is estimated here at 1 m based on the simple observation that the thinnest sheet lava units in the TVC are ~1 m thick. The mean flow velocity, however, is sensitive to changes in h_0 and would vary between 28 m s^{-1} and 0.1 m s^{-1} if values of 0.5 m and 2 m are used for h_0 in the calculation, respectively. At a mean flow velocity of 14 m s^{-1} the sheet flow unit would reach its terminus in the southern drainage 2 km away from the vent in 2.3 minutes.

An effusion rate can be calculated using a derivation of the same equation by adding the width (w) of the sheet lava flow unit in

$$E_f = \frac{w h^3 g \rho_l \sin \theta}{3\eta} \left[1 - \frac{3\tau_0}{2\tau} + \frac{1}{2}\left(\frac{\tau_0}{\tau}\right)^3 \right]$$

and results in an effusion rate of 290 m^3 s^{-1} based on the variables that result in a mean flow velocity of 14 m s^{-1} (Moore, 1987; Harris, 2013). Gregg and Fornari (1998) calculated maximum flow lengths for submarine lavas at different flow velocities. Velocities comparable to the Bingham velocity of the TVC sheet lava result in maximum submarine lava flow lengths between 10^5 and 10^6 m (Gregg and Fornari, 1998). It may be a bit dubious to compare a simple Bingham velocity for subaqueous TVC sheet lavas to lava flow lengths based on initial convective cooling of flow surfaces through the glass transition temperature and subsequent conductive cooling calculations, but inferences can be drawn from the comparison. First, though the Bingham velocity and effusion rates most likely overstate true emplacement velocities of the sheet flows, the length of the sheet lava flows are within maximum flow lengths calculated by Gregg and Fornari (1998) and thus attest to the insulative capacity of quickly forming surface glassy rinds. Second, the distal-most, western sheet flow units are thin and laterally extensive, and therefore most likely not cooling-limited, nor are the thicker sheet flow units to the east, some of which extend across the drainage and abut the northern slopes of Koosick bluff.

The pillow lavas that make up the sinuous, diffuse ridges are, by definition, cooling-limited. Pillow lavas propagate at local effusion rates <1 m^3 s^{-1} when the internal driving pressure gradient in the pillow exceeds the tensile strength of the quickly cooling glassy rind (Klingelhöfer et al., 1999). As long as the critical driving pressure exceeds the tensile strength of the chilled pillow surface, the advective transport of heat to the propagating pillow lava front will continue and the pillow will propagate forward. The critical driving pressure can be expressed as a function of the pillow radius as R$^{3.85}$ (Klingelhöfer et al., 1999). Klingelhöfer (1999) concludes that the local effusion rate, or critical pressure, and the lava viscosity control pillow lava morphology (Moore, 1975; Griffiths and Fink, 1992b; Gregg and Fink, 1995).

Pillow lavas exposed in the pillow lava ridges rarely exceed lengths of a couple of meters. The longest visible pillow lavas are found at the base of the pillow lava ridge near the southern drainage, and the longitudinal exposures of these basal pillows is ~6 m. It is quite possible that longer individual pillow lavas exist but are buried within the pillow lava ridges. Surficial pillow lavas on the ridges are rarely longer than 2 m and are smooth-skinned and sinuous. Smooth-skinned pillow lavas indicate higher emplacement rates than pillow lavas that display tensional surface fractures, because at faster emplacement rates the pillow surface deforms plastically and cools at faster rates (Moore, 1975; Chadwick and Embley, 1994; Kennish and Lutz, 1998). The result of quicker surface cooling is shorter pillow lavas (Moore, 1975; Moore and Calk, 1991; Chadwick and Embley, 1994).

Calculations of heat transfer from pillow lavas in glaciovolcanic environments is centered on the dissipation of heat from pillows and pillow piles that form proximal to the source vent or fissure (Höskuldsson and Sparks, 1997; Gudmundsson, 2003; Tuffen, 2007). At the TVC, pillow lavas are emplaced under thick ice away from the source vent where eruption rates are much higher than the local effusion. The heat content of 2-m-long pillow lava 0.5 m in diameter is 1.60×10^9 J and is given by (Gudmundsson, 2003):

$$q_l = \rho_l V_l [L_l + C_l (T_l - T_w)]$$

Where q is the heat content, ρ_l is the density of lava, V_l is the volume of lava, L_l is the latent heat of crystallization, C_l is the heat capacity of lava, T_l and T_w are the temperature of the lava and meltwater, respectively (Gudmundsson, 2003). Using the same equation, a volume of lava (V_l) represented by a characteristic 1000 m long section of a TVC pillow lava ridge 8 m wide and 5 m high results in a heat content of 2.56×10^{14} J. If the total heat content in the 6.28×10^4 m^3

volume of lava was used to melt the overlying ice, the volume of ice melted (V_i) would be 7.30x10^5 m^3 given by:

$$V_i = \frac{V_l \rho_l \left(L_l + C_l(T_l - T_w)\right)}{\rho_i L_i}$$

Where ρ_i is the density of ice and L_i is the heat of fusion of ice (Gudmundsson et al., 2004).

Emplacement of the pillow lavas that form the ridge occurs over many hours in meltwater that is likely flowing at a variable discharge rate. Though the heat of the individual pillow lavas is added to the aggregate system, heat dissipated to the system is transported during the TVC eruption, the increasing volume of meltwater created by the transfer of heat from the erupted lava to the surrounding ice probably affected the capacity of the subglacial drainage system to transport water and thus affected local meltwater flow rates around the pillow lava ridge. After emplacement, the efficiency of the complete pillow lava ridge mass to melt the surrounding ice would be diminished by the flux of meltwater through the drainage system as the individual pillow lavas are emplaced over time. d away from the immediate surroundings by the flow of meltwater around the pillow lava ridge.

The burial of pillow lavas by the subsequent emplacement of overlying pillow lavas also affects the dissipation of heat to the meltwater and ultimately the overlying ice. If the local effusion rate is high, then the heat flux from the pillow pile will be elevated over lavas emplaced at lower effusion rates, yet the heat exchange efficiency will diminish as recently emplaced pillow lavas are buried and their thermal flux diminishes (Höskuldsson and Sparks, 1997; Gudmundsson, 2003). At lower local extrusion rates, individual pillow lavas will efficiently dissipater their heat to the environment but the aggregate heat flux will be smaller at lower extrusion rates.

A 2-km-long, 10-m-wide and 2-m-high sheet lava lobe is roughly the same volume of a 1000 m section of pillow lava ridge and therefore the estimates of the total heat content is roughly the same. This idealized sheet lava lobe is a single lobe and its cooling rate is a function of its surface-area-to-volume ratio. Like the pillow lava ridges, the efficiency of heat loss to the environment of a single lobe is greater than when buried by other sheet flow units, but the aggregate heat flux would be greater if the sheet flow units were emplaced in rapid succession.

4.4.2   The glacial environment

A 500 to 1400 m thick ice mass overlying the flanks of Mount Edziza at the time of the TVC eruption is a reasonable assumption given ice thickness estimates of the CIS during Late Fraser and, possibly, Younger Dryas glacial events (Fulton, 1991a; Ryder and Maynard, 1991; Menounos et al., 2009). The existing ice sheet was also temperate or wet-based and a regional subglacial drainage system was active. At Mount Edziza, meltwater was transported away and west through the coast mountain range by a regional drainage system now occupied by the Stikine River (Spooner and Osborn, 2000).

Subglacial drainage systems under a temperate ice sheet transport meltwater via flow in a thin layer at the ice-substrate interface, flow through a series of channels and other conduits, and as groundwater (Boulton et al., 1995; Boulton et al., 2007). The rigidity and permeability of the substrate determines which flow scenario is favored. Groundwater flow requires a permeable bed below the ice, whereas water films at the glacier base require rigid impermeable substrates as do well developed channels and conduits (Walder, 1986; Boulton et al., 1995; Boulton et al., 2007). Another subglacial flow conduit system has been described as a system of broad shallow pathways, or canals, as defined by Walder and Fowler (1994), cut into deformable, and usually

135

relatively impermeable, clay-bearing substrate beds (Clark and Walder, 1994; Walder and Fowler, 1994).

Subglacial meltwater drainage systems are commonly described as either a system of efficient drainage channels incised into basal ice that are stable at low hydrostatic pressures, or channeled systems that form anastomosing drainage paths in deformable beds that are stable at high hydrostatic pressures (Clark and Walder, 1994; Brennand, 2000; Walder, 2010). A drainage system of mainly hemicylindrical Röthlisberger (R channels) cut into the basal ice preferentially form over rigid beds, whereas anastomosing channel systems are common on deformable beds (Walder, 1986; Clark and Walder, 1994). Within the TVC there is evidence of both an R channel system north and west of the southern drainage and a channeled system around the southern drainage.

4.4.2.1 Subglacial drainage on a rigid bed

The stability of R channel systems as compared to channeled systems over deformable beds is reflected in the direct relationship between meltwater discharge (Q) and the effective pressure (P_E). The effective pressure of an R channel system is the difference between the pressure exerted by the overlying ice mass (P_I) to reduce the volume of the channel and the pressure exerted by meltwater (P_W) to expand the volume of the R channel. In R channel systems, with no or little change in P_I in the short term, any increase in Q through the channel will decrease the water pressure in the system. Though comparatively more stable than channel systems formed over deformable beds, R channels do deform, and the rate of deformation is a balance between the rate of channel radius expansion due to melting of the surrounding ice walls by the meltwater (U_m), and channel radius decrease by the inward flow of the surrounding ice (U_c). The rate of

channel deformation (U) is the difference between U_c and $U_{m,}$. The channel radius decrease is given by:

$$U_c = r \left[\frac{P_E}{nA} \right]^n$$

Where R is the channel radius, n and A are Glen's flow law parameters for ice (Nye, 1953). The parameter n is a empirically derived constant ≈ 3 in most ice stress regimes, which include stress regimes found in thick basal ice (Hooke, 2005). The flow law parameter A is an ice viscosity parameter that increases as the ice viscosity increases. Ice viscosity is a function of ice temperature, water content, ice crystal microstructure, among other variables, and softer, less viscous ice deforms more quickly than more viscous ice. The value of U_c is sensitive to a change in A, and for comparison, the change in A from measured values of 1.2×10^5 to 2.0×10^5 Pa a$^{1/3}$ result in a 4.6-fold increase in the U_c of an R channel (Rothlisberger, 1972; Hooke, 1984). The viscosity of the basal ice overlying the TVC at the time of the eruption is unknown and therefore must be estimated. Tuffen (2007) used a value for A of 5.3×10^7 Pa s$^{1/3}$ to describe the deformation of a cavity over a vent or fissure in a subglacial eruption, and Clarke (2003) used a value of 5.28×10^{-7} to describe cavity deformation in subglacial outburst floods. The later value is used here to calculate U_c.

The rate of R channel radius increase due to meltwater is given by:

$$U_m = k \frac{Q G v_j}{P_m L_i}$$

Where k is ≈ 0.68 and corrects for the energy required to maintain water at the ice melting point, P_m is the perimeter of the cavity roof, L_i is the latent heat of fusion per unit mass, v_i is the specific volume of ice and G is the hydraulic gradient (Rothlisberger, 1972; Walder, 1986). For a channel

under "typical" glacial conditions where the meltwater temperature is near the ice pressure melting point the equation then becomes

$$U = r \left[\frac{P_E}{nA} \right]^n - k \frac{QGv_j}{P_m L_i}.$$

Subglacial drainage systems in glaciovolcanic terrains are often subjected to elevated meltwater temperatures which affect values of U_m (Gudmundsson et al., 1997; Gudmundsson et al., 2004; Tuffen, 2007). Measurement of meltwater sampled during the 1996 Gjálp eruption were 20° C and Gudmundsson (2004) suggested that meltwater temperatures during subglacial eruption may approach 100° C. Classic models for subglacial channel deformation do not account for elevated meltwater temperatures found during glaciovolcanic events, yet recent work on jökulhlaup events, spurred by the 1996 Gjálp eruption, has focused on the thermal evolution of glacial channels during these flood events (Clarke, 2003; Russell et al., 2007). Clarke (2003) further developed an equation first derived by Nye (1976) and Spring and Hutter (1982) that describes R channel deformation (U_s) at meltwater temperatures elevated above the pressure melting point at the base of the glacier.

$$U_s = \frac{m}{\rho_i} - 2sin(p_E) \left[\frac{|P_E|}{nA} \right]^n S$$

Where ρ_i is the density of ice, S is the cross sectional area of the channel, and

$$m = 0.023 Pr^{2/5} Re^{4/5} \left[\frac{P_m K_w (T_w - T_i)}{4 L_i R_H} \right].$$

The parameter Pr is the Prandtl number, Re is the Reynolds number, K_w is the thermal conductivity of water, T_i is the temperature of the ice and R_H is the hydraulic radius of the channel (Nye, 1976; Spring and Hutter, 1982; Clarke, 2003). Nye (1976) describes the Prandtl

number as a material constant which for water is 13.5, and the Reynolds number can be calculated by the equation;

$$Re = \frac{4\rho_w \bar{v} R_H}{\eta_w}.$$

The parameter $\bar{v}$ is the mean meltwater velocity through the R channel, η_w is the viscosity of water and R_H is the hydraulic radius of the R channel.

To illustrate the effect of elevated meltwater temperatures on the R channel system, we look at a stable pressure regime at the base of an ice mass where the deformation rate of an R channel is zero ($U = U_c - U_m = 0$), but the meltwater transported through the system is at temperatures elevated above the near-pressure melting point temperatures. Equations describing the deformation under normal conditions would show no change in the R channel cross-sectional area. Conversely, the (Clarke, 2003) equation describes an increase in the cross-sectional area over time-dependent meltwater temperature. To numerically represent the variance between the two approaches, values for the meltwater discharge (Q), velocity ($\bar{v}$) and pressure gradient (G) though an R channel must be assigned. Values for these three parameters are based on estimates of an R channel initial cross-sectional area (S) and slope values found within the TVC area prior to the eruption. If a value for the cross sectional area (S) is assigned, the discharge rate (Q) can be estimated by

$$\bar{v} = Q/S$$

where

$$\bar{v} = (2\pi)^{-2/3} \left[\frac{v_w G}{g} \right]^{1/2} S^{1/3} \acute{n}^{-1}.$$

The parameter v_w is the specific volume of water and $\acute{n}$ is the Manning's roughness coefficient (Nye, 1976; Walder, 1986). In the case of subglacial drainage systems, the Manning's roughness coefficient values range between 0.005 m$^{-1/3}$ s from studies on jökulhlaup events and 0.2 m$^{-1/3}$ s on small radius (<1 m) and subglacial channels with rough channel walls (Seaberg et al., 1988; Björnsson, 1991; Hock and Hooke, 1993; Hooke, 2005). Hooke (2005) suggests using an intermediate value of 0.1 m$^{-1/3}$ s and Walder (1986) estimates mean velocities with this value in the absence of empirical data. This value is thus used here to estimate the Manning's roughness coefficient. The meltwater pressure gradient (G) in an R channel system at or before the time of the TVC eruption is unknown and can be estimated using:

$$G = \frac{dP_w}{dx} + \rho_w g \sin \theta .$$

The slope of the underlying substrate does not exceed 7° above or east of the terminal moraine. A slope of 6° is therefore used in calculating the meltwater pressure gradient. The change in water pressure over a distance x is not known and thus values are compared to those found in the literature. Calculated with a slope of 6° and a semicircular channel radius of 0.5 m, the values for G vary between 10^3 and 10^6 Pa m^{-1} and result in mean flow velocities ($\bar{v}$) between 2 and 69 m s^{-1} based on values of $\frac{dP_w}{dx}$ that range between 1 and 10^6 Pa m^{-1} (table 4.2). Walder (1986) uses values for $\frac{dP_w}{dx}$ that are less than 100 Pa m^{-1} to describe flow velocities in conduits with radii less than 1 m. These $\frac{dP_w}{dx}$ values coincide with velocities less than 2.3 m s^{-1} illustrated in table 4.2, and are velocities driven by pressure gradients due to gravity on a shallow slope rather than the pressure from $\frac{dP_w}{dx}$. An intermediate value of 50 Pa m^{-1} is used for $\frac{dP_w}{dx}$ in calculations of mean flow velocity and R channel deformation rates.

Table 4.3. Ranges of mean meltwater velocity in R channels*

dP_w/dx	G	$\bar{v}$
(Pa m^{-1})	(Pa m^{-1})	(m s^{-1})
1	1025	2.209
10^1	1034	2.218
10^2	1124	2.312
10^3	2024	3.103
10^4	11024	7.243
10^5	101024	21.93
10^6	1001024	69.02

* Calculated using $\theta = 6^o$ and a cross-sectional radius of 0.5 m.

For convenience, the cross-section normal to the flow path of meltwater through an R channel is assumed to be a semi-circle with a radius of 0.5 m. A cross-sectional radius of 0.5 m results in $S = 0.3$ m^2. Given S and a hydraulic gradient (G) of 1.0×10^7 Pa m^{-1} the mean flow velocity ($\bar{v}$) through the R channel is 2 m s^{-1}. Placing the velocity value into the Reynolds number equation a value of 700 is obtained for the Reynolds number. Using the Reynolds number we obtain a value for m, the mass melting rate value used in calculating the deformation rate of the R channel cross-sectional area. Finally, the discharge rate of meltwater through the R channel system is the mean velocity multiplied with the Cross-sectional area and equals 0.8 m s^{-1}. These values are reasonable and coincide with values reported by Walder (1986) and lie within the estimates of 1-to -3 m s^{-1} summarized by Clark and Walder (1994).

In a pressure regime where the R channel deformation rate is equal to zero under typical thermal conditions at the glacier base would result in no change in the cross-section area of the channel. However, at an elevated meltwater temperature of 20° C, a discharge rate Q of 0.9 m s^{-1} in an R channel with an initial radius of 0.5 m, for example, the channel cross-sectional area would increase 31% in 36 hours. If the meltwater is at 35° C the cross-section area would

increase by 61% (Figure 4.6). In an extreme example where meltwater temperatures are 100° C, the channel cross-sectional area would increase 295% in 36 hours. These estimates do not account for the thermal and mechanical effect of suspended sediment, which would be expected in the TVC drainage system and would likely increase the deformation rate of the R channel system.

Deformation of R Channel Cross-sectional Area
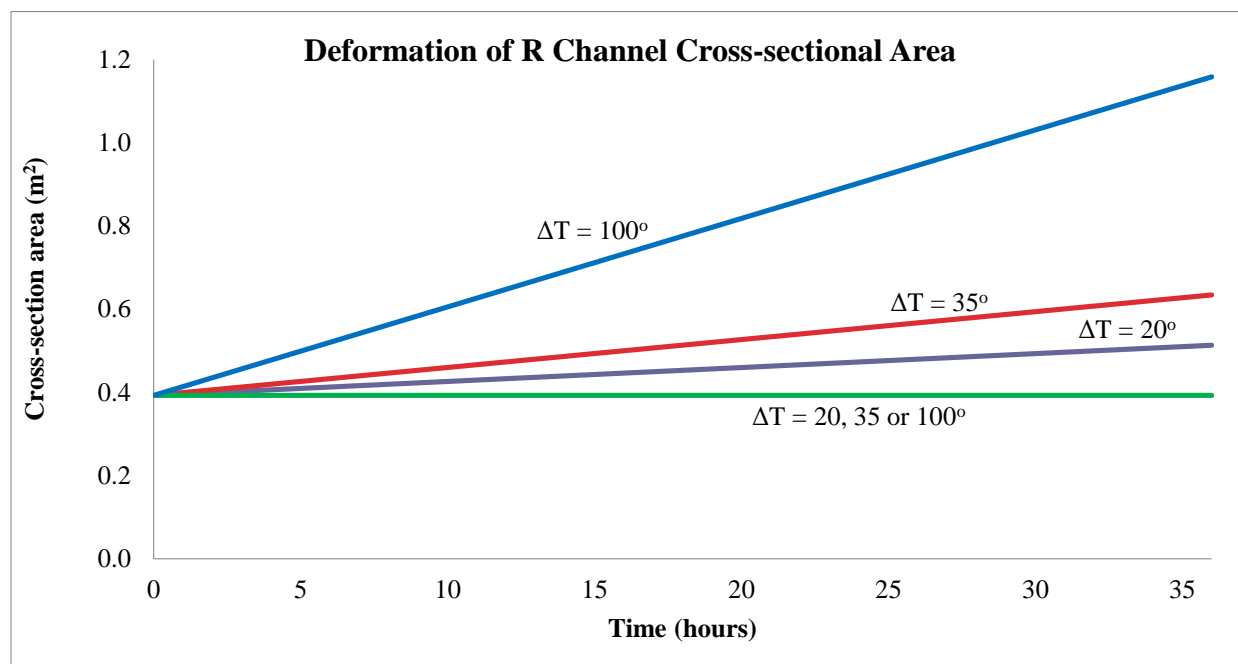
Figure 4.6. Cross-sectional deformation of an R channel.
The deformation rate is calculated with a 1 m radius at $P_I = P_W$ with both the Clarke (2003) equation for elevated meltwater temperatures and the equation based on Nye (1953), which does not account for elevated meltwater temperatures. The Nye based equation (horizontal green line) represents no change in the cross-section area at either ΔT values and the Clarke (2003) equation illustrates greater rates of change with larger ΔT values. The parameters for each calculation are held constant except the ΔT value.

The hydraulic capacity of the subglacial channel system prior to the TVC eruption is not evident but the development or expansion of the system would be expected over the rigid base of Ice Peak Formation lava flows because the thermal dissipation of heat from the coherent and

volcaniclastic lavas increases the volume of meltwater during the initial phases of the TVC eruption. Ryder and Maynard (1991) and Spooner and Osborn (2000) suggest that a subglacial drainage system existed in the region prior to the TVC eruption. TVC lava bearing glaciofluvial sediments (described in chapter 3) coevally deposited with TVC lava flows indicate a subglacial drainage system transported sediment laden meltwater west into Sezill Creek. Bedded sequences of these glaciofluvial sediments onlap the lateral slopes of the sinuous pillow ridge and pillow lava ridges and also form an esker that continues from the terminus of a pillow ridge and pillow lava ridge. This esker represents the deposition of TVC lava-derived, glaciofluvial sands and gravels in an R channel (e.g, Clark and Walder, 1994), and suggests a subglacial drainage system that included R channels developed in the presence of increasing volumes of meltwater at elevated temperatures during the TVC eruption.

4.4.2.2 Subglacial drainage on a deformable bed

In the area of the southern drainage at the TVC, the sheet lavas overlie diamict lodgment till to the east and coevally deposited diamict glaciofluvial sediments to the west and downstream in the drainage system. The lodgment till underlies both the sheet lavas and the diamict glaciofluvial sediments. The clay-rich diamict till represents a deformable bed that favors the development of a channel system cut into the substrate at elevated meltwater volumes (Clark and Walder, 1994; Walder and Fowler, 1994). Although a substrate may accommodate Darcian groundwater flow, a thin, clay-bearing substrate till can quickly be overwhelmed if substrate pore water pressures exceed critical values in the presence of elevated meltwater discharge rates (Q) (Clark and Walder, 1994; Walder and Fowler, 1994; Brennand, 2000). A thin sheet of meltwater may form at the substrate-ice contact with an elevated meltwater flux, but these meltwater sheets are unstable and rapidly form a channel or a system of anastomosing or

braided channels (Walder, 1986; Walder and Fowler, 1994). A channel will preferentially form as either a canal or a channel in the deformable bed. Canals are channels cut into the underlying substrate, but, unlike other channels, canals are much wider than deep and are formed by both fluvial erosion and bed deformation (Figure 4.7; Walder and Fowler, 1994; Brennand, 2000). The preferential formation of either a canal or channel is dependent on the meltwater discharge and the slope of ice surface, given the pressure gradient at the base of the ice is ~ 11 times more dependent on the ice surface than the substrate slope. At larger Q (>1 m^3 s^{-1}) both canals and channels will commonly incise equally into the glacier base and substrate till on steeper ($\geq 3^o$) ice surface slopes, but canals preferentially form on shallower slopes (Walder and Fowler, 1994). Most importantly, a system that comprises either channels or canals, or both, is only stable when the water pressure is greater than, or at least equal to, the pressure of the overlying ice (P$_W \geq$ P$_I$), and the meltwater flux is greater than the maximum flux of groundwater flow in the deformable substrate bed (Walder and Fowler, 1994). Unlike a R channel drainage system formed over a rigid bed, a decrease in water pressure in the deformable bed channel system decreases its stability, and once the water pressure falls below the pressure exerted by the ice mass, the drainage system degrades or fails (Clark and Walder, 1994; Walder and Fowler, 1994). Conversely, an increase of Q increases the water pressure in the deformable bed channel system (Clark and Walder, 1994).

The coeval diamict beds intercalated in the western sheet flow units indicate glaciofluvial flow between the ice base and the underlying lodgment till substrate. Downstream of the western sheet lavas, sequences of glaciofluvially deposited sediments comprising TVC derived and other oligomict lithic clasts illustrate the variations of Q as both the sorting and mean clast size varies within individual beds. Some of these sediments are overlain by a pillow ridge and pillow lava

ridge. These deposits indicate an active drainage system in the area of the existing southern drainage during the TVC eruption and it was subject to variations of Q and/or variations in the spatial distribution of the Q throughout at least the initial stages of the eruption when the sheet lavas were emplaced.
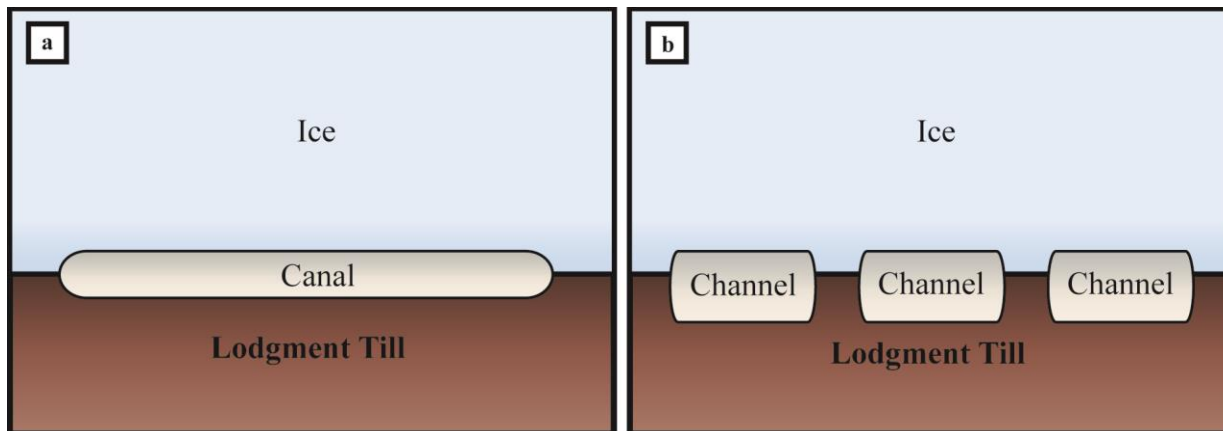
Figure 4.7. A cartoon of canals and channels in deformable beds.
(a) Canals are comparatively wide in cross-section and incise into the underlying deformable till bed. (b) Channels cut deeper into the deformable bed and are not as laterally extensive as canals.

4.5   DISCUSSION

4.5.1   Lava flow emplaced under thick ice

The sheet lavas and pillow lavas in ridges were emplaced under at least 500 m of ice. The cone is 500 m above the outcrops of sheet lavas and as much as 800 m higher than the most distal TVC pillow lava outcrop in the north head of Sezill Creek valley. The volcaniclastic deposits that compose the highest strata of Tennena Cone are interpreted to be subaqueously erupted volcaniclastic deposits as discussed in chapter 3. This suggests the cone was never

emergent and was emplaced entirely subaqueously. Tennena Cone is a positive topographic feature and no other landform exists in the vicinity that would have ponded water around the cone. The cone therefore was constructed in meltwater confined by an ice cauldron. The ice mass forming the cauldron was not likely to have been limited to an area surrounding the cone. No feasible topographic feature(s) would have dammed water above Sezill creek to create a perched body of meltwater needed to emplace the subaqueous lavas emanating from Tennena Cone. And given the proximity of the cauldron to the vent during the 1996 Gjálp eruption, the ice cauldron was most likely restricted to the near vicinity of vents at Tennena Cone (Gudmundsson et al., 2004).

The distal lavas are presumed to have emanated from vents on Tennena Cone or now buried by the volcaniclastic deposits that form the cone (Souther, 1992). There is no evidence of vent deposits elsewhere within the TVC and exposed dikes are confined to the cone edifice and trend west-northwest. The exposed TVC lavas overlie relatively impermeable Ice Peak Formation lava flows north and west of the southern drainage, but in areas surrounding the subglacial drainage TVC lavas overlie older diamict glacial tills and coevally deposited glaciofluvial sediments. Where exposed, the basal contact of the glacial tills overlies Ice Peak Formation lavas and the till is not more than 2 m thick, yet the coevally emplaced glaciofluvial sediments overlying the till and Ice Peak lavas can be up to 5 m thick.

Groundwater flow in the southern drainage area may have been a mechanism of meltwater transport prior to the TVC eruption, but as volumes of meltwater increased through the eruption, any groundwater flow capacity, constrained by a finite volume in the few meters of till overlying an aquatard of impermeable Ice Peak lavas, would have been quickly overwhelmed. The deposition of glaciofluvial sediments that include clasts derived from TVC

146

lavas suggests any groundwater flow system was saturated quickly within the first stages of the TVC eruption, and suggests channelized flow quickly became the mechanism of drainage of a sediment-laden meltwater.

The existing Tennena Cone edifice is roughly 1200 m long and 1000 m wide and has been subject to mechanical erosion by subsequent glaciations. If the dimensions of the ice cauldron, which formed around the cone as discussed in chapter 3, are conservatively estimated to be within 100 m of the existing edifice and assuming the ice is 500 m thick at the cone, the volume of meltwater can be estimated by calculating the volume of ice melted to form the cauldron. This conservative estimate results in a volume of 2.5×10^9 m^3 of meltwater produced by melting the overlying ice. Both plastic flow of ice into the cauldron, described by Nye's Law (1972), and brittle deformation of the ice surrounding the cauldron, exposed further volumes of ice to melt in the presence of meltwater at elevated temperatures. The deposits emplaced distally under the ice mass also increased the volume of meltwater that drained west into Sezill Creek valley. Transport of meltwater at elevated temperatures and mechanical excavation from sediment-laden meltwater further increased meltwater volumes in the drainage system. Elevated meltwater temperatures were most likely suppressed by entrained lithic sediments initially near or at the pressure melting point. The lithic sediments acted as heat sinks depressing the mean ambient temperature while entrained in the system. Once away from the heat sources, further melting of the drainage walls further suppressed meltwater temperatures.

4.5.2   Emplacement of Sheet lavas.

The massive sheet lavas are interpreted to be the initial high-effusion-rate lavas erupted during the TVC eruption. The sheet lavas were emplaced distally over deformable sediment beds in an unstable, laterally extensive subglacial channel or canal system. The sheet flow units advanced southwest and west below the ice mass over lodgment till and later over glaciofluvial sediments deposited prior and during the advancement of sheet flow units. The last sheet lavas may have been emplaced as meltwater hydrostatic pressures were dissipating while the local discharge rates decreased. The last sheet lavas are thin ($\leq$ 1 m) and laterally extensive ($\geq$ 10 m^2). Their morphology may be a function of their extrusion between the underlying sheet flow units and the overlying ice.

Sheet lava represents subaqueous basaltic lava emplaced at suggested local effusion rates between 1 m^{3}s^{-1} and 100 m^{3}s^{-1} (Griffiths and Fink, 1992b; Gregg and Fink, 1995; Gregg and Fink, 2000), and were emplaced at rates much greater than the capacity of a lava flow to melt into an ice mass. Maximum ice melting rates are less than 10^{-2} m s^{-1} and the sheets commonly advanced at velocities near 10 m s^{-1} given Bingham calculations estimating lava flow velocities. Individual sheet flow units may have been constrained laterally by ice or channel walls but they were not constrained in the direction of flow by ice until near Koosick bluff where their advance may have been thwarted by the northern slopes of Koosick Bluff or ice in the southern drainage. Some sheet flows do display rosette-style radial jointing, a cooling texture that may indicate ice contact.

The westernmost sheet flow is thin (~1 m) and flowed west under the cliffs of Koosick Bluff. The flow was constrained by Koosick Bluff and flowed along the scarp until it stopped 3 km away. The sheet lavas do not seem to have been cooling-limited and most likely were either

supply-limited or physically stopped by ice or topography. Yet the flows did not thicken much if at all through damming by ice or another topographic feature. The sheet lavas are single or stacked and each can be laterally extensive, although some are not. But they are not continuous lavas, and it is not clear if each sheet flow unit represents a lava flow directly from the source vent or a bifurcated lobe. The surface of the plateau above the sheet lavas has been modified by subsequent glaciation and it is impossible to trace individual sheet flow units back to the vent. At their termini, the sheet lavas vary in thickness and lateral extent throughout the outcrop. Given that thicker submarine lavas travel farther, these sheet lava units are shorter than their cooling-limited length (Gregg and Fornari, 1998).

The sheet lavas are interpreted to have been emplaced into a laterally extensive channel incised into the underlying deformable bed. The eastern most bed has a conical cross-sectional shape, narrowing upslope to the east. This cross- sectional shape may reflect the emplacement of this sheet lobe in the upslope extent of the meltwater lens (Figure 4.2a). No other sheet lava lobe displays this conical cross-sectional shape. The higher aspect-ratio, large-entablature basal lava units that underlie extensive sheet lavas may reflect the initial increase in discharge rates and may have exploited the initial channels cut into the deformable substrate. The channel system over a deformable bed is dependent on hydrostatic pressure being at or greater than the cryostatic pressure exerted by the overlying ice. The volume of the sheet lava unit initially displaces the volume of meltwater in the channel or canal and thus increases the hydrostatic pressure. The increase in hydrostatic pressure is offset, however, by the introduction of additional heat available to melt the overlying ice. But if the thermal flux from the sheet lava is efficiently dissipated and available to melt the overlying ice, the volume difference of ice melted to meltwater created will decrease the water pressure in the channel. This scenario, of course, could

be inconsequential if the discharge through the channel system remains elevated or increases. Furthermore, the addition of more sheet flow units into the meltwater volume may become critical and impede the flow of meltwater through the channel system. The western sheet flows may actually be the last vestige of sheet lava intrusion before the channel system collapsed.

4.5.3   Emplacement of pillow lavas in R channels

Most descriptions of pillow lava mounds and ridges detail the emplacement of vent-proximal pillow lavas piled at the vent. Loughlin (2002) and Smellie and Skilling (1994) recognized distinctive pillow lava ridges emplaced distal to the source vent or from an unknown source. Smellie and Skilling (1994) recognized that volcaniclastic assemblages at Mt Pinafore, Antarctica, that appeared to be eskers comprising volcanic sediments that once filled R channels. Later Loughlin (2002) recognized these features at Eyjafjallajökull, Iceland. He saw coherent lava tubes surrounded by hyaloclastite which he interpreted to have been emplaced within R channels. Loughlin (2002) suggested that lavas and associated sediments filled R channels and created new channels that resulted in a system of anastomosing tunnels. Loughlin (2002) therefore implied the emplacement of lavas in R channels may further expand the drainage system.

The TVC Pillow lava ridges extend west away from the source vent on the southwest flank of Tennena Cone. The pillow lavas advanced towards Sezill Creek, probably exploiting R channels that were thermally excavated by heated meltwater produced during the TVC eruption. The pillow lavas advanced through the R channel system to the area now occupied by a terminal moraine deposited during recent glaciation. There, the pillow lava ridges bifurcate into a system

of channels that either propagate west and feed the distal TVC lavas, or propagate south and terminate near the southern drainage.

Unlike proximal pillow lava mounds, these lavas did not propagate from a point-source vent or a fissure system where a multitude of pillow lavas may form simultaneously. This does not preclude the formation and emplacement of multiple pillow lavas within the R channel system concurrently but a multitude of pillow lavas forming from a distal source of local effusion rates favoring pillow seems less likely.

TVC pillow lavas in ridges tend not to be longer than 3 m and pillow lavas and are smooth-skinned. This fast growth surface allows stretching and deformation but these smooth-surfaced pillows do not grow to long sizes because the confining crust becomes too thick (Moore, 1975; Ballard and Moore, 1977; Walker, 1992; Kennish and Lutz, 1998). Distal TVC pillow lavas display tensile fracturing of the skin and surface corrugations, which indicate slower emplacement rates and brittle failure to accommodate growth.

Basaltic pillow lavas are emplaced at local emplacement rates at or below 1 m s^{-1}. At this effusion rate, a 100-m-long section of a ridge, 8 m wide and 5 m high would take 1.75 hours to emplace that volume. The pillow ridge cross-sectional area would not be the same as the R channel because the heat flux emanating from the pillow ridge would increase the cross-sectional area of the R channel at some rate ± the meltwater discharge. If the heat from the pillow lavas did not melt the ice, the meltwater discharge through the R channel would decrease and the pillow ridge would effectively plug the channel. Conversely, the heat flux from the pillow lavas would increase the R channel radius or the channel may shift to the left or right of the pillow ridge to accommodate meltwater discharge through the channel in a similar manner that R channels accommodate the deposition of sediments that form (Hooke, 2005). An en-masse

emplacement of pillow lavas would potentially lead to an R channel-filling scenario and is most likely not a viable emplacement scenario. Walker (1992) suggested that pillow ridge and pillow lava piles found in submarine environments are likely cored by a megapillow lava that serves as a master tube to distally emplaced lavas. This may be a plausible emplacement scenario of TVC lavas but the only mega pillows found in distal TVC lavas are those that lie on flat to shallowly dipping substrate and exist with vertical pillow and hollow pillow lavas. This does not preclude their existence inside the pillow lava ridges but no megapillow lava has been seen in a pillow lava ridge.

The pillow lava ridges on slopes below 10° at the TVC are hemi-elliptical and diffuse in cross-section: pillow lavas at the base of the ridge may spread laterally within a 1-2 m from the base. The cross-section of these pillow ridges does not mimic the form of an R channel cross-section. These diffuse pillow lava ridges may have been emplaced as one or a few pillow lavas propagating at a time through the R channel and slowly built up as with time (Figures 4.8c, 4.8d). The resultant deposit would be a diffuse ridge sequence with basal, lateral pillows propagating sub-parallel to the ridge axis and potentially abutting ice at the ice-substrate contact. The resultant diffuse, wider-than-tall pillow lava ridges seen with the TVC distal lava terrain most likely is emplaced in this manner.
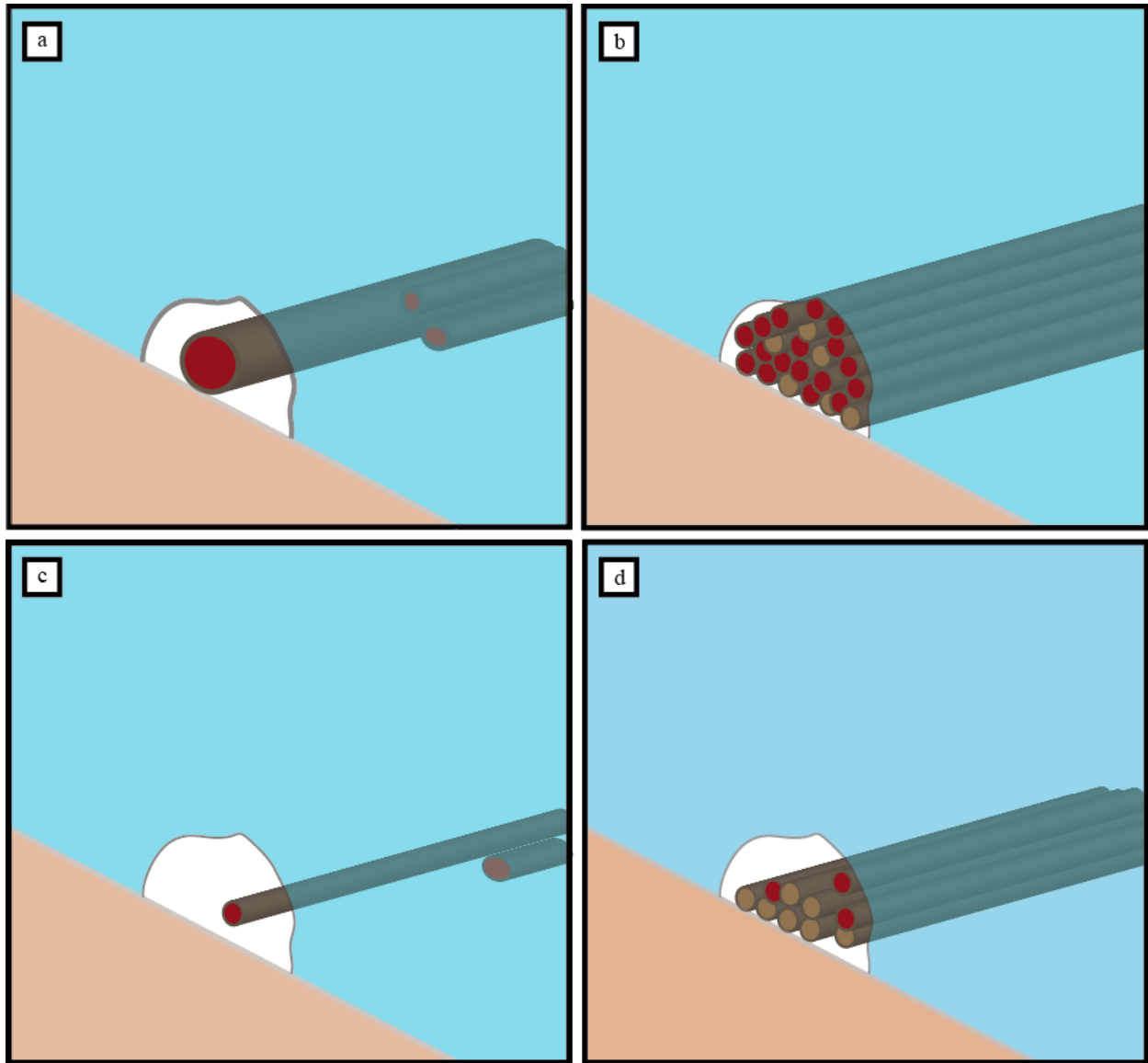
Figure 4.8. Different emplacement scenarios of pillow lava ridges.

(a) Scenario 1; an initial emplacement of a megapillow lava and subsequent breakouts from the megapillow. This is representative of the scenario proposed by Walker (1992). (b) Scenario 2; pillow lavas are emplaced en masse and fill the R channel. (c) Scenario 3; pillow lavas are emplaced in the R channel not en mass but in a few at a time and do not fill the R channel. (d) Scenario 3 continued; the pillows form a pile but upper pillow lavas propagate sub-parallel to the ridge axis and potentially abut ice at the ice-substrate contact in the R channel.

153

4.6   CONCLUSION

Although sheet lava and pillow lavas are ubiquitous in submarine environments and pillow lavas are quite common in glaciovolcanic terrain, sheet lava flows and pillow lavas are not commonly recognized in as distal coherent deposits in glaciovolcanic terrains. The distal sheet lavas and pillow lavas at TVC are unique in that they represent basaltic glaciovolcanic lava flows that were emplaced distally under a thick ice mass. This study is the first to describe these lava morphologies in detail and also to describe their emplacement under a thick ice mass. The sheet lavas represent the initial, high-effusion-rate lavas emplaced at or soon after the inception of the eruption. These lavas were emplaced more than 3 km from the source vent under the extant Tennena Cone and exploited a system of subglacial drainage channels or canals incised into a deformable till bed and the overlying ice by fluvial erosion brought about by elevated meltwater discharge. The individual sheet flow units were progressively emplaced to the west where the last sheet lavas intruded a diminishing lens of meltwater overlying recently emplaced sheets intercalated with diamict glaciofluvial sediments.

The late-stage pillow lavas formed ridges in a system of R channels that expanded with the increased discharge of meltwater at elevated temperatures. Thermal erosion of R channels was exacerbated by the emplacement of the pillow lava ridges but the thermal input of the initial pillow lavas emplaced in the channels was negligible as the elevated Q through the system transported the het downstream. R-channels were only partially filled with pillow lavas and

discharge through the system continued as pillow lavas continued down the channel path. The pillow lava ridges abutted the lower lateral edges of the R channels and melted them away. Meltwater, however, continued to flow above the pillow lava ridges until the ridges cooled to ambient temperatures after emplacement. The identification and description of the distally placed lava flows may represent terrestrial analogues for similar deposits in glaciovolcanic terrains, submarine volcanic terrains and possibly as well as lavas emplaced in similar environments on Mars.

5.0 EXPOSURE DATING OF EXPLOSIVE EVENTS AT THE SUMMIT CALDERA OF MAUNA LOA WITH COSMOGENIC CHLORINE-36

5.1 INTRODUCTION

Mauna Loa, the largest active volcano on Earth, is the most well dated volcano on Earth (Trusdell, 2007; Trusdell, 2012). Extensive, detailed mapping of both historic and prehistoric lava flows has elucidated the spatial and temporal distribution of past activity on Mauna Loa (e.g., Lockwood and Lipman, 1987). Lava flows and minor volumes of explosive deposits less than 10 ka cover approximately 98% of Mauna Loa's subaerial surface (Fig. 1; Lockwood et al., 1988; Lockwood, 1995; Trusdell, 1995). Historical records extend back over the last 170 years and document 33 historical eruptions since the first documented historic eruption of 1843. These historical eruptions have re-surfaced 14% of the surface of Mauna Loa (Trusdell, 1995), yet, no explosive activity has been attributed to these eruptions beyond Hawaiian-type fire fountaining or littoral cone production from lava flows entering the sea.

The evolution of a Hawaiian volcano tends to follow a characteristic eruption sequence from inception to dormancy. Mauna Loa volcano, like Kilauea Volcano, is currently in the shield-building stage. This stage is characterized by the dominance of Hawaiian-type eruptions

156
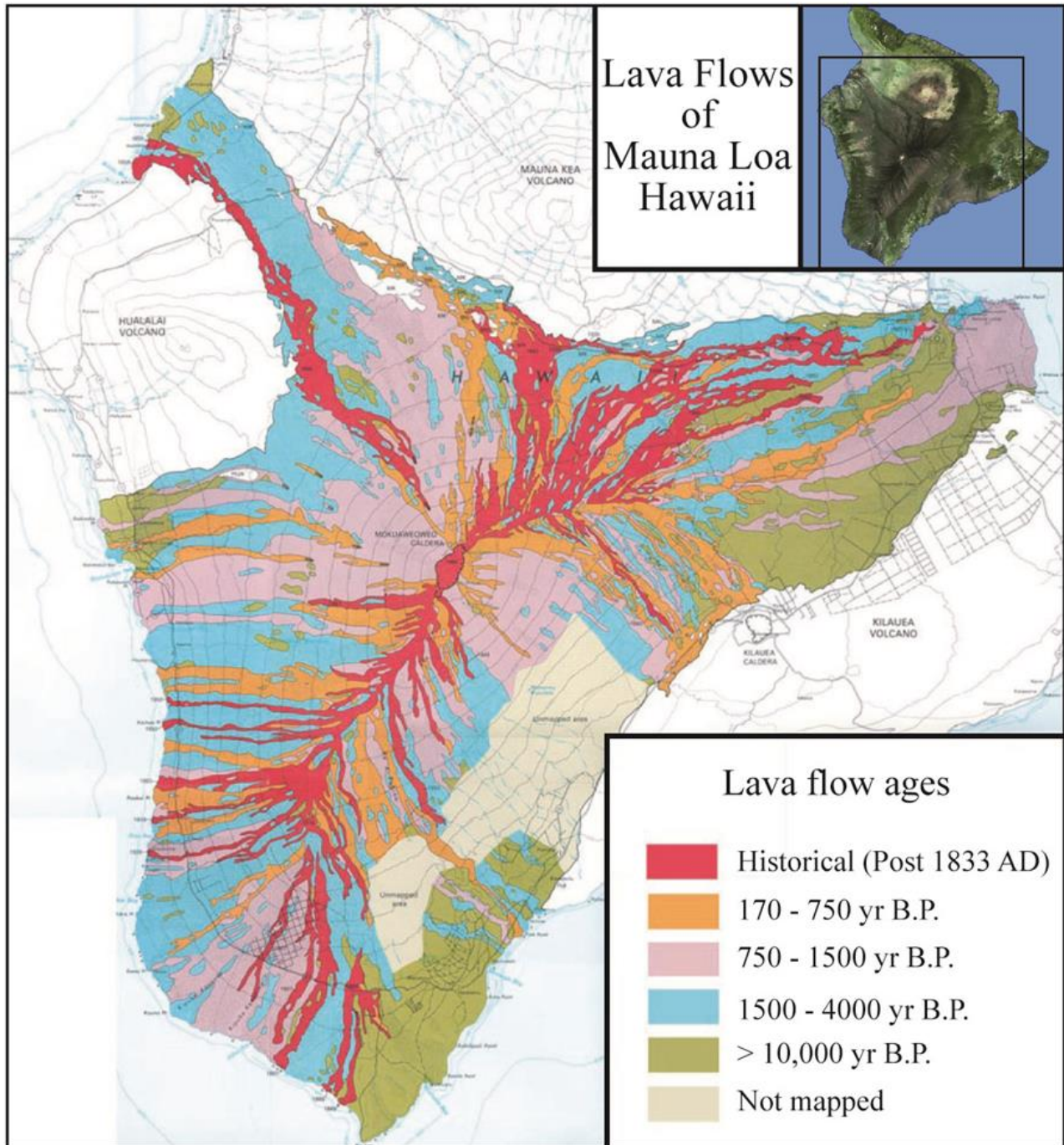
Figure 5.1. Map of Mauna Loa surface lava flows.

The location of the map On the Island of Hawai`i is indicated in the box in the upper right hand corner of the figure.

(Data source: USGS)

comprising fire fountaining and effusive production of predominantly tholeiitic basalt pahoehoe and a`a lava flows (Stearns, 1946). Previous contemplations of explosive activity during the subaerial, shield building, characterized it as ancillary at most. And, unlike Kilauea Volcano, explosive activity at the summit of Mauna Loa is largely enigmatic. Yet, at Kilauea Volcano explosive activity has been directly observed, and the debris of numerous prehistoric explosive events have been identified and mapped (e.g., Jaggar and Finch, 1924; Mastin, 1997; Mastin et al., 2004; Fiske et al., 2009; Houghton et al., 2011; Swanson et al., 2012a; Swanson et al., 2012b). Investigators now realize explosive activity occurs more frequently than previously thought. Several periods of explosive activity at Kilauea over the last ~2000 years are recorded in the strata surrounding the caldera and beyond. Explosive activity at Kilauea was largely described as hydrovolcanic in nature (e.g., Mastin, 1997) until recent events at Halema`umau, the summit crater at Kilauea. Rather than magma interaction with meteoric water, recent explosive activity at Kilauea Volcano seems to have been fueled by the confinement of exsolving magmatic gasses (Houghton et al., 2011).

It is unknown whether hydrovolcanic or magmatic explosive activity distributed the explosive ejecta in the debris fans near the summit caldera at Mauna Loa, but, either by proximity or type, contemplations of the mechanism of ejecta distribution is biased by evidence of explosive activity at Kilauea. Mafic explosive events have often been attributed to interaction between dike impounded groundwater and a magmatic heat source (Mastin, 1997). Problems exist with such a model for emplacement of the debris fans around Mauna Loa's caldera, because the summit of the volcano is thought to be too porous to maintain a water table. Alternative sources of explosive propellant may include magmatic volatiles, snowpack, or permafrost.

There have been no observations of explosive activity in the historical record at Mauna Loa, and the only record of prehistoric explosive activity on Mauna Loa exists in four dispersal lobes of explosive debris near the summit caldera, Moku`aweoweo (Figure 5.2). These areas of explosive debris were recognized and initially mapped as phreatic explosive ejecta by Macdonald (1971). Previous to this study, the timing of the explosive events that dispersed these ejecta was constrained by the known respective ages of the youngest underlying lava flows. The timing of the actual events that distributed the ejecta in these four areas is difficult to date with ^{14}C because the deposits do not extend downslope to vegetated areas. The use of cosmogenic nuclides, specifically ^{36}Cl in this case, allows us to use exposure-dating techniques to constrain the explosive events. Otherwise these explosive events would normally go undated by conventional radiocarbon techniques.

Prior to historical records the chronological record is based almost entirely on radiocarbon dates (Lipman, 1980b; Holcomb et al., 1986; Lockwood and Lipman, 1987; Lockwood, 1995; Trusdell and Lockwood 2006, 2009). USGS scientists have recovered more than 400 samples of charcoal baked in soils beneath advancing lava flows (Lockwood, 1995). Mauna Loa is the most thoroughly dated volcano on Earth because of the recovery of these charcoal samples.

The surface of Mauna Loa volcano has been extensively mapped, yet only ~35% of the mapped lava flows are either of a known historic age, or have been dated with radiocarbon techniques (Trusdell; per comm. 2011; Trusdell and Lockwood, 2006, 2009). There are unavoidable problems that make it impossible to completely date all Mauna Loa flows: (i) Charcoal forms beneath lava flows under restricted conditions of temperature and oxygen availability (Lockwood and Lipman, 1980). These conditions are commonly met where fast

159
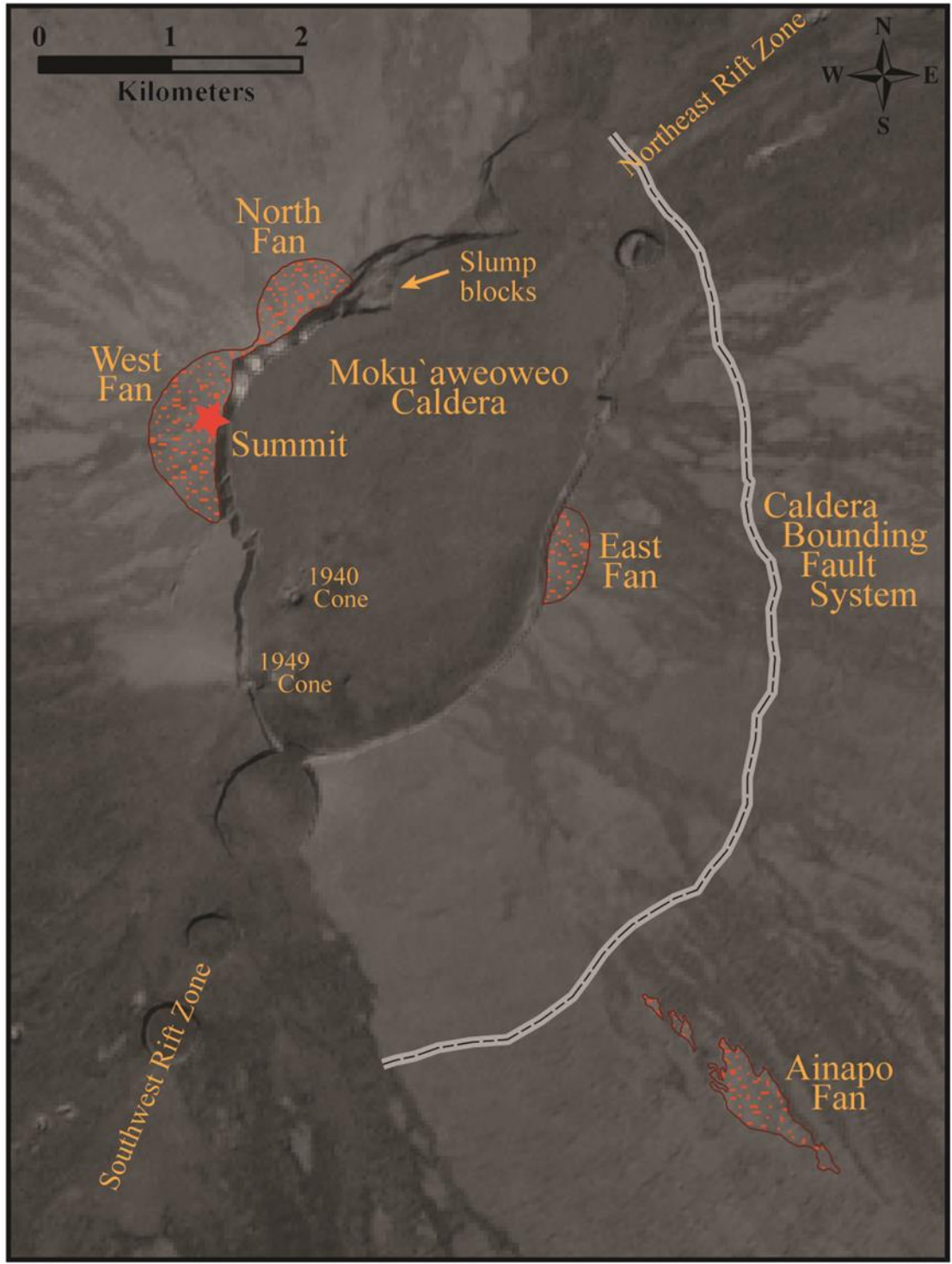
Figure 5.2. Image of the summit area of Mauna Loa.

The location of the four explosive debris fans relative to Moku`aweoweo Caldera and the summit is illustrated. Other prominent features of the summit area are labeled. (data source: USGS)

moving pahoehoe flows overrun forests growing on mature, fine-textured soils, but less so beneath a`a flows and pyroclastic deposits (Lockwood and Lipman, 1980). Even beneath pahoehoe, sites favorable to charcoal formation are not always accessible and/or present. (ii) Charcoal samples are also rarely found above the tree line, where there is insufficient soil to sustain plant growth to form recoverable charcoal. There are very few radiocarbon dates above 2548 m elevation on the rainy (east) side of Mauna Loa, and few above 2950 m on the drier (west) side. Given the summit altitude of 4171 m, the surface above treeline represents ~20% of the volcano's subaerial area, and is also the area of most recent eruptive activity (Lipman, 1995). Prehistoric flows surrounding Moku`aweoweo, the summit caldera on Mauna Loa, represent the products of lava lake activity and long-lived eruptions at elevations high above the treeline. These lava flows would go undated if radiocarbon recovery and analysis were the only means to date the eruptive activity.

Until recently, the frequency Mauna Loa's eruptive activity has largely been assessed through radiocarbon dating, which leaves the significant portion of the volcano's surface above the treeline undated due to the lack of suitable material available for radiocarbon dating. For the lavas above the treeline, exposure dating of using the *in situ* production of cosmogenic nuclides provides the capacity to date lavas that are not possible to date using radiocarbon. And, given the relatively young age of surface lavas on Mauna Loa exposure dating has distinct advantages over radiocarbon. These advantages are: (i) The target flows are stable, with well-preserved surfaces and is perfectly suited for exposure dating. Problems of surface preservation that complicate exposure dating – erosion, burial by younger deposits and soil development – become more acute with age. These are unlikely to present problems for dating lavas less than a few thousand years old, above the treeline where soils form slowly. (ii) Exposure dating increases in sensitivity

with increasing altitude. Nuclide production rates increase rapidly with altitude, leading to higher concentrations and allowing more precise isotopic measurements for a given exposure age. Thus the technique is most sensitive at high elevation where lack of vegetation precludes radiocarbon dating. (iii) It has been noted that contamination by meteoric cosmogenic nuclides (produced in the atmosphere), anthropogenic ^{36}Cl, and nuclide concentrations inherited from magma are potential problems for dating very young lavas. Our results from very young lavas show that the latter is not a problem at Mauna Loa. Anthropogenic and meteoric ^{36}Cl which cannot be easily removed by leaching are a source of scatter in our data, however (see below). (iv) Cosmogenic nuclide production rates are modulated by the same solar and geomagnetic effects that modulate ^{14}C production. However, production rate variations are integrated during nuclide build-up; smoothing and averaging the fluctuations. Moreover, the paleomagnetic data records required to hindcast production rates (e.g., Dunai, 2001; Gosse and Phillips, 2001; Desilets and Zreda, 2003) are better known for the past few millennia than for earlier periods of time given measurements on archeological materials such as pottery and hearthstones (McElhinny and Senanayake, 1982).

Dating young, prehistoric lavas is best done by radiocarbon, and exposure dating of cosmogenic nuclides. Where charcoal is not available exposure dating using cosmogenic nuclides is the only robust technique to obtain reliable ages. Measuring relative concentrations of radiogenic nuclides ^{36}Cl and ^{3}He are the established means for obtaining these ages in basaltic volcanic systems. In dating aphanitic basalts we are left to using ^{36}Cl dating techniques to obtain exposure ages. For porphyritic rocks ^{3}He exposure dating has been demonstrated to produce viable ages good for pyroxene and olivine bearing rocks, while ^{36}Cl is viable for feldspar porphyritic samples. This work demonstrated that it is possible to obtain viable ^{36}Cl exposure ages of samples as young as 150 BP in the explosive clasts of the east debris fan.

Given these advantages of cosmogenic nuclide exposure dating, the major obstacle to exposure dating young Mauna Loa lavas is analytical sensitivity. Very few studies have attempted to date lavas, or other geomorphic features, younger than a few thousand years. To do so with cosmogenic ^{36}Cl requires sensitive accelerator mass spectrometry (AMS), reliable separation of isobaric ^{36}S and other interferences, and careful control of laboratory blanks.

This paper reports ^{36}Cl cosmogenic isotope measurements of samples collected from four debris fans near the summit of Mauna Loa volcano. Exposure dating of these debris fans is designed to determine; 1) to establish the dates of the explosive events that dispersed the ejecta, 2) to introduce possible recurrence intervals for explosive events and 3) demonstrate the capacity to date young, prehistoric lavas.

5.2   GEOLOGIC SETTING

5.2.1   Mauna Loa

The Island of Hawai`i comprises five volcanoes of which Mauna Loa is the largest. Lava flows from Mauna Loa account for 50% of the Island's area (Trusdell, 1995; Trusdell, 2012). Since its inception less than 1 Ma B.P., Mauna Loa has grown to an estimated volume of 80,000 km^3, and is well into its tholeiitic shield building stage (Lipman, 1995). Eruptive activity on Mauna Loa during the shield building stage is dominated by initial Hawaiian-type fire fountaining along the trend of the NE and SW rift zones from fissures. As the eruption progresses eruptive activity is focused into a single vent or a set of vents where copious amounts of lava emanate and feed advancing lava flows.

Though among one of Earth's most active volcanoes, Mauna Loa does not erupt as frequently as Kilauea Volcano, also in the tholeiitic shield building stage, where lava accumulation rates are greater (Lipman, 1995). Yet lava effusion rates at Mauna Loa tend to be much greater than at Kilauea. During the three-week, 1984 eruption, for example, initial effusion rates were determined to be $1\text{x}10^6 \, m^3 \, hr^{-1}$ At this effusion rate, the volume of lava erupted in 20 minutes on Mauna Loa is equivalent to a full days' worth of lava erupted at Kilauea.

While Looking back on Mauna Loa's geologic record through the Holocene Lockwood (1995) recognized a cyclical nature in eruptive activity. Eruptive activity alternated between the rift zones and the summit. Summit activity is characterized by either lava lake or fissure activity feeding flows that may exit the caldera and cascade downslope. After cessation of summit activity, up until 1950, eruptive activity was then followed flank eruptions along either the SW and NE rift zones within 12 to 24 months (Lockwood, 1990). Trusdell (2011), however, has proposed that eruptive activity at Mauna Loa is inversely correlated to eruptive activity at Kilauea.

The summit caldera, Moku`aweoweo, is estimated to have formed between 600 to 1000 Y.B.P. when the volcano's summit collapsed; possibly into the evacuated magma chamber beneath the summit (Lockwood, 1995). Subsequent eruptions began filling the roughly 2.8 x 4.6 km Moku`aweoweo and the collapse pits at either end of the caldera (Lockwood, 1995). At present the summit of the volcano lies along the NE wall of Moku`aweoweo and is 183 m above the caldera floor, which is paved with historical flows (Figure 5.2). In 1841 the caldera floor was estimated at 275 m below the summit (Barnard, 1995).

The caldera walls tend to be near vertical and in places is mantled by scree and talus aprons at the base. A prominent slump feature 3.5 km north of the 1940 cone and 1.2 km

northeast of the summit comprises a set of faulted blocks that extend out 400 m from the caldera wall. Several pieces of explosive ejecta have been found on these slump blocks, which lie near an area of explosive debris.

5.2.2   The explosive ejecta clasts

The explosive ejecta in the dispersal lobes vary in vesicularity and crystalline texture. The variance in the explosive ejecta rock textures indicates the clasts were derived from different strata within the volcanic edifice and thus provide evidence of the nature of the explosive events. The clasts found in the east, west, northwest and southeast (Ainapo) fans are classified based on the vesicularity, crystalline nature, and whether the clasts are juvenile or lithic. The clasts are grouped into four categories, and the categories are labeled type I through type IV.

5.2.2.1 Type I clasts

Type I clasts are dense to poorly vesicular and aphanitic to porphyritic. These clasts vary from mildly altered to highly-altered. Mildly altered clasts are angular, dark gray to grey-green and vary in size from coarse lapilli to 2 m boulders (Figure 5.3a). Mildly altered type I clasts are also aphanitic to mildly porphyritic with microphenocrysts of either plagioclase, or olivine. These clasts are typically dense but 1 to 3 cm wide bands of millimeter scale vesicles are not uncommon.

Well altered clasts are commonly sub-angular to rounded with low sphericity tend to be less than 30 cm in their long axis. Rinds of these clasts are oxidized red to mustard yellow in color and interiors of these clasts are brown to red-brown. These well altered clasts, like the mildly altered type I clasts, are aphanitic to mildly porphyritic.

Given their dense nature and the presence of bands of coarse vesicles, the type I clasts are interpreted as fragmented lithic blocks from intra-caldera ponded lavas. Coarsely vesicular bands, dark grey in color, found in these clasts have been interpreted as segregation veins common to lavas solidified in lava lakes at Kilauea (Helz et al., 1989; Swanson et al., 2012b).

5.2.2.2 Type II clasts:

Type II clasts are defined by their coarse-grained, macrocrystalline texture. The macrocrystalline Type II clasts are gabbros, and the great majority of these clasts are olivine bearing gabbros. The olivine gabbro clasts are 5 to 50 cm along their long axis, sub-angular to sub-rounded and have brown weathering rinds. Exposed fresh surfaces display a medium grained, roughly equigranular texture of olivine, pyroxene and plagioclase crystals (Figure 5.3b). The non-olivine bearing gabbro clasts tend to be angular, no larger than 15 cm long and dark gray on weathered surfaces. Fresh surfaces display a subophitic texture of 1-6 mm lathes of plagioclase and prismatic to tabular pyroxene. These gabbro and olivine gabbro clasts originated from deep seeded (~1000 m) solidification zones of lava lakes within the summit area (McCarter et al., 2006).
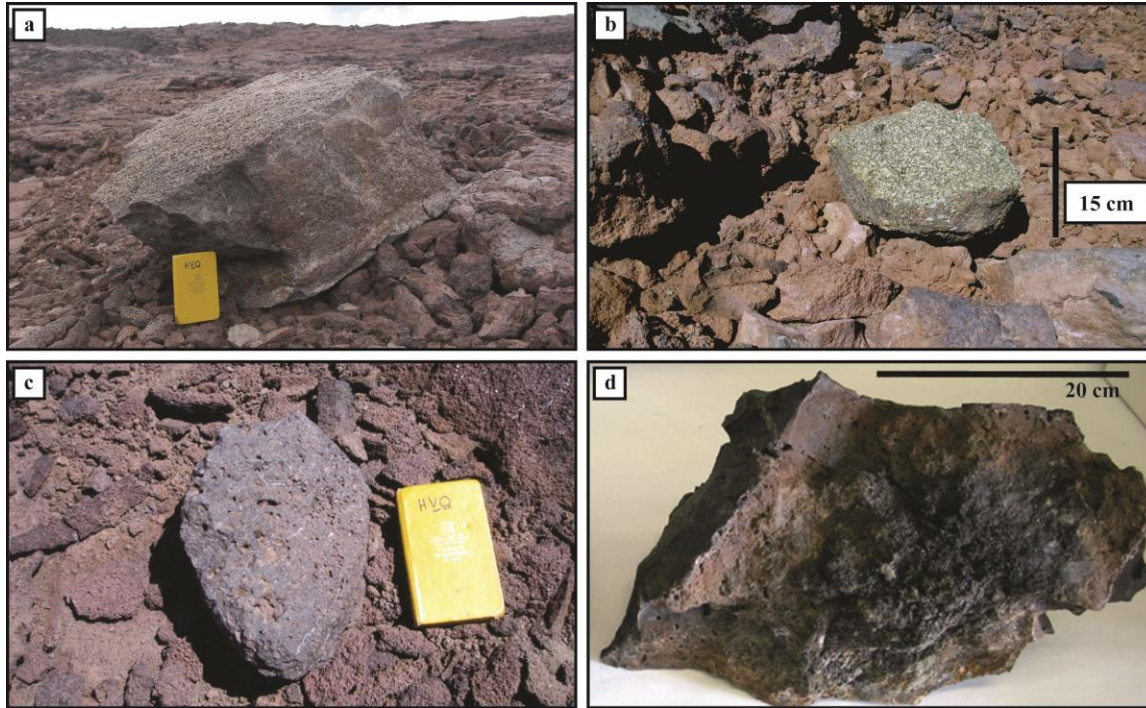
Figure 5.3. Images of examples of the four classes of explosive ejecta.

(a) An image of a large, dense type I explosive ejecta clast lying atop pahoehoe substrate. The book is 19 cm tall. (b) An image of an equigranular olivine gabbro type II explosive ejecta clast lying atop an a`a lava substrate. (c) An image of a vesicular, plagioclase porphyritic type III explosive ejecta clast atop regolith in a local topographic low on pahoehoe lava substrate. (d) An image of a fractured juvenile type IV explosive ejecta clast with a spongy vesicular core and glassy crust with a jigsaw fracture pattern.

5.2.2.3 Type III clasts:

Type III clasts are defined by their vesicularity (Figure 5.3c). These clasts are sub-round to sub-angular lapilli sized fragments to 25cm blocks that contain 15 to 50% vesicles. Type III clasts vary from not altered to highly altered. Non-altered clasts are dark gray to black while altered clasts to an oxidized red. Clasts are aphanitic to porphyritic with 2 to 6 mm phenocrysts of olivine or plagioclase.

Given their vesicularity Type III clasts are interpreted as lithic fragments of archetypal effusive lava flows. Some regions of the source lava flows were subject to post emplacement

hydrothermal alteration. This spatially variant alteration occurred prior to the explosive events that strewn the type III clasts over the substrate underlying the ejecta fans.

5.2.2.4 Type IV clasts:

Type IV clasts are defined as juvenile as opposed to lithic type I, II and III clasts. Though rare, these clasts are distinctive in their black to dark gray, dense, "jigsaw" fractured surface texture (Figure 5.3d). The type IV clasts are, angular and 8 to 35cm in length. When exposed, clast interiors display a gradient of increasing vesicularity towards a microcrystalline, spongy center of > 60% vesicles. The juvenile clasts are mildly porphyritic with up to 2 mm plagioclase phenocrysts. Given their vitric jigsaw surface texture and spongy core, the type IV clasts are interpreted as basaltic breadcrust bombs that represent juvenile ejecta strewn about during the explosive events.

5.2.3   The explosive debris fans

The discovery of four dispersal debris fans of explosive ejecta in the summit area indicates there is an explosive component to Mauna Loa's eruptive history beyond Hawaiian-type fountaining. We were able to assign ages to three of the four explosive eruptions responsible for the deposition of the debris fans. The four areas of explosive ejecta were first mapped by Macdonald (1971). The fans are named for their relative positions to the center of the caldera. The northwest, west and east debris deposits terminate at the walls of the caldera. The fourth area, referred to as the Ainapo fan, lies on the Ainapo Trail 1.2 km down slope of the caldera bounding fault system (Fig 5.2). The four dispersal lobes of explosive debris are referred to as fans because the ejecta dispersal pattern of the three areas truncated by the cliffs of

Moku`aweoweo were first mapped as semicircular or semi-elliptical areas, which resemble fan shapes. The Ainapo fan does not share this dispersal lobe shape because most of the deposit is buried by summit flows but is colloquially referred to as a fan by default.

The explosive ejecta lie atop substrates of a`a and pahoehoe lava flows. The substrate lava flows under the northwest west and east fans are truncated by the caldera walls. These flows propagated downslope away from source vents that existed within the general area the caldera now occupies. The difference in surface texture between a`a and pahoehoe substrate flows affected the distribution of the explosive debris within the ejecta dispersal lobes. Only clasts larger than the interstices between surficial clinker are visible on a'a substrates. Smaller clasts tend to fall or settle through the surficial a`a clinker. Clast populations on a'a substrates, therefore, are lower than those expected on pahoehoe substrates of similar age in the same vicinity. Clast counts on pahoehoe substrates also vary. On hard, locally elevated pahoehoe substrate the clast counts are significantly lower than those pahoehoe surfaces that lie between local topographic highs. This population count variance could be the result of clasts reflecting or bouncing off high substrates and eventually coming to rest in topographic lows. Commonly, clasts fractured upon impact on hard pahoehoe substrate thus increasing the clast count within the ejecta dispersal lobes. There also exists evidence of larger, dense clasts fracturing upon impact with a`a substrate (Figure 5.4a).

Other factors that could affect clast distribution include: age (long exposure), number of explosive events, vent geometry and location, and meteoric conditions (high winds (> 100 mph) and high rainfall) to name a few.

5.2.3.1 The northwest and west debris fans

Mapped by McDonald (1971) as two dispersal lobes overlying a`a and pahoehoe substrate, the northwest and west debris fans are truncated by the west wall of Moku`aweoweo. The southern extent of the northwest fan and the northern region of the west fan overlap one another (Fig 5.2). The northwest debris fan extends ~ 400 m from the caldera wall and has an area of approximately 0.28 km^2. The west fan extends roughly 550 m from the caldera wall and covers an area of approximately 0.55 km^2.

In the northwest debris fan the dense, angular type I clasts are the predominant lithic ejecta. Over 90% of the distal clasts are type I clasts (Figure 5.4a). The largest clasts are also type I blocks up to 1.5 m in diameter. Vesicular type III clasts are the second most abundant close to the caldera wall but their clast population density dissipates to zero at half the distance to the distal boundary of the debris fan extent. The type II clasts gabbros are the third most abundant clast lithology in the northwest debris fan, though they are not present in the northern half of the northwest debris fan. Rare, juvenile type III clasts are found in the proximal to medial areas of the northwest debris fan.

Clast population densities are approximately 15 per m^2 at the caldera wall and diminish to 0.2 per m^2 at the distal reaches of the northwest debris fan. Adjacent to the northern section of the northwest debris fan there are large slump blocks that lie below and against the caldera wall (Fig 5.2). There are type I lithic blocks on the horizontal steps of the slump blocks that are strewn about at a population density less than 0.2 clasts per m^2.

The west debris fan lies to the southwest of the northwest debris fan (Figure 5.4b). The summit of Mauna Loa lies at the edge of the caldera approximately 200 m from the north extent of the fan. The southern extent of the west debris fan is obscured by a veneer of tephra deposited
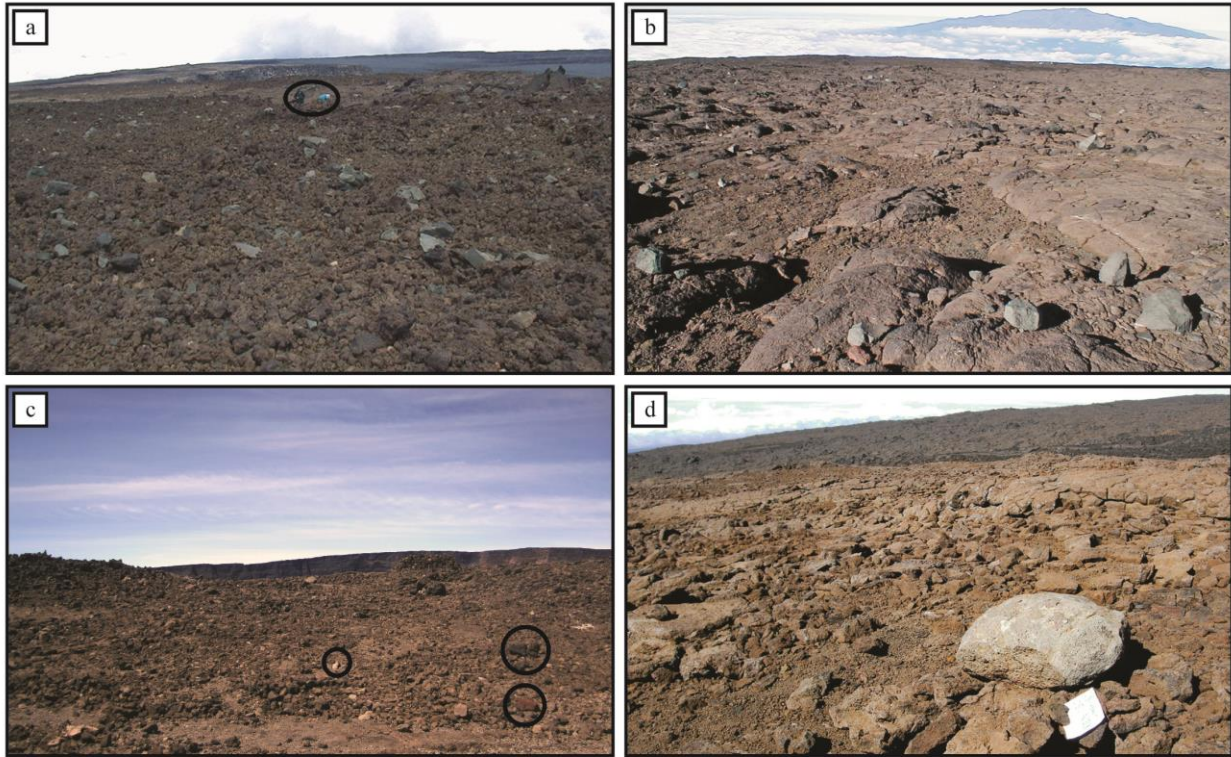
Figure 5.4. Images of the explosive debris fans.

(a) An image looking ENE over an a`a lava flow with blocks of Type I lying atop the surface clinker in the north debris fan. Behind the two people in the middle back of the image is Moku`aweoweo Caldera. **(b)** An image looking NNE over an area of the west fan populated by a majority of dense, altered green type I ejecta. These ejecta lie atop a pahoehoe substrate. Mauna Kea is in the background. **(c)** An image looking northwest over the debris in the east fan. A few clasts are circled as example clasts. **(d)** An image looking southwest at a rounded, weathered ejecta block lying atop an older pahoehoe flow of the Ainapo debris fan. The younger lava flows that form the kipuka and define the shape of the Ainapo debris fan are in the background. No explosive debris is found on the surrounding younger lava flows.

during the 1949 eruption. Much like the northwest fan, the west debris fan is populated primarily by type I clasts. Type II clasts are the second most populous clast type and are found in all but the distal regions of the debris fan. Vesicular type III clasts are, like the northwest debris fan, are common in the regions proximal and medial to the caldera wall but are absent in the distal regions of the fan. Juvenile type IV clasts are rare but found in the northern sections of the debris fan. Type IV clasts are fewer in number versus the northwest fan but tend to be larger (30 cm).

Compared to the northwest debris fan ejecta clast population densities are lower in the west debris fan. Distally, type I clasts lay about at population densities less than 0.2 clasts per m^2, which is comparable to distal clast population densities in northwest debris fan. The population counts, however, in the proximal and medial regions with respect to the caldera wall are lower than those found in the northwest debris fan. Clast population densities do not exceed 10 clasts per m^2 in the west debris fan.

5.2.3.2 The East debris fan

The east debris fan is a 0.18 km^2 hemi-elliptical dispersal lobe of ejecta that is truncated by the east wall of the caldera (Figure 5.2). The debris fan extends approximately 750 m along the eastern caldera wall and, at its widest point the debris fan extends approximately 300 m from the caldera wall. The summit cabin, which is roughly half the distance along the eastern wall of Moku`aweoweo Caldera, lies within the eastern debris fan.

The distribution of explosive ejecta in the east debris fan, which lie atop a`a and pahoehoe lava flows, has been mapped (Trusdell and Swannell, 2003). The ejecta found in the debris fan comprise type I and type III clasts (Figure 5.4c). No macrocrystalline type II or juvenile type IV clasts are found within the east debris fan. Type I and III clast density, however, is greater than the other debris fans with values reaching 50 clasts per m^2 less than 200 m from

the caldera wall. Average clast sizes for areas with high clast density averaged between 12 and 14 cm along the long axis (Trusdell and Swannell, 2003).

5.2.3.3 The Ainapo debris fan

This debris fan lies approximately 5 km southwest of the summit and 500 m downslope from the caldera bounding fault system (Figure 5.2). The clasts lie on an older substrate that is partially buried by younger caldera flows that create the irregular shape of the Ainapo debris fan. No ejecta are found on the younger lava flows surrounding the older substrate. The resultant area on which the explosive ejecta lie is 0.3 m^2 and represents only a fraction of the original dispersal lobe.

Type I and Type III clasts are found in the Ainapo debris fan. These clasts are well weathered compared to similar clasts in the three debris fans around the caldera (Figure 5.4d). The clasts vary from 50 cm to less than 10 cm in their long axis and are distributed about the fan area in on particular order. The clast population density is similar to the distal areas of the northwest and west debris fans where clast densities are lower than 0.2 clasts per m^2.

5.3   METHODS

5.3.1   Sample collection

Samples of the explosive ejecta were collected from the four debris fans as well as samples of a few of the substrate lava flows for ^{36}Cl analysis. The details of the sample sites are given in Table 5.1. Explosive debris clasts were sampled from local topographic highs to minimize shielding effects of nearby topographic highs. Clast samples on horizontal surfaces or shallowly dipping substrate were chosen and the substrate slope and the sample horizon profile were recorded. Samples greater than 500 g and 10 cm thick with intact surfaces or rinds were chosen. Samples were also collected if they appeared to have not been disturbed or moved from their post explosive deposition place of rest.

Intact, 0.5 to 1.5 kg, pieces pahoehoe lava flows from each of the four debris fans were sampled. The samples have are at least 10 cm thick. Like the sampled clasts of explosive ejecta, samples of the substrate were chosen for their intact surface rinds and low horizon obstruction. The coordinates and altitudes of each of the samples were also recorded.

5.3.2   Laboratory analyses and calculation:

Samples were crushed to a 125-250 μm grain size. Initial analyses were made on samples leached in de-ionized water to avoid reaction of fresh, glassy basalt during leaching. Historic basalts leached with water were found to contain excess ^{36}Cl resulting in old apparent ages. The

174

Table 5.1. Exposure dating sample locations (North Aamerican Datum 1983)

Sample	Rock Type	Latitude (deg. N)	Longitude (deg. W)	Altitude (m)
Ainapo Fan				
Ejecta				
08-HW-051-APEX_NXHN	Type III	19.430	155.569	3784
08-HW-052-APEX-NXHN	Type III	19.430	155.569	3740
Underlying substrate				
08-HW-053-APSS-NXHN	Pahoehoe	19.430	155.569	3755
08-HW-054-APSS-NXHN	Pahoehoe	19.430	155.568	3770
East Fan				
Ejecta				
08-HW-057-CABEX	Type III	19.466	155.580	4038
08-HW-058-CABEX	Type III	19.466	155.580	4037
Underlying substrate				
MLE00-PHH-CAB	Pahoehoe	19.465	155.580	4035
08-HW-059-CABPH	Pahoehoe	19.466	155.580	4037
Adjacent flow				
08-HW-060-CABAA-NXHN	A`a flow	19.465	155.581	4039
08-HW-061-CABAA-NXHN	A`a flow	19.466	155.581	4040
West Fan				
Ejecta				
MLE00-E20	Type I	19.478	155.610	4148
MLE00-E22	Type II	19.476	155.610	4151
MLE00-E24	Type II	19.479	155.640	4142
Underlying substrate				
MLE00-E25	Pahoehoe	19.480	155.609	4145
Northwest Fan				
Ejecta				
MLE00-1E26	Type I	19.484	155.603	4136
L-02-500	Type II	1.0000	0.951	1.322

excess 36Cl is most likely fallout from nuclear testing in the 1960s. In an attempt to remove this without damage to reactive, fresh basalt glass, some samples were re-analyzed after leaching in a sequence of reagents: 0.05 M nitric acid, followed by 0.1M oxalic acid, 0.05M NaOH and 0.05M nitric acid, separated by repeated rinsing in de-ionized water. After leaching, the dried samples were split into aliquots for ^{36}Cl extraction, chloride measurement by isotope dilution, and bulk chemical analysis. Chlorine was extracted using standard methods (Stone et al., 1996, Stone, 2001), and analysed for ^{36}Cl using the 14UD pelletron accelerator at the Australian National University (Fifield and Morgenstern, 2009). Procedural blanks run in parallel with the samples had ^{36}Cl/Cl ratios $< 10^{-15}$ (*c.* 10^4 atoms ^{36}Cl), requiring blank corrections ≤5% for the youngest samples. Chloride concentrations were measured by isotope dilution with ^{37}Cl on 0.5–1 g aliquots of the crushed rock samples. Trace-element neutron producers (U, Th) and absorbers (B, Sm, Gd) were analyzed by ICP-MS.

Chlorine-36 production in the samples is dominated by spallation of Ca and neutron capture by ^{35}Cl. Spallation of K, Fe and Ti make only minor contributions, and due to the high altitude of the sites, muon reactions with Ca are also relatively unimportant. Exposure age calculations are therefore based principally on the calibrations of Stone and Ballantyne (2006) and Phillips et al. (2001) for the two main reactions. In addition, the ^{36}Cl production model used in the calculations incorporates the K spallation rate of Evans et al. (1997), muon induced reactions on Ca and K (Stone et al., 1998; Fifield et al., 2002) and minor contributions to ^{36}Cl production from Ti and Fe (Masarik and Reedy, 1995; Stone, unpublished data). Production rates are scaled from their respective calibration sites using the scaling model of Lal (1991). To account for inherited ^{36}Cl in lavas at the time of eruption we used an initial ^{36}Cl/Cl ratio of (4 ±

3)x10^{-16}, measured on a fresh sample of Pu'u O'o lava. Uncertainties in the exposure ages account for both analytical errors and production rates uncertainties.

5.4   RESULTS

Analytical results and exposure ages are shown on Table 5.2. Results for substrate and explosive debris exposure ages for the three debris fans truncated by the walls of Moku`aweoweo caldera are robust and thus represent valid exposure ages given their low analytical errors. However, the exposure ages derived for the substrate and explosive clasts of the Ainapo fan are problematic. The resultant exposure ages for the explosive ejecta and substrate in the Ainapo fan are much older, but we have not been able to obtain consistent results from these samples The resultant ages most likely do not represent either the age of the substrate within the kipuka or the timing of the explosive event.

Analysis of the explosive clasts and substrate samples produced low ^{36}Cl concentration levels and ^{36}Cl/^{35}Cl concentrations. The values, however, produced comparative ages for substrates within the northwest, west and east debris fans that are within 1σ uncertainty limits of independently found ages and blank corrections were less than 2.1 ± 1.4%.

5.4.1   The Age of the northwest and west fans and substrate

Two distinct explosive sample ages were extracted from the data from these debris fans. Sample MLE00-E26 is an explosive debris sample collected from the northwest fan. The

measured cosmogenic ^{36}Cl concentration for the sample is 27415±2530 atoms and the resultant exposure age is 519±53 yr. B.P.

Samples MLE00-E20, -E22, -E24 are explosive clasts from the west fan and have measured cosmogenic ^{36}Cl concentrations between 36927±3973 and 24780±3002 atoms. Exposure ages for these samples are 858±95, 946±101, and 788±98 yr. B.P., respectively. Sample MLE00-E25 has a ^{36}Cl concentration of 55657±6151 which results in an exposure age of 1019±117 yr. B.P. The exposure age of the substrate sample MLE00-E25 is within error of calculated ages of the underlying lava flows determined by independently obtained radiocarbon dates. The ^{14}C ages of 1090 – 1200 ^{14}C yr B.P. (980 – 1080 cal. yr B.P.) on the substrate flows were produced from charcoal beneath the same flows at lower altitude (Frank Trusdell, *pers. comm.*).

5.4.2   The age of the east debris fan and substrate

The analysis of two samples of explosive ejecta in the east debris fan, samples, 08-HW-057 and 08-HW-058, resulted in exposure ages of 219±22 and 154±22 yr. B.P. given their cosmogenic ^{36}Cl concentrations of 9984±985 and 7404±1015 atoms, respectively. A`a substrate samples 08-HW-060 and 08-HW-061 yield $^{36}$Cl concentrations of 51249±3714 and 54793±4030 atoms and the two pahoehoe substrate samples, MLE00-PHH-CAB and 08-HW-059,   have $^{36}$Cl concentrations of 53045±3920 and 53694±2775 atoms. Exposure ages for the a`a substrate, represented by samples 08-HW-060 and 08-HW-061, are 979±75 and 1010±80 yr. B.P., respectively. Exposure ages for pahoehoe substrate samples MLE00-PHH-CAB and 08-HW-059 are 979±83 and 959±58 yr. B.P., respectively. These substrate samples are statistically similar to independently reported values derived from radiocarbon dating.

5.4.3 The age of the Ainapo debris fan and substrate

Given a significant variance between the measured ^{36}Cl concentrations in the explosive debris and substrate samples, the resultant age calculations produced suspect values. ^{36}Cl concentrations of ejecta clast samples 08-HW-051 and 08-HW-52 are 1099149±52523 and 444380±22910 atoms and result in exposure ages are 28078±1618 and 10381±617 yr. B.P., respectively. The calculated exposure ages for substrate samples 08-HW-053 and 08-HW-054 are 9385±579 and 10319±655 yr. B.P., given ^{36}Cl concentrations or 415894±22692 and 416747±23223 atoms, respectively. The explosive deposits within Ainapo debris fan at 3750 m are much older than the explosive debris from the other fans, but we have not been able to obtain consistent results from these samples.

Table 5.2. Exposure dating results

Sample	Scaling factor (spallation)[1]	Scaling factor (muons)[1]	Horizon correction	Thickness correction (spallation)	Thickness correction (thermal n)	Thickness correction (epithermal n)	$[^{36}Cl]_c$ (x10^4 g^{-1})[2]	Production rate (atom g^{-1} yr^{-1})	Exposure age (kyr)
Ainapo Fan									
Ejecta									
08-HW-051-APEX_NXHN	8.018	3.172	0.9989	0.981	1.114	1.119	109.9 ± 5.3	40.4 ± 1.2	28.1 ± 1.6
08-HW-052-APEX-NXHN	8.018	3.172	0.9989	0.970	1.193	1.163	44.4 ± 2.3	43.3 ± 1.2	10.4 ± 0.6
Underlying substrate									
08-HW-053-APSS-NXHN	8.034	3.176	0.9993	0.960	1.228	1.206	41.6 ± 2.3	44.8 ± 1.2	9.4 ± 0.6
08-HW-054-APSS-NXHN	8.034	3.176	0.9993	0.977	1.149	1.132	41.7 ± 2.3	40.9 ± 1.2	10.3 ± 0.7
East Fan									
Ejecta									
08-HW-057-CABEX	9.264	3.499	1.0000	0.943	1.300	1.282	1.00 ± 0.10	45.6 ± 1.2	0.22 ± 0.02
08-HW-058-CABEX	9.260	3.498	1.0000	0.932	1.355	1.313	0.74 ± 0.10	48.0 ± 1.3	0.15 ± 0.02
Underlying substrate									
MLE00-PHH-CAB	9.251	3.496	1.0000	0.975	1.181	1.121	5.30 ± 0.39	54.3 ± 2.2	0.98 ± 0.08
08-HW-059-CABPH	9.260	3.498	1.0000	0.973	1.159	1.164	5.37 ± 0.28	56.0 ± 1.7	0.96 ± 0.06
Adjacent flow									
08-HW-060-CABAA-NXHN	9.269	3.500	1.0000	0.967	1.182	1.190	5.12 ± 0.37	52.4 ± 1.4	0.98 ± 0.08
08-HW-061-CABAA-NXHN	9.273	3.501	1.0000	0.963	1.210	1.209	5.48 ± 0.40	54.3 ± 1.6	1.01 ± 0.08
West Fan									
Ejecta									
MLE00-E20	9.769	3.629	1.0000	0.935	1.404	1.218	3.69 ± 0.40	43.1 ± 1.2	0.86 ± 0.10
MLE00-E22	9.782	3.632	1.0000	0.943	1.353	1.234	3.78 ± 0.39	40.0 ± 1.1	0.95 ± 0.10
MLE00-E24	9.741	3.622	1.0000	0.951	1.295	1.243	2.48 ± 0.30	31.5 ± 0.9	0.79 ± 0.10
Underlying substrate									
MLE00-E25	9.755	3.625	1.0000	0.957	1.331	1.138	5.57 ± 0.62	54.7 ± 1.7	1.02 ± 0.12
Northwest Fan									
Ejecta									
MLE00-1E26	9.714	3.615	1.0000	0.951	1.335	1.194	2.74 ± 0.25	52.8 ± 2.2	0.52 ± 0.05

1. Lal (1991), Stone (2000).   2. Cosmogenic 36Cl; corrections for radiogenic 36Cl < 1%

5.5   DISCUSSION

5.5.1   Debris fan ages

Viable exposure ages have been obtained for the three explosive debris fans truncated by Moku`aweoweo Caldera. The exposure ages for the substrate below these debris fans correlate with independently obtained radiocarbon dates for these lavas. The exposure ages for Ainapo fan explosive debris and substrate are suspect and may not be representative of the true timing of the explosive event(s) or the age of the underlying pahoehoe lavas.

5.5.1.1 The Northwest and West debris fans

The age of a pahoehoe lava flow below the west debris fan is 1019±117 yr. B.P. according the ^{36}Cl exposure age. This result is consistent with ages for the substrate lava flows with ^{14}C ages of 1090 – 1200 C yr. B.P. (980 – 1080 cal. Yr. B.P.) from recovered charcoal beneath the same flows at lower elevations (Trusdell and Lockwood, 2009). The cosmogenic age determinations and the independent lava flow substrate ages based on geologic mapping are stratigraphically consistent with the younger exposure ages obtained for the debris clasts in the northwest and west fan. The results for the west fan explosive ejecta ages are between 946±101 and 788±98 yr. BP, and for the northwest fan the exposure age is 519±53 yr. B.P. These ages represent the age of the explosive events.

Up until this point the west and northwest fans were treated as independent explosive events of the same eruption. Based on their cosmogenic ages, these two debris fans have ages that do not lie within analytical uncertainty of each other. These two debris fans therefore represent two exclusive explosive events. Further, the clast distribution implies that at a minimum 2, or more explosions resulted in the dispersal of the ejecta the northwest and west debris fans. Therefore, at least two of the explosions were from two temporally exclusive eruptive events approximately 850 and 519 yr. B.P. Further mapping of the spatial distribution of the different clast types will provide insight to the number of explosive events and possibly the temporal difference between the explosive events.

The northwest and west debris fans were of 2 temporally exclusive explosive eruptions because; 1) the dates of clasts are not within error of each other, 2) all clast types are not evenly distributed in both fans, 3) clast population densities and are markedly different in the two fans, and 4) distribution of the clast types overlaps the traces of the two debris fans. Though the occurrence of one or two of these points of evidence may not simply indicate explosive events from a single eruption, the presence of these four points suggests the explosive events occurred as exclusive events and ejected clasts were most likely derived from more than one a spatially confined lithic source. Preliminary ballistic ejecta modeling and the distribution of the lithic debris within two fans suggest there were two distinct sources that produced the two or more dispersal lobes found in the northwest and west debris fans.

5.5.1.2 The east fan

There are exposure dates for two substrate lava flows; one an a`a flow and the other a pahoehoe flow. The dates are 979 and 1010 yr. B.P. for the a`a flow and 979 and 959 yr. B.P. for the pahoehoe flows. These ages are not in agreement with field observations where the a`a flow is

stratigraphically above, thus younger than, the pahoehoe substrate. The reported ages are within error of each other and therefore no stratigraphic inference should be drawn from them. The dates obtained for the ejecta clasts are 219 and 154 yr. B.P. are younger than the substrate ages and thus do not violate the stratigraphic order.

The explosive ejecta within the east debris fan are aphanitic to porphyritic, dense to vesicular Type I and III clasts that are derived from ponded lavas and lava flows. Source rocks for the east debris fan clasts do not include the Type II gabbros and gabbronorites found in the northwest and west debris fan.

5.5.1.3 The Ainapo fan

The substrate ages of the Ainapo fan were estimated to be approximately 4500 to 5500 years old given the relative extent of their surface weathering to other flows (Lipman, 1980a; Lockwood et al., 1988). The age of younger lavas forming the kipuka around the older substrate is estimated to be ^{14}C ages of 1360 C yr. B.P. (Trusdell and Lockwood, 2009). The rough event time window of the explosive event that deposited the clasts of the Ainapo debris fan is between 5000 and 1360 yr. BP. The most reasonable exposure age for the explosive ejecta suggests the explosive event occurred 10317±655 yr. B.P., at least 5300 years earlier than expected. This exposure age value is obviously suspect, and, therefore, reliable exposure ages for the explosive debris in the Ainapo debris fan were not obtained. The substrate ages, however, are within error of each other and suggest the substrate may be older than original estimates for the pahoehoe flow.

5.5.2   Timing and Recurrence of explosive activity near summit

The discovery of four dispersal debris fans of explosive ejecta in the summit area indicates there is an explosive component to Mauna Loa's eruptive history beyond Hawaiian-type fountaining. Ages for three of the four explosive eruptions responsible for the deposition of the debris fans were obtained. Though it is clear the clasts of the Ainapo debris fan represent an event much older than the other two events, a statistically significant age cannot be assigned to this event though it can be bracketed by the substrate and surrounding lava that form the kipuka. It is possible, however, to assign accurate dates to the explosive events that were responsible for the creation of the northwest, west and the east fans.

The summit has erupted explosively at least 3 times over the last 900 years (Figure 5.5). The northwest and west debris fans do overlap but appear to be temporally distinguishable from one another. These two debris fans were the result of explosive eruptions that occurred approximately 800 and 520 years ago. The east debris fan was deposited by an eruption occurring approximately 200 years ago. The explosive eruption that deposited the debris in the Ainapo fan most likely occurred more than 1400 years ago, though this age is not well constrained.

Lockwood (1995) suggests there was a transition from summit centric eruptive activity to eruptive activity centered on the rift zones of Mauna Loa near the time of the explosive eruption represented by the northwest and west debris fans about 900 years ago. This transition to rift zone centric eruptive activity is thought to have coincided with the collapse of the summit are an and the formation of a summit caldera now recognized as Moku`aweoweo Caldera. The truncated flows that lie around the present caldera are presumed to be lavas that overflowed from summit lava lakes predating the summit collapse. Ages for these lava flows, including those
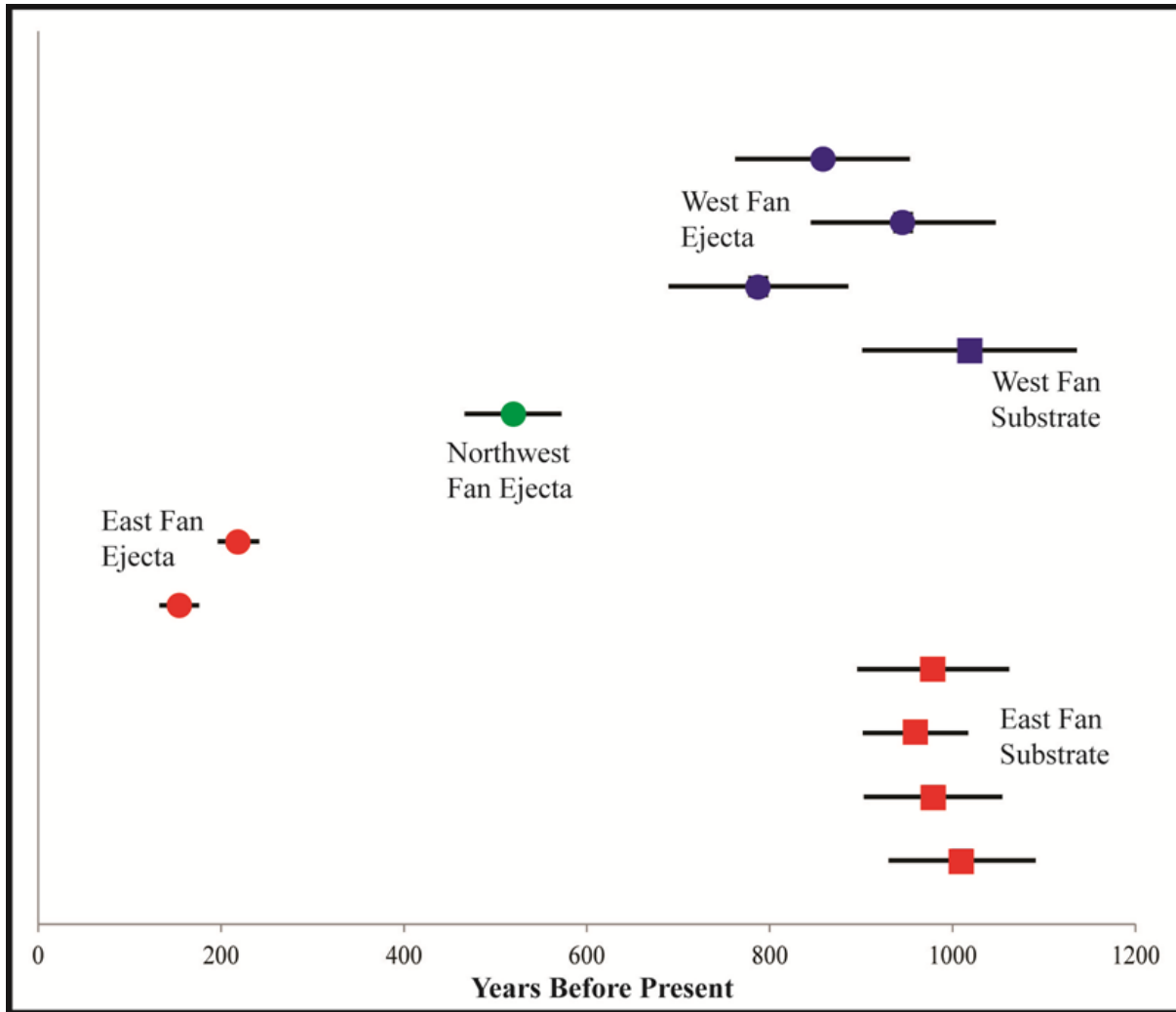
Figure 5.5. The exposure ages of explosive debris fans and substrate lavas.

reported here, indicate these lavas were emplaced between 1200 and 950 yrs. B.P. and thus constrain the upper age of caldera forming events. The timing of the caldera collapse event, however, is not well constrained but is thought to have occurred 750 to 900 years ago (Lockwood and Lipman, 1987).

The relative timing of the explosive activity and caldera formation is not well constrained, and it is unclear whether the explosive events occurred before or after formation of the summit caldera. Yet, the lack of sequential evidence does not necessarily mean that the

collapse occurred after the explosive events. However, based on geologic mapping, lava flows of ~1,000 yr B.P. flowed both eastward and westward, away from source vents that were active before the caldera-forming collapse events that formed the present caldera (Trusdell and Lockwood, 2009). There are no flows of a younger age on the northwest and southeast flanks outside of the caldera walls that originated from the caldera. Therefore, the most recent caldera forming episode occurred within 1,000 yr B.P. The east debris fan has an age of 220 yrs. B.P. Thus, the eastern explosive event occurred much later than the most recent episode of caldera formation. The northwest fan was deposited 520 yrs. B.P., which according to Lockwood and Lipman (1987), occurred after at least the initiation of caldera forming events. The deposition of the west fan at 850 yrs. B.P. may have coincided with collapse events that resulted in caldera formation (Lockwood and Lipman, 1987).

Though not found in the east fan the macrocrystalline type II clasts represent ejecta sourced from the bottom of a ponded lava lake(s) at least 500 m deep (McCarter et al., 2006). There are, however, type II rocks in the northwest and west fans. McCarter (2006) suggests the macrocrystalline type II clasts in the northwest and abundant in the west debris fan did form in pooled lava bodies that existed within a summit caldera. If these clasts were not exposed to cosmogenic rays until they were excised by explosive activity the exposure ages of the explosive clasts are valid, and the exposure ages would indicate the initial caldera collapse occurred before the explosive events 850 yrs. B.P, which is possibly older than the assumed age range of the caldera collapse.

5.5.3 Cosmogenic nuclide dating of young, prehistoric lavas

This work has shown that cosmogenic dating is a useful tool to date young prehistoric lavas. The substrate has been successfully dated and correlated with other analytically derived dates on these lavas. The problem of low ^{36}Cl production rates has been overcome by using sensitive mass spectrometer and superior sample preparation techniques. We have dated young lavas where ^{14}C is either not available since the lava flows do not extend into the forested or vegetation zone.

5.6   CONCLUSION

This work has established that Mauna Loa indeed has an explosive past with at least three explosive eruptions in the past 1000 years. Viable ages were obtained for three of the four explosive events that deposited ejecta in four debris fans in the summit area of Mauna Loa volcano that cannot be dated through radiocarbon dating or other common techniques. Exposure dating using cosmogenic ^{36}Cl nuclides proved effective in assigning dates to three of the four explosive events evidenced in the debris fans in the summit region. The three events represented by three debris fans of explosive ejecta truncated by the walls of Moku'aweoweo caldera all occurred within the last 1000 years. Samples analyzed from the ejecta within the much older Ainapo debris fan southwest of the caldera did not produce a reliable exposure age. Therefore, the age was not constrained any more than the estimates between 5000 and 1340 yrs. B.P. derived from the substrate and the younger surrounding lavas. Exposure dates derived from the three debris fans above the caldera walls indicate three explosive eruptions that occurred approximately 200, 520 and 850 yrs. B.P. Exposure ages for the substrate flows below the east

and west fans were emplaced before caldera forming events and constrain the age of these event to within 960 yrs. B.P. With an exposure age of ~850 yrs. B.P., the west debris fan may have been emplaced before any caldera collapse event and the deposition of the northwest and east debris fans most likely postdated initial caldera collapse events. This work has demonstrated the capacity of exposure dating using cosmogenic ^{36}Cl nuclides to assign robust dates to young (> 1 ka), low K basalts with precise analytical methods. If this capacity were not perfected through the work performed here these explosive events would remain undated.

6.0   CONCLUDING REMARKS

The goal of my PhD research has been to recognize basaltic lava flows in glaciovolcanic environments, describe how these lavas are emplaced in these unique glaciovolcanic environments and provide a robust manner in which to temporally constrain their emplacement. Subglacial lava flows may prove to be a better indicator of paleo-ice conditions than vent proximal deposits because vent proximal deposits are commonly subject to variability in cryostatic/hydrostatic pressures as near-vent meltwater levels are subject to fluctuation. Variances in the efficiency of the drainage system in removing meltwater from the ice cauldron surrounding the vent and the integrity of the ice cauldron itself tend to create a dynamic, ever-evolving eruptive environment at the source vent. Evidence of such a dynamic eruptive environment lies within the exposed volcaniclastic deposits in Tennena Cone. The distal sheet lavas and pillow lava ridges, however, indicate a dynamic subglacial system that is still dominated by the greatest variable, the thickness of the overlying ice.

Any investigation into glaciovolcanic terrain is greatly enhanced by the analysis of remotely sensed imagery. When attempting to identify specific lava flows, a classification scheme that successfully identifies lava flow types is of great utility. The classification scheme developed in this study was successful in differentiating glaciated lava flows from non-glaciated flows on the target volcanic terrain on Mauna Kea volcano. The classification scheme also proved moderately successful in differentiating ice-contact lava flows from subaerial lava flows

subjected to subsequent glaciation. While the classification scheme was of use on Mauna Kea, its utility was not directly transferrable to another volcanic terrain that exhibits evidence of recent glaciation, in this case the Snowshoe Lava Field of Mount Edziza. Though this classification proved not to be directly transferrable to another glaciovolcanic terrain, the outcome elucidated the variables to be addressed in the creation of a more robust classification scheme. An investigation into a remote volcanic terrain should begin with a perusal of the existing literature of the target terrain to 1) identify lava chemistry, 2) identify the source of flow surface textures and 3) if possible, identify a known lava flow as glaciated or as ice contact in the remotely sensed scene.

Though of not great utility in identifying glaciated and subglacial lava flows at Mount Edziza, the classification scheme did corroborate evidence of suspect lava flows within the Tennena volcanic center. The TVC preserves a unique record of an effusion dominated eruption of a basaltic lava flow field beneath thick ice. The lack of any subaerial lava suggests that the eruption occurred entirely in the presence of meltwater and ice. Coherent lavas emanating from Tennena Cone vents were either emplaced against ice of the cauldron walls or exploited an expanding subglacial meltwater drainage system delivering water to an existing CIS drainage system. Descriptions of the coherent lavas within the Tennena volcanic center offer accessible analogues for sheet flow and pillow lava emplacement in submarine environments.

Given the lavas of the TVC are too young to accurately date using Ar/Ar, and the lack of radiogenic carbon, we propose the use of cosmogenic chlorine-36 exposure dating techniques to constrain the age of the TVC eruption. We prepared two samples for analysis and are waiting for the results. This recommended dating technique was tested on relatively young, prehistoric explosive debris distributed in dispersal lobes around the summit caldera on Mauna Loa volcano,

Hawai`i. This work has demonstrated the capacity of exposure dating using cosmogenic ^{36}Cl nuclides to assign robust dates to young (> 1 ka), low K basalts with precise analytical methods. This work also established that Mauna Loa indeed has an explosive past with at least three explosive eruptions in the past 1000 years. If this capacity were not perfected through the work performed here these explosive events would remain undated.

BIBLIOGRAPHY

Abraham, A.-C., Francis, D. and Polvé, M., 2005. Origin of recent alkaline lavas by lithospheric thinning beneath the northern Canadian Cordillera. Canadian Journal of Earth Science, 42: 1073-1095.

Allen, C.C., 1979. Volcano-ice interactions on mars. Journal of Geophysical Research, 84: 8048-8059.

Allen, C.C., 1980. Icelandic subglacial volcanism - thermal and physical studies. Journal of Geology, 88(1): 108-117.

Allen, C.C., Jercinovic, M.J. and Allen, J.S.B., 1982. Subglacial volcanism in north-central British-Columbia and Iceland. Journal of Geology, 90(6): 699-715.

Anslow, F.S., Clark, P.U., Kurz, M.D. and Hostetler, S.W., 2010. Geochronology and paleoclimatic implications of the last deglaciation of the Mauna Kea Ice Cap, Hawaii. Earth and Planetary Science Letters, 297(1–2): 234-248.

Aoki, K., Ishiwaka, K. and Kanisawa, S., 1981. Fluorine geochemistry of basaltic rocks from continental and oceanic regions and petrogenetic application. Contributions to Mineralogy and Petrology, 76(1): 53-59.

Asimow, P.D. and Ghiorso, M.S., 1998. Algorithmic modifications extending MELTS to calculate subsolidus phase relations. American Mineralogist, 83(9-10): 1127-1132.

Ballard, R.D., Holcomb, R.T. and Vanandel, T.H., 1979. Galapagos rift at 86-degrees-w .3. Sheet flows, collapse pits, and lava lakes of the rift valley. Journal of Geophysical Research, 84(NB10): 5407-5420.

Ballard, R.D. and Moore, J.G., 1977. Photographic atlas of the Mid-Atlantic Ridge rift valley. Springer-Verlag : New York, United States.

Barnard, W.M., 1995. Mauna Loa Volcano; historical eruptions, exploration, and observations (1779-1910). Geophysical Monograph, 92: 1-19.

Basaltic Volcanism Study, P., 1981. Basaltic volcanism on the terrestrial planets. Pergamon Press, New York.

Batiza, R. and White, J.D.L., 2000. Submarine lavas and hyaloclastite. In: H. Sigurdsson, Houghton, B. F., McNutt, S. R., Rymer, H., Stix, J. (Editor), Encyclopedia of Volcanoes. Academic Press, San Diego, CA, United States, pp. 361-381.

Bauchy, M., Guillot, B., Micoulaut, M. and Sator, N., 2013. Viscosity and viscosity anomalies of model silicates and magmas: A numerical investigation. Chem. Geol., 346: 47-56.

Bear, A.N. and Cas, R.A.F., 2007. The complex facies architecture and emplacement sequence of a Miocene submarine mega-pillow lava flow system, Muriwal, North Island, New Zealand. Journal of Volcanology and Geothermal Research, 160(1-2): 1-22.

Benn, D.I. and Evans, D.J.A., 1998. Glaciers & glaciation. Arnold : London, United Kingdom, United Kingdom.

Bennett, M.R., Huddart, D. and Gonzalez, S., 2009. Glaciovolcanic landsystems and large-scale glaciotectonic deformation along the Brekknafjoll-Jarlhettur, Iceland. Quaternary Science Reviews, 28(7-8): 647-676.

Bennett, M.R., Huddart, D. and Waller, R.I., 2006. Diamict fans in subglacial water-filled cavities - a new glacial environment. Quaternary Science Reviews, 25(21-22): 3050-3069.

Björnsson, H., 1991. Jökulhlaups in Iceland: prediction, characteristics and simulation. Annals of Glaciology, 16: 95-106.

Blard, P.H., Lave, J., Pik, R., Wagnon, P. and Bourles, D., 2007. Persistence of full glacial conditions in the central Pacific until 15,000 years ago. Nature, 449(7162): 591-U510.

Boardman, J.W. and Kruse, F., 1994. Automated spectral analysis: a geological example using AVIRIS data, north Grapevine Mountains, Nevada, Proceedings of the Thematic Conference on Geologic Remote Sensing. Environmental Research Institute of Michigan, pp. I-407.

Bottinga, Y. and Weill, D.F., 1972. The viscosity of magmatic silicate liquids; a model calculation. American Journal of Science, 272(5): 438-475.

Boulton, G.S., Caban, P.E. and Van Gijssel, K., 1995. Groundwater flow beneath ice sheets: Part I — Large scale patterns. Quaternary Science. Reviews, 14(6): 545-562.

Boulton, G.S., Lunn, R., Vidstrand, P. and Zatsepin, S., 2007. Subglacial drainage by groundwater-channel coupling, and the origin of esker systems: Part 1-glaciological observations. Quaternary Science Reviews, 26(7-8): 1067-1090.

Brennand, T.A., 2000. Deglacial meltwater drainage and glaciodynamics: inferences from Laurentide eskers, Canada. Geomorphology, 32(3): 263-293.

Burke, M.J., Brennand, T.A. and Perkins, A.J., 2012. Evolution of the subglacial hydrologic system beneath the rapidly decaying Cordilleran Ice Sheet caused by ice-dammed lake drainage: implications for meltwater-induced ice acceleration. Quaternary Science Reviews, 50(0): 125-140.

Byrnes, J.M., Ramsey, M.S. and Crown, D.A., 2004. Surface unit characterization of the Mauna Ulu flow field, Kilauea Volcano, Hawai′i, using integrated field and remote sensing analyses. Journal of Volcanology and Geothermal Research, 135(1): 169-193.

Cameron, B.I., Wright, M., Skilling, I.P., Hungerford, J.D.G., Edwards, B. and Anonymous, 2008. Accurate ice thickness estimates from volatile contents of subglacial glasses from northern British Columbia, Canada. Abstracts with Programs - Geological Society of America, 40(5): 25.

Cas, R.A.F., Landis, C.A. and Fordyce, R.E., 1989. A monogenetic, Surtla-type, Surtseyan volcano from the Eocene Oligocene Waiareka-Deborah volcanics, Otago, New Zealand - a model. Bulletin of Volcanology, 51(4): 281-298.

Chadwick, W.W. and Embley, R.W., 1994. Lava flows from a mid-1980s submarine eruption on the cleft segment, Juan-de-Fuca ridge. Journal of Geophysical Research-Solid Earth, 99(B3): 4761-4776.

Clague, J.J. and Mathewes, R.W., 1989. Early Holocene thermal maximum in western North America - new evidence from Castle Peak, British Columbia. Geology, 17(3): 277-280.

Clark, P.U. and Walder, J.S., 1994. Subglacial drainage, eskers, and deforming beds beneath the Laurentide and Eurasian ice sheets. Geological Society of America Bulletin, 106(2): 304-314.

Clarke, G.K., 2003. Hydraulics of subglacial outburst floods: new insights from the Spring-Hutter formulation. Journal of Glaciology, 49(165): 299-313.

Clarke, G.K.C., 2005. Subglacial processes, Annual Review of Earth and Planetary Sciences. Annual Review of Earth and Planetary Sciences, pp. 247-276.

Daly, R.A., 1910. Pleistocene glaciation and the coral reef problem. American Journal of Science, 298: 12.

Desilets, D. and Zreda, M., 2003. Spatial and temporal distribution of secondary cosmic-ray nucleon intensities and applications to in situ cosmogenic dating. Earth and Planetary Science Letters, 206(1-2): 21-42.

Dimroth, E., Cousineau, P., Leduc, M. and Sanschagrin, Y., 1978. Structure and organization of Archean subaqueous basalt flows, Rouyn-Noranda area, Quebec, Canadian Journal of Earth Science, 15(6): 902-918.

Dixon, J.E., Filiberto, J.R., Moore, J.G. and Hickson, C.J., 2002. Volatiles in basaltic glasses from a subglacial volcano in northern British Columbia (Canada): implications for ice sheet thickness and mantle volatiles. Geological Society, London, Special Publications, 202(1): 255-271.

Dorn, R.I., Phillips, F.M., Zreda, M.G., Wolfe, E.W., Jull, A.J.T., Donahue, D.J., Kubik, P.W., Sharma, P. and Anonymous, 1991. Glacial chronology of Mauna Kea, Hawaii, as constrained by surface-exposure dating. Abstracts with Programs - Geological Society of America, 23(5): 239.

Dunai, T.J., 2001. Influence of secular variation of the geomagnetic field on production rates of in situ produced cosmogenic nuclides. Earth and Planetary Science Letters, 193(1-2): 197-212.

Edwards, B., Magnússon, E., Thordarson, T., Guđmundsson, M.T., Höskuldsson, A., Oddsson, B. and Haklar, J., 2012. Interactions between lava and snow/ice during the 2010 Fimmvörduháls eruption, south-central Iceland. Journal of Geophysical Research-Solid Earth, 117(B4): B04302.

Edwards, B.R. and Russell, J.K., 1999. Northern Cordilleran volcanic province: A northern Basin and Range? Geology, 27(3): 243-246.

Edwards, B.R. and Russell, J.K., 2000. Distribution, nature, and origin of Neogene-Quaternary magmatism in the northern Cordilleran volcanic province, Canada. Geological Society of America Bulletin, 112(8): 1280-1295.

Edwards, B.R., Russell, J.K. and Anderson, R.G., 2002. Subglacial, phonolitic volcanism at Hoodoo Mountain Volcano, northern Canadian Cordillera. Bulletin of Volcanology, 64(3-4): 254-272.

Edwards, B.R., Russell, J.K. and Simpson, K., 2011. Volcanology and petrology of Mathews Tuya, northern British Columbia, Canada: glaciovolcanic constraints on interpretations of the 0.730 Ma Cordilleran paleoclimate. Bulletin of Volcanology, 73(5): 479-496.

Edwards, B.R., Skilling, I.P., Cameron, B., Haynes, C., Lloyd, A. and Hungerford, J.H.D., 2009. Evolution of an englacial volcanic ridge: Pillow Ridge tindar, Mount Edziza volcanic complex, NCVP, British Columbia, Canada. Journal of Volcanology and Geothermal Research, 185(4): 251-275.

Einstein, A., 1906. Eine neue bestimmung der moleküldimensionen. Annalen der Physik, 324(2): 289-306.

Evans, D.J.A. and Benn, D.I., 2004. A practical guide to the study of glacial sediments. Arnold; Distributed in USA by Oxford University Press, London; New York.

Evans, J.M., Stone, J.O.H., Fifield, L.K. and Cresswell, R.G., 1997. Cosmogenic chlorine-36 production in K-feldspar. Nuclear Instruments & Methods in Physics Research Section B-Beam Interactions with Materials and Atoms, 123(1-4): 334-340.

Fifield, L.K., Evans, J.M., Stone, J.O. and Anonymous, 2002. Calibration of the production rate of (super 36) Cl from potassium. Geochimica et Cosmochimica Acta, 66(15A): 234.

Fifield, L.K. and Morgenstern, U., 2009. Silicon-32 as a tool for dating the recent past. Quaternary Geochronology, 4(5): 400-405.

Fiske, R.S., Rose, T.R., Swanson, D.A., Champion, D.E. and McGeehin, J.P., 2009. Kulanaokuaiki Tephra (ca. AD 400-1000): Newly recognized evidence for highly explosive eruptions at Kilauea Volcano, Hawai'i. Geological Society of America Bulletin, 121(5-6): 712-728.

Flowers, G.E. and Clarke, G.K.C., 2002. A multicomponent coupled model of glacier hydrology - 1. Theory and synthetic examples. Journal of Geophysical Research-Solid Earth, 107(B11): ECV 9-1–ECV 9-17.

Fornari, D.J., Gregg, T.K.P., Fink, J.H., Perfit, M.R., Haymon, R.M., Edwards, M.H. and Anonymous, 1994. Effusion rates of young volcanic flows on the East Pacific Rise crest near 9 degrees 50'N. Eos, Transactions, American Geophysical Union, 75(44, Suppl.): 602.

Fox, C.G., Matsumoto, H. and Lau, T.K.A., 2001. Monitoring Pacific Ocean seismicity from an autonomous hydrophone array. Journal of Geophysical Research-Solid Earth, 106(B3): 4183-4206.

Fox, C.G., Murphy, K.M. and Embley, R.W., 1988. Automated display and statistical analysis of interpreted deep-sea bottom photographs. Marine geology, 78(3): 199-216.

Fulton, R.J., 1991a. A conceptual model for growth and decay of the Cordilleran Ice-Sheet. Geographie Physique Et Quaternaire, 45(3): 281-286.

Fulton, R.J., 1971. Radiocarbon geochronology of southern British Columbia. Department of Energy, Mines and Resources.

Fulton, R.J., 1991b. A conceptual model for growth and decay of the Cordilleran Ice Sheet. Géographie physique et Quaternaire, 45(3): 281-286.

Gabrielse, H., 1963. McDame map-area, Cassiar District, British Columbia. Dept. of Mines and Technical Surveys, Canada.

Ghiorso, M.S. and Sack, R.O., 1995. Chemical mass transfer in magmatic processes; IV, A revised and internally consistent thermodynamic model for the interpolation and extrapolation of liquid-solid equilibria in magmatic systems at elevated temperatures and pressures. Contributions to Mineralogy and Petrology, 119(2-3): 197-212.

Giordano, D. and Dingwell, D.B., 2003. Non-Arrhenian multicomponent melt viscosity: a model. Earth and Planetary Science Letters, 208(3): 337-349.

Giordano, D., Russell, J.K. and Dingwell, D.B., 2008. Viscosity of magmatic liquids: A model. Earth and Planetary Science Letters, 271(1-4): 123-134.

Gosse, J.C. and Phillips, F.M., 2001. Terrestrial in situ cosmogenic nuclides: theory and application. Quaternary Science Reviews, 20(14): 1475-1560.

Goto, Y. and McPhie, J., 2004. Morphology and propagation styles of Miocene submarine basanite lavas at Stanley, northwestern Tasmania, Australia. Journal of Volcanology and Geothermal Research, 130(3-4): 307-328.

Gregg, T.K.P. and Fink, J.H., 1995. Quantification of submarine lava-flow morphology through analog experimants. Geology, 23(1): 73-76.

Gregg, T.K.P. and Fink, J.H., 1996. Quantification of extraterrestrial lava flow effusion rates through laboratory simulations. Journal of Geophysical Research-Planets, 101(E7): 16891-16900.

Gregg, T.K.P. and Fink, J.H., 2000. A laboratory investigation into the effects of slope on lava flow morphology. Journal of Volcanology and Geothermal Research, 96(3-4): 145-159.

Gregg, T.K.P. and Fornari, D.J., 1998. Long submarine lava flows: Observations and results from numerical modeling. J. Geophys. Res.-Solid Earth, 103(B11): 27517-27531.

Gregg, T.K.P., Fornari, D.J., Perfit, M.R., Haymon, R.M. and Fink, J.H., 1996. Rapid emplacement of a mid-ocean ridge lava flow on the East Pacific Rise at 9 degrees 46'-51'N. Earth and Planetary Science Letters, 144(3-4): E1-E7.

Gregg, T.K.P. and Smith, D.K., 2003. Volcanic investigations of the Puna Ridge, Hawai'i: relations of lava flow morphologies and underlying slopes. Journal of Volcanology and Geothermal Research, 126(1-2): 63-77.

Gregory, H.E. and Wentworth, C.K., 1937. General features and glacial geology of Mauna Kea, Hawaii. Geological Society of America Bulletin, 48(12): 1719-1742.

Griffiths, R.W. and Fink, J.H., 1992a. The morphology of lava flows in planetary environments - predictions from analog experiments. Journal of Geophysical Research-Solid Earth, 97(B13): 19739-19748.

Griffiths, R.W. and Fink, J.H., 1992b. Solidification and morphology of submarine lavas: a dependance on extrusion rate. Journal of Geophysical Research-Solid Earth, 97(B13): 19729-19737.

Gudmundsson, M.T., 2003. Melting of ice by magma-ice-water interactions during subglacial eruptions as an indicator of heat transfer in subaqueous eruptions. American Geophysical Union, Washington, DC, ETATS-UNIS, 12 pp.

Gudmundsson, M.T., Sigmundsson, F. and Bjornsson, H., 1997. Ice-volcano interaction of the 1996 Gjalp subglacial eruption, Vatnajokull, Iceland. Nature, 389(6654): 954-957.

Gudmundsson, M.T., Sigmundsson, F., Björnsson, H. and Högnadóttir, T., 2004. The 1996 eruption at Gjálp, Vatnajökull ice cap, Iceland: efficiency of heat transfer, ice deformation and subglacial water pressure. Bulletin of Volcanology, 66(1): 46-65.

Gurenko, A.A., Belousov, A.B., Trumbull, R.B. and Sobolev, A.V., 2005. Explosive basaltic volcanism of the Chikurachki Volcano (Kurile arc, Russia): Insights on pre-eruptive magmatic conditions and volatile budget revealed from phenocryst-hosted melt inclusions and groundmass glasses. Journal of Volcanology and Geothermal Research, 147(3-4): 203-232.

Harder, M. and Russell, J.K., 2007. Basanite glaciovolcanism at Llangorse mountain, northern British Columbia, Canada. Bulletin of Volcanology, 69(3): 329-340.

Harris, A.I., 2013. Lava flows. Modeling Volcanic Processes: The Physics and Mathematics of Volcanism: 85.

Harris, A.J. and Allen, J.S., 2008. One-, two-and three-phase viscosity treatments for basaltic lava flows. Journal of Geophysical Research-Solid Earth (1978–2012), 113(B9).

Harris, A.J., Dehn, J. and Calvari, S., 2007. Lava effusion rate definition and measurement: a review. Bulletin of Volcanology, 70(1): 1-22.

Helz, R.T., Kirschenbaum, H. and Marinenko, J.W., 1989. Diapiric transfer of melt in Kilauea Iki lava lake, Hawaii - a quick, efficient process of igneous differentiation. Geological Society of America Bulletin, 101(4): 578-594.

Hess, K.-U., Dingwell, D. and Rössler, E., 1996. Parametrization of viscosity-temperature relations of aluminosilicate melts. Chemical Geology, 128(1): 155-163.

Hock, R. and Hooke, R.L., 1993. Evolution of the internal drainage system in the lower part of the ablation area of Storglaciären, Sweden. Geological Society of America Bulletin, 105(4): 537-546.

Holcomb, R., Champion, D. and McWilliams, M., 1986. Dating recent Hawaiian lava flows using paleomagnetic secular variation. Geological Society of America Bulletin, 97(7): 829-839.

Hooke, R.L., 1984. On the role of mechanical energy in maintaining subglacial water conduits at atmospheric-pressure. Journal of Glaciology, 30(105): 180-187.

Hooke, R.L., 2005. Principles of glacier mechanics. Cambridge university press, London, UK.

Höskuldsson, A., Sparks, R. and Carroll, M., 2006. Constraints on the dynamics of subglacial basalt eruptions from geological and geochemical observations at Kverkfjöll, NE-Iceland. Bulletin of Volcanology, 68(7): 689-701.

Höskuldsson, A. and Sparks, R.S.J., 1997. Thermodynamics and fluid dynamics of effusive subglacial eruptions. Bulletin of Volcanology, 59(3): 219-230.

Hoskuldsson, A., Sparks, R.S.J. and Carroll, M.R., 2006. Constraints on the dynamics of subglacial basalt eruptions from geological and geochemical observations at Kverkfjoll, NE-Iceland. Bulletin of Volcanology, 68(7-8): 689-701.

Houghton, B.F., Swanson, D.A., Carey, R.J., Rausch, J. and Sutton, A.J., 2011. Pigeonholing pyroclasts: Insights from the 19 March 2008 explosive eruption of Kilauea volcano. Geology, 39(3): 263-266.

Irvine, T.N. and Baragar, W.R.A., 1971. A guide to the chemical classification of the common volcanic rocks. Canadian Journal of Earth Sciences, 8(5): 523-548.

Jaggar, T.A., Jr. and Finch, R.H., 1924. The explosive eruption of Kilauea in Hawaii, 1924. American Journal of Science, 8(47): 353-374.

Johnston, W.A., 1926. The Pleistocene of Cariboo and Cassiar Districts, British Columbia, Canada. Transactions of the Royal Society of Canada, ser, 3(20): 137-147.

Kadish, S.J., Head, J.W., Parsons, R.L. and Marchant, D.R., 2008. The Ascraeus Mons fan-shaped deposit: Volcano-ice interactions and the climatic implications of cold-based tropical mountain glaciation. Icarus, 197(1): 84-109.

Kavanagh, J.L., Menand, T. and Sparks, R.S.J., 2006. An experimental investigation of sill formation and propagation in layered elastic media. Earth and Planetary Science Letters, 245(3-4): 799-813.

Kennish, M.J. and Lutz, R.A., 1998. Morphology and distribution of lava flows on mid-ocean ridges: a review. Earth-Science Reviews, 43(3-4): 63-90.

Keszthelyi, L. and Denlinger, R., 1996. The initial cooling of pahoehoe flow lobes. Bulletin of Volcanology, 58(1): 5-18.

Keszthelyi, L.P., Jaeger, W.L., Dundas, C.M., Martinez-Alonso, S., McEwen, A.S. and Milazzo, M.P., 2010. Hydrovolcanic features on Mars: Preliminary observations from the first Mars year of HiRISE imaging. Icarus, 205(1): 211-229.

Kilburn, C.R.J., 2000. Lava flows and flow fields. In: H. Sigurdsson, Houghton, B. F., McNutt, S. R., Rymer, H., Stix, J. (Editors), Encyclopedia of Volcanoes. Academic Press, San Diego, CA, United States, pp. 291-305.

Klingelhöfer, F., Hort, M., K¸mpel, H.J. and Schmincke, H.U., 1999. Constraints on the formation of submarine lava flows from numerical model calculations. Journal of Volcanology and Geothermal Research, 92(3-4): 215-229.

Lal, D., 1991. Cosmic ray labeling of erosion surfaces: *in situ* nuclide production rates and erosion models. Earth and Planetary Science Letters, 104(2): 424-439.

Langmuir, C.H., Klein, E.M. and Plank, T., 1992. Petrological systematics of mid-ocean ridge basalts: Constraints on melt generation beneath ocean ridges. Geophysical Monograph Series, 71: 183-280.

Le Bas, M.J., Le Maitre, R.W., Streckeisen, A. and Zanettin, B.A., 1986. Chemical classification of volcanic rocks based on the total alkali-silica diagram. Journal of Petrology, 27(3): 745-750.

Lescinsky, D.T. and Fink, J.H., 2000. Lava and ice interaction at stratovolcanoes: Use of characteristic features to determine past glacial extents and future volcanic hazards. Journal of Geophysical Research-Solid Earth, 105(B10): 23711-23726.

Lescinsky, D.T. and Sisson, T.W., 1998. Ridge-forming, ice-bounded lava flows at Mount Rainier, Washington. Geology, 26(4): 351-354.

Lipman, P.W., 1980a. Rates of volcanic activity along the southwest rift zone of Mauna Loa Volcano, Hawaii. Eos, Transactions, American Geophysical Union, 61(6): 69.

Lipman, P.W., 1980b. The southwest rift zone of Mauna Loa; implications for structural evolution of Hawaiian volcanoes. American Journal of Science, Vol. 280-A(Part 2): 752-776.

Lipman, P.W., 1995. Declining growth of Mauna Loa during the last 100,000 years; rates of lava accumulation vs. gravitational subsidence. Geophysical Monograph, 92: 45-80.

Livingstone, S.J., Clark, C.D. and Tarasov, L., 2013. Modelling North American palaeo-subglacial lakes and their meltwater drainage pathways. Earth and Planetary Science Letters, 375(0): 13-33.

Lloyd, S., 1982. Least squares quantization in PCM. Information Theory, IEEE Transactions on Information Theory, 28(2): 129-137.

Lockwood, J.P., 1990. Implications of historical eruptive-vent migration on the northeast rift zone of Mauna Loa Volcano, Hawaii. Geology, 18(7): 611-613.

Lockwood, J.P., 1995. Mauna Loa eruptive history; the preliminary radiocarbon record. Geophysical Monograph, 92: 81-94.

Lockwood, J.P. and Lipman, P.W., 1980. Recovery of datable charcoal beneath young lavas; lessons from Hawaii. Bulletin Volcanologique, 43(3): 609-615.

Lockwood, J.P. and Lipman, P.W., 1987. Holocene eruptive history of Mauna Loa Volcano. 1044-9612, U. S. Geological Survey : Reston, VA, United States, United States.

Lockwood, J.P., Lipman, P.W., Petersen, L.D. and Warshauer, F.R., 1988. Generalized ages of surface lava flows of Mauna Loa Volcano, Hawaii. U. S. Geological Survey : Reston, VA, United States, United States.

Lodge, R.W.D. and Lescinsky, D.T., 2009. Fracture patterns at lava-ice contacts on Kokostick Butte, OR, and Mazama Ridge, Mount Rainier, WA: Implications for flow emplacement and cooling histories. Journal of Volcanology and Geothermal Research, 185(4): 298-310.

Loughlin, S.C., 2002. Facies analysis of proximal subglacial and proglacial volcaniclastic successions at the Eyjafjallajökull central volcano, southern Iceland. Geological Society, London, Special Publications, 202(1): 149-178.

Macdonald, G.A., 1971. Geologic map of the Mauna Loa Quadrangle, Hawaii. U.S. Geol. Surv., United States.

Manga, M., Castro, J., Cashman, K.V. and Loewenberg, M., 1998. Rheology of bubble-bearing magmas. Journal of Volcanology and Geothermal Research, 87(1): 15-28.

Manga, M. and Loewenberg, M., 2001. Viscosity of magmas containing highly deformable bubbles. Journal of Volcanology and Geothermal Research, 105(1): 19-24.

Manley, C.R., 1992. Extended cooling and viscous flow of large, hot rhyolite lavas: implications of numerical modeling results. Journal of Volcanology and Geothermal Research, 53(1-4): 27-46.

Marsh, B., 1981. On the crystallinity, probability of occurrence, and rheology of lava and magma. Contributions to Mineralogy and Petrology, 78(1): 85-98.

Masarik, J. and Reedy, R.C., 1995. Terrestrial cosmogenic-nuclide production systematics calculated from numerical simulations. Earth and Planetary Science Letters, 136(3-4): 381-395.

Mastin, L.G., 1997. Evidence for water influx from a caldera lake during the explosive hydromagmatic eruption of 1790, Kilauea volcano, Hawaii. Journal of Geophysical Research-Solid Earth, 102(B9): 20093-20109.

Mastin, L.G., Christiansen, R.L., Thornber, C., Lowenstern, J. and Beeson, M., 2004. What makes hydromagmatic eruptions violent? Some insights from the Keanakako'i Ash, Kilauea Volcano, Hawai'i. Journal of Volcanology and Geothermal Research, 137(1-3): 15-31.

Mathews, W.H., 1947. 'Tuyas,' flat-topped volcanoes in northern British Columbia. American Journal of Science, 245(9): 560-570.

McCarter, R.L., Fodor, R.V. and Trusdell, F., 2006. Perspectives on basaltic magma crystallization and differentiation: Lava-lake blocks erupted at Mauna Loa volcano summit, Hawaii. Lithos, 90(3-4): 187-213.

McElhinny, M.W. and Senanayake, W.E., 1982. Variations in the geomagnetic dipole-1 - the past 50,000 years. Journal of Geomagnetism and Geoelectricity, 34(1): 39-51.

McGarvie, D., 2009. Rhyolitic volcano-ice interactions in Iceland. Journal of Volcanology and Geothermal Research, 185(4): 367-389.

Mee, K., Tuffen, H. and Gilbert, J.S., 2006. Snow-contact volcanic facies and their use in determining past eruptive environments at Nevados de Chillan volcano, Chile. Bulletin of Volcanology, 68(4): 363-376.

Menounos, B., Osborn, G., Clague, J.J. and Luckman, B.H., 2009. Latest Pleistocene and Holocene glacier fluctuations in western Canada. Quaternary Science Reviews, 28(21-22): 2049-2074.

Moore, H., 1987. Preliminary estimates of the rheological properties of 1984 Mauna Loa lava. US Geological Survey Professional Paper, 1350: 1569-1588.

Moore, J.G., 1975. Mechanism of formation of pillow lava. American Scientist, 63(3): 269-277.

Moore, J.G. and Calk, L.C., 1991. Degassing and differentiation in subglacial volcanoes, Iceland. Journal of Volcanology and Geothermal Research, 46(1-2): 157-180.

Moore, J.G. and Charlton, D.W., 1984. Ultrathin lava layers exposed new San Louis Obsipo Bay, California. Geology, 12(9): 542-545.

Moore, J.G., Hickson, C.J. and Calk, L.C., 1995. Tholeiitic-alkalic transition at subglacial volcanoes, Tuya region, British Columbia, Canada. Journal of Geophysical Research-Solid Earth, 100(B12): 24577-24592.

Moore, J.G., Phillips, R.L., Grigg, R.W., Peterson, D.W. and Swanson, D.A., 1973. Flow of lava into sea, 1969-1971, Kilauea Volcano, Hawaii. Geological Society of America Bulletin, 84(2): 537-546.

Newman, S. and Lowenstern, J.B., 2002. VOLATILECALC: a silicate melt-H_2O-CO_2 solution model written in Visual Basic for excel. Computers & Geosciences, 28(5): 597-604.

Nye, J., 1976. Water flow in glaciers: jokulhlaups, tunnels and veins. Journal of Glaciology, 17(76).

Nye, J.F., 1953. The flow law of ice from measurements in glacier tunnels, laboratory experiments and the Jungfraufirn borehole experiment. Proceedings of the Royal Society of London. Series A. Mathematical and Physical Sciences, 219(1139): 477-489.

Pedersen, G.B.M., Head, J.W., III and Wilson, L., 2010. Formation, erosion and exposure of Early Amazonian dikes, dike swarms and possible subglacial eruptions in the Elysium Rise/Utopia Basin Region, Mars. Earth and Planetary Science Letters, 294(3-4): 424-439.

Phan-Thien, N. and Pham, D., 1997. Differential multiphase models for polydispersed suspensions and particulate solids. Journal of Non-Newtonian Fluid Mechanics, 72(2): 305-318.

Phan-Thien, N. and Pham, D., 2000. Differential multiphase models for polydispersed spheroidal inclusions: thermal conductivity and effective viscosity. International journal of engineering science, 38(1): 73-88.

Phillips, F.M., Stone, W.D. and Fabryka-Martin, J.T., 2001. An improved approach to calculating low-energy cosmic-ray neutron fluxes near the land/atmosphere interface. Chemical Geology, 175(3-4): 689-701.

Pigati, J.S., Zreda, M., Zweck, C., Almasi, P.F., Elmore, D. and Sharp, W.D., 2008. Ages and inferred causes of late Pleistocene glaciations on Mauna Kea, Hawai'i. JQS. Journal of Quaternary Science, 23(6-7): 683-702.

Pinkerton, H. and Stevenson, R., 1992. Methods of determining the rheological properties of magmas at sub-liquidus temperatures. Journal of Volcanology and Geothermal Research, 53(1): 47-66.

Porter, S.C., 1979a. Geologic map of Mauna Kea Volcano, Hawaii. Geological Society of America, [Boulder, CO], pp. 4.

Porter, S.C., 1979b. Quaternary stratigraphy and chronology of Mauna Kea, Hawaii; a 380,000-yr record of mid-Pacific volcanism and ice-cap glaciation. Geological Society of America Bulletin, 90(7): 609-611, 980-1093.

Porter, S.C., 1986. Glaciation of Mauna Kea, Hawaii. Quaternary Science Reviews, 5: 181-182.

Porter, S.C., 1987. Pleistocene subglacial eruptions on Mauna Kea. U. S. Geological Survey Professional Paper: 587-598.

Porter, S.C., 2005. Pleistocene snowlines and glaciation of the Hawaiian Islands. Quaternary International, 138: 118-128.

Porter, S.C., Stuiver, M. and Yang, I.C., 1977. Chronology of Hawaiian glaciations. Science, 195(4273): 61-63.

Ramsey, M.S. and Fink, J.H., 1999. Estimating silicic lava vesicularity with thermal remote sensing: a new technique for volcanic mapping and monitoring. Bulletin of Volcanology, 61(1-2): 32-39.

Resing, J.A., Rubin, K.H., Embley, R.W., Lupton, J.E., Baker, E.T., Dziak, R.P., Baumberger, T., Lilley, M.D., Huber, J.A. and Shank, T.M., 2011. Active submarine eruption of boninite in the northeastern Lau Basin. Nature Geoscience, 4(11): 799-806.

Rhodes, J.M., 1988. Geochemistry of the 1984 Mauna Loa eruption - implications for magma storage and supply. Journal of Geophysical Research-Solid Earth and Planets, 93(B5): 4453-4466.

Richards, J.A. and Jia, X., 1999. Remote Sensing Digital Image Analysis: An Introduction. Springer-Verlag New York, Inc., 363 pp.

Roots, E.F., 1954. Geology and mineral deposits of Aiken Lake map-area, British Columbia. E. Cloutier.

Roscoe, R., 1952. The viscosity of suspensions of rigid spheres. British Journal of Applied Physics, 3(8): 267.

Rothlisberger, H., 1972. Water pressure in subglacial channels. Journal of Glaciology, 11(62): 177-203.

Rowland, S.K. and Walker, G.P.L., 1990. Pahoehoe and aa in Hawaii: volumetric flow rate controls the lava structure. Bulletin of Volcanology, 52(8): 615-628.

Russell, A.J., Gregory, A.R., Large, A.R., Fleisher, P.J. and Harris, T.D., 2007. Tunnel channel formation during the November 1996 jokulhlaup, Skeiethararjokull, Iceland. Annals of Glaciology, 45(1): 95-103.

Russell, J.K., Giordano, D., Dingwell, D.B. and Kai-Uwe, H., 2002. Modelling the non-Arrhenian rheology of silicate melts Numerical considerations. European journal of mineralogy, 14(2): 417-427.

Ryder, J.M. and Maynard, D., 1991. The Cordilleran ice-sheet in northern British Columbia. Geographie Physique Et Quaternaire, 45(3): 355-363.

Ryerson, F., Weed, H. and Piwinskii, A., 1988. Rheology of subliquidus magmas: 1. Picritic compositions. Journal of Geophysical Research-Solid Earth (1978–2012), 93(B4): 3421-3436.

Sanchez, M.C., Sarrionandia, F., Juteau, T. and Ibarguchi, J.I.G., 2012. Structure and organization of submarine basaltic flows: sheet flow transformation into pillow lavas in shallow submarine environments. International Journal of Earth Sciences, 101(8): 2201-2214.

Sansone, F., 1990. Lava meets the sea: Honolulu. LavaVideo Productions, 27.

Schopka, H.H., Gudmundsson, M.T. and Tuffen, H., 2006. The formation of Helgafell, southwest Iceland, a monogenetic subglacial hyaloclastite ridge: Sedimentology, hydrology and volcano-ice interaction. Journal of Volcanology and Geothermal Research, 152(3-4): 359-377.

Seaberg, S.Z., Seaberg, J.Z., Hooke, R.L. and Wiberg, D.W., 1988. Character of the englacial and subglacial drainage system in the lower part of the ablation area of Storglaciären, Sweden, as revealed by dye-trace studies. Journal of Glaciology, 34: 217-227.

Shaw, H., 1972. Viscosities of magmatic silicate liquids; an empirical method of prediction. American Journal of Science, 272(9): 870-893.

Shaw, H.R., 1969. Rheology of basalt in the melting range. Journal of Petrology, 10(3): 510-535.

Skilling, I.P., 1994. Evolution of an englacial volcano: Brown Bluff, Antarctica. Bulletin of Volcanology, 56(6): 573-591.

Skilling, I.P., 2002. Basaltic pahoehoe lava-fed deltas; large-scale characteristics, clast generation, emplacement processes and environmental discrimination. Geological Society Special Publications, 202: 91-113.

Skilling, I.P., 2009. Subglacial to emergent basaltic volcanism at Hlödufell, south-west Iceland: A history of ice-confinement. Journal of Volcanology and Geothermal Research, 185(4): 276-289.

Smellie, J.L., 2000. Subglacial eruptions. In: H. Sigurdsson, Houghton, B. F., McNutt, S. R., Rymer, H., Stix, J. (Editors), Encyclopedia of Volcanoes. Academic Press, San Diego, CA, United States, pp. 403-419.

Smellie, J.L., 2001. Lithofacies architecture and construction of volcanoes erupted in englacial lakes; icefall nunatak, Mount Murphy, eastern Marie Byrd Land, Antarctica. Special Publication of the International Association of Sedimentologists, 30: 9-34.

Smellie, J.L., 2008. Basaltic subglacial sheet-like sequences: Evidence for two types with different implications for the inferred thickness of associated ice. Earth-Science Reviews, 88(1-2): 60-88.

Smellie, J.L. and Hole, M.J., 1997. Products and processes in Pliocene-Recent, subaqueous to emergent volcanism in the Antarctic Peninsula: Examples of englacial Surtseyan volcano construction. Bulletin of Volcanology, 58(8): 628-646.

Smellie, J.L., Hole, M.J. and Nell, P.A.R., 1993. Late Miocene valley-confined subglacial volcanism in northern Alexander Island, Antarctic Peninsula. Bulletin of Volcanology, 55(4): 273-288.

Smellie, J.L., Johnson, J.S., McIntosh, W.C., Esser, R., Gudmundsson, M.T., Harnbrey, M.J. and de Vries, B.V., 2008. Six million years of glacial history recorded in volcanic lithofacies of the James Ross Island Volcanic Group, Antarctic Peninsula. Palaeogeography Palaeoclimatology Palaeoecology, 260(1-2): 122-148.

Smellie, J.L., McIntosh, W.C. and Esser, R., 2006. Eruptive environment of volcanism on Brabant Island: Evidence for thin wet-based ice in northern Antarctic Peninsula during the Late Quaternary. Palaeogeography Palaeoclimatology Palaeoecology, 231(1-2): 233-252.

Smellie, J.L. and Skilling, I.P., 1994. Products of subglacial volcanic eruptions under different ice thicknesses - 2 examples from Antarctica. Sedimentary Geology, 91(1-4): 115-129.

Souther, J.G., 1971. Geology of the Telegraph Creek map-area, British Columbia. Open File Report Geological Survey of Canada, Report, 68(30).

Souther, J.G., 1992. The late Cenozoic Mount Edziza volcanic complex, British Columbia. Memoir Geological Survey of Canada, Report, 420(320).

Souther, J.G., Armstrong, R.L. and Harakal, J., 1984. Chronology of the peralkaline, late Cenozoic Mount Edziza volcanic complex, northern British Columbia, Canada. Geological Society of America Bulletin, 95(3): 337-349.

Spooner, I.S. and Osborn, G.D., 2000. Geomorphology and Late Wisconsinan sedimentation in the Stikine River Valley, northern British Columbia. Quaternary International, 68–71(0): 285-296.

Spooner, I.S., Osborn, G.D., Barendregt, R.W. and Irving, E., 1995. A record of Early Pleistocene glaciation on the Mount Edziza plateau, northwestern British Columbia. Canadian Journal of Earth Science, 32(12): 2046-2056.

Spörli, K.B. and Rowland, J.V., 2006. 'Column on column' structures as indicators of lava/ice interaction, Ruapehu andesite volcano, New Zealand. Journal of Volcanology and Geothermal Research, 157(4): 294-310.

Spring, U. and Hutter, K., 1982. Conduit flow of a fluid through its solid phase and its application to intraglacial channel flow. International Journal of Engineering Science, 20(2): 327-363.

Stearns, H.T., 1945. Glaciation of Mauna Kea, Hawaii. Geological Society of America Bulletin, 56(3): 267-274.

Stearns, H.T., 1946. Geology of the Hawaiian Islands. Hawaii, Division of Hydrography : Honolulu, HI, United States, United States.

Stearns, H.T. and Macdonald, G.A., 1942. Geology and ground-water resources of the Island of Maui, Hawaii. Bulletin - State of Hawaii, Division of Hydrography: 344.

Stevenson, J.A., McGarvie, D.W., Smellie, J.L. and Gilbert, J.S., 2006. Subglacial and ice-contact volcanism at the Öræfajökull stratovolcano, Iceland. Bulletin of Volcanology, 68(7-8): 737-752.

Stevenson, J.A., Smellie, J.L., McGarvie, D.W., Gilbert, J.S. and Cameron, B.I., 2009. Subglacial intermediate volcanism at Kerlingarfjöll, Iceland: Magma-water interactions beneath thick ice. Journal of Volcanology and Geothermal Research, 185(4): 337-351.

Stone, J.O. and Ballantyne, C.K., 2006. Dimensions and deglacial chronology of the Outer Hebrides Ice Cap, northwest Scotland: implications of cosmic ray exposure dating. Journal of Quaternary Science, 21(1): 75-84.

Stone, J.O.H., Evans, J.M., Fifield, L.K., Allan, G.L. and Cresswell, R.G., 1998. Cosmogenic chlorine-36 production in calcite by muons. Geochimica Et Cosmochimica Acta, 62(3): 433-454.

Stumpf, A.J., Broster, B.E. and Levson, V.M., 2000. Multiphase flow of the late Wisconsinan Cordilleran ice sheet in western Canada. Geological Society of America Bulletin, 112(12): 1850-1863.

Swanson, D.A., Rose, T.R., Fiske, R.S. and McGeehin, J.P., 2012a. Keanakako'i Tephra produced by 300 years of explosive eruptions following collapse of Kilauea's caldera in about 1500 CE. Journal of Volcanology and Geothermal Research, 215: 8-25.

Swanson, D.A., Zolkos, S.P. and Haravitch, B., 2012b. Ballistic blocks around Kilauea Caldera: Their vent locations and number of eruptions in the late 18th century. Journal of Volcanology and Geothermal Research, 231,Äì232(0): 1-11.

Tonooka, H., Sakuma, F., Kudoh, M. and Iwafune, K., 2004. ASTER/TIR onboard calibration status and user-based recalibration, Remote Sensing. International Society for Optics and Photonics, pp. 191-201.

Trusdell, F.A., 1995. Lava flow hazards and risk assessment on Mauna Loa Volcano, Hawaii. Geophysical Monograph, 92: 327-336.

Trusdell, F.A., 2007. Assessing lava flow hazards from Mauna Loa; a natural laboratory. Eos, Transactions, American Geophysical Union, 88(52, Suppl.): @AbstractV14A-01.

Trusdell, F.A., 2012. Mauna Loa; history, hazards and risk of living with the world's largest volcano, U. S. Geological Survey : Reston, VA, United States, United States.

Trusdell, F.A. and Swannell, P., 2003. Explosive deposits on Mauna Loa. Abstracts - International Volcanological Congress, 3: 135-135.

Tuffen, H., 2007. Models of ice melting and edifice growth at the onset of subglacial basaltic eruptions. J. Geophys. Res.-Solid Earth, 112(B3): 14.

Tuffen, H., Owen, J. and Denton, J., 2010. Magma degassing during subglacial eruptions and its use to reconstruct palaeo-ice thicknesses. Earth-Science Reviews, 99(1-2): 1-18.

Walder, J.S., 1986. Hydraulics of subglacial cavities. J. Glaciol, 32(112): 439-445.

Walder, J.S., 2010. Rothlisberger channel theory: its origins and consequences. Journal of Glaciology, 56(200): 1079-1086.

Walder, J.S. and Fowler, A., 1994. Channelized subglacial drainage over a deformable bed. Journal of Glaciology, 40(134): 3-15.

Walker, G.P.L., 1992. Morphometric study of pillow-size spectrum among pillow lavas. Bulletin of Volcanology, 54(6): 459-474.

Wells, G., Bryan, W.B. and Pearce, T.H., 1979. Comparative Morphology of Ancient and Modern Pillow Lavas. The Journal of Geology, 87(4): 427-440.

Wentworth, C.K., 1935. Mauna Kea, the White Mountain of Hawaii. Mid-Pacific Magazine, 48(4): 290-296.

Wentworth, C.K. and Powers, W.E., 1941. Multiple glaciation of Mauna Kea, Hawaii. Geological Society of America Bulletin, 52(8): 1193-1217.

Werner, R. and Schmincke, H.U., 1999. Englacial vs lacustrine origin of volcanic table mountains: evidence from Iceland. Bulletin of Volcanology, 60(5): 335-354.

White, J.D.L., 2000. Subaqueous eruption-fed density currents and their deposits. Precambrian Research, 101(2-4): 87-109.

White, J.D.L. and Houghton, B.F., 2006. Primary volcaniclastic rocks. Geology, 34(8): 677-680.

Wilson, L. and Head, J.W., III, 2002. Heat transfer and melting in subglacial basaltic volcanic eruptions: implications for volcanic deposit morphology and meltwater volumes. Geological Society, London, Special Publications, 202(1): 5-26.

Wolfe, E.W., Wise, W.S. and Dalrymple, G.B., 1997. The geology and petrology of Mauna Kea Volcano, Hawaii; a study of postshield volcanism. U. S. Geological Survey Professional Paper: 129-129, 124 sheets.

Yamagishi, H., 1985. Growth of pillow lobes - evidence from pillow lavas of Hokkaido, Japan, and North Island, New Zealand. Geology, 13(7): 499-502.

Yamagishi, H., 1991. Morphological features of miocene submarine coherent lavas from the green tuff basins - examples from basaltic and andesitic rocks from the Shimokita peninsula, Northern Japan. Bulletin of Volcanology, 53(3): 173-181.